# Neutrino-Induced Muons in the MINOS Far Detector

Brian J. Rebel

Submitted to the faculty of the University Graduate School
in partial fulfillment of the requirements
for the degree
Doctor of Philosophy
in the Department of Astronomy,
Indiana University
August 25, 2004

Accepted by the Graduate Faculty, Indiana University, in partial fulfillment of the requirements for the degree of Doctor of Philosophy.

Stuart L. Mufson, Ph.D.

James A. Musser, Ph.D.

Mark D. Messier, Ph.D.

Constantine Delyannis, Ph.D.

August 25, 2004

© 2004
Brian J. Rebel ALL RIGHTS RESERVED

To Mom, Dad, Chad and Jenny.

# Acknowledgments

There are so many people that deserve a word of thanks for helping me to reach this point in my career. Some of the names at the top of that list belong to the members of my committee. Stuart Mufson deserves more thanks than I can put into words here. He has been an outstanding adviser and I know that I could not have been as involved in MINOS or had such a successful graduate career without his guidance. Even more than that, I consider him a good friend. I want to thank Jim Musser for encouraging and pushing me to really understand my plots. I thank Mark Messier for teaching me so much about neutrinos and plot-craft. I thank Con Delyannis for always showing an interest in my work.

I also want to thank the people of the IU Astronomy Department who made my time here so enjoyable. Thanks to the students who went before and showed me that it really is possible to finish - Bob Berrington, Todd Hillwig, Shawn Slavin, Aaron Steinhauer and Adam Rengstorf. Many thanks to those who will still be here after I leave for helping to keep me sane these last few months - Stella Kafka, who alternately kept me caffeinated or got me to relax, Nick Mostek for being a fun officemate and weight lifting partner, and Steve Margheim for the many parties thrown at his place. Thanks to Brenda Records for answering all of my questions about IU policies and for the many birthday cakes and assorted goodies I have enjoyed over the years.

Thanks also to Eric Ost and Christina Lirot for keeping the computing facilities up and running.

I would like to thank the people of the Research and Technical Services department of Indiana University, especially George Turner. They were a great help in getting me set up to use and abuse the AVIDD clusters. Without those machines, I would probably still be waiting for the data to finish my dissertation.

Finally, I thank my parents, Gary and Carolyn, who have always told me I could do anything I set my mind to do. I feel very fortunate to be their son. I also want to thank my adopted parents, Keith and Jean Ross. I can't express how much all the Sunday dinners followed by naps taken during sporting events have meant to me these last 6 years.

Brian J. Rebel

Department of Astronomy

Indiana University

Neutrino-Induced Muons in the MINOS Far Detector

The Main Injector Neutrino Oscillation Search (MINOS) is an experiment designed to probe the phenomenon of neutrino oscillations. When MINOS is completed it will consist of a neutrino beam and two detectors, which are separated by a distance of 735 km. The near detector measures the energy distribution and flux of a beam of muon neutrinos produced at Fermilab, while the far detector, located in Soudan, MN, measures these same neutrino properties 735 km away. The signal for a detection of neutrino oscillations is a deficit of neutrinos at the far detector compared to expectations based on the near detector measurements.

In addition to measuring beam neutrinos, the far detector can be used to measure neutrinos produced in cosmic ray interactions in the atmosphere. While waiting for the beam to begin running, the far detector was used in this mode. Several previous experiments, such as Super-K and MACRO, have suggested that the atmospheric neutrinos oscillate between different flavor states. This dissertation looks for an oscillation signal in the atmospheric neutrinos by using muons resulting from the interaction of the atmospheric neutrinos in the rock surrounding the MINOS far detector. MINOS has the advantage of a flat overburden allowing it to measure neutrino-induced muons coming from above the horizon. This advantage allows for the search for an oscillation signal to be extended into new regions of parameter space. In addition, MINOS is the first magnetized underground neutrino detector,

an advantage that allows it to distinguish between muons created by neutrinos and those created by anti-neutrinos.

A total of 50 neutrino-induced muon events were found in the data. A fit for the oscillation parameters $\sin^2 2\theta$ and $\Delta m^2$ shows that the data are consistent with both the null oscillation hypothesis and the observation of oscillations at the 90% confidence level. The data were also analyzed for evidence of $CPT$-violation in neutrino oscillations and the data are consistent with $CPT$ being conserved at 68% confidence. The predicted confidence contours for the neutrino oscillation and $CPT$-violation analyses indicate that a 4 year exposure should allow MINOS to make a definite statement for both analyses.

# Contents

**1 Introduction** **1**
1.1 Neutrino History . . . . . 1
1.2 Neutrino Interactions . . . . . 3
1.3 Neutrino Mass . . . . . 6
1.4 Personal Contributions to the MINOS Experiment . . . . . 9

**2 Neutrino Oscillation Phenomenology** **13**
2.1 Oscillations in Vacuum . . . . . 13
2.1.1 Two Neutrino Oscillations . . . . . 19
2.1.2 Three Neutrino Oscillations . . . . . 21

**3 Neutrino Oscillation Experiments** **23**
3.1 Hints of Neutrino Oscillations . . . . . 23
3.1.1 Radiochemical Experiments . . . . . 25
3.1.2 Water-Cherenkov Experiments . . . . . 27
3.2 SNO and Solar Neutrino Oscillations . . . . . 29
3.2.1 Comparison of Results with Prediction . . . . . 31
3.3 Reactor Experiments . . . . . 35
3.4 Short Baseline Experiments . . . . . 39
3.5 Atmospheric Neutrino Experiments . . . . . 40
3.5.1 Contained Vertex Event Analyses . . . . . 42
3.5.2 Neutrino-Induced Muon Analyses . . . . . 45
3.6 Long Baseline Experiments . . . . . 49
3.7 Conclusions . . . . . 52

**4 The MINOS Far Detector** **57**
4.1 Introduction . . . 57
4.2 Scintillator System . . . 65
4.2.1 Scintillator Characteristics . . . 65
4.2.2 Fiber Characteristics . . . 66
4.2.3 Optical Connectors . . . 67
4.2.4 MUX Box Design and Construction . . . 70
4.2.5 The Multiplexing Pattern . . . 72
4.3 Timing Calibrations . . . 76
4.3.1 Intra-Crate Timing Constants . . . 77
4.3.2 Inter-Crate Timing Offsets . . . 81
4.3.3 Quality and Stability of $t_0$ Corrections . . . 84

**5 The Far Detector Demultiplexing Algorithm** **92**
5.1 Introduction . . . 92
5.2 Basics of the Algorithm . . . 94
5.2.1 DeMuxing Individual Planes . . . 95
5.2.2 Determining the Event Length and Direction . . . 99
5.3 Reconstructing the Event . . . 100
5.3.1 Beam Events . . . 101
5.3.2 Cosmic Ray Events . . . 112

**6 Cosmic Ray Muons** **124**
6.1 Introduction . . . 124
6.2 Detector Acceptance and Efficiencies . . . 125
6.3 Cosmic Ray Muon Distributions . . . 132
6.4 Vertical Single Muon Intensity . . . 140
6.5 Charge Sign Determination . . . 142
6.5.1 $N_{\mu^+}/N_{\mu^-}$ Ratio from Data . . . 146
6.5.2 Monte Carlo Studies of Charge Identification . . . 155
6.6 Summary . . . 176

**7 Atmospheric $\nu$ Event Rates** **179**
7.1 Introduction . . . 179

7.2 Atmospheric $\nu$ Flux Calculations . . . . . 180
7.2.1 Analytic Approximations of the Atmospheric $\nu$ Flux . . . . . 181
7.2.2 Uncertainties in the Calculations . . . . . 186
7.3 Analytic Approximations of the Neutrino Production Heights . . . . . 187
7.4 Neutrino Cross Sections . . . . . 192

**8 Neutrino Oscillation Analysis 197**
8.1 Identifying Neutrino-Induced Upward-going and Horizontal Muons . . 197
8.1.1 Upward-Going Muons . . . . . 198
8.1.2 Horizontal Muons . . . . . 208
8.2 Event Distributions . . . . . 213
8.3 Oscillation Analysis . . . . . 217
8.3.1 Fitting the Data . . . . . 217
8.3.2 Confidence Intervals . . . . . 222
8.4 Results for $\nu_\mu \rightarrow \nu_\tau$ Oscillations . . . . . 228
8.5 *CPT*-Violation Search . . . . . 230
8.6 4 Year Predictions . . . . . 234

**9 Conclusions 238**

# List of Figures


2.1 Neutrino survival probability as a function of neutrino energy and $\Delta m^2$. 20

3.1 Flux for various solar neutrinos as a function of energy. . . . . 25
3.2 Fluxes of $B^8$ solar neutrinos deduced from the SNO measurement. . . 33
3.3 Allowed region for the solar neutrino oscillation parameter space. . . 34
3.4 The reported KamLAND Energy Spectrum. . . . . 37
3.5 The oscillation probability for KamLAND parameters. . . . . 38
3.6 The KamLAND parameter space confidence intervals. . . . . 39
3.7 Atmospheric $\nu_\mu$ fluxes at an underground detector. . . . . 43
3.8 The Super-K multi-GeV $\cos\theta$ distribution. . . . . 45
3.9 Confidence intervals for the Super-K neutrino-induced muon analysis [1]. 47
3.10 Results for the MACRO neutrino-induced muon analysis [2]. . . . . 48
3.11 Measured energy spectrum from the K2K experiment. . . . . 51
3.12 Confidence intervals for the K2K experiment. . . . . 51
3.13 $\text{Mass}^2$ spectrum for the three neutrino mass states [3]. . . . . 53
3.14 Aerial view of Fermilab. . . . . 55

4.1 Schematic of the MINOS far detector. . . . . 58
4.2 An instrumented plane of the far detector. . . . . 59
4.3 Schematic of the light path from particle interaction in a scintillator strip to the PMT. . . . . 60
4.4 A 20 strip wide scintillator module. . . . . 61
4.5 Fiber optic cables running from the modules to the steel boxes. . . . 62
4.6 Several views of the M16 phototube. . . . . 62
4.7 The completed MINOS far detector. . . . . 64
4.8 The magnetic field map for planes in the far detector. . . . . 65

4.9 Uniformity of scintillator in the far detector. . . . . 67
4.10 Drawing for an M-type connector. . . . . 69
4.11 Drawing for a C-type connector. . . . . 69
4.12 Drawing for a MUX box. . . . . 71
4.13 Mechanical drawing of the cookie used to couple fibers to PMTs. . . . 72
4.14 Lacing order for pixels connected to one plane of the far detector. . . 73
4.15 Distribution of $\chi^2/ndf$ for the fit track of cosmic ray events. The tracks in the unshaded region are kept to generate the timing calibrations. . 78
4.16 Values of $\Delta t_0$ for each channel in the detector after 1 iteration (solid line) and after 5 iterations (dashed line). . . . . 82
4.17 Histogram of differences in $\overline{t_0}$ between sets of crates. . . . . 83
4.18 The $t_0$ corrections in ns vs logical strip number. . . . . 84
4.19 Distributions of $1/\beta$ for different numbers of planes crossed in an event. 86
4.20 Distribution of the differences in the transverse position of a hit along a strip as given by timing and tracking. . . . . 88
4.21 Coverage of strips hit at least 20 times in the data set. . . . . 89
4.22 Coverage of strips hit at least 75 times in the data set. . . . . 89
4.23 The rms of the $t_0$ corrections for channels in the Far Detector. . . . . 90
4.24 Histogram of the differences in $t_0$ corrections from different sets of runs. 91

5.1 Flow chart for the first steps of the DeMuxing Algorithm. . . . . 93
5.2 Fraction of signal mated in the top three hypotheses for a plane in beam events. . . . . 98
5.3 Flow chart for the beam DeMuxing Algorithm. . . . . 102
5.4 Flow chart for the beam DeMuxing sliding window algorithm. . . . . 106
5.5 Fraction of total signal correctly DeMuxed in shower regions. . . . . 109
5.6 Fraction of total signal in a shower as a function of the correctly DeMuxed fraction of the total. . . . . 109
5.7 Example beam event containing a large shower. . . . . 110
5.8 Example beam event where the shower was misreconstructed in the UZ view as the crosses in planes 300 - 320 do not overlap with the circles. The display is explained in figure 5.7 . . . . . 111
5.9 Fraction of total strips in a track correctly DeMuxed. . . . . 111
5.10 Example beam event showing a reconstructed track. . . . . 112

5.11 Flow chart for the cosmic ray DeMuxing Algorithm. . . . . 115
5.12 Flow chart for the Sliding Window Algorithm. . . . . 117
5.13 Results of the single module DeMuxing test. . . . . 119
5.14 Fraction of stray planes in an event versus total valid planes. . . . . 120
5.15 Event 96 from run 2532. . . . . 122
5.16 Event 102 from run 2532. . . . . 122
5.17 Event 138 from run 2532. . . . . 123

6.1 Projected area of the MINOS far detector in $\cos\theta$ and azimuth. . . . 126
6.2 Efficiency of the MINOS far detector in $\cos\theta$ and azimuth. . . . . 126
6.3 Difference in degrees between the truth and reconstructed zenith angle for cosmic ray Monte Carlo events. . . . . 129
6.4 Difference in degrees between truth and reconstructed zenith angle as a function of truth zenith angle. . . . . 130
6.5 Difference in degrees between the truth and reconstructed azimuthal angle for cosmic ray Monte Carlo events. . . . . 131
6.6 Difference in degrees between truth and reconstructed azimuthal angle as a function of truth azimuthal angle. . . . . 131
6.7 Acceptance of the MINOS far detector in $\cos\theta$ and azimuth. . . . . 132
6.8 $\cos\theta$ distribution for downward-going muons. . . . . 133
6.9 Azimuthal distributions for cosmic ray muons. . . . . 135
6.10 $\cos\theta$ distribution for Monte Carlo events. . . . . 136
6.11 Azimuthal distribution for Monte Carlo events. . . . . 138
6.12 Right ascension distribution for cosmic ray muons. . . . . 139
6.13 Declination distribution for cosmic ray muons. . . . . 140
6.14 Measured vertical muon intensity for the MINOS data. . . . . 141
6.15 Global vertical muon intensity as a function of slant depth. . . . . 143
6.16 $\cos\theta$ distributions for $\mu^+$ and $\mu^-$. . . . . 147
6.17 Azimuthal distributions (top) for the $\mu^+$ and $\mu^-$. . . . . 148
6.18 Fit momentum distributions for the $\mu^+$ and $mum$. . . . . 149
6.19 Ratio of $\mu^+$ to $\mu^-$ vertical intensity. . . . . 149
6.20 $N_{\mu^+}/N_{\mu^-}$ as a function of $(q/p)/\sigma_{q/p}$. . . . . 151
6.21 Detector acceptance and $N_{\mu^+}/N_{\mu^-}$ in several 2-dimensional views. . . 152

6.22 Detector acceptance and $N_{\mu^+}/N_{\mu^-}$ based on Monte Carlo $p_{\text{truth}}$ in several 2-dimensional views. . . . . 153
6.23 $N_{\mu^+}/N_{\mu^-}$ in several 2-dimensional views based on Monte Carlo $p_{\text{fit}}$. . 154
6.24 $N_{\mu^+}/N_{\mu^-}$ as a function of $z$-position. . . . . 156
6.25 Ratio of cosmic ray Monte Carlo $\mu^+$ to $\mu^-$. . . . . 157
6.26 Efficiency for selecting $\mu^+$ and $\mu^-$. . . . . 158
6.27 Purity of charge identification as a function of azimuth. . . . . 159
6.28 Purity of charge identification as a function of azimuth using fit $q/p$. . 160
6.29 Purity of charge identification as a function of azimuth for various momenta. . . . . 162
6.30 Purity of charge identification as a function of impact parameter for Monte Carlo events. . . . . 164
6.31 Purity of charge identification as a function of track length for Monte Carlo events. . . . . 165
6.32 Purity of charge identification as a function of $(q/p)/\sigma_{q/p}$ for Monte Carlo events. . . . . 166
6.33 Ratio of cosmic ray Monte Carlo $\mu^+$ to $\mu^-$ for events passing the charge identification cuts as a function of azimuth. . . . . 167
6.34 Ratio of data $N_{\mu^+}/N_{\mu^-}$ to Monte Carlo $N_{\mu^+}/N_{\mu^-}$ as a function of $\cos\theta$. 168
6.35 Ratio of data $N_{\mu^+}/N_{\mu^-}$ to Monte Carlo $N_{\mu^+}/N_{\mu^-}$ as a function of azimuth. . . . . 169
6.36 Ratio of data $N_{\mu^+}/N_{\mu^-}$ to Monte Carlo $N_{\mu^+}/N_{\mu^-}$ as a function of fit momentum. . . . . 170
6.37 Relative error in fit $q/p$ for data and Monte Carlo. . . . . 171
6.38 Relative error in fit $q/p$ for Monte Carlo events reconstructed with uniformly altered field maps. . . . . 172
6.39 Fit $q/p$ for Monte Carlo events reconstructed with uniformly altered field maps. . . . . 173
6.40 Relative error in fit $q/p$ for the standard field map and the map altered for gap and chemistry corrections. . . . . 175
6.41 Relative error in fit $q/p$ for Monte Carlo with the standard field map (solid) and with the field map varied for only 10% of the planes. . . . 176

7.1 Relative contributions of $\pi$'s and $K$'s to atmospheric neutrinos and cosmic ray muons. . . . . 184
7.2 Zenith angle dependence of atmospheric neutrino flux . . . . . 185
7.3 Fraction of atmospheric $\nu_\mu$ and $\overline{\nu}_\mu$ from $\pi/K$ and $\mu$ decay. . . . . 191
7.4 Production heights for neutrinos from $\pi/K$ decays and $\mu$ decays. . . . 192
7.5 Average $\nu_\mu$ baseline as a function of $\cos\theta$. . . . . 193
7.6 Energy distribution for neutrinos producing muons. . . . . 194
7.7 Neutrino and anti-neutrino cross sections. . . . . 195
7.8 Ratio of neutrino and anti-neutrino cross sections to energy as a function of energy. . . . . 195
7.9 Ratio of neutrino to anti-neutrino cross sections. . . . . 196

8.1 Distribution of $\chi^2/ndf$ for the time vs $y$-position fit for cosmic ray events. . . . . 199
8.2 $1/\beta$ distribution. . . . . 200
8.3 Potential upward-going muon event from run 23692. . . . . 205
8.4 Potential upward-going muon event from run 18761. . . . . 206
8.5 Potential upward-going muon event from run 23087. . . . . 207
8.6 Example upward-going muon event, run 21361, snarl 12693. . . . . 209
8.7 The $\cos\theta$ distribution for downward-going muons showing an exponential fit to the region $0.1 \leq \cos\theta \leq 0.2$. . . . . 212
8.8 The $\cos\theta$ distribution for the entire data set. . . . . 214
8.9 The $\cos\theta$ distributions for the data set with charge sign and momentum information included. . . . . 215
8.10 The fit momentum distributions for the data set. . . . . 216
8.11 All-sky map of neutrino-induced muons. . . . . 217
8.12 The 68%, 90%, and 99% confidence limits for a bounded physical region. 226
8.13 Confidence intervals for the oscillation parameter measurement based on the shape of the $\cos\theta$ distribution. . . . . 229
8.14 The $\cos\theta$ distributions of the data with the best fit shown by the dotted line. . . . . 230
8.15 Confidence intervals for oscillation parameter measurement using charge sign and momentum information. . . . . 231
8.16 Confidence intervals for the $CPT$-violation measurement. . . . . 233

8.17 Predicted event rates for the various $\cos\theta$, charge sign, and momentum bins for a 4 year exposure. . . . . 235
8.18 Predicted confidence intervals for a measurement of the oscillation parameters after 4 live years. . . . . 236
8.19 Predicted confidence intervals for a measurement of $CPT$-violation after 4 live years. . . . . 236
8.20 Predicted confidence intervals for a measurement of $CPT$-violation after 4 live years . . . . . 237

# List of Tables


3.1 Reactions of the *pp* chain. . . . . 24
3.2 Reactions of the *CNO* tricycle. . . . . 24
3.3 Predicted Fluxes for Solar Neutrinos [3] . . . . . 24
3.4 Measured Fluxes of Solar Neutrinos [3]. . . . . 32

4.1 Multiplexing Scheme for the MINOS Far Detector. . . . . 75
4.2 Cuts used to identify events used to determine timing calibrations. . . 77

6.1 Cuts used to select data events for analysis. . . . . 127

7.1 Example values for the parameters in eq (7.4) and eq (7.7) [4] . . . . 183
7.2 Values for the parameters in eq (7.9) and eq (7.10) [5] . . . . . 188

8.1 Cuts used to select upward-going events. . . . . 199
8.2 Potential Upward-going Muon Events from SM1 Data Set. . . . . 201
8.3 Potential Upward-going Muon Events from SM1+SM2 Data Set. . . . 203
8.4 Neutrino oscillation fit parameters. . . . . 230
8.5 *CPT*-violation fit parameters. . . . . 233

# Chapter 1

# Introduction

## 1.1 Neutrino History

The Standard Model of particle physics (SM) states that the fundamental particles in the Universe are the six quarks, six leptons, the quark and lepton anti-particles, and the gauge bosons. The quarks are bound in combinations of quarks and anti-quarks to make up the baryons and mesons. Protons and neutrons are examples of baryons, while pions and kaons are examples of mesons. In the SM, the leptons are not composite particles. The lepton family includes electrons, muons, and taus, along with their associated neutrinos, $\nu_e$, $\nu_\mu$, and $\nu_\tau$. The gauge bosons mediate the force interactions and include the photon, the eight gluons, $W^\pm$, and $Z^0$. The photon mediates the electromagnetic force and the gluons mediate the strong force. The charged $W^\pm$ and neutral $Z^0$ bosons mediate the weak force and are important

in interactions involving neutrinos as neutrinos couple only to the weak force.

The electrons, muons and taus all carry electric charge while the $\nu_e, \nu_\mu$, and $\nu_\tau$ do not. The pairings of the charged leptons and their associated neutrinos are known as the lepton flavors. While our understanding of quarks, the charged leptons, and most of the bosons is quite extensive, knowledge of neutrinos has been more difficult to obtain. The reason for this difficulty is that the neutrinos interact only through the weak force and as a result rarely interact.

The existence of the neutrino was first postulated by W. Pauli in 1930 as an attempt to explain the seeming lack of energy and momentum conservation in radioactive beta decays. In these decays, a neutron was seen to decay into a proton and an electron. The puzzle lay in the fact that the electrons are emitted with a continuous energy spectrum, rather than a discrete energy as expected for a two body decay. Pauli suggested that an uncharged particle was carrying away the remaining energy and that the particle did not interact strongly in matter [6]. It would be 23 years until the first neutrino was detected in an experiment designed by F. Reines and C. Cowan [7]. The observed neutrino signal came from an inverse beta decay, where an anti-neutrino interacted with a proton to produce a neutron and positron. The detection signal comes when the positron produces scintillation light and the neutron produces a coincident gamma ray when it is captured on cadmium several microseconds later. Over the rest of the twentieth century, many advances in neutrino physics were made. The neutrino was shown always to have its spin and

momentum vectors anti-parallel by M. Goldhaber *et al.* in 1958 [8]. Particles with anti-parallel spin and momentum vectors are said to be "left-handed." There are no "right-handed" neutrinos in nature. The muon neutrino was proposed in 1959 by Pontecorvo [9] and observed in 1962 in an experiment at Brookhaven National Lab [10]. The tau was first seen in 1975 [11], which implied the existence of the $\nu_\tau$. The $\nu_\tau$ was observed by the DONUT collaboration in 2000 [12].

## 1.2 Neutrino Interactions

Neutrinos interact only through the weak force mediated by the $W^\pm$ and $Z^0$ bosons. By making precise measurements of the spread in the invariant mass of decaying $Z^0$s, known as the $Z^0$ decay width, the LEP experiments [13] have shown that only three light neutrino species interact through the weak force. These 3 neutrino species are the "active" neutrinos $\nu_e$, $\nu_\mu$, and $\nu_\tau$. The neutrino interactions display different characteristics depending on whether the mediating boson is charged or neutral. Interactions involving the $W^\pm$ bosons are referred to as charged-current (CC) interactions and produce a charged lepton in the final state. An example reaction is

$$\nu_\mu + N \longrightarrow \mu^- + X, \tag{1.1}$$

where $N$ is a nucleon and $X$ is the final hadronic state. These CC reactions were first seen in accelerator experiments done in the 1960's [6]. The interactions mediated by

the $Z^0$ boson are called neutral-current (NC) interactions because no charged lepton is produced. An example NC interaction is

$$\nu_\mu + N \longrightarrow \nu_\mu + X. \tag{1.2}$$

Notice that in CC and NC reactions the flavor of the lepton in the final state is the same as the initial, a process that is referred to as lepton number conservation. In particular, if a $\nu_\mu$ interacts with a nucleus in a CC interaction, the produced lepton is the $\mu^-$.

The CC and NC interactions can be classified according to the amount of momentum transferred between the neutrino and nucleon. In elastic scattering (ES) and quasi-elastic scattering (QES) the momentum of the nucleon in the final state is low. In ES reactions the nucleon recoils intact from the interaction as does the neutrino. In QES reactions the neutrino interacts with the nucleon to produce a different nucleon and lepton in the final state. The ES and QES interactions are important for neutrinos with energies $E_\nu \lesssim 1$ GeV. At this energy scale the the nucleus can be modeled as a point mass. At somewhat higher energies, $E_\nu \sim 1$ GeV, neutrinos can also excite resonant states of the nucleons in the final state that decay and emit a single pion. Such interactions are called single pion modes. For interactions with high energy and momentum transfers, $E_\nu >$ few GeV, the neutrino interacts with the constituent quarks of the nucleus. The nuclei are broken apart allowing new quark

combinations, such as mesons to form. Such interactions are called deep inelastic scattering (DIS) interactions. The DIS interactions are called inclusive processes because the final hadronic state is not restricted to nucleons, instead it can consist of mesons as well.

While weak interactions appear to conserve lepton number in the SM, they violate other symmetries such as charge conjugation ($C$) and parity conservation ($P$). The charge conjugation operation takes a particle to its anti-particle. For neutrinos, the result of the $C$ operation is to make a "left-handed" anti-neutrino which is not seen in nature. The parity operation is an inversion of spatial coordinates, $(x, y, z) \rightarrow (-x, -y, -z)$. The parity operation on a neutrino reverses the momentum vector but not the spin vector, making a "right-handed" neutrino. Such neutrino states are not seen in nature [14]. If both $C$ and $P$ operate on a neutrino, then a "left-handed" neutrino becomes a "right-handed" anti-neutrino. Because the action of $C$ and $P$ taken in turn on a neutrino produce an anti-neutrino, weak interactions do not violate $CP$ in the SM. Another important operation is that of time reversal ($T$). Time reversal conservation means that one should be able to observe both a reaction and its inverse reaction. The $CPT$ theorem states that all interactions are invariant under the successive operations of $C$, $P$ and $T$ taken in any order [14].

## 1.3 Neutrino Mass

One of the most important questions in neutrino physics is that of the neutrino mass. The mass of a particle is one of its fundamental properties. However, neutrinos have been known to exist for over 70 years without a precise bound on the neutrino mass being determined. This lack of knowledge of a fundamental neutrino property is a testament to the low reaction probability of weak interactions. Although the neutrino masses are not well known, non-zero neutrino masses may be the key to the observed excess of baryons over anti-baryons, referred to as baryogenesis, in the Universe [15]. Neutrino masses may also have influenced the formation of galaxies in the early Universe [16]. Additionally, neutrino masses may even provide clues to new physics at very high energies [15]. Given these fundamental questions, it is imperative to determine whether neutrinos have non-zero masses and the implications of non-zero neutrino mass.

One probe of neutrino mass uses Fermi's suggestion of identifying the end-point of the energy spectrum of $\beta$ particles from decay. Given the reaction

$$(Z, A) \longrightarrow (Z + 1, A) + e^- + \overline{\nu}_e, \tag{1.3}$$

the most energy the electron can have is

$$E_{max} = m_i - m_f - m_\nu, \tag{1.4}$$

where $m_i$ is the mass of the initial nucleus, $m_f$ is the mass of the daughter nucleus and $m_\nu$ is the neutrino mass. Several experiments have attempted to measure the $\nu$ mass using $\nu_e$ by studying the end-point of the Tritium beta decay spectrum. Current upper limits on the mass are between 2.2 and 2.5 eV/c$^2$ [17].

Another method that can indicate whether neutrinos have mass is the examination of the rates of neutrinoless double $\beta$ decay,

$$(Z, A) \longrightarrow (Z + 2, A) + e^- + e^-. \tag{1.5}$$

In this reaction, the original nucleus emits a pair of virtual $W^-$ bosons and in the process the nucleus turns into a different nucleus. The $W^-$ bosons exchange a neutrino state with mass to create two out-going electrons [18]. The neutrino emitted by one $W^-$ must be absorbed as an anti-neutrino by the other. The only way for the neutrino to be absorbed as an anti-neutrino is if the neutrino is identical to its own anti-particle. A particle that has mass and is identical to its anti-particle is called a Majorana particle. Clearly eq (1.5) violates lepton number conservation and if observed would indicate physics beyond the SM. The decay rate is proportional to the square of the "effective Majorana" mass of the $\nu_e$ [17], which is an average over the neutrino states with mass, $\langle m_\nu \rangle$. A signal for neutrinoless double $\beta$ decay in $^{76}$Ge has been reported in the literature giving $\langle m_\nu \rangle < 0.34$ eV at the 90% confidence level [19]. This result has not been confirmed by other experiments [20]. A

lower limit for the lifetime of the neutrinoless double $\beta$ decay has been reported as $5.5 \times 10^{23}$ yr [20].

A different approach to measuring neutrino mass is to understand how neutrinos influenced the formation of matter in the early Universe. The Wilkenson Microwave Anisotropy Probe (WMAP) experiment measured several cosmological parameters by studying the temperature fluctuations in the cosmic microwave background. One such measurement is the limit on the sum of the masses of the neutrino species which were light enough to decouple while still relativistic. The analysis is based on the power spectrum of density perturbations in the early Universe [16]. The basic idea behind the analysis is that relativistic neutrinos suppress the growth of density fluctuations until the neutrinos become nonrelativistic. The analysis of the WMAP data combined with the large scale structure seen by the 2dF Galaxy Redshift Survey limits the contribution of neutrinos to the energy density of the Universe. This limit on the neutrino energy density leads to a limit on the combined mass of the neutrino species [16]

$$\sum_i m_{\nu_i} < 0.71 \text{ eV}. \tag{1.6}$$

Another method for probing non-zero neutrino mass was proposed by Pontecorvo in 1964 [21]. He claimed that if the neutrino flavor states, $\nu_e, \nu_\mu, \nu_\tau$, are a superposition of mass eigenstates, then there is a nonzero probability that a neutrino created in flavor state $\alpha$ with energy $E$ will be observed in state $\beta$ after traveling a distance

$L$. This phenomenon, known as neutrino oscillations, will be explained in detail in Chapter 2. Chapter 3 reviews the experimental evidence for neutrino oscillations.

The goal of this dissertation is to use neutrinos produced by interactions of cosmic rays in the atmosphere to probe the parameters governing the neutrino oscillations. Further, the charge separation of the leptons produced by the neutrino interactions will determine the relative number of neutrinos and anti-neutrinos produced by cosmic ray interactions. With this information it is possible to directly probe the potential for $CPT$ violation in the weak interactions.

## 1.4 Personal Contributions to the MINOS Experiment

My contributions to the MINOS experiment include both hardware and software responsibilities.

My first contributions to the MINOS experiment were helping to set up the MUX box production factory at Indiana University. While the design phase of the boxes and connectors was essentially finished when I joined the group, I was involved in designing the MUX box construction procedures. I also designed the database that holds information about the MUX boxes, as well as the interface that allows users to enter and access that data. I also wrote the software used when testing MUX box performance.

As a requirement of writing a dissertation using MINOS data, each graduate student on the experiment has to fulfill a six month commitment of detector installation at either the near or far detector sites. I met this requirement at the Soudan site from August 2001 through January 2002 during the initial six months of installation. My time there was both exciting and extremely busy. For the first few months I helped to train the construction crew on how to handle and install the clear fiber optic cables at both the module and MUX box. The training was a long process as each plane required a different routing of the clear cables once the plane was erected. During the training period I continually watched the crew to make sure that they did not damage the fly-cut polishing of the connector faces or violate the fiber safe bend radius. The crew became very capable at these duties and after the initial training period they performed these tasks with minimal oversight. Another of my duties was to check out the MUX boxes shipped from both the Indiana and Tufts factories. I helped to set up a test stand like the ones used by the factories and tested several shipments of boxes. After the boxes were installed, I would check them for light tightness and then install the readout electronics.

After the hardware was all in place, the location information of the components needed to be stored. I developed a system that allowed users at the mine to access the MUX box factory database and obtain logical connection maps for such things as which strip end from a plane routed to which location on a PMT pixel. The system would then combine that information with the electronics cabling information and

enter the entire set into the offline software database tables. I created a similar system to generate a high voltage database file for PMT operation used by the PMT high voltage control program.

Although I no longer spend a large amount of time at the far detector, I am still responsible for an aspect of the detector maintenance. I have written the algorithm to calibrate the timing system of the far detector. The algorithm and its performance are discussed in Chapter 4.

My major contribution to the collaboration software was the demultiplexing (DeMux) package. This software package is described in detail in Chapter 5. Its determines which strip end alternative produced which signal in an event. I spent close to three years writing and testing this program with both Monte Carlo and far detector data. It is an integral part of the offline reconstruction software and must be implemented before any other reconstruction or analysis software when examining far detector data.

Since data taking began in 2002, I have had an active roll in the data analysis. I am a member of the Far Detector Non-oscillation Physics and Atmospheric Neutrino analysis working groups. As part of the Far Detector Non-oscillation group I have been involved in the measurement of the relative numbers of $\mu^+$ and $\mu^-$ in the cosmic rays. This work required extensive study of the Monte Carlo events to tune the reconstruction software. As part of the Atmospheric Neutrino group I have tackled the problem of identifying the neutrino-induced muons and using those data to make

a measurement of neutrino oscillation parameters.

# Chapter 2

# Neutrino Oscillation Phenomenology

## 2.1 Oscillations in Vacuum

If neutrinos have mass, the neutrino electroweak flavor states $\nu_\alpha$, where $\alpha = e, \mu, \tau$, can be represented as linear combinations of the mass eigenstates, $\nu_i$, where $i = 1, 2, 3$, in the following manner,

$$|\nu_\alpha\rangle = \sum_i U^*_{\alpha i} |\nu_i\rangle. \tag{2.1}$$

The matrix $U$ is a unitary matrix and is called the leptonic mixing matrix. The form of the matrix depends on the number of flavor states involved in the mixing. To

derive the general expressions describing neutrino flavor oscillations, only the fact that $U$ is unitary is important. The following discussion uses units where $c = \hbar = 1$.

To understand how flavor change occurs, the prescription for how the wave function of the neutrino changes over time must be found. This prescription is called the propagator. In the rest frame of a neutrino of mass eigenstate, $i$, the proper time for the neutrino is $\tau_i$. The evolution of the eigenstate in time is given by the Schrödinger equation,

$$i\frac{\partial}{\partial \tau_i}|\nu_i(\tau_i)\rangle = H|\nu_i(\tau_i)\rangle. \tag{2.2}$$

In the mass eigenstate rest frame the energy of the neutrino state is its mass and

$$H|\nu_i(\tau_i)\rangle = m_i|\nu_i(\tau_i)\rangle. \tag{2.3}$$

Inserting eq (2.3) into eq (2.2) gives,

$$i\frac{\partial}{\partial \tau_i}|\nu_i(\tau_i)\rangle = m_i|\nu_i(\tau_i)\rangle \tag{2.4}$$

$$\Rightarrow |\nu_i(\tau_i)\rangle = e^{-im_i\tau_i}|\nu_i(0)\rangle. \tag{2.5}$$

The propagator is then

$$\langle\nu_i(0)|\nu_i(\tau_i)\rangle = e^{-im_i\tau_i}. \tag{2.6}$$

Translating into the reference frame of the lab using Lorentz invariance, the neutrino

travels a distance $L$ in time $t$,

$$m_i\tau_i = E_i t - p_i L \cong (E_i - p_i)L, \tag{2.7}$$

where $E_i$ and $p_i$ are the energy and momentum, respectively, of the mass eigenstate, and the last approximation is valid for relativistic neutrinos. Assuming that all the mass eigenstates have the same energy, $E_i = E$, the momentum of each state is

$$p_i = \sqrt{E^2 - m_i^2} \cong E - \frac{m_i^2}{2E}. \tag{2.8}$$

The assumption that each mass eigenstate has the same energy is called the equal energy construction. Inserting the result of eq (2.8) into eq (2.7), gives

$$m_i\tau_i = \left[E - (E - \frac{m_i^2}{2E})\right]L = \frac{m_i^2 L}{2E}. \tag{2.9}$$

The expression for the propagator, eq (2.6), may now be written as,

$$\langle\nu_i(0)|\nu_i(\tau_i)\rangle = e^{-i\frac{m_i^2 L}{2E}}. \tag{2.10}$$

Then the state vector for a neutrino created as flavor state $\alpha$ after it travels a distance $L$ is

$$|\nu_\alpha(L)\rangle = \sum_i U^*_{\alpha i} e^{-i(\frac{m_i^2 L}{2E})}|\nu_i\rangle. \tag{2.11}$$

It is possible to invert eq (2.1) using the unitarity of $U$ to write the mass eigenstates as a linear combination of the flavor eigenstates.

$$|\nu_i\rangle = \sum_\beta U_{\beta i}|\nu_\beta\rangle. \tag{2.12}$$

The flavor index is changed to $\beta$ to indicate that the mass eigenstate is represented by a combination of flavor states. The amplitude for the flavor change process $\nu_\alpha \to \nu_\beta$ can be written using eq (2.11) and eq (2.12)

$$\begin{aligned} A(\nu_\alpha \to \nu_\beta) &= \langle \nu_\beta | \nu_\alpha(L)\rangle \\ &= \langle \nu_\beta | \sum_\beta \left( \sum_i U^*_{\alpha i} e^{-i\frac{m_i^2 L}{2E}} \right) U_{\beta i} |\nu_\beta\rangle \\ &= \sum_i U^*_{\alpha i} e^{-i\frac{m_i^2 L}{2E}} U_{\beta i}. \end{aligned} \tag{2.13}$$

It is reasonable to wonder if the result in eq (2.13) is dependent on the assumption that all the mass states have the same energy. The equal momentum construction says that all the mass eigenstates have the same momentum, $p_i = p$, and the energy for each eigenstate is

$$E_i = \sqrt{p^2 + m_i^2} \cong p + \frac{m_i^2}{2p}. \tag{2.14}$$

In this case eq (2.7) becomes

$$m_i \tau_i = (E_i - p)L \cong (p + \frac{m_i^2}{2p} - p)L = \frac{m_i^2 L}{2p} = \frac{m_i^2 L}{2E}, \tag{2.15}$$

which is the same result as in eq (2.10).

The probability for a neutrino of flavor $\alpha$ to change to one of flavor $\beta$ is the square of the amplitude for that process,

$$\begin{aligned} P(\nu_\alpha \to \nu_\beta) &= |A(\nu_\alpha \to \nu_\beta)|^2 \\ &= \delta_{\alpha\beta} - 4\sum_{i>j} Re[U^*_{\alpha i}U_{\beta i}U_{\alpha j}U^*_{\beta j}]\sin^2[\frac{\Delta m^2_{ij}L}{4E}] \\ &+ 2\sum_{i>j} Im[U^*_{\alpha i}U_{\beta i}U_{\alpha j}U^*_{\beta j}]\sin[\frac{\Delta m^2_{ij}L}{2E}], \end{aligned} \tag{2.16}$$

where $\Delta m^2_{ij}$ is called the mass splitting and is defined as

$$\Delta m^2_{ij} \equiv m^2_i - m^2_j. \tag{2.17}$$

This derivation was done for neutrinos. However, the result for anti-neutrinos is easy to obtain in the following manner. To find the probability for $\overline{\nu}_\alpha \to \overline{\nu}_\beta$, use *CPT* invariance to show that it is the same as the probability for $\nu_\beta \to \nu_\alpha$. That probability is the same as the probability for $\nu_\alpha \to \nu_\beta$ with the $U$ terms in the sums replaced by $U^*$. Thus, the probability for anti-neutrino oscillations is the same as for neutrino oscillations, with the (+) sign in front of the imaginary term replaced by a (−) sign.

Several consequences of eq (2.16) should be noted. It shows that neutrino flavor change is the result of neutrinos having mass and the mass eigenstates being

non-degenerate. If the values of the $m_i = 0$ or $\Delta m^2_{ij} = 0$, then the probability for oscillations, $\alpha \rightarrow \beta$, becomes $\delta_{\alpha\beta}$. Also the probability for flavor change is an oscillatory function of $L/E$, which accounts for the phenomenon being called neutrino oscillations. Moreover,

$$\frac{\Delta m^2_{ij} L}{4E} \approx O(1) \tag{2.18}$$

for the oscillations to occur. The condition in eq (2.18) means that an experiment looking for neutrino oscillations will be sensitive to

$$\Delta m^2_{ij} \gtrsim (\frac{L}{4E})^{-1}. \tag{2.19}$$

Reinserting the omitted factors of $\hbar$ and $c$, and letting $m^2_i$,$L$ and $E$ be measured in units of (eV)$^2$, km and GeV respectively, the argument of the sine function in eq (2.16) becomes

$$1.27 \Delta m^2_{ij} (eV)^2 \frac{L(\text{km})}{E(\text{GeV})}. \tag{2.20}$$

Another consequence of eq (2.16) is that a measure of the oscillation can tell us the size of the mass-squared splittings, but not the absolute scale of the mass spectrum. Finally, the oscillation process alters the relative numbers of each neutrino flavor in a beam of neutrinos but it does not alter the total number of neutrinos. That is, a neutrino produced in a beam may oscillate between different flavors, but it will not cease to exist due to oscillations.

### 2.1.1 Two Neutrino Oscillations

The simplest case of neutrino oscillations occurs when only 2 states mix appreciably in vacuum. In this case the mixing matrix $U$ takes the form

$$U = \begin{bmatrix} \cos\theta & \sin\theta \\ -\sin\theta & \cos\theta \end{bmatrix}, \tag{2.21}$$

where $\theta$ is called the leptonic mixing angle. This angle represents the rotation from the mass basis into the electroweak flavor basis [22]. The columns of the matrix $U$ correspond to the mass eigenstates, and the rows correspond to flavor states. In the case of two flavor oscillations we insert the above expression for $U$ into eq (2.16) to get

$$\begin{aligned} P(\nu_\alpha \to \nu_{\beta\neq\alpha}) &= 4\cos^2\theta\sin^2\theta\sin^2[\frac{\Delta m^2_{ij}L}{4E}] \\ &= \sin^2(2\theta)\sin^2[\frac{\Delta m^2_{ij}L}{4E}]. \end{aligned} \tag{2.22}$$

The probability for no transition to occur, known as the neutrino survival probability, is given by

$$P(\nu_\alpha \to \nu_\alpha) = 1 - P(\nu_\alpha \to \nu_{\beta\neq\alpha}). \tag{2.23}$$

When only two flavors mix in vacuum, eq (2.22) shows that there is no difference in the mixing probability for $\overline{\nu}$ versus $\nu$. Also notice the dependence of the probability for oscillation on the mixing angle. The values for $\sin^2 2\theta$ can range between $0 \leq \sin^2 2\theta \leq 1$. The maximum value occurs when $\theta = \pi/4$ and in this case the mixing

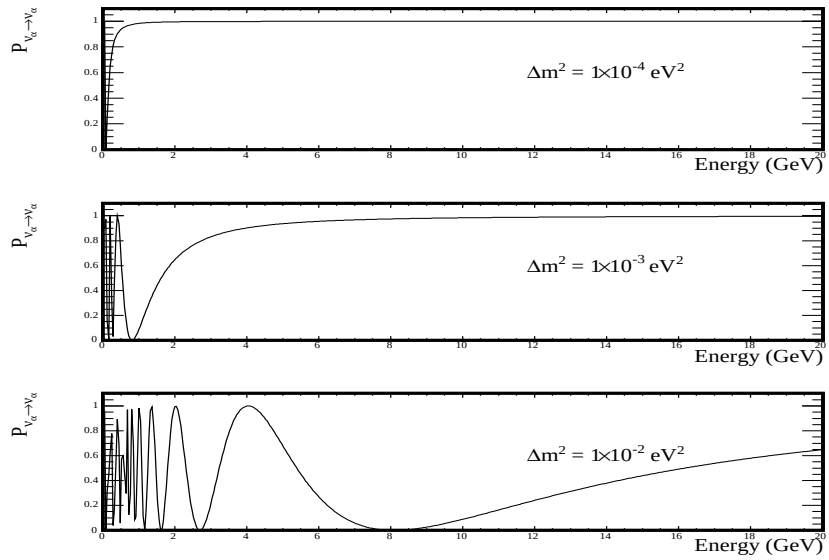


Figure 2.1: Neutrino survival probability as a function of neutrino energy for neutrinos traveling 1000 km in vacuum with maximal mixing and $\Delta m^2 = 1 \times 10^{-4}$ eV$^2$ (top), $\Delta m^2 = 1 \times 10^{-3}$ eV$^2$ (middle) and $\Delta m^2 = 1 \times 10^{-2}$ eV$^2$ (bottom).

is said to be maximal.

Fig. 2.1 shows the vacuum survival probability for neutrinos traveling a distance of 1000 km as a function of the neutrino energy for three values of $\Delta m^2$ and maximal mixing. For $\Delta m^2 = 1 \times 10^{-4}$ eV$^2$, neutrinos with energies greater than 1 GeV have a high survival probability. For $\Delta m^2 = 1 \times 10^{-3}$ eV$^2$, neutrinos with energies near 1 GeV are very likely to oscillate into another flavor; as the neutrino energy increases to 5 GeV and above, the survival probability approaches 1. For $\Delta m^2 = 1 \times 10^{-2}$ eV$^2$ neutrino oscillation is quite pronounced below 8 GeV; as the neutrino energy increases above 8 GeV, the survival probability begins to approach 1.

### 2.1.2 Three Neutrino Oscillations

Eq (2.16) can also be used to find the flavor change probability for the case when three mass eigenstates contribute to the flavor change. However, a simple closed form for the probability similar to eq (2.22) does not exist for the three neutrino oscillation case. The mixing matrix for the three neutrino oscillation case can be written as a product of mixing matricies for each two neutrino oscillation and a matrix of *CP* violating phase factors,

$$U = \begin{bmatrix} 1 & 0 & 0 \\ 0 & c_{23} & s_{23} \\ 0 & -s_{23} & c_{23} \end{bmatrix} \begin{bmatrix} c_{13} & 0 & s_{13}e^{-i\delta} \\ 0 & 1 & 0 \\ -s_{13}e^{-i\delta} & 0 & c_{23} \end{bmatrix} \begin{bmatrix} c_{12} & s_{12} & 0 \\ -s_{12} & c_{12} & 0 \\ 0 & 0 & 1 \end{bmatrix} \begin{bmatrix} e^{i\alpha_1/2} & 0 & 0 \\ 0 & e^{i\alpha_2/2} & 0 \\ 0 & 0 & 1 \end{bmatrix}, \tag{2.24}$$

where the $c_{ij} = \cos\theta_{ij}$, $s_{ij} = \sin\theta_{ij}$, and the $\alpha_i$ and $\delta$ are *CP* violating phases. The *CP* violating phases are included for $U$ to have most general form of a rotation in three dimensions. They are not included in the two dimensional case because in two dimensions the rotation can be made in such a way to exclude any phase dependence.

It is possible to make the form of the three neutrino oscillation probability look similar to the two neutrino case if there are two distinct mass splittings for the mass eigenstates. If one mass splitting is much larger than the other, for example $\nu_3$ is much more massive than $\nu_1$ and $\nu_2$, then the masses of the states satisfy $m_3 \gg m_2 \cong m_1$.

In this case, let the larger mass splitting be $\Delta M^2$ and the smaller $\Delta m^2$, such that

$$\frac{\Delta m^2 L}{4E} \ll 1. \tag{2.25}$$

Then eq (2.16) becomes

$$\begin{aligned} P(\nu_\alpha \to \nu_\beta) &= -4Re[U^*_{\alpha 3} U_{\beta 3}(U_{\alpha 1} U^*_{\beta 1} + U_{\alpha 2} U^*_{\beta 2})] \sin^2[\frac{\Delta M^2 L}{4E}] \\ &= 4|U_{\alpha 3}|^2 |U_{\beta 3}|^2 \sin^2[\frac{\Delta M^2 L}{4E}], \end{aligned} \tag{2.26}$$

where the last step makes use of the unitarity of $U$. This approximation brings the three neutrino oscillation probability into a form similar to that for two neutrino oscillations.

# Chapter 3

# Neutrino Oscillation Experiments

## 3.1 Hints of Neutrino Oscillations

The fusion of hydrogen into helium in the Sun follows well known reaction chains. The most basic one is the *pp* chain named after the first reaction which fuses two protons. The reactions in the chain are shown in Table 3.1 along with the neutrino energies of the neutrino producing reactions [23]. Another reaction chain that fuses hydrogen with carbon, nitrogen and oxygen and produces neutrinos in the process is called the *CNO* tricycle. The reactions for this cycle are shown in Table 3.2 [23]. Table 3.3 taken from [3] shows all the neutrino producing reactions in the Sun as well as their predicted fluxes. The predicted flux of these solar neutrinos as a function of energy is shown in Fig. 3.1 [3].

Table 3.1: Reactions of the *pp* chain.

| Reaction | $E_\nu$ |
|---|---|
| $\mathrm{H} + \mathrm{H} \longrightarrow \mathrm{H}^2 + \mathrm{e}^+ + \nu$ | 0.3 MeV |
| $\mathrm{H}^2 + \mathrm{H} \longrightarrow \mathrm{He}^3 + \gamma$ | - |
| $\mathrm{He}^3 + \mathrm{He}^3_2 \longrightarrow \mathrm{He}^4 + 2\mathrm{H}$ | - |
| $\mathrm{He}^3 + \mathrm{He}^4 \longrightarrow \mathrm{Be}^7 + \gamma$ | - |
| $\mathrm{Be}^7 + \mathrm{e}^- \longrightarrow \mathrm{Li}^7 + \nu$ | 0.8 MeV |
| $\mathrm{Li}^7 + \mathrm{H} \longrightarrow 2\mathrm{He}^4$ | - |
| $\mathrm{Be}^7 + \mathrm{H} \longrightarrow \mathrm{B}^8 + \gamma$ | - |
| $\mathrm{B}^8 \longrightarrow \mathrm{Be}^8 + \mathrm{e}^+ + \nu$ | 7.2 MeV |
| $\mathrm{Be}^8 \longrightarrow 2\mathrm{He}^4$ | - |

Table 3.2: Reactions of the *CNO* tricycle.

| Reaction | $E_\nu$ |
|---|---|
| $\mathrm{C}^{12} + \mathrm{H} \longrightarrow \mathrm{N}^{13} + \gamma$ | - |
| $\mathrm{N}^{13} + \mathrm{e}^+ \longrightarrow \mathrm{C}^{13} + \nu$ | 0.71 MeV |
| $\mathrm{C}^{13} + \mathrm{H} \longrightarrow \mathrm{N}^{14} + \gamma$ | - |
| $\mathrm{N}^{14} + \mathrm{H} \longrightarrow \mathrm{O}^{15} + \gamma$ | - |
| $\mathrm{O}^{15} + \mathrm{e}^+ \longrightarrow \mathrm{N}^{15} + \nu$ | 1.0 MeV |
| $\mathrm{N}^{15} + \mathrm{H} \longrightarrow \mathrm{He}^4 + \mathrm{C}^{12}$ | - |
| $\mathrm{N}^{15} + \mathrm{H} \longrightarrow \mathrm{O}^{16} + \gamma$ | - |
| $\mathrm{O}^{16} + \mathrm{H} \longrightarrow \mathrm{F}^{17}\gamma$ | - |
| $\mathrm{F}^{17} + \mathrm{e}^+ \longrightarrow \mathrm{O}^{17} + \nu$ | 0.94 MeV |
| $\mathrm{O}^{17} + \mathrm{H} \longrightarrow \mathrm{He}^4 + \mathrm{N}^{14}$ | - |

Table 3.3: Predicted Fluxes for Solar Neutrinos [3]

| Reaction | Abbreviation | Flux ($\mathrm{cm}^{-2}\mathrm{s}^{-1}$) |
|---|---|---|
| $pp \longrightarrow de^+\nu$ | *pp* | $5.95(1.00^{+0.01}_{-0.01}) \times 10^{10}$ |
| $pe^-p \longrightarrow d\nu$ | *pep* | $1.40(1.00^{+0.015}_{-0.015}) \times 10^{8}$ |
| $\mathrm{He}^3p \longrightarrow \mathrm{He}^4e^+\nu$ | *hep* | $9.3\times10^{3}$ |
| $\mathrm{Be}^7e^- \longrightarrow \mathrm{Li}^7\nu + \gamma$ | $\mathrm{Be}^7$ | $4.77(1.00^{+0.010}_{-0.010}) \times 10^{9}$ |
| $\mathrm{B}^8 \longrightarrow \mathrm{Be}^8e^+\nu$ | $\mathrm{B}^8$ | $5.05(1.00^{+0.20}_{-0.16}) \times 10^{6}$ |
| $\mathrm{N}^{13} \longrightarrow \mathrm{C}^{13}e^+\nu$ | $\mathrm{N}^{13}$ | $5.48(1.00^{+0.21}_{-0.17}) \times 10^{8}$ |
| $\mathrm{O}^{15} \longrightarrow \mathrm{N}^{15}e^+\nu$ | $\mathrm{O}^{15}$ | $4.80(1.00^{+0.25}_{-0.19}) \times 10^{8}$ |
| $\mathrm{F}^{17} \longrightarrow \mathrm{O}^{17}e^+\nu$ | $\mathrm{F}^{17}$ | $5.63(1.00^{+0.25}_{-0.25}) \times 10^{6}$ |

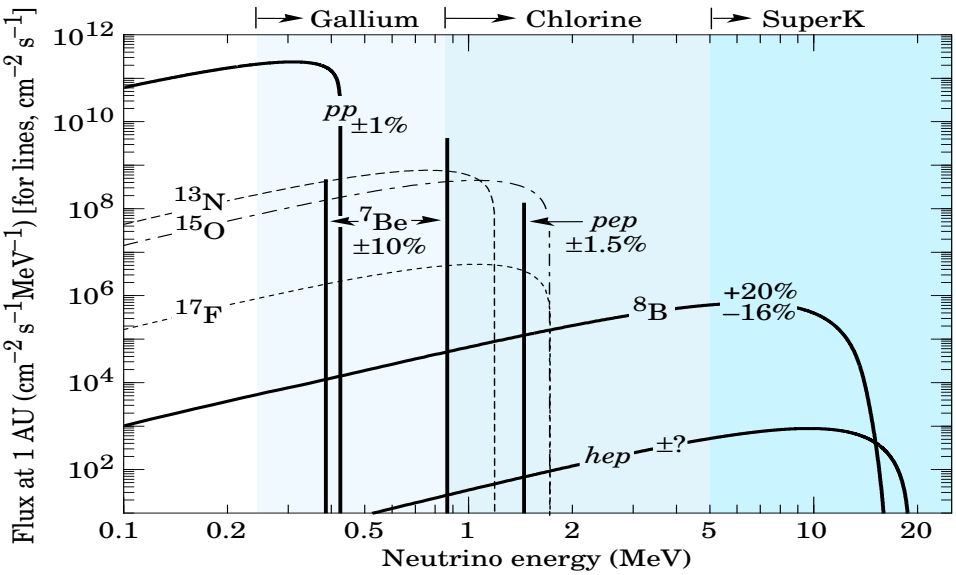


Figure 3.1: Flux for various solar neutrinos as a function of energy.

### 3.1.1 Radiochemical Experiments

The first experiment to observe solar neutrinos was the Homestake experiment, and it was the first in a class of experiments to use radioactive decay products to identify these neutrinos as well. This type of experiment is known as a radiochemical experiment. The Homestake detector was a large tank holding 615 tons of liquid perchloroethylene, a cleaning solution, located in the Homestake mine in South Dakota. The reason for placing the detector underground was to use the rock above the detector, known as the overburden, to shield the detector from background high energy particles produced by cosmic ray interactions in the atmosphere. The solar neutrinos interacted with chlorine atoms in the solution to produce a radioactive species of argon. The argon atoms were extracted from the detector after a period of time

corresponding to two or three half-lives of the radioactive isotope. These radioactive atoms were counted to determine the total number of neutrino interactions. The energy needed by the $\nu_e$ to initiate the interaction,

$$^{37}\mathrm{Cl} + \nu_e \longrightarrow ^{37}\mathrm{Ar} + e^-, \tag{3.1}$$

is 814 keV. Fig. 3.1 shows that the Homestake experiment was sensitive to the $^7$Be, *pep*, $^8$B, $^{13}$N, $^{15}$O, $^{17}$F, and *hep* neutrinos. Over the course of 24 years, the Homestake collaboration found a solar neutrino capture rate that is about 1/3 of that predicted by the model of Bahcall and Pinsonneault [24] called the standard solar model (SSM).

The discrepancy between the predicted and observed flux of neutrinos in the Homestake experiment was named the "solar neutrino deficit" and led to the proposal for other radiochemical experiments to check the neutrino flux for the main *pp* neutrino reaction in Table 3.1. These experiments use gallium as the target nucleus instead of chlorine because the energy needed by the neutrino to initiate the reaction is only 233 keV. The lower threshold energy means that the gallium experiments detect neutrinos from the main *pp* reaction as well as those from the other reactions. Moreover, the flux of these *pp* neutrinos is much greater than those from the other neutrino producing reactions, as seen in Fig. 3.1 and Table 3.3. To detect these low

energy neutrinos, GALLEX and SAGE use the interaction

$$^{71}\mathrm{Ga} + \nu_e \longrightarrow ^{71}\mathrm{Ge} + e^-. \tag{3.2}$$

The GALLEX collaboration reported a capture rate that was about 1/2 the predicted rate as did SAGE [3].

### 3.1.2 Water-Cherenkov Experiments

Another class of experiment built to observe solar neutrinos uses the Cherenkov effect. The detector medium in these experiments is a large contained volume of water surrounded by photomultiplier tubes. These experiments observe the ($\nu$e) elastic scattering (ES) reaction,

$$\nu_\alpha + e^- \longrightarrow \nu_\alpha + e^-. \tag{3.3}$$

It should be noted that $\nu_\alpha$ in eq (3.3) refers to all active neutrino flavors, $\nu_e$,$\nu_\mu$, $\nu_\tau$. The sensitivity to $\nu_\mu$ and $\nu_\tau$ is much smaller than that of $\nu_e$, with the ratio of the reaction cross sections given by [3],

$$\sigma(\nu_{\mu,\tau}, e) \approx 0.16\sigma(\nu_e, e). \tag{3.4}$$

When a neutrino scattered electron traverses a medium with a velocity faster than the speed of light in the medium, $v_{crit}$, Cherenkov radiation is produced. The photomultiplier tubes collect this light from electrons with $v > v_{crit}$. Water-Cherenkov experiments allow the neutrino interaction to be observed directly, unlike the radiochemical experiments. The advantage of "direct" observation is that detailed information about the reaction can be determined, such as the energy released in the interaction and the directions of particles coming out of the reaction. Radiochemical experiments can only record that a reaction took place. Moreover, the water-Cherenkov detectors are able to separate signal from background by observing the directional correlation between the incoming neutrino from the Sun and the scattered electron.

The Kamiokande and Super-Kamiokande (Super-K) detectors are water-Cherenkov detectors. The Kamiokande detector had a mass of 3kT and was located under Mt. Ikenoyama in Japan. Super-K is located under the same mountain, although in a different tunnel, and it has a mass of 50 kT. The water-Cherenkov experiments have high energy thresholds for the neutrino to interact, 7 Mev for Kamiokande and 5 MeV for Super-K, which means that they observe the $^8$B neutrinos almost exclusively because of the negligible contribution of the *hep* neutrinos, as shown in Fig. 3.1 and Table 3.3. Both collaborations measured values for the solar neutrino flux that were about 1/2 the predicted value [3].

Given the fact that all the experiments that observe solar neutrinos report a

significantly reduced flux than expected, it is reasonable to wonder whether the SSM is an accurate representation of the Sun. One way to test the SSM is to compare its predictions for the sound speed at different radii in the Sun to the observations from helioseismology. The sound speeds calculated using the SSM and those measured using helioseismology were shown to be in excellent agreement with fractional differences of $\lesssim 0.1\%$ for all radii [25]. The fractional uncertainty in the sound speed at a given radius translates directly to the fractional error in the temperature at that radius [26]. The neutrino flux for reactions in the Sun are proportional to $T^n$ where $T$ is the temperature at which the reaction takes place and $n$ ranges from $-1.1$ for $pp$ reactions to $+24$ for the $B^8$ reaction [26]. Even allowing the maximal fractional error in temperature of $\sim 0.1\%$, the resulting changes in the neutrino fluxes would only be several percent or less, which is not enough to resolve the observed deficits of solar neutrnios [26]. These results imply that the deep interior of the Sun where neutrino production occurs is well modeled [25] and the solar neutrnio deficit is not the result of poor modeling.

## 3.2 SNO and Solar Neutrino Oscillations

The Sudbury Neutrino Observatory (SNO) experiment was built to test whether the solar neutrino deficit could be explained by matter enhanced neutrino oscillations inside the Sun. The enhancement of neutrino oscillations in the presence of matter

was first examined by Wolfenstein [27] and Mikheyev and Smirnov [28], and the effect is now commonly referred to as MSW oscillations. The matter effect is the result of the coupling of the $W^{\pm}$ bosons to electrons and $\nu_e$. A $\nu_e$ passing through matter will scatter due to the electrons in the material in such a way that its phase changes but not its momentum. This scattering is called coherent forward scattering. The SNO experiment, located in the Sudbury Mine in Ontario, Canada, is a spherical acrylic vessel containing 1000 tons of ultra-pure heavy water ($D_20$). The detector measures the $^8$B solar neutrinos through the charged current reactions

$$\nu_e + d \longrightarrow e^- + p + p, \tag{3.5}$$

and the neutral current reaction

$$\nu_\alpha + d \longrightarrow \nu_\alpha + p + n. \tag{3.6}$$

As a water detector, the experiment is also sensitive to the ES reaction of eq (3.3). Eq (3.5) shows the detector is sensitive to only electron neutrinos through the CC interaction that produces an electron as the final state lepton. The NC interaction of eq (3.6) is sensitive to all active neutrinos. The most recent flux values reported by the SNO collaboration for the different reactions, CC, NC, and ES, are [29]

$$\phi_{CC}^{SNO}(\nu_e) = (1.76^{+0.06}_{-0.05} \pm 0.09) \times 10^6 \mathrm{cm}^{-2}\mathrm{s}^{-1}, \tag{3.7}$$

$$\phi_{NC}^{SNO}(\nu_\alpha) = (5.05^{+0.44+0.46}_{-0.43-0.43}) \times 10^6 \mathrm{cm}^{-2}\mathrm{s}^{-1}. \tag{3.8}$$

$$\phi_{ES}^{SNO}(\nu_\alpha) = (2.39^{+0.24}_{-0.23} \pm 0.12) \times 10^6 \mathrm{cm}^{-2}\mathrm{s}^{-1}, \tag{3.9}$$

The fluxes for the CC and ES reactions, which are mostly due to $\nu_e$, are well below the predicted value shown in Table 3.3. The result for the NC flux agrees quite well with the predicted value.

### 3.2.1 Comparison of Results with Prediction

Table 3.4, adapted from [3], shows the results of the radiochemical and water-Cherenkov solar neutrino experiments, along with the predicted rates of Bahcall [24]. The rates for the radiochemical experiments are given in Solar Neutrino Units (SNU) which are defined as 1 SNU = $10^{-36}$ captures per atom per second. All the results except for the SNO NC measurement show that the measured values are much less than the predicted rates. The NC measurement reflects interactions from all neutrino flavors. indicating that a substantial fraction of the solar neutrinos may oscillate from $\nu_e \rightarrow \nu_\alpha$.

The CC flux measured by SNO, $\phi_{SNO}^{CC}(\nu_e)$, and the ES flux measured by Super-K, $\phi_{SK}^{ES}(\nu_\alpha)$, should be equal if neutrinos are massless and do not oscillate because the interaction cross sections are the same. In that case, the only neutrinos observed

Table 3.4: Measured Fluxes of Solar Neutrinos [3].

| Experiment | Flux ($\times 10^6 \mathrm{cm}^{-2}\mathrm{s}^{-1}$) | Cl (SNU) | Ga (SNU) |
|---|---|---|---|
| Homestake | - | $2.56 \pm 0.16 \pm 0.16$ | - |
| GALLEX | - | - | $77.5 \pm 6.2^{+4.3}_{-4.7}$ |
| SAGE | - | - | $67.2^{7.2+3.5}_{-7.0-3.0}$ |
| Kamiokande | $2.80 \pm 0.19 \pm 0.33$ | - | - |
| Super-K | $2.32 \pm 0.03^{+0.8}_{-0.07}$ | - | - |
| SNO (CC) | $1.76^{+0.06}_{-0.05} \pm 0.09$ | - | - |
| SNO (ES) | $2.39^{+0.24}_{-0.23} \pm 0.12$ | - | - |
| SNO (NC) | $5.09^{+0.44+0.46}_{-0.43-0.43}$ | - | - |
| Prediction | $5.05(1.00^{+0.20}_{-0.16})$ | $7.6^{+1.3}_{-1.1}$ | $128^{+9}_{-7}$ |

from the sun must be $\nu_e$. However, the results from SNO indicate

$$\phi_{SK}^{ES}(\nu_\alpha) - \phi_{SNO}^{CC}(\nu_e) = (0.57 \pm 0.17) \times 10^6 \mathrm{cm}^{-2}\mathrm{s}^{-1}, \tag{3.10}$$

which is a $3\sigma$ difference from 0 and implies a component to the solar neutrino flux that is not made of $\nu_e$. One explanation for the existence of other flavors in the solar neutrino flux is given by neutrino oscillations.

Fig. 3.2 plots the flux observed by SNO due to the combined $\nu_\mu$ and $\nu_\tau$ components of the solar neutrino flux versus the $\nu_e$ flux. The CC flux has no dependence on the $\nu_\mu$ and $\nu_\tau$ flux as it is sensitive only to $\nu_e$ and is represented by a band of constant $\nu_e$ flux. The ES flux has a small dependence on $\nu_\mu$ and $\nu_\tau$ as seen in § 3.1.2. The flux due to NC interactions is equally likely to be from $\nu_e$ or $\nu_\mu$ and $\nu_\tau$ and has a slope of 1 in the figure. The prediction based on the Standard Solar Model (SSM) of Bahcall [24] is shown as well.

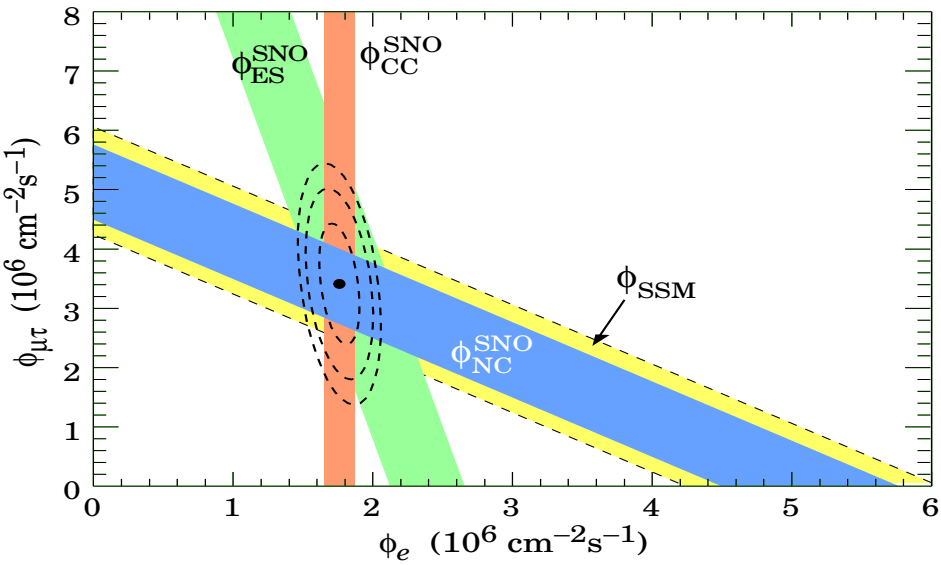


Figure 3.2: Fluxes of $B^8$ solar neutrinos deduced from the SNO charged current (CC), neutral current (NC), and elastic scattering (ES) results, along with the prediction of the Standard Solar Model (SSM) of Bahcall. Also shown are the 68%, 90% and 97% joint probability contours for $\phi(\nu_e)$ and $\phi(\nu_\mu, \nu_\tau)$ [3].

To first order, the flux for the non-$\nu_e$ component of the solar neutrinos is the difference between the measured NC flux due to all neutrino flavors and the CC flux due to just the $\nu_e$. A small value to account for $\nu_\mu$ and $\nu_\tau$ component of the ES flux must be added back into the NC and CC flux difference. The resulting flux due to $\nu_\mu$ and $\nu_\tau$ is

$$\phi_{\nu_\mu,\nu_\tau} = 3.41^{+0.66}_{-0.64} \times 10^6 \text{cm}^{-2}\text{s}^{-1}, \tag{3.11}$$

where the statistical and systematic errors are added in quadrature. The result differs from 0 by $5.3\sigma$ making the case for neutrino oscillations in the solar neutrinos very strong indeed.

The SNO collaboration published the allowed regions for the solar neutrino oscil-

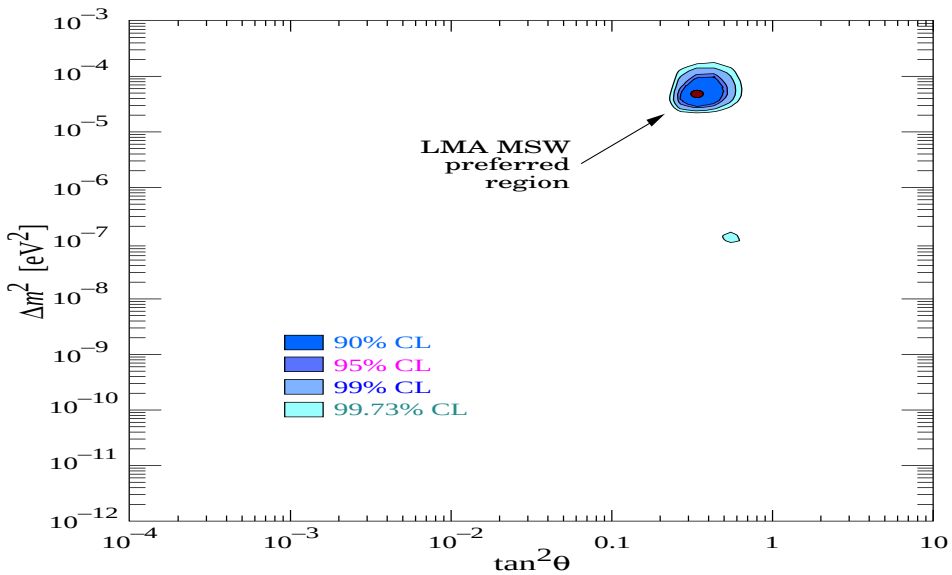


Figure 3.3: Allowed region for the solar neutrino oscillation parameter space. The parameters are the vacuum oscillation parameters [3].

lation parameters for oscillations between two neutrino flavors in matter in Fig. 3.3 [3]. The best fit point shown is at $\tan^2\theta = 0.3$ and $\Delta m^2 = 6 \times 10^{-5}\text{eV}^2$. The choice to use $\tan^2\theta$ rather than $\sin^2 2\theta$ reflects the fact that the neutrino oscillations are enhanced by $\nu_e$ interactions with electrons in the Sun and Earth. The acronym LMA marking the preferred region stands for Large Mixing Angle and reflects the fact that the mixing angle, $\theta \sim 30°$, is very different from 0. The values of $\Delta m^2$ and $\tan^2\theta$ quoted are the vacuum oscillation parameter values which when enhanced by matter interactions produce the observed oscillation signal.

## 3.3 Reactor Experiments

An independent check of the oscillation parameters measured by SNO comes from the anti-neutrinos produced as byproducts of commercial power production in fission reactors. In the context of neutrino oscillations, $CP$ invariance means the the probability for a $\nu_e$ to oscillate into a $\nu_\alpha$ is the same as the probability for a $\overline{\nu}_\alpha$ to oscillate into a $\overline{\nu}_e$,

$$CP: \; P(\nu_e \rightarrow \nu_\alpha) = P(\overline{\nu}_\alpha \rightarrow \overline{\nu}_e). \tag{3.12}$$

Using the time reversal invariance means that the probability for $\overline{\nu}_\alpha \rightarrow \overline{\nu}_e$ oscillations is the same as for $\overline{\nu}_e \rightarrow \overline{\nu}_\alpha$,

$$T: \; P(\overline{\nu}_\alpha \rightarrow \overline{\nu}_e) = P(\overline{\nu}_e \rightarrow \overline{\nu}_\alpha). \tag{3.13}$$

Thus, the $CPT$ theorem shows that the $\overline{\nu}_e$ produced by fission reactors should oscillate with the same probability as $\nu_e$. The reactor $\overline{\nu}_e$ can serve as a useful test of the solar neutrino parameters. The advantages of using reactor $\overline{\nu}_e$ are that the flux is well known as the power companies are required to keep careful records of the power output and a detector can be located at the appropriate distance away from the source to observe maximal oscillations. Oscillation experiments using reactor $\overline{\nu}_e$ look for the same signal that Reines and Cowan [30] did in their original experiment to detect neutrinos, namely the detection of an $e^+$ and the 2.2 MeV $\gamma$ ray from

neutron capture on a proton in delayed coincidence, both resulting from inverse $\beta$ decay.

Several experiments, such as CHOOZ and Palo Verde, have made use of this technique and did not find a signal for oscillations. They also operated during a time when the mixing parameters were not as well-known, resulting in the detectors being positioned at a distance from the source which was not optimal for seeing an oscillation signal [31]. However, these experiments did provide a limit to the size of the mixing angle between the heaviest and lightest mass eigenstates, $\theta_{13}$, of $\sin^2 2\theta_{13} \lesssim 0.03$ [32]. A recent experiment to look for oscillations of reactor $\overline{\nu}_e$ is the Kamioka Liquid scintillator Anti-Neutrino Detector (KamLAND) experiment which is located at the site of the previous Kamiokande experiment. KamLAND observes neutrinos from several reactors at a variety of distances, but the flux is dominated by only a few of those reactors between 138 and 214 km away, with an average distance of ∼180 km. Given the known fluxes from the reactors and the relatively narrow range of distances from the detector, KamLAND should witness a distortion of the $\overline{\nu}_e$ energy spectrum for oscillation parameters that are similar to those reported by SNO [31]. The detector records interactions from $\overline{\nu}_e$ with energies above 1.8 MeV. One source of background contamination are the $\overline{\nu}_e$ with $E_{\overline{\nu}_e} \leq 2.49$ MeV emitted by $^{238}$U and $^{232}$Th in the earth, called geo-neutrinos. The experiment requires that the energy measured to be above a threshold of 2.6 MeV to minimize this background. This experiment has collected a 766.3 ton-yr exposure [33]. The

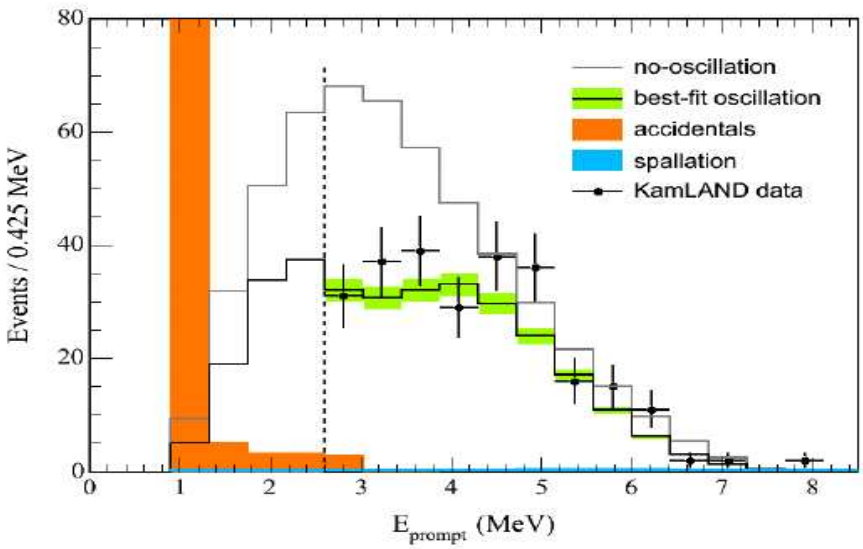


Figure 3.4: The reported energy spectrum of from fission reactors for the KamLAND experiment [33].

collaboration reports a distortion in the energy spectrum above the threshold as seen in Fig. 3.4 [33]. The figure shows the expected energy spectrum for no oscillations as the thin line. The background from the geo-neutrinos and the accidental triggers is the filled solid histogram. The data are the points, and the best fit to the data is shown by the thick line. The best fit parameters for vacuum oscillations are , $\sin^2 2\theta = 0.83$ and $\Delta m^2 = 8.3 \times 10^{-5}\text{eV}^2$ [33]. The collaboration reports a total of 258 observed neutrino events where $365 \pm 24$ (syst) were expected for the no oscillation case with 7.5 background events expected. The deficit of events compared to the no oscillation case is given by [33]

$$\frac{N_{obs} - N_{BG}}{N_{expected}} = 0.686 \pm 0.044(\text{stat}) \pm 0.045(\text{syst}). \tag{3.14}$$

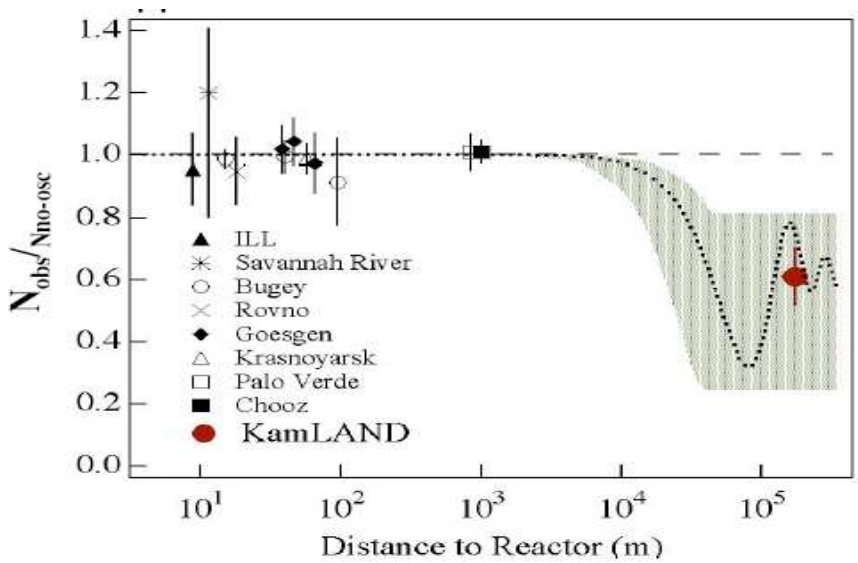


Figure 3.5: The oscillation probability for $\overline{\nu}_e$ as a function of $L/E$ for the oscillation parameters measured by KamLAND [31].

Fig. 3.5 [31] shows the ratio of the number of observed neutrinos in the various reactor experiments to the expected number for the no oscillation scenario as a function of the distance between the reactor and the detector in meters. This value is analogous to the survival probability for $\overline{\nu}_e$ to travel the distance indicated. The shaded band indicates the expected values for the best fit oscillation parameters. No oscillations are seen for distances of less than $\sim 10^3$ m. As seen in the figure, KamLAND is far enough away from the reactors to see an oscillation signal. Fig. 3.6 [33] shows the regions of parameter space for $\overline{\nu}_e$ oscillations that are allowed and excluded by the KamLAND measurement. The excluded regions based on the observed rate alone are the areas filled by dots. The allowed regions based on all the KamLAND data are shown by the remaining filled areas. Also shown in the figure is the LMA-

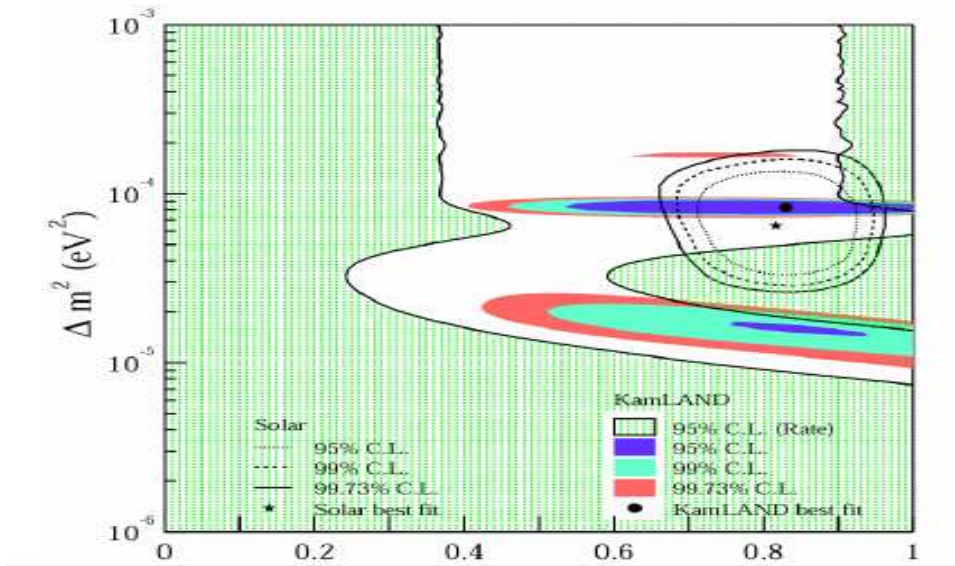


Figure 3.6: The confidence intervals for the oscillation parameters measured by KamLAND [33].

MSW allowed region determined by SNO. The oscillation parameters measured by KamLAND agree well with those measured by SNO.

## 3.4 Short Baseline Experiments

Short baseline experiments produce low energy neutrinos and attempt to observe oscillations for neutrinos traveling only a few 10's of meters. One such experiment that reported seeing an oscillation signal is the Liquid Scintillator Neutrino Detector (LSND). This experiment looked at $\overline{\nu}_\mu$ coming from the decay of $\mu^+$ at rest,

$$\mu^+ \rightarrow \overline{\nu}_\mu + \nu_e + e^+. \tag{3.15}$$

LSND claims to have seen an excess of $\overline{\nu}_e$ over the expected background, despite the fact that the decay of $\mu^+$ does not produce $\overline{\nu}_e$. The presence of these $\overline{\nu}_e$ was interpreted by the LSND collaboration as oscillations of $\overline{\nu}_\mu$ into $\overline{\nu}_e$. A similar experiment, the Karlsruhe Rutherford Medium Energy Neutrino (KARMEN) experiment, did not see a signal of $\overline{\nu}_e$. However, the KARMEN baseline was only 18 meters, while the LSND baseline was about 30 meters. If the LSND signal is confirmed, it would imply oscillation parameters of $\Delta m^2_{LSND} \sim 1\text{eV}^2$ and a mixing angle $\sin^2 2\theta_{LSND} \sim 0.004$ [3]. Currently, the Mini-BooNE experiment at FNAL is attempting to confirm the LSND signal.

## 3.5 Atmospheric Neutrino Experiments

Cosmic rays that impinge on the upper atmosphere can interact in the atmosphere to create mesons. These mesons are mostly pions and kaons and they decay into leptons, including neutrinos. The decay chain for pions is

$$\pi^\pm \longrightarrow \mu^\pm + \nu_\mu(\overline{\nu}_\mu). \tag{3.16}$$

Kaons decay in a similar manner,

$$K^\pm \longrightarrow \mu^\pm + \nu_\mu(\overline{\nu}_\mu). \tag{3.17}$$

The $\overline{\nu}_\mu$ occurs in the $\pi^-(K^-)$ decay. The muons also decay,

$$\mu^\pm \longrightarrow e^\pm + \overline{\nu}_\mu(\nu_\mu) + \nu_e(\overline{\nu}_e), \tag{3.18}$$

with the $\nu_\mu$ and $\overline{\nu}_e$ occurring for the $\mu^-$ decay. The neutrinos produced in these decays are known as "atmospheric" neutrinos. The left side of Fig. 3.7 shows a schematic of the interactions and decays producing the atmospheric neutrinos.

Experiments designed to measure atmospheric neutrinos are located deep underground for the same reason as the solar neutrino experiments, namely to shield the detector from the muons produced by the cosmic ray interactions. The atmospheric neutrinos can be detected in two ways. The first is to detect the observable particles when the neutrino interacts within the detector. These interactions are called "contained vertex events" because the point of interaction, or vertex, is inside the detector. The second method for observing atmospheric neutrinos is by observing the $\mu$ produced when a $\nu_\mu$ interacts in the rock surrounding the detector. The muons for these analyses must come from a direction where the amount of rock between the detector and atmosphere is large enough to filter out the majority of the cosmic ray muons. The muons observed from neutrino interactions in the rock are called "neutrino-induced muons."

### 3.5.1 Contained Vertex Event Analyses

Looking at eqs (3.16) - (3.18), one expects the ratio of the number of muon neutrinos, $N_{\nu_\mu}$, and anti-neutrinos, $N_{\overline{\nu}_\mu}$, to electron neutrinos, $N_{\nu_e}$, and anti-neutrinos, $N_{\overline{\nu}_e}$, to be

$$\frac{N_{\nu_\mu} + N_{\overline{\nu}_\mu}}{N_{\nu_e} + N_{\overline{\nu}_e}} \approx 2. \tag{3.19}$$

Comparing the ratio measured by the detector to the expected ratio is one way of searching for atmospheric neutrino oscillations. The solar neutrino results show that $\nu_e$ oscillate in vacuum only when the energy of the $\nu_e$, $E_{\nu_e}$, is of order 1 MeV. As the atmospheric $\nu_e$ have energies greater than several hundred MeV, the oscillation probability is too small for $\nu_e$ oscillations to be observed. However, if the $\nu_\mu$ oscillation parameters are such that they have a high oscillation probability in this energy range, a ratio different from 2:1 would be measured because some $\nu_\mu$ would oscillate into different flavors.

Another way to look for atmospheric $\nu_\mu$ oscillations makes use of the fact that the neutrino flux should be up/down symmetric for neutrinos with energies above a few GeV, since the flux of cosmic rays producing these neutrinos is isotropic [3]. The symmetry in the upward-going and downward-going fluxes can be understood from Fig. 3.7. The right side of this figure uses the Super-K detector as an example and shows that neutrinos produced either above the detector's horizon or below it can have trajectories that intersect the detector. If there are no oscillations to

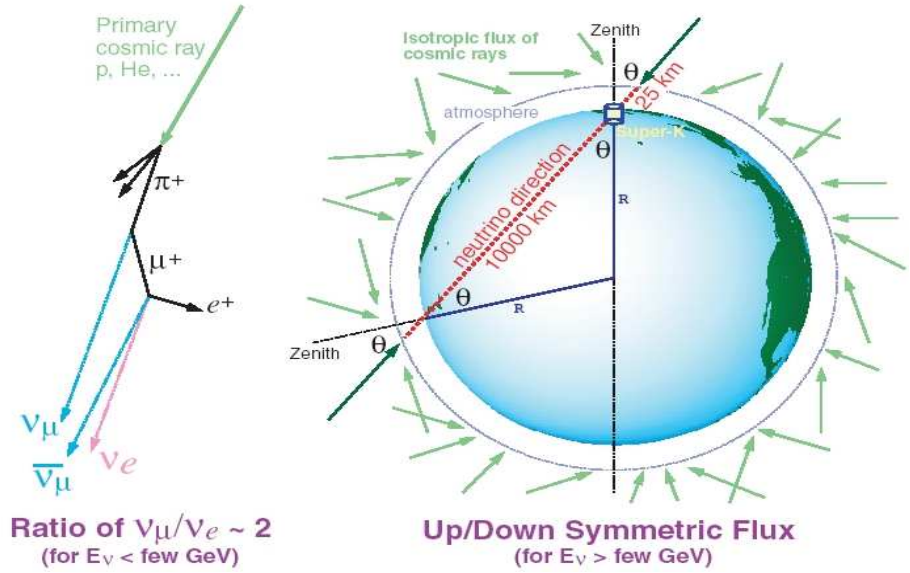


Figure 3.7: Atmospheric $\nu_\mu$ fluxes at an underground detector. The left side of the figure shows the interactions and decays producing atmospheric neutrinos. The right side of the figure shows the geometric argument for an up/down symmetry in the atmospheric neutrino flux.

decrease the $\nu_\mu$ flux, then the number of $\nu_\mu$ from below the detector's horizon with trajectories that intersect the detector will be the same as the number of $\nu_\mu$ produced above the detector's horizon with the opposite trajectories. Because neutrinos have very low interaction probabilities and the flux of atmospheric neutrinos is so large, it is safe to make the approximation that every neutrino produced with a trajectory that intersects the detector will do so. In that case the number of interactions from downward-going $\nu_\mu$ in the detector should be the same as the number of interactions from upward-going $\nu_\mu$.

The Super-K collaboration reported observations consistent with neutrino oscillations in the atmospheric neutrinos. The collaboration used both the ratio of flavors

as well as the expected symmetry in upward- and downward-going neutrino fluxes to show evidence for oscillations. Specifically, they used a technique of taking the ratio of $N_\mu$ to $N_e$ in the data and divided that ratio by the same ratio given by a Monte Carlo simulation. The expected ratio is 1 when no oscillations occur. For those events with energies of less than 1 GeV, the Super-Kamiokande collaboration reports a ratio of [34]

$$\frac{(N_\mu/N_e)_{Data}}{(N_\mu/N_e)_{MC}} = 0.649 \pm 0.016(stat) \pm 0.051(syst). \tag{3.20}$$

For events with energy greater than 1.33 GeV, the ratio is

$$\frac{(N_\mu/N_e)_{Data}}{(N_\mu/N_e)_{MC}} = 0.699^{+0.032}_{-0.030}(stat) \pm 0.083(syst). \tag{3.21}$$

Both of these values are significantly different from the expected ratio of 1:1.

To determine the direction from which an atmospheric neutrino came and the distance it traveled, the angle of the neutrino's trajectory with respect to the zenith, the point directly above the detector, can be measured. This angle is known as the zenith angle, $\theta$, with neutrinos coming from directly overhead having $\cos\theta = 1$ and those from the horizon have $\cos\theta = 0$. Differences in the shape of the observed and simulated neutrino flux over several regions in both $\cos\theta$ and neutrino energy can be used to determine the oscillation parameters by comparing the data to Monte Carlo expectations. The $\cos\theta$ distribution of $\nu_\mu$ interactions resulting in muons with

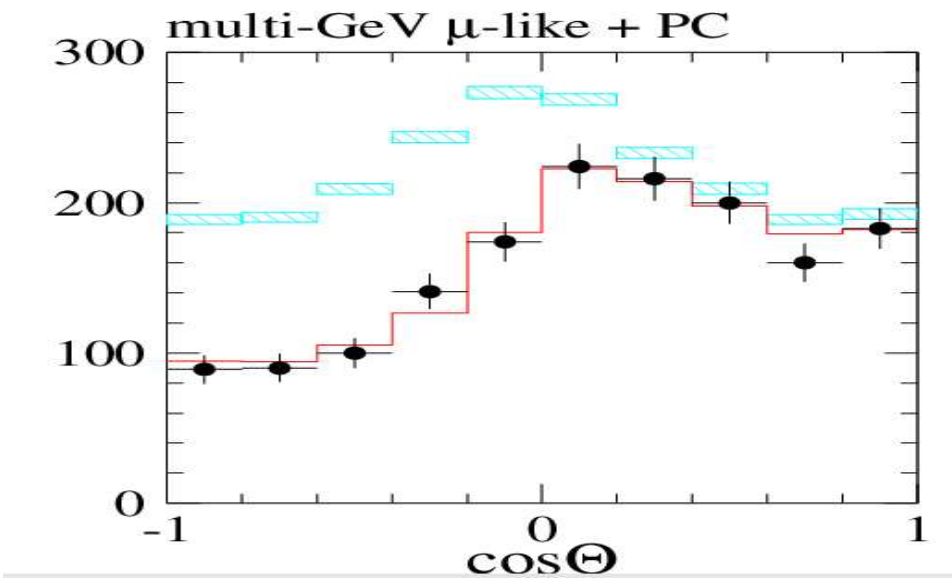


Figure 3.8: The $\cos\theta$ distribution of neutrino events producing multi-GeV muons and partially contained events for the Super-K data [34].

energies greater than 1.33 GeV and events that exit the Super-K detector are shown in Fig. 3.8 [34]. The collaboration reports the values of the oscillation parameters to be $\sin^2 2\theta = 1.0$ and $\Delta m^2 = 2.0 \times 10^{-3}\text{eV}^2$.

### 3.5.2 Neutrino-Induced Muon Analyses

The Super-K collaboration also reported results using upward-going, neutrino-induced muons. The collaboration looked at events which stopped in the detector and those that traversed the detector. The former are referred to as "stopping events" and the latter are "through-going" events. The stopping muons have lower energy than the through-going muons because the stopping muons do not have enough energy to traverse the detector's volume. The neutrinos creating the stopping muons have

lower energy on average than those creating through-going muons as well. The neutrino-induced muon events were separated into several bins in energy and $\cos\theta$. The shape of the flux distribution over those bins was analyzed to see if it was consistent with the neutrino oscillation hypothesis. The reported best fit to the shape was found to correspond to oscillations of $\nu_\mu \longrightarrow \nu_\tau$ with parameters of $\sin^2 2\theta = 1.0$ and $\Delta m^2 = 3.9 \times 10^{-3}\mathrm{eV}^2$ [1]. The 68% (dotted line), 90% (thick solid line) and 99% (dashed line) confidence intervals for this result are shown in Fig. 3.9 [1]. Also shown are the 90% confidence contours based on the ratio of the number of stopping to through-going events alone (marked with arrow) and the contained event analysis (thin solid line).

Another experiment that examined the upward-going neutrino-induced muons was MACRO. The experiment consisted of a large liquid scintillator detector located under the Gran Sasso in Italy and it operated from 1989-2000. The MACRO collaboration performed two analyses of the upward-going events. The first analysis looked at the distortion of the shape of the zenith angle distribution of events, while the second looked for the distortion of the muon energy distribution predicted by oscillations. The results for the analysis based on the shape of the $\cos\theta$ distribution are shown in Fig. 3.10 [2]. The data are the points, the expected flux is indicated by the shaded region and the best fit is shown with the dashed line. The second analysis used the observed amount of scattering undergone in the absorbing material by a muon due to Coulomb scattering from nuclei in the detector to estimate the energy of

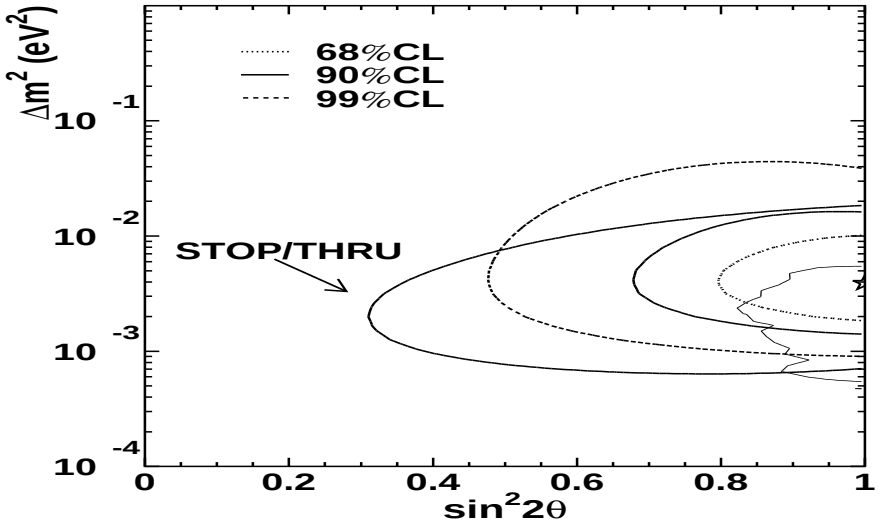


Figure 3.9: Confidence intervals for the Super-K neutrino-induced muon analysis [1]. The 68% (dotted line), 90% (thick solid line) and 99% (dashed line) confidence intervals for the neutrino-induced muon analysis are shown, as is the 90% confidence contour (thin solid line) for the contained event analysis. The contour labeled STOP/THRU is the 90% contour based on the ratio of the number of stopping to through going muons alone.

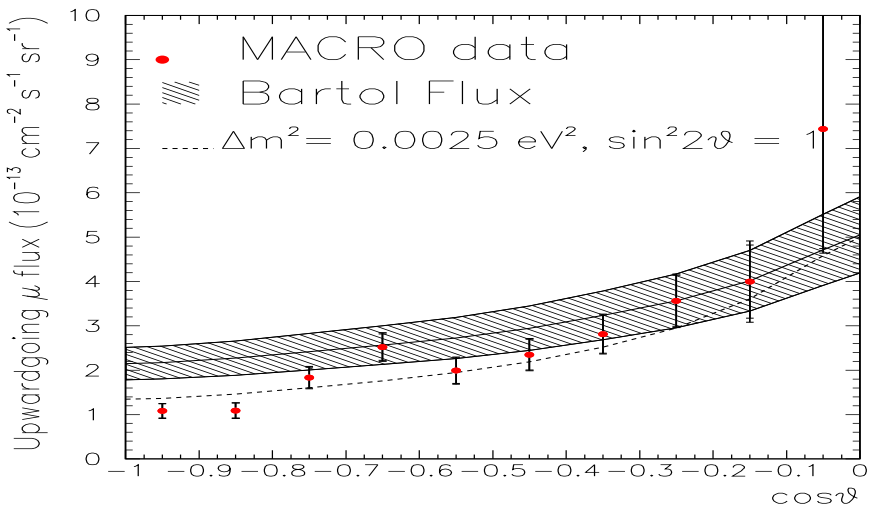


Figure 3.10: The $\cos\theta$ distribution for the MACRO neutrino-induced muon analysis [2]. The data are shown by the points, the expected flux is indicated by the shaded region and the best fit is the dashed line.

the muon. This scattering is known as multiple Coulomb scattering and the energy estimate came from observing the deflection of the muon's trajectory from a straight line as it traversed the detector. More energetic muons suffer smaller deflections from a straight line. The sample of through-going events was divided into 4 energy regimes and the number of observed events as a function of $\cos\theta$ was compared to the Monte Carlo predictions. Both analyses indicated a positive signal for neutrino oscillations with $\sin^2 2\theta = 1.0$ and $\Delta m^2 = 2.5 \times 10^{-3}\mathrm{eV}^2$ [2].

## 3.6 Long Baseline Experiments

Long baseline experiments are another probe of neutrino oscillations. These accelerator-based experiments attempt to determine the oscillation parameters for a given oscillation scenario to very high precision by controlling both the distance traveled by the neutrinos and the neutrino energy. These experiments consist of a neutrino source and two detectors. The source is a beam of $\nu_\mu$ generated by accelerating protons to high energies and having them strike a target to produce mesons. These mesons decay according to the chains in eqs (3.16) and (3.18). One detector is near the neutrino source to measure the energy distribution of the $\nu_\mu$ beam and its flux. The second detector is located several hundred kilometers away and measures the energy distribution and flux again. The large separation between the source and the far detector in these experiments gives rise to the long baseline designation. If both detectors are made with the same technology, a ratio of the fluxes in the near and far detectors leads to the cancellation of systematic uncertainties in the flux determination. This type of experiment compares both the observed and expected number of events in the far detector as well as the shape of the energy distributions in both detectors to determine oscillation parameters.

An example of a long baseline experiment is the KEK to Kamioka (K2K) experiment in Japan. The neutrino beam source and near detector of K2K are at the KEK proton synchrotron facility and the far detector is the Super-Kamiokande detector,

which is 250 km away. The experiment generates the neutrino beam from 12 GeV protons incident on an aluminum target. The resulting neutrinos are 98% pure $\nu_\mu$ with a mean energy of 1.3 GeV [35]. The location of the far detector as well as the energy of the neutrino beam were chosen to look for oscillations of $\nu_\mu \rightarrow \nu_\tau$ with the parameters suggested by the atmospheric neutrino measurements. One measure of the number of neutrinos produced by the beam is the number of protons that were incident on the target material, a value known as "protons on target" (POT). A total exposure of $4.8 \times 10^{19}$ POT was observed between June 1999 and July 2001, with an expected number of $80^{+6.2}_{-5.4}$ beam neutrino events in the far detector. Only 56 events were observed. Additionally, the energy spectra differed in the two detectors, with the far detector showing a deficit of events with low energies, as expected for oscillations according to eq (2.22). Fig. 3.11 [35] shows the measured energy spectrum. The data are the points, the expectation in the absence of neutrino oscillations are the boxes and the best fit for oscillations is shown by the solid line. The collaboration found the results for this exposure were best fit by $\sin^2 2\theta = 1.0$ and $\Delta m^2 = 2.8 \times 10^{-3}\text{eV}^2$, in good agreement with the Super-K and MACRO atmospheric neutrino results. The allowed regions for the measurement are shown in Fig. 3.12 [35] where the dashed, solid and dot-dashed lines are the 68.4%,90%, and 99% contours respectively.

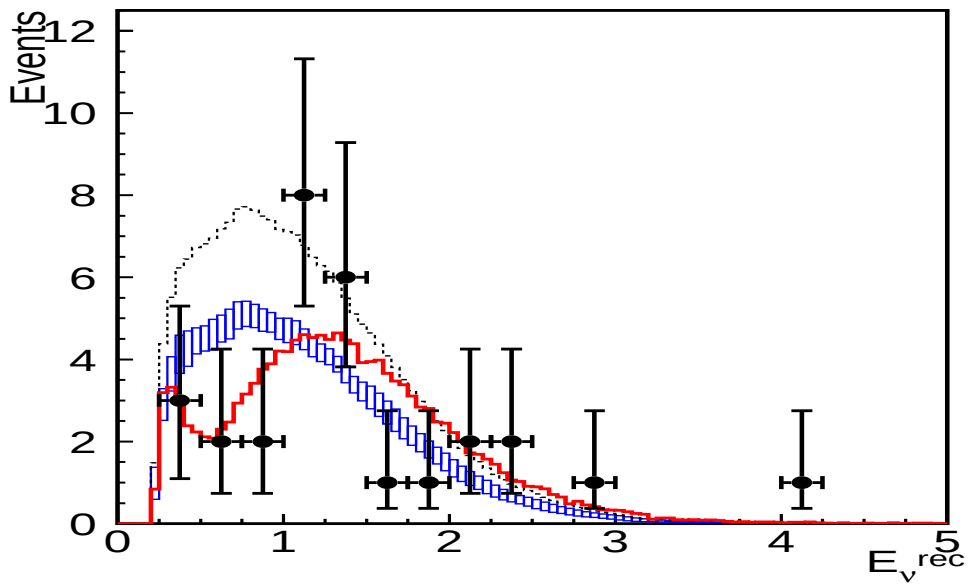


Figure 3.11: Measured energy spectrum from the K2K experiment. The measured energies of the $\nu_\mu$ (points) along with the expected spectrum for no oscillations (boxes) and the best fit (solid line). [35]

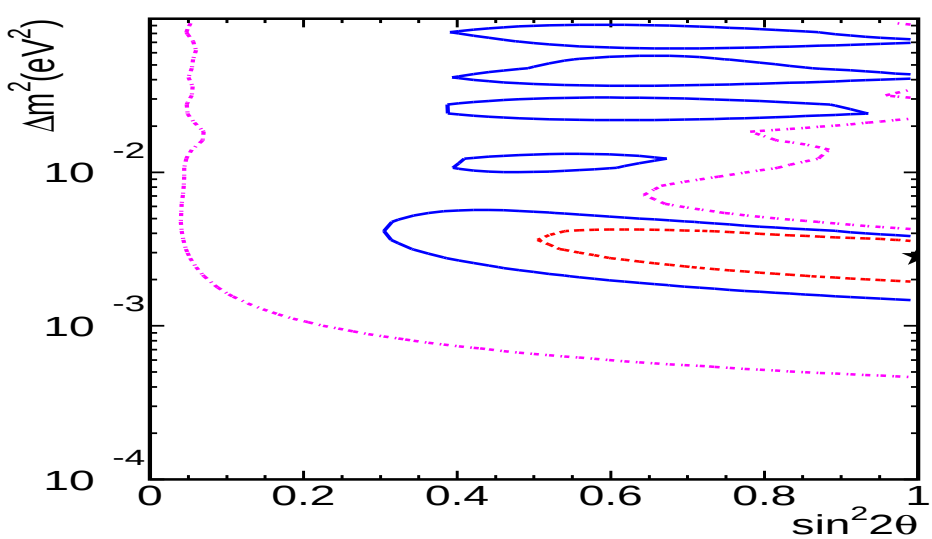


Figure 3.12: Confidence intervals for the K2K experiment. The dashed, solid and dot-dashed lines are the 68.4%,90%, and 99% contours respectively. [35]

## 3.7 Conclusions

The evidence is strongly in favor of neutrino oscillations. The solar and reactor experiments suggest that $\nu_e$ and $\overline{\nu}_e$ oscillate with a large mixing angle, $\theta \sim 30°$, and a small mass splitting, $\Delta m^2 \approx 6{\times}10^{-5}\mathrm{eV}^2$. The atmospheric and beam neutrino experiments suggest that $\nu_\mu \rightarrow \nu_\tau$ oscillations occur maximally with $\Delta m^2 \approx 3 \times 10^{-3}\mathrm{eV}^2$. In the following discussion, only the solar and atmospheric neutrino oscillation results are considered.

The two different orders of magnitude in the mass splittings for the $\nu_e$ and $\nu_\mu$ oscillations imply a mass hierarchy where two of the mass states are quite close together and the third is very different from the first two. The hierarchy can be either "normal" with the two close states being lighter than the third, or "inverted" with the two close states being much heavier than the third. Fig. 3.13 shows the "normal" hierarchy with the mass squared values increasing from bottom to top. The zero point of the scale is not known. In this figure, the lowest splitting represents the solar neutrinos and the larger splitting is for the atmospheric neutrinos. This figure also illustrates the fraction of each flavor state in the mass eigenstates. The $\nu_e$ contribution is shown by cross-hatching, the $\nu_\mu$ contribution is represented by right-leaning diagonals and the $\nu_\tau$ contribution by left-leaning diagonals. The amount that each flavor contributes to a mass state is reflected by the size of the mixing angles. Notice that the relative size of the $\nu_\mu$ and $\nu_\tau$ flavors are equal in each mass

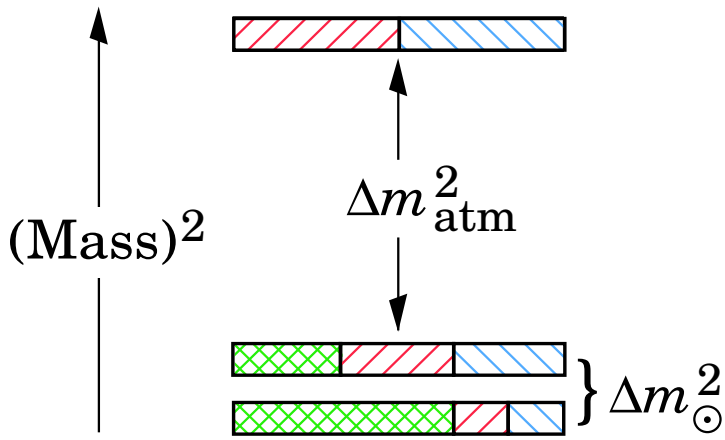


Figure 3.13: Mass$^2$ spectrum for the three neutrino mass states [3]. The $\nu_e$ fraction of each mass state is indicated by the cross-hatching, the $\nu_\mu$ fraction is shown by the right-leaning diagonals and the $\nu_\tau$ fraction is the left leaning diagonals. This spectrum assumes normal mass hierarchy.

state, reflecting the maximal mixing observed in the atmospheric neutrinos between those flavors. The lowest mass state, $\nu_1$, corresponds mostly to $\nu_e$. The amount of $\nu_e$ contribution in the second mass eigenstate, $\nu_2$, is given by the solar neutrino mixing angle. The heaviest mass eigenstate is almost entirely composed of $\nu_\mu$ and $\nu_\tau$. The amount that $\nu_e$ contributes to $\nu_3$ is one of the most important questions in the field of neutrino physics because the *CP*-violating phase factors are determined by the mixing between those states. It is the potential *CP*-violation in neutrinos that may have led to baryogenesis [15]. The size of the $U_{e3}$ component of the mixing matrix in eq (2.24) is still unknown, although reactor experiments suggest that the mixing angle for that component, $\theta_{13}$, is expected to be $\lesssim 10^\circ$ [32].

Thanks to the results of the experiments described in this chapter, a new phase

in neutrino physics has begun. The oscillation parameters for $\nu_e \rightarrow \nu_\alpha$ and $\nu_\mu \rightarrow \nu_\tau$ are now thought to be fairly well-understood. Future experiments will work to more precisely determine the parameters. One such experiment is the Main Injector Neutrino Oscillation Search (MINOS). This is a long baseline experiment designed to observe $\nu_\mu \rightarrow \nu_\tau$ oscillations. The neutrino beam for this experiment is to be generated at Fermilab and sampled by a near detector approximately 1 km from the target. The far detector is located 735 km away in the Soudan Underground Mine in Soudan, MN. Fig. 3.14 shows an aerial view of the Fermilab complex with the Main Injector and MINOS near detector locations indicated. A map marking the locations of the MINOS detectors is shown in the inset. The MINOS beam will be generated by accelerating protons to 120 GeV and making them incident on a carbon target. Magnetic focusing horns will focus the mesons to produce a neutrino beam with a mean energy of a few GeV and a long high energy tail. The location of the far detector and the beam energy were designed to make a precision measurement of the $\sin^2 2\theta$ and $\Delta m^2$ governing $\nu_\mu \rightarrow \nu_\tau$ oscillations.

The construction of the MINOS far detector began in 2001 and it has taken data using atmospheric neutrinos and cosmic ray muons since 2002. These data, presented in following chapters, will show that the detector performance is understood and will provide a measurement of the atmospheric neutrino oscillation parameters. In this analysis MINOS has the advantage of a flat overburden allowing it to observe neutrino-induced muons coming from above the horizon. This advantage allows

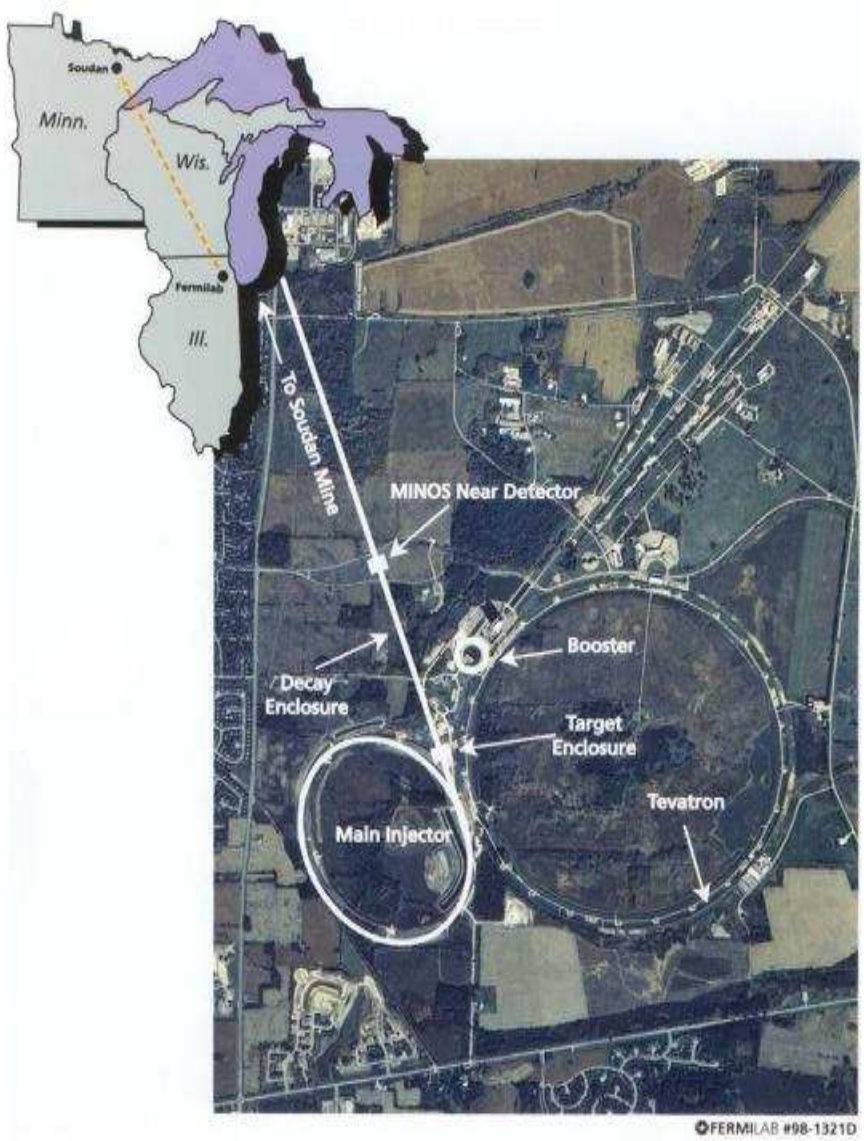


Figure 3.14: Aerial view of Fermilab. The locations of the MINOS near (Fermilab) and far (Soudan, MN) detectors are shown in the inset. The distance between the detectors is 735 km.

for the measurement of oscillations to be extended into new regions of parameter space. In addition, MINOS is the first magnetized underground neutrino detector, an advantage that allows it to distinguish between muons created by neutrinos and and those created by anti-neutrinos.

# Chapter 4

# The MINOS Far Detector

## 4.1 Introduction

The Main Injector Neutrino Oscillation Search is a long baseline neutrino oscillation experiment as described in § 3.6 and §3.7. The MINOS far detector is located in the Soudan Underground Mine, Soudan, Minnesota, USA. The detector is on the 27th level of the mine, 2341 feet below the surface. The detector hall is 82.3 m $\times$ 13.8 m $\times$ 11.6 m (height). Four major sub-systems make up the MINOS far detector, the active detector, steel absorber planes, electronics and magnetic coil systems.

The detector is shown schematically in Fig. 4.1. The detector has an octagonal cross section that is 8 m in width; it is approximately 30 m long. A 30 cm circular opening is centered at the middle for the current carrying wire of the magnetic coil. The detector is divided into two major sections called supermodules (SM), that are

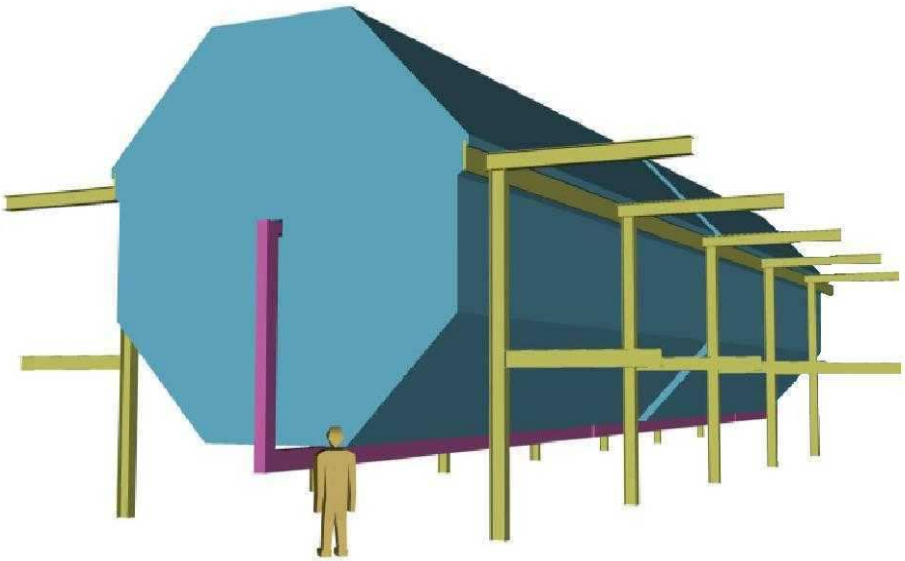

Figure 4.1: Schematic of the MINOS far detector.

made of alternating layers of 2.54 cm thick steel absorber and 1 cm thick plastic scintillator active detector. The scintillator is encased in aluminum to create a light tight barrier. There is an air gap of $\sim$ 2.54 cm between each steel/scintillator layer. A layer of scintillator mounted on steel is called an instrumented plane; steel planes that do not have scintillator mounted on them are called uninstrumented planes. The first plane in each SM is uninstrumented. For the remainder of this discussion, the term plane refers to an instrumented plane unless otherwise noted.

The scintillator is mounted directly on the steel as shown in Fig. 4.2. The bright skin of the aluminum casings can be seen. As seen in the figure, 8 "modules" make up the scintillator layer for each plane. The modules are composed of extruded strips of polystyrene that are each 4.16 cm wide. There are two types of scintillator modules, those with 20 strips and those with 28. Four 20 wide modules, labeled 3-6 in the

Figure 4.2: An instrumented plane of the far detector. The scintillator is encased in aluminum and is mounted on top of the steel.

figure, cover the inner portion of a steel plane and the strips are generally 8 m long. The only strips which are shorter than 8 m in these modules are located in the region bordering the coil hole. Four 28 strip modules are on the outer portions of the steel planes, labeled 1, 2, 7 and 8 in the figure. The strips in these modules range from $\sim$ 4-8 m in length. A total of 192 scintillator strips cover the face of each steel plane. A schematic of the light path for the photons from the scintillator to the readout photomultiplier tube (PMT) is shown in Fig. 4.3. The upper section of the figure shows the interaction of a muon passing through a single scintillator strip. As the muon traverses the scintillator, it deposits energy that is converted into photons. A photon produced in the scintillator is shown with a few representative bounces off the strip walls before entering the fiber optic wave guide. The lower section of the figure

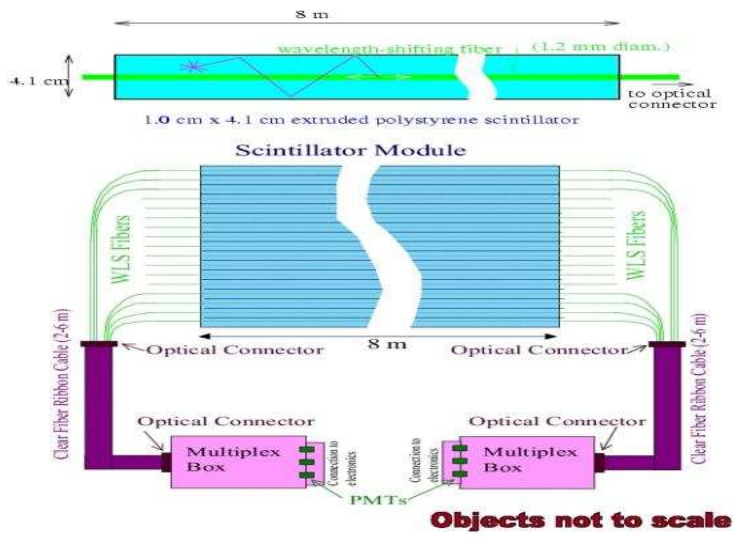


Figure 4.3: Schematic of the light path from particle interaction in a scintillator strip to the PMT.

shows several strips with their ends connected to fiber optic cables. The cables are connected at their other ends to boxes housing the PMTs. Fig. 4.4 shows a module with the aluminum skin removed, revealing the strips making up the module.

A groove is placed in the middle of each strip during the extrusion process. The groove runs the length of the strip and a wave length shifting (WLS) optical fiber is placed in each groove. The scintillation light produced by a particle traversing the strip is collected in the fiber. The scintillation light is UV, but the fiber contains fluors such that the UV light is absorbed and reemitted as green light. At the end of each module the fibers are mounted in injection molded plastic connectors. A second connector is mated to the module connector, which butts clear optical fiber to the WLS fiber. The clear fiber carries the signal to the PMTs. The clear fibers

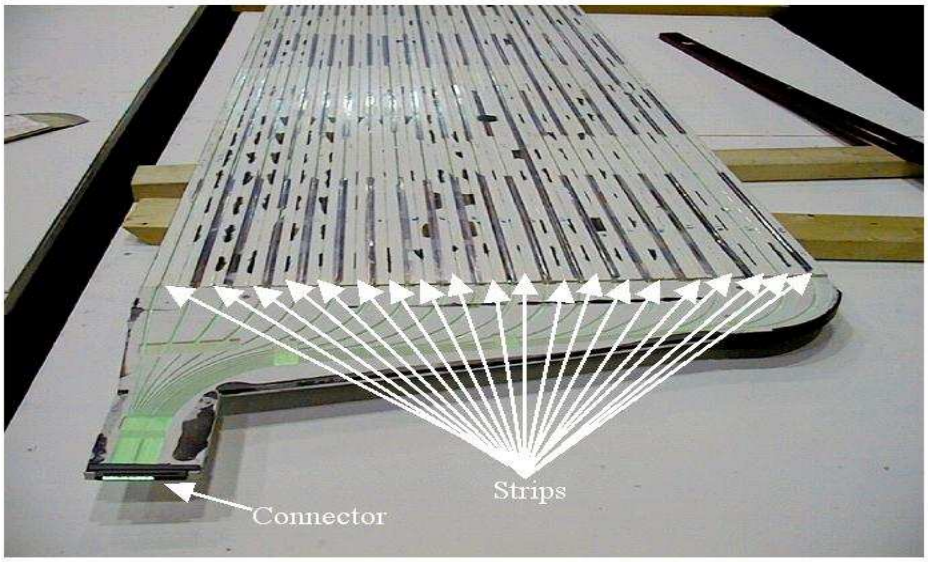


Figure 4.4: A 20 strip wide scintillator module.

are placed inside flexible black plastic conduit to provide a light tight environment for them. The bundles of clear fiber are called cables. Another connector is at the far end of the cable and mates to a connector on a steel box containing the PMTs. Fig. 4.5 shows several cables running from the modules to the steel boxes. A small amount of clear fiber inside each PMT box routes the signal from the cables the PMTs. The routing is discussed in detail in § 4.2.5.

The PMTs used in the MINOS far detector are Hamamatsu R5900U-00-M16 (M16) phototubes, which are multi-anode phototubes with 16 photosensing pixels. The pixels are each approximately 4 mm $\times$ 4 mm in area. Fig. 4.6 shows several views of an M16. This phototube was chosen because it has been used in a variety of experiments and applications [36], and has been shown to be reliable. Another reason for choosing this PMT is that the multiple pixels allow several signal channels

Figure 4.5: Fiber optic cables running from the modules to the steel boxes.

to be read out using the same electronics, thereby reducing the number of readout devices needed. To save construction costs further, 8 signal fibers are readout by each PMT pixel. The M16 PMT has good quantum efficiency, but the pixel-to-pixel response is not particularly uniform. However, this is not a problem for MINOS as the non-uniformities are simply calibrated out of the data [36] using information

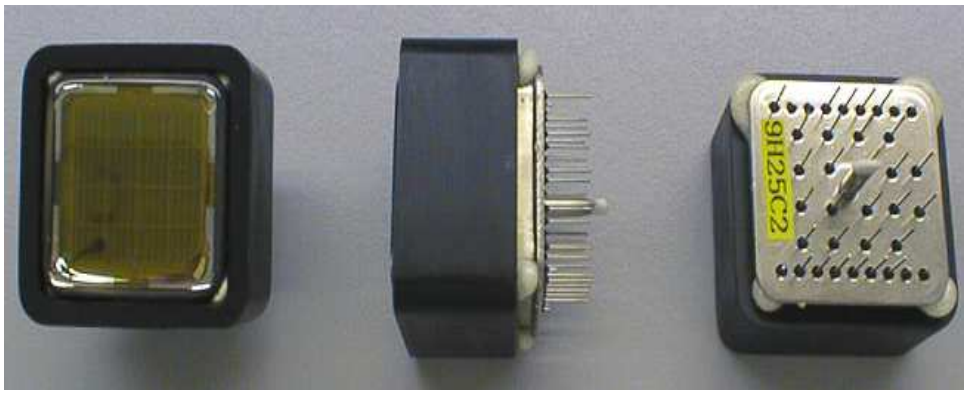


Figure 4.6: Several views of the M16 phototube.

obtained from testing the PMTs. These PMTs have time resolution of less than 2 ns for a signal of more than 10 observed photo-electrons [36]. The M16, like other multi-anode PMTs, is vulnerable to optical and electronic cross-talk, resulting in signal appearing in channels that were not directly illuminated. The pixels most likely to see cross-talk signal are those that share a side with a pixel that observes a signal. While the average cross-talk level is only a few percent, excursions of up to 10% are not uncommon [36].

The signals from the PMTs are routed to several electronics crates located along the detector. The signal from one side of 64 planes is collected in a single crate. There are 8 crates on the west side of the detector and 8 crates on the east side. The electronics crates send the signal to the main data acquisition processors, where they are placed into the data stream.

The detector coordinate system has the $y$-direction increasing radially outward from the center of the Earth. The $z$-direction increases from south to north. The $x$-direction points to the west to make a right-handed coordinate system. The modules mounted on consecutive steel planes are orthogonal to each other to allow two tracking views of particles traversing the detector. The first orientation has the ends of the strips located on the lower level on the east side of the detector and the upper level on the west side. This orientation is called the U view. The other orientation, called the V view, has the strip ends on the lower west side and upper east side. The U and V views represent a rotation of the $x$- and $y$-directions about the $z$-axis. The

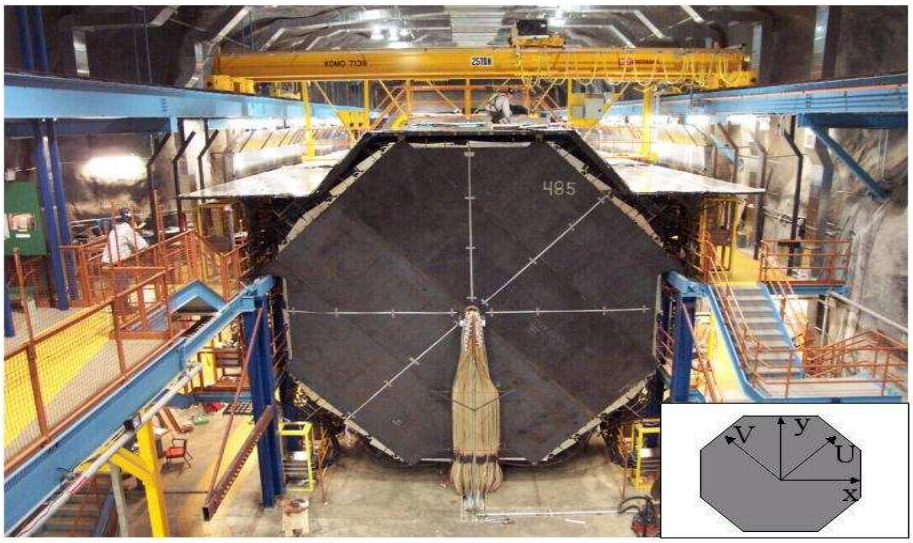


Figure 4.7: The completed MINOS far detector.

reason for this rotation is that it makes detector construction easier because all the module ends are accessible. The finished detector as seen from the north end of the hall is shown in Fig. 4.7. An inset shows the detector coordinate system, including the U and V directions.

The magnetic field of the detector is produced by a coil of current carrying wires running through the length of each SM. The magnetic field is toroidal and has significant components in only the $x$ and $y$ directions. A finite element analysis was done to model the field for each $x$ and $y$ coordinate in a steel plane. Fig. 4.8 shows the resulting map of the magnetic field for a steel plane in the far detector. In this figure, the magnitude of the field in teslas for each location is shown by the color scale at the right. The field is assumed to be identical for each plane in the detector. The field is strongest near the coil with a maximum value of 1.7 T. It falls off as the

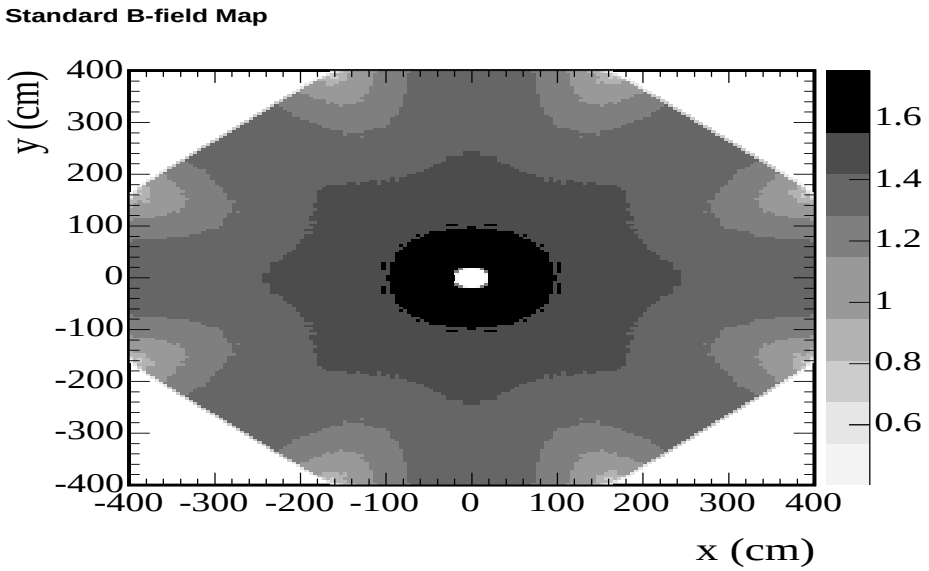


Figure 4.8: The magnetic field map for planes in the far detector.

distance from the coil increases, and has its lowest value of $\sim$ 1 T at the octagon verticies.

## 4.2 Scintillator System

Indiana University's hardware responsibilities for MINOS are focused on the scintillator system.

### 4.2.1 Scintillator Characteristics

The scintillator strips used by MINOS are made from extruded polystyrene infused with PPO and POPOP fluors. The groove for the fiber in each strip is made during the extrusion process and is 1.3 mm deep. A reflective coating of $TiO_2$ is added to

each strip when it is extruded. This reflective coating covers the entire strip except for the area near the groove. The decision to use solid scintillator in the detector was based on several considerations. The scintillator provides good resolution of the energy, $E$, deposited in electromagnetic (EM) and hadronic showers. The expected resolution for the scintillator is $\sim 23\%/\sqrt{E}$ for EM showers and $53\%/\sqrt{E}$ for hadronic showers, where $E$ is given in GeV. The scintillator allows for good coverage of the steel plates as the gaps between strips are $< 1$ mm. The collaboration tested the scintillator for its uniformity in light output by comparing the output of a strip from a given location in a module to the average for all strips from that location. Radioactive sources provided the particles used to test the light output. The results of the comparisons are shown in Fig. 4.9 and the data are described very well by a Gaussian distribution with a $\sigma$ of 11%. Several aging tests were performed and these tests showed a loss of light output of about 10% can be expected over the lifetime of the experiment [36].

### 4.2.2 Fiber Characteristics

Both the WLS and clear fiber are produced by Kurary, and are 1.2 mm in diameter. The fiber core is 1.0 mm in diameter and has an index of refraction of 1.49. Two layers of cladding encase the core, with the first layer having $n = 1.55$ and the second having $n = 1.59$. The decision to use two different types of fiber was based on the short attenuation length of the WLS fiber. The WLS attenuation length of 5 m

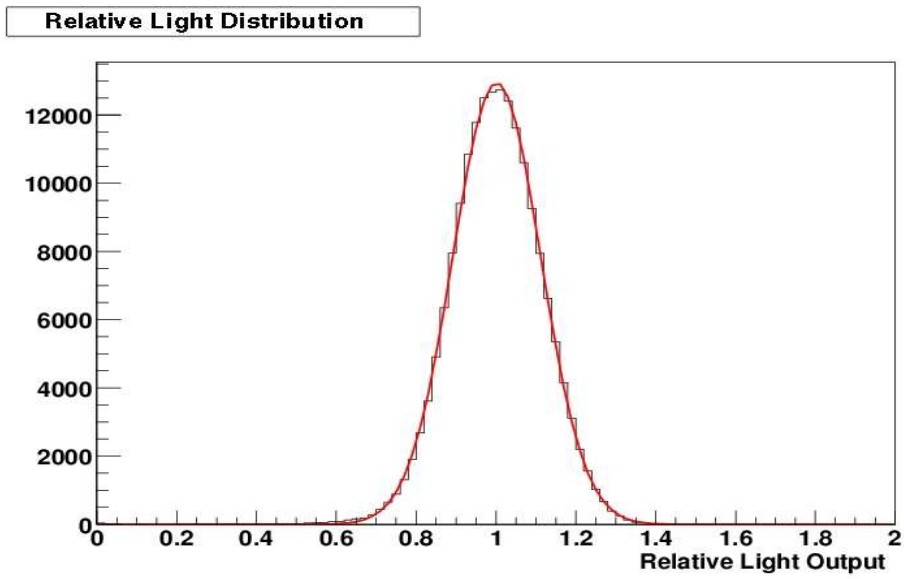


Figure 4.9: Uniformity of scintillator in the far detector.

is acceptable for routing the photons along the length of a scintillator strip where the maximum longitudinal distance traveled by a photon is 8 m. However, this attenuation length is too short to serve as a practical waveguide to the PMTs. The clear fiber has a much longer attenuation length of 11 m and can route the photons from the scintillator to the PMTs with much smaller losses than the WLS fiber.

### 4.2.3 Optical Connectors

The optical connectors were designed at Indiana University, and are injection molded delron plastic. Two types of connectors are used in the far detector, module/MUX (M-type) and cable (C-type) connectors. Figures 4.10 and 4.11 show the mechanical drawings for the M- and C-type connectors respectively. The three sets of ten holes in the middle of the connector hold the fibers. The number of fiber holes was chosen

to be 30 so that both 20 and 28 strip wide modules could use the same connectors whether loaded from the left or right sides. The 3 groups of 10 holes provide structural stability to the connector for the injection molding process. The outer-most holes are used to mount the connectors to the modules in the M-type connectors and are not used in the C-type connectors. The next holes in from the ends are for the screws that hold the connector pairs together. The next set of holes are for alignment dowel pins that assure the fibers from each connector in a pair are aligned well with the other connector. The dowel pin holes are different sizes to ensure that the connectors cannot be mated incorrectly. The distinguishing characteristic of M-type from C-type connectors is the extra fiber strain relief area on the back of the C-type connector. Once the fibers are glued into a connector, the front face of the connector is flycut using an industrial grade diamond cutter. This procedure produces a high grade optical finish on the fiber ends. The connectors create a very good optical interface at the module/cable and cable/MUX box connections. Measurements taken at Indiana University show the light transmission from fibers in one connector to fibers in another across an air gap of a few microns is at the level of 90%. With Bicron optical grease, which has the same index of refraction as the fiber core, placed in the gap between connectors the transmission increases to 95%.

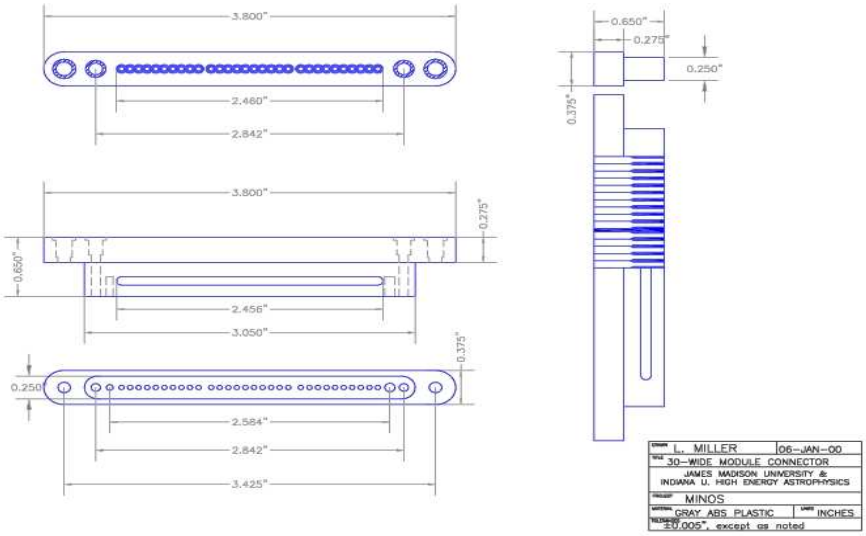


Figure 4.10: Drawing for an M-type connector.

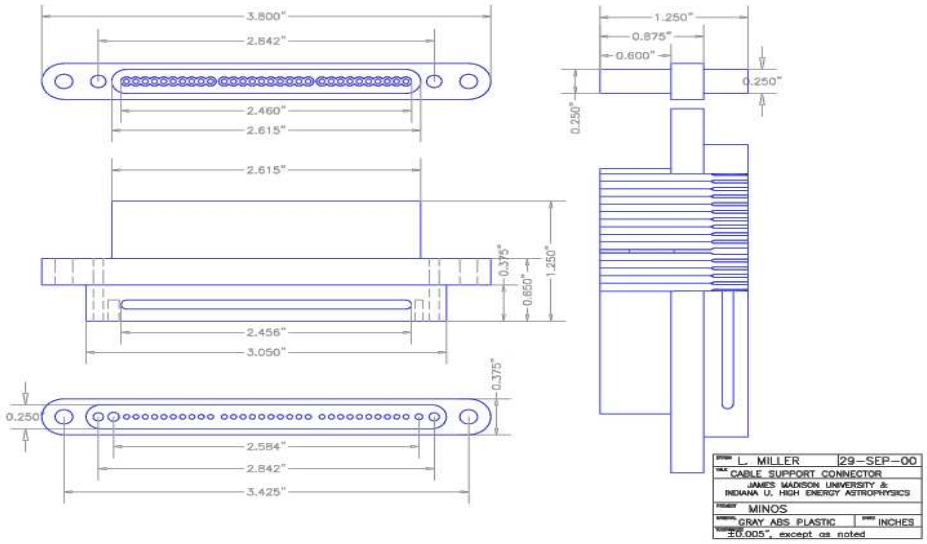


Figure 4.11: Drawing for a C-type connector.

### 4.2.4 MUX Box Design and Construction

The device for routing the clear fibers from the cables to the PMTs is the multiplexing or MUX box. Each MUX box is made of steel and houses 3 M16 phototubes. The boxes were made out of steel to reduce the effect of the detector's magnetic field on the PMTs. The details of the mapping, or multiplexing, of the signal fibers to the PMT pixels is discussed in § 4.2.5. The assembly drawing for the MUX boxes is shown in Fig. 4.12. Two compartments are in a MUX box and they are separated by the piece labeled "Cookie Mounting Plate" in the figure. The 16 slots in the MUX box frame hold the optical connectors. The routing of the fibers from each strip in the detector to its readout PMT is accomplished using a short length ($\sim$ 30 cm) of fiber running from the MUX box optical connectors to injection molded plastic "cookies". The compartment holding the connectors and fiber is called the fiber compartment. The cookies are mounted on the Cookie Mounting Plate and their functions are to group the fibers into bundles of 8, align the fiber bundles with the PMT pixels, and press the fibers to the face of the PMT. Fig. 4.13 shows the mechanical drawing for the cookie. Each cookie has 16 square slots cut into it which are aligned with the PMT pixels. The fibers for a given pixel fit tightly into the slot in the arrangement indicated in the figure. Glue is poured into the well shown in Fig. 4.13 to keep the fibers in place. The compartment on the side of the Cookie Mounting Plate opposite the fiber compartment houses the PMTs, and their readout and high voltage (HV) cables. This compartment was made to be accessible for PMT equipment changes by

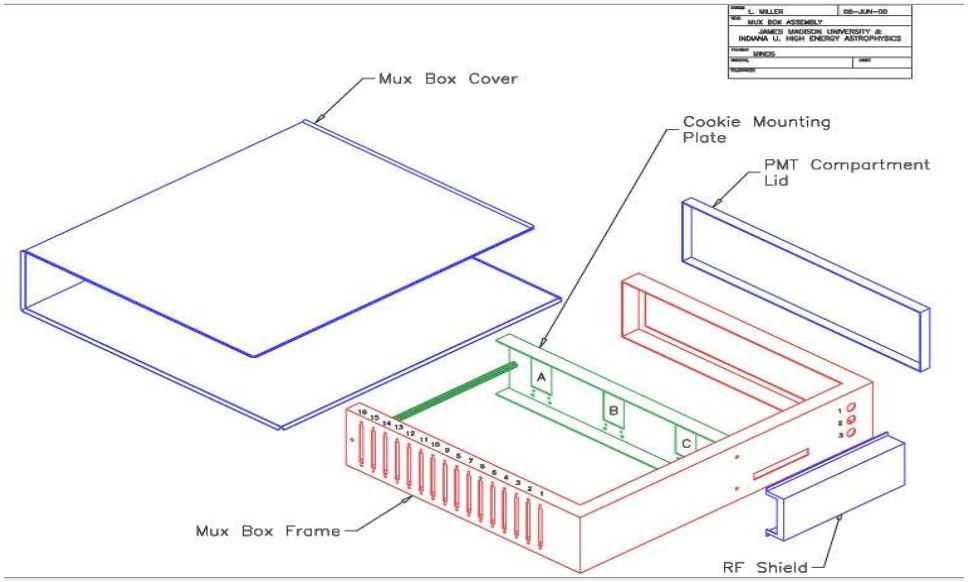


Figure 4.12: Drawing for a MUX box.

designing the removable "PMT Compartment Lid" seen in the figure. The "MUX Box Cover" slides over the frame and is attached to it using screws. The MUX box is made light tight through generous application of RTV around every opening. The PMT readout board is shielded from radio frequency (RF) noise by the "RF Shield."

The procedure for assembling a MUX box follows. First fibers are mounted into the cookies and glue is poured into the well shown in Fig. 4.13. The cookie was designed to allow the glue to fill in any gaps between the fibers and form an even surface around the fibers on the front face of the cookie. That face is flycut with a diamond cutter to polish it. The cookie is then mounted in the box. The other ends of the cookie's fibers are placed into the appropriate connectors at the front of the MUX box and glued into the connectors. Those fibers are also flycut with the

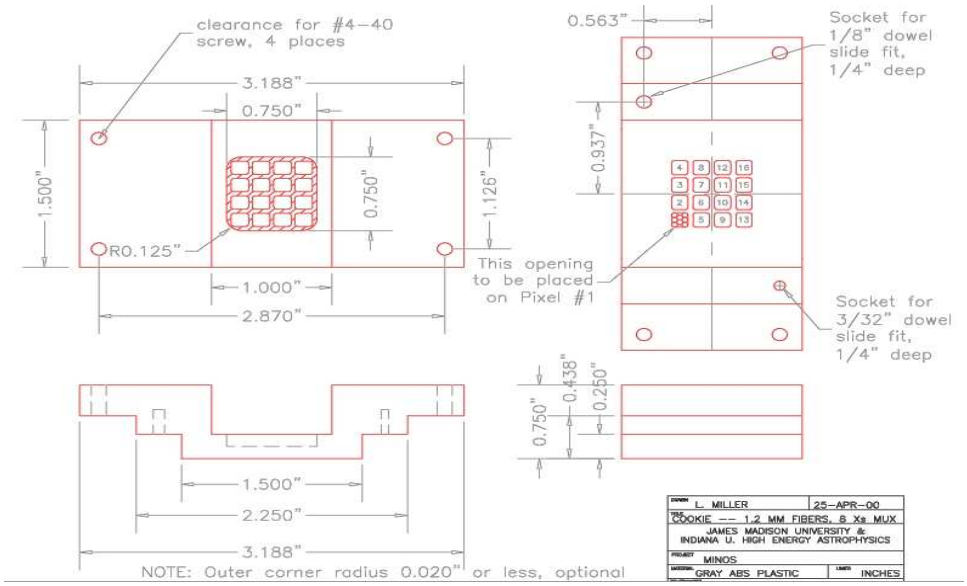


Figure 4.13: Mechanical drawing of the cookie used to couple fibers to PMTs.

diamond cutter. The areas of the box where light could leak in are sealed with RTV. The PMTs are mounted to the cookies and the box is tested for light leaks. The procedure for testing for light leaks is to place the box in a darkened room, connect the readout electronics and HV, and then shine a flashlight over each seal in the box. A rate meter monitors the signal rate in the PMTs and spikes if a leak is present. Each box is also tested to see that a signal can be read out from each fiber. This test is done by injecting a uniform light signal into each fiber in a connector and reading out the signal from the PMT connected to those fibers.

### 4.2.5 The Multiplexing Pattern

Each MUX box has 16 optical connectors containing either 20 or 28 fibers. Since each plane has eight modules, the fibers from one side of two planes are routed to

| | | | |
|---|---|---|---|
| 1 | 13 | 2 | 14 |
| 15 | 3 | 16 | 4 |
| 5 | 17 | 6 | 18 |
| 19 | 7 | 20 | 8 |

| | | | |
|---|---|---|---|
| 9 | 21 | 10 | 22 |
| 23 | 11 | 24 | 12 |
| - | - | - | - |
| - | - | - | - |

Figure 4.14: Lacing order for pixels connected to one plane of the far detector. For the second plane, pixel 1 starts on the first unused pixel in the second phototube and continues the checkerboard pattern onto a third phototube.

each MUX box. The two planes connected to a box are from consecutive planes with the same view (U, V). Since each plane has 192 signal fibers, a total of 384 signal fibers are routed to the 48 pixels of the 3 M16 PMTs. The 192 fibers from the first plane map to the 16 pixels of the PMT closest to the readout electronics and the first 8 pixels of the middle PMT. The fibers from the second plane map to the last 8 pixels of the middle PMT and the 16 pixels of the remaining PMT. The scheme that determines the mapping of the signal fibers to the pixels is called the multiplexing pattern.

The multiplexing pattern adopted by the MINOS collaboration is one that reads out fibers separated by 24 strips with the same PMT pixel. This choice results from the typical 1-meter shower width expected for neutrino interactions in the

8-meter far detector. A second consideration in the selection of the multiplexing pattern is the requirement that cross-talk amongst the M16 pixels be minimized. Since approximately 10% of the signal on a given pixel may leak onto neighboring pixels [37], it is important that adjacent scintillator strips be mapped to nonadjacent pixels to avoid confusion in event reconstruction. The third consideration is that the mapping on the west side of the detector must differ from the east side in order to provide a mechanism to resolve the possible 8-fold ambiguities that arise from the large multiplicity of hits in shower regions. An example illustrates the need for the different mappings on the east and west sides. Assume that the mappings for the two sides were identical. If the first pixel of the first PMT on the west side saw a signal, then so would the first pixel of the first PMT on the east side. The fibers mapped to these PMTs would be the same 8 fibers from the plane and the hit location is known to be one of those 8 fibers, but no more information is given to narrow the hit location to the 1 fiber that was actually hit. If the patterns differ, then it is possible to narrow the hit location further. A pattern that meets these requirements is shown in Fig. 4.14. Fig. 4.14 is a schematic representation of the two PMTs mapping to the first plane connected to a MUX box. Table 4.1 details the mapping of each strip to its readout pixel. The strip column gives the strip number in a plane modulo 24, reflecting the 24 pixels used by the strips of a single plane. The column labeled "Pixel W" indicates the pixel number in Fig. 4.14 that the strip maps to in a west side box. The remaining 8 columns indicate the east side mappings. For the first 24

Table 4.1: Multiplexing Scheme for the MINOS Far Detector.

| Strip | Pixel W | E(0) | E(1) | E(2) | E(3) | E(4) | E(5) | E(6) | E(7) |
|---|---|---|---|---|---|---|---|---|---|
| $1+24n$ | 1 | 1 | 3 | 6 | 8 | 9 | 11 | 14 | 16 |
| $2+24n$ | 3 | 3 | 6 | 8 | 9 | 11 | 14 | 16 | 17 |
| $3+24n$ | 6 | 6 | 8 | 9 | 11 | 14 | 16 | 17 | 19 |
| $4+24n$ | 8 | 8 | 9 | 11 | 14 | 16 | 17 | 19 | 22 |
| $5+24n$ | 9 | 9 | 11 | 14 | 16 | 17 | 19 | 22 | 24 |
| $6+24n$ | 11 | 11 | 14 | 16 | 17 | 19 | 22 | 24 | 2 |
| $7+24n$ | 14 | 14 | 16 | 17 | 19 | 22 | 24 | 2 | 4 |
| $8+24n$ | 16 | 16 | 17 | 19 | 22 | 24 | 2 | 4 | 5 |
| $9+24n$ | 17 | 17 | 19 | 22 | 24 | 2 | 4 | 5 | 7 |
| $10+24n$ | 19 | 19 | 22 | 24 | 2 | 4 | 5 | 7 | 10 |
| $11+24n$ | 22 | 22 | 24 | 2 | 4 | 5 | 7 | 10 | 12 |
| $12+24n$ | 24 | 24 | 2 | 4 | 5 | 7 | 10 | 12 | 13 |
| $13+24n$ | 2 | 2 | 4 | 5 | 7 | 10 | 12 | 13 | 15 |
| $14+24n$ | 4 | 4 | 5 | 7 | 10 | 12 | 13 | 15 | 18 |
| $15+24n$ | 5 | 5 | 7 | 10 | 12 | 13 | 15 | 18 | 20 |
| $16+24n$ | 7 | 7 | 10 | 12 | 13 | 15 | 18 | 20 | 21 |
| $17+24n$ | 10 | 10 | 12 | 13 | 15 | 18 | 20 | 21 | 23 |
| $18+24n$ | 12 | 12 | 13 | 15 | 18 | 20 | 21 | 23 | 1 |
| $19+24n$ | 13 | 13 | 15 | 18 | 20 | 21 | 23 | 1 | 3 |
| $20+24n$ | 15 | 15 | 18 | 20 | 21 | 23 | 1 | 3 | 6 |
| $21+24n$ | 18 | 18 | 20 | 21 | 23 | 1 | 3 | 6 | 8 |
| $22+24n$ | 20 | 20 | 21 | 23 | 1 | 3 | 6 | 8 | 9 |
| $23+24n$ | 21 | 21 | 23 | 1 | 3 | 6 | 8 | 9 | 11 |
| $24+24n$ | 23 | 23 | 1 | 3 | 6 | 8 | 9 | 11 | 14 |

fibers [E(0)], the east side mapping is the same as the west side. The next 24 fibers [E(1)] have a mapping that is permuted by 1 pixel relative to the previous mapping. The next 6 sets of 24 fibers are also permuted in a similar manner. Fibers from the second plane attached to a box are mapped to pixels 25-48 in exactly the same manner as the fibers from the first plane are mapped to pixels 1-24.

## 4.3 Timing Calibrations

The MINOS detector uses a timing system that is capable of a time resolution of a few nanoseconds based on the PMT resolution. To account for variations in the PMTs and other electronics, the system must be calibrated. Once the calibration is done, the nanosecond resolution makes it is possible to identify the directionality of the events by looking at the timing of the points along the track.

The downward-going, cosmic ray muons that enter and pass through the detector are used to find the relative timing differences between each electronics channel. Each muon passing through the detector is relativistic. Coupling the assumption that the muons are traveling at $c$ with the knowledge of the position of each hit along a track allows the determination of the correct timing for each hit. To obtain good calibrations, it is important to have each strip in the detector hit many 10's of times. A data set of order $10^6$ muons is enough to fulfill this requirement. On average it takes 1-2 months to collect the necessary muons.

The timing system in the far detector operated under two distinct configurations. In the first configuration the clocks for the electronics crates were connected in a daisy-chain using copper wire. This wire allowed for a large, nonuniform offset between the crates and produced up to a 12 ns difference from one crate to the other. The second configuration used optical fiber as the link between the crates and the crate to crate offset is on the order of 1 ns in this state. The method for finding

Table 4.2: Cuts used to identify events used to determine timing calibrations.

| Number | Cut | Events Passing Cumulative Cuts |
|---|---|---|
| | Total Sample | 8053167 (100%) |
| 1 | Track Length | 7538835 (93.6%) |
| 2 | Fit Quality | 6925623 (85.9%) |
| 3 | End Points | 6882961 (85.5%) |
| 4 | Tracklike | 6864211 (85.2%) |

the timing constants is the same for both configurations.

### 4.3.1 Intra-Crate Timing Constants

In order to achieve the best timing resolution, only the most reliable events are used to determine the timing calibration constants. Only single muon events are used for the timing calibration procedure because the algorithm that removes the ambiguity of a hit location due to the multiplexing can fail for multiple muon events where the muons are not well separated in the $z$-direction. Events that fail the internal checks for the demultiplexing algorithm are also excluded. The cuts shown in Table 4.2 were made on the data set to select events to use in the calibration. The table shows a number and name for each cut, along with the total amount of the data passing the cumulative cuts. The data used in the table come from July, 2003 through April, 2004 and are from the finished and magnetized detector. The "Track Length" cut (1) requires that the tracks used cross at least 2.0 m in the detector. This cut is made to select tracks that have enough information for the tracking algorithm to distinguish the start of the track from the end using the timestamps. The "Fit Quality" cut

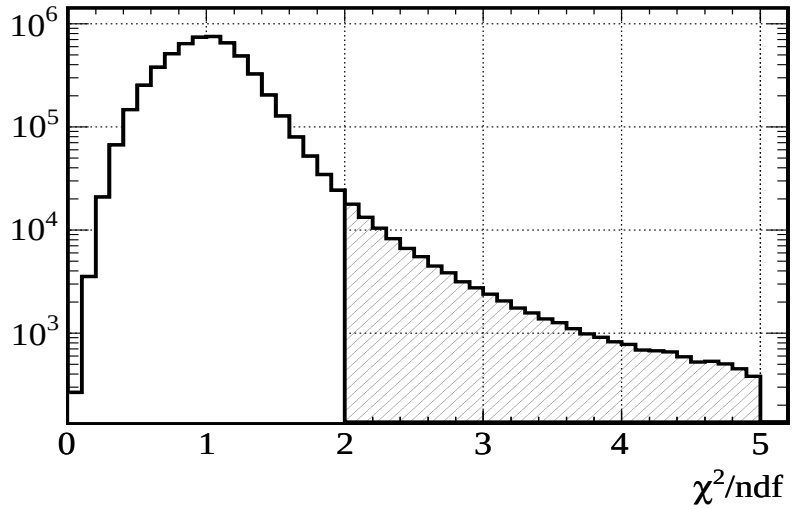


Figure 4.15: Distribution of $\chi^2/ndf$ for the fit track of cosmic ray events. The tracks in the unshaded region are kept to generate the timing calibrations.

(2) has three components. First, it requires that the track passes the track fitting algorithm's internal consistency checks. Second, the $\chi^2/ndf$ must be $< 2.0$ for the fit. The distribution used to determine the cut value for the $\chi^2$ of the fit track is shown in Fig. 4.15. As seen in the figure, the cut on $\chi^2$ is loose as it only excludes 1.4% of the data sample. The third component of the cut is that the number of planes used from each view be approximately the same. This requirement removes events where the track fitting algorithm stops tracking planes in one of the views and is found from the asymmetry in the number of planes from each view,

$$\mathcal{A} = \frac{N_U - N_V}{N_U + N_V}, \tag{4.1}$$

where $N_{U(V)}$ is the number of planes in the U(V) view. The cut on $\mathcal{A}$ has an empirically determined value of $\mathcal{A} \leq 0.11$. This cut corresponds to requiring that the view with fewer planes not have fewer than 80% of the total planes in the orthogonal view. The "End Points" cut (3) requires the $(x, y)$ coordinates of the track vertex and end locations have realistic values, ($|x| < 4.5$ m, $|y| < 4.5$ m). Reconstructed end points outside the allowed region are outside of the detector and are the result of poor tracking in one view. The "Tracklike" cut (4) removes events that may be electromagnetic or hadronic showers in the detector. This empirically determined cut requires either 40% of the total signal and 40% of the total planes hit in an event be used in the track, or the track be at least 4.0 m long, or the track cross at least 60 planes.

The detector data stream provides a timestamp for each signal. The tracking software corrects the timestamp value for the time it takes the light to propagate from the muon interaction point in the scintillator through the WLS and clear fiber to the PMT. This correction is called the "time of flight correction". The tracking software also applies a correction for the time it takes a signal to reach the electronics threshold and be read out. This delay is called "timewalk" and its correction is an empirical value. The form of the correction was determined by Jim Musser of Indiana University to be

$$t_{i,adc} = t_i - \frac{2093}{102 + \mathrm{ADC}^{1.2}}, \tag{4.2}$$

where ADC is the digitized signal size in counts. The timewalk and time of flight corrected times are labeled as $t'_i$ in the following discussion. Only strips that had signal read out on both sides are used to find the calibrations because those signals are least likely to be noise hits with times that are not associated with the muon.

For a track to be used in the timing calibrations for the channels connected to an electronics crate, the muon must have crossed at least 30 of the planes connected to that crate. The algorithm for finding the $t_0$ corrections for the section of a track within a given crate is:

1. Determine the time it takes for a muon traveling at a velocity of $c$ to go from the vertex of the track to each point along the track, $t_{ds_i} = s_i/c$, where $s_i$ is the path length from the vertex to the $i^{th}$ hit along the track.

2. Find the average value of the $t_{0,i} \equiv t'_i - t_{ds_i}$ for the track. The average value, $\overline{t_0}$, is the time each hit of the track would have occurred in the crate if each plane were crossed simultaneously.

3. Examine the values of $t_{0,i}$ and reject any that are more than 10 ns from $\overline{t_0}$. These values are most likely noise hits that the event reconstruction software placed along the track. Recalculate the mean using the remaining points.

4. Find the difference $\Delta t_0 \equiv \overline{t_0} - t_{0,i}$ to obtain one measurement of the correction to the timing, $t_0$ for each channel along the track. Store this value of the correction for each channel.

5. Use the remaining tracks that pass the criteria mentioned above to find more measurements of the correction for each channel.

6. Find the average correction for each channel in the detector. If any measurement for a channel is more than 10 ns different from the mean for that channel, reject it and recalculate the mean.

7. Repeat the above steps 5 times to refine the corrections and allow them to converge.

The effect of the iteration in the algorithm can be seen from Fig. 4.16. It shows a histogram of the values of $\Delta t_0$ for all hits in the examined files after the first iteration (solid line), and after 5 iterations (dashed line). The narrow distribution for the fifth iteration shows that the corrections after several interactions are small and the constants are well determined.

### 4.3.2 Inter-Crate Timing Offsets

The method for finding the inter-crate offsets is merely an extension of the method for finding corrections within a crate. The difference in $\overline{t_0}$ between each crate that has at least 30 hits from a given track is found. This value is one measure of the offsets between the crates. Each track in the data sample is examined to find the average offset between each set of linked crates. Fig. 4.17 shows histograms of the offsets between several sets of crates including 0 and 2 on the east side and 1 and

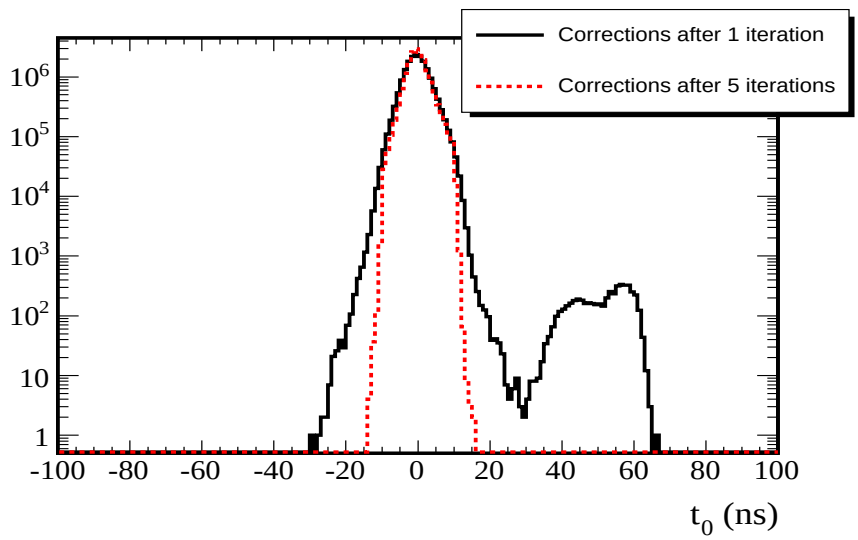


Figure 4.16: Values of $\Delta t_0$ for each channel in the detector after 1 iteration (solid line) and after 5 iterations (dashed line).

3 on the west side. This figure shows that the offset between sets of crates on the same side is non-negligible and the average offset can be as large as $\pm 15$ ns. The figure also shows a histogram of the offsets for crates 0 and 1, which are connected to the same planes in the detector but on different sides. It shows that the timing offsets between crates on the two sides of the detector is non-negligible as well. When applying these inter-crate offsets, crates 0 and 1 were arbitrarily chosen to be the zero points for the east and west sides respectively. All offsets on a side are relative to those crates. Additionally, crate 0 is the zero point for the detector.

Fig. 4.18 shows the $t_0$ values for each channel in the detector. The $y$-axis in the figure is the $t_0$ correction in ns, and the $x$-axis is a logical strip number given by the

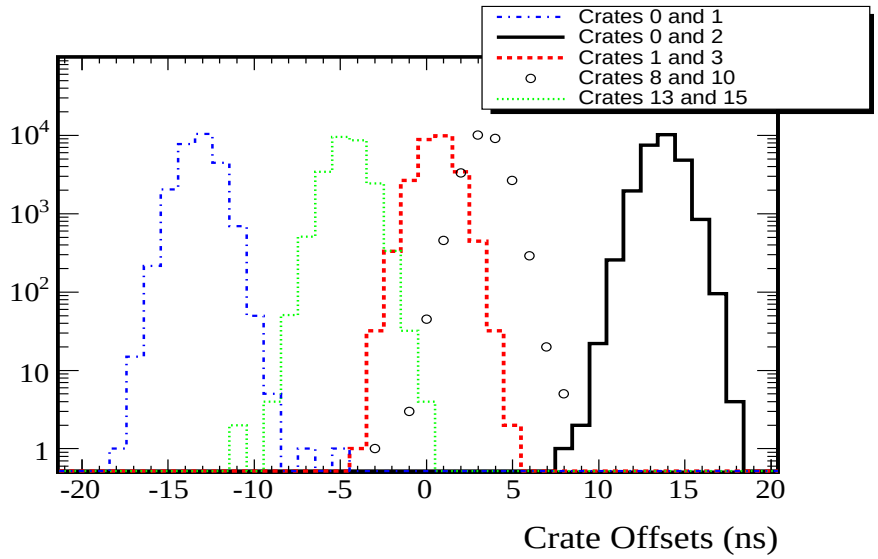


Figure 4.17: Histogram of differences in $\overline{t_0}$ between sets of crates. Crates 0, 2, 8 and 10 are on the east side of the detector while crates 1, 3, 13, and 15 are on the west side.

expression

$$x = 192(p - 1) + s \tag{4.3}$$

where $s$ is the strip in plane $p$. The west side values have a constant offset of 15 ns applied to them to make it easier to distinguish the values on the two sides. Notice the regular patterns that repeat every 12,288 logical strips, which corresponds to 64 planes, or 1 crate. There is also a finer structure within those patterns that reflects the the timing differences between the different readout components in a crate. The patterns are different on the east and west sides because the electronics were connected differently.

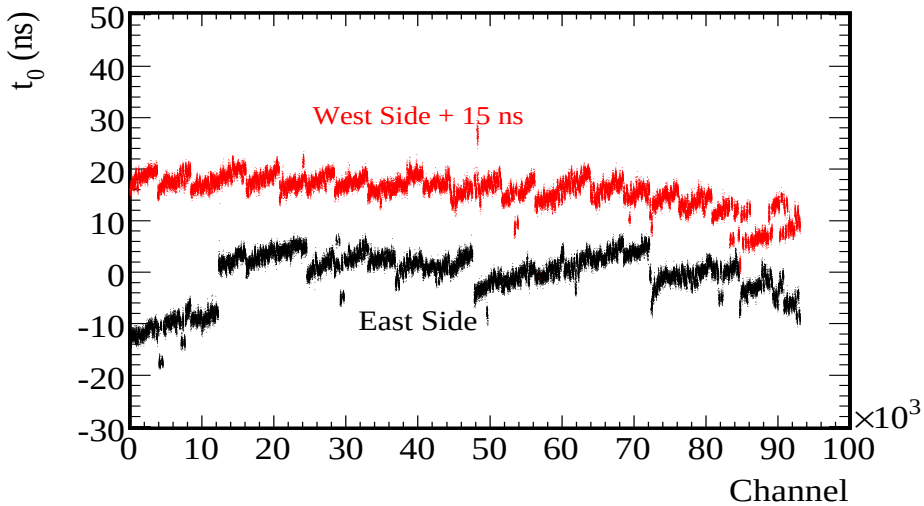


Figure 4.18: The $t_0$ corrections in ns vs logical strip number. The west side is offset from zero by 15 ns. The large jumps in the $t_0$ values every 12,288 strips are due to the inter-crate offsets.

### 4.3.3 Quality and Stability of $t_0$ Corrections

It is important to determine the quality of the $t_0$ corrections and their stability over time. The quality of the $t_0$ corrections can be examined in several ways. One of the clearest indicators of quality is the width of the velocity distributions found when using the calibrations. The value of $1/\beta = 1/(v/c)$ is used because the majority of the error in the measurement comes from the timing measurement, not the position measurement. The value of $1/\beta$ for each track is found by fitting a straight line to the set of points $(s_i, t_i)$ for the track, where $s_i$ is the path length from the vertex of the track to hit $i$ along the track and the $t_i$ is the corrected time for the hit. The value of $1/\beta$ should be greater than 0 if the identified vertex is actually the point of interaction in the detector because the time of the hits after the interaction

must increase with increasing distance from the vertex. Only strips that have signal recorded from each end are included in the fit and the signal on each side of the strip is weighted according to the uncertainty of the digit's arrival time. The uncertainty in the arrival time was determined by Roy Lee of Harvard using a simple Monte Carlo that calculates the arrival time of the first photo-electron as a function of the number of photo-electrons associated with the signal. The Monte Carlo assumes a 2 ns rise time and 8 ns decay time of the fluor in the scintillator. The uncertainty, $\sigma_t$, is given by

$$\sigma_t = \begin{cases} 0.9 + 8/N_{pe}, & (N_{pe} < 10) \\ 5.0 \exp\{-0.5 \log(N_{pe})\}, & (N_{pe} \geq 10) \end{cases} \tag{4.4}$$

where $N_{pe}$ is the number of photo-electrons. The weight given each signal is the inverse of the uncertainty. A simple least-squares fit is performed, and points that have residuals of more than 10 ns are removed from the set. The remaining points are refit as long as there are: at least 4 points left to fit, 20% of the data points remain, and there are no points with residuals greater than 10 ns. The slope of the fitted line is the inverse velocity of the muon. Fig. 4.19 shows three distributions of the $1/\beta$ values for tracks crossing the number of planes indicated by the label of each histogram. A Gaussian is fit to each distribution and the parameters of the fits are shown in the lower right section of the figure. The widths decrease with increasing numbers of planes crossed, and for events with more than 50 planes crossed $\sigma = 0.04$.

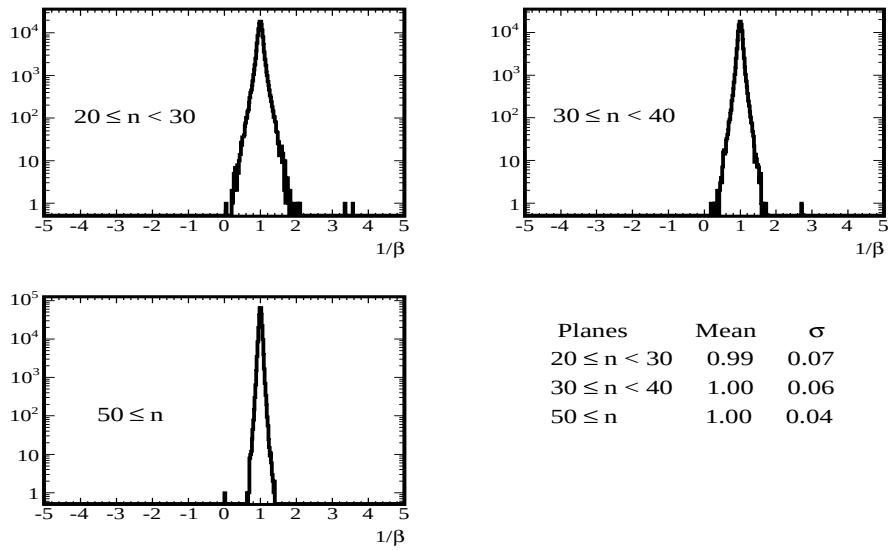


Figure 4.19: Distributions of $1/\beta$ for different numbers of planes crossed in an event.

Another measure of the quality of the calibrations is found by comparing the position of a hit along the length of strip as given by the tracking of the event and the position given by the difference in timing between the two sides. The time at each end of a strip is given by

$$t_E = \frac{\frac{L}{2} - d}{v} + \frac{f_E}{v} + t_{0,E} + t_{timewalk,E}, \tag{4.5}$$

$$t_W = \frac{\frac{L}{2} + d}{v} + \frac{f_W}{v} + t_{0,W} + t_{timewalk,W}, \tag{4.6}$$

where $t_{E(W)}$ is the time recorded for the digit on the east (west) side of the detector, $L$ is the length of the strip, $d$ is the transverse location of the hit, $f_{E(W)}$ is the length of the WLS pigtail and clear fiber on the east (west) side of the strip, $v$ is the speed of light in the fiber and $t_{0,E(W)}$ and $t_{timewalk,E(W)}$ are the values of the timing calibration

and timewalk corrections for the east (west) side. Solving for $d$ gives the expected position of the hit along the length of the strip,

$$d = \frac{v}{2}\left(t_W - t_E + t_{0,E} + t_{timewalk,E} - t_{0,W} - t_{timewalk,W}\right) + \frac{f_E - f_W}{2}. \tag{4.7}$$

The average difference, $\Delta$, between $d$ and the transverse location of the hits given by the tracking is recorded. Events where $\Delta < 1.0$ m have both good tracking and good timing reconstruction. Fig. 4.20 shows a histogram of these differences for several hundred runs. The average $\Delta$ is 0.41 m and the timing resolution is

$$\sigma_t = \frac{\sigma_\Delta}{c} = 2.4 \text{ ns}, \tag{4.8}$$

where $\sigma_\Delta = 0.17$ m is the position resolution, and $c$ is the speed of light. It is worth noting that 99.8% of events have $\Delta < 1.0$ m.

The coverage of the strips in the detector is also a good indication of the quality of the timing constants. Each strip in the detector should be hit by several 10's of muons in order to get several measurements for that strip. Figures 4.21 and 4.22 show the strip number versus plane number for each strip that had at least 20 and 75 hits, respectively, in the data set used. Notice that the highest and lowest strips for the end planes are not covered well because there are only 36 planes connected to the last crate making it difficult to pass the requirement of having 30 planes hit in that crate. There are some gaps in the detector corresponding to PMT/base failures.

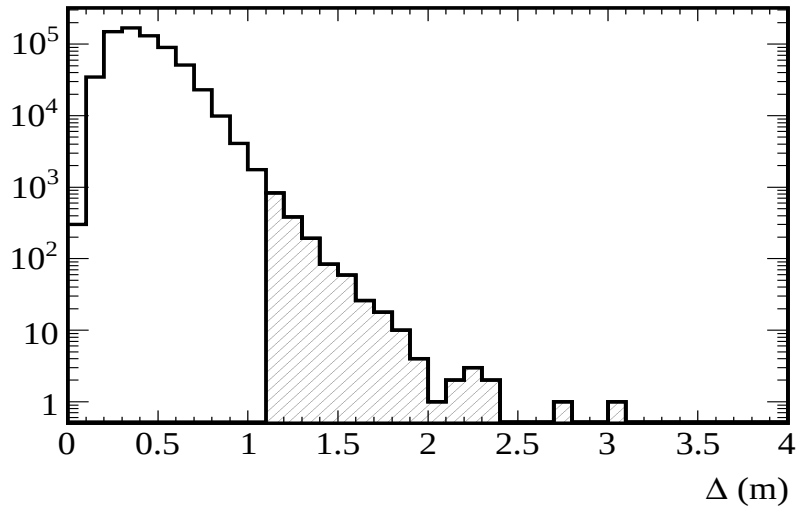


Figure 4.20: Distribution of the differences in the transverse position of a hit along a strip as given by timing and tracking.

The coverage can be improved by allowing the data set to cover a longer period of time. However, before doing so it is important to check that the constants do not change significantly with time. MINOS has taken several months worth of data and subsets of those data can be compared to see how the corrections change. Fig. 4.23 shows histograms of the rms of the $t_0$ calibrations for each east and west channel in the far detector. The average rms is $\sim 3$ ns. Fig. 4.24 shows the differences in the $t_0$ calibration constant for each channel between data from August-September, 2003 (August), October-November, 2003 (October), and April, 2004 (April). Each data set contains all the runs taken in the indicated months. It is clear that almost all channels change by only a few ns. Those channels that change by several ns are the

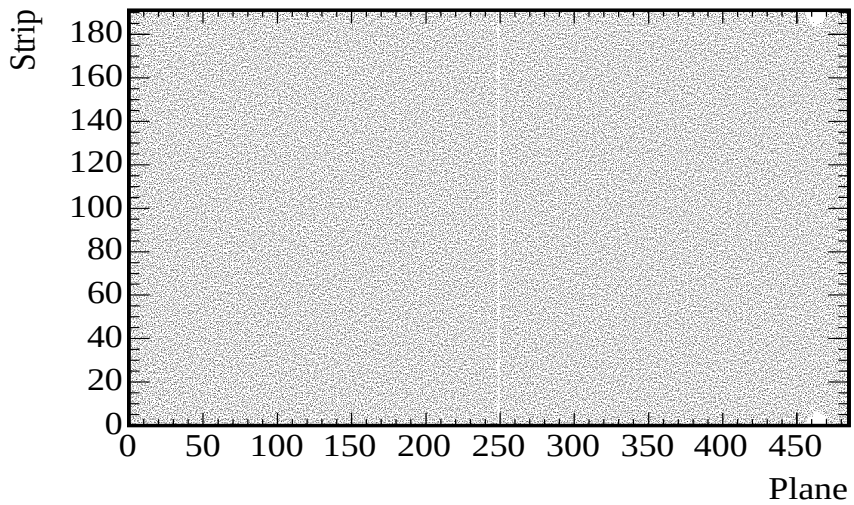


Figure 4.21: Coverage of strips hit at least 20 times in the data set.

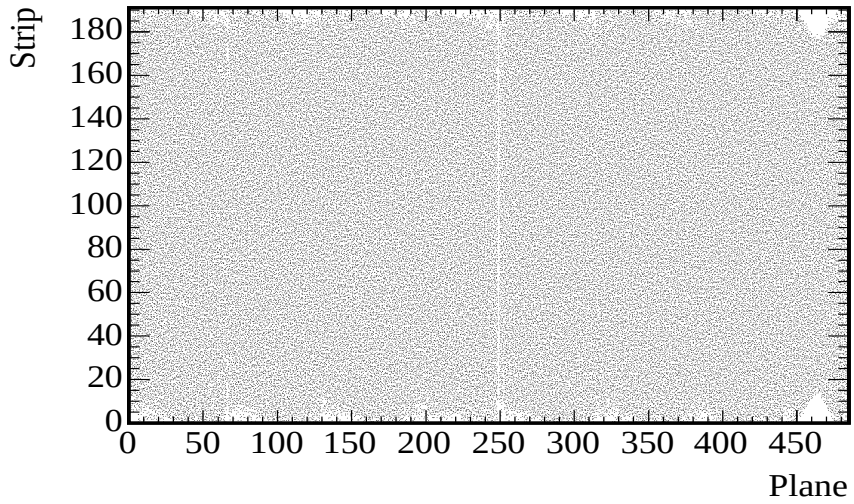


Figure 4.22: Coverage of strips hit at least 75 times in the data set.

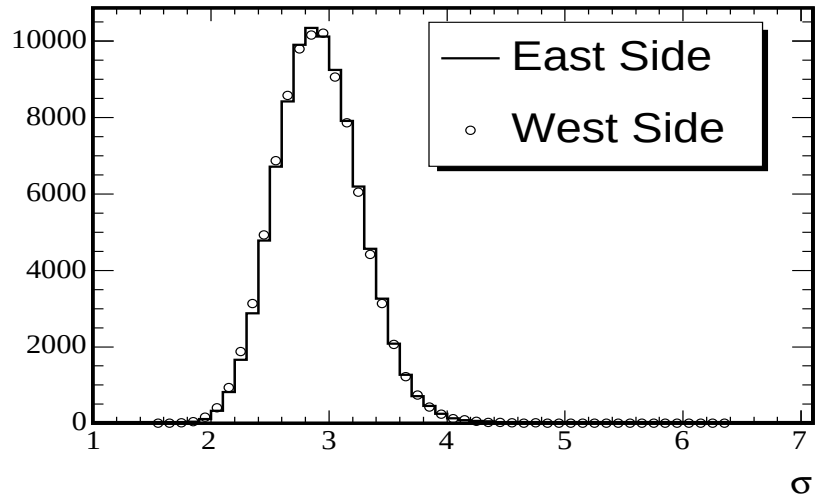


Figure 4.23: The rms of the $t_0$ corrections for channels in the Far Detector. West side channels are the points, east side channels are the solid line.

result of hardware changes. The large peak near $\Delta t_0 = 7$ ns between the August data and the October and April data is the result of 3 MUX box electronics boards being replaced. The smaller peak in the same location for the comparison of the October and April data is the result of a different MUX box electronics board replacement. Because the average difference between the measurements of $t_0$ for the different data sets is 0 and the average resolution of channels in the detector is $\sim 2.4$ ns, it can be said that to within the errors, the $t_0$ calibrations do not change over a period of several months.

The calibration plan is to recompute the constants every few months. Several quality check plots similar to those shown in the above discussion are produced for each set of constants. Tests are made of the widths of the $1/\beta$ distributions for

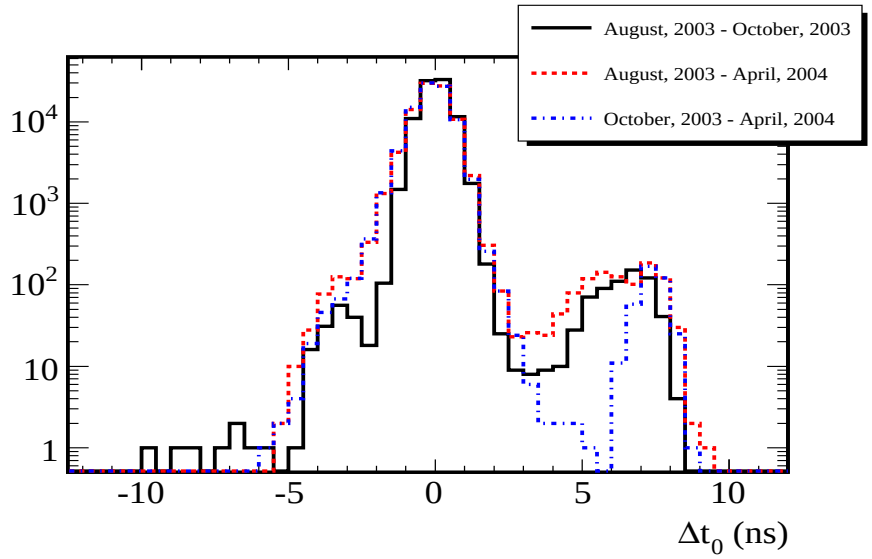


Figure 4.24: Histogram of the differences in $t_0$ corrections from different sets of runs.

given numbers of planes crossed. If these widths are larger than the allowed values shown in Fig. 4.19 the new constants are not uploaded to the database. This type of failure is usually the result of a hardware change made to the detector and alerts the person monitoring the timing constant generation that the data set should be examined to see when the change occurred and that two or more sets of constants should be generated. The value of the constant for each channel that is uploaded to the database is the difference between the value for the channel found by the method detailed in this section and the average value of all channels in the detector.

# Chapter 5

# The Far Detector Demultiplexing Algorithm

## 5.1 Introduction

Chapter 4 describes the instrumentation of the planes in the far detector, as well as the multiplexing pattern. This chapter focuses on the implementation of demultiplexing algorithms for the far detector, both for beam and cosmic ray events. The original idea for the hypothesis testing method outlined below was developed by Stuart Mufson of Indiana University and Adam Para of Fermilab. The algorithms are written in the C++ programming language. They were rigorously tested and modified to optimize efficiency.

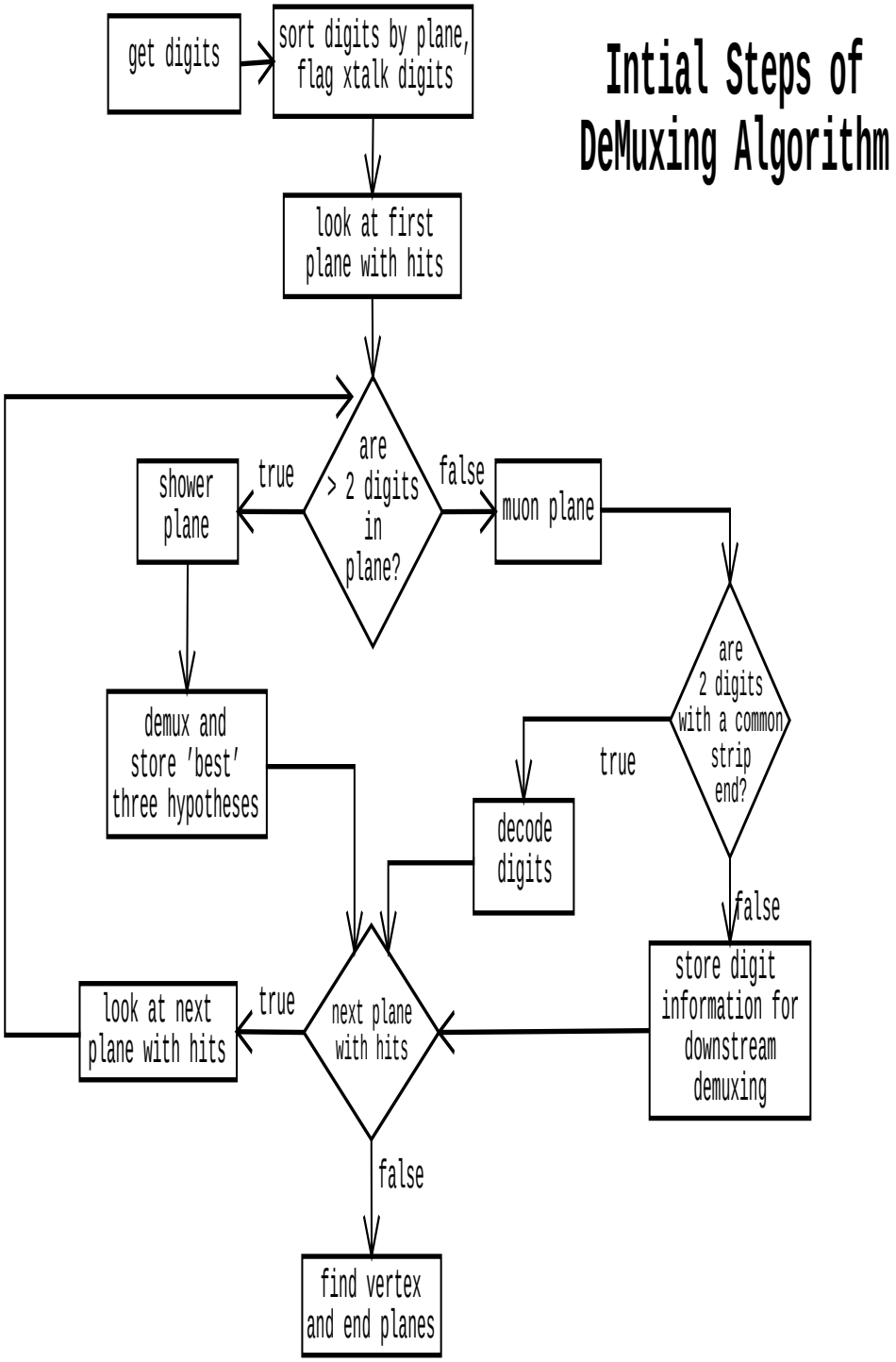


Figure 5.1: Flow chart for the first steps of the DeMuxing Algorithm.

## 5.2 Basics of the Algorithm

The initial steps in demultiplexing (DeMuxing) beam or cosmic ray events in the far detector are the same. The algorithm outlined in Fig. 5.1 shows these basics. The digitized signal from one electronics channel in the detector is called a digit. Each digit contains information about the size of the signal, its timestamp, the plane to which the electronics signal was connected, and the strips of the plane that map to the electronics channel. The set of 8 strips that map to an electronics channel are called its "strip alternatives". After getting the digits for an event the first step is to sort them into groups corresponding to the instrumented planes from which they come. While sorting the digits, the algorithm also checks to make sure that a digit is not a result of cross-talk. The empirical criteria for labeling a digit as coming from cross-talk is that its signal is less than 10% of the summed signal from the four pixels sharing a side with the digit's pixel. The remaining digits from each plane are counted and the planes are sorted into "shower" and "muon" planes based on the number of digits to which they correspond. Shower planes are defined to be those instrumented planes in the event that register more than two digits and muon planes are those instrumented planes that register two digits or one digit. Shower planes are DeMuxed using the "hypothesis testing" method described in § 5.2.1.1. Muon planes with two digits that share a common strip alternative are uniquely decoded to that strip, but the ambiguities in muon planes with only one digit can only be

resolved using information from planes upstream and downstream from it.

### 5.2.1 DeMuxing Individual Planes

#### 5.2.1.1 Shower Planes: The Hypothesis Testing Method

When three or more digits are found on a single plane, it is called a shower plane and the algorithm uses the hypothesis testing approach to DeMuxing. This method divides planes into logical modules, or hypotheses, each 24 strips wide. The hypotheses overlap such that the first hypothesis, $i = 0$, contains strips 0 to 23, the next 1 to 24, and so on for a total of 169 hypotheses in a plane. The spacing for a hypothesis was chosen to be 24 strips because it corresponds to the width of the multiplexing. The digits from a plane are examined and for each hypothesis the algorithm selects the strip alternative of each digit that lies within the boundaries of the hypothesis. Certain digits from the permuted east side will not have strip end alternatives every 23 strips. Instead they will have a separation of more than 23 strips between two alternatives. Digits that do not have strip alternatives within a hypothesis are not used in the reconstruction of that hypothesis.

Once the reconstruction for each hypothesis in a shower plane is found, the algorithm determines whether the reconstruction of each hypothesis is acceptable or not by evaluating two criteria. First, a minimum fraction, $f$, of the total signal in the hypothesis must come from opposite sides of the same strips in the hypothesis. Digits that occur on the opposite ends of the same strip are said to be mated. The

second condition for a hypothesis to be considered an acceptable potential solution is that it must use all of the available digits which are not identified as coming from cross-talk. A hypothesis passing both criteria is called a "valid" hypothesis because the reconstruction it represents is acceptable.

The algorithm uses a goodness of fit statistic to choose which of the valid hypotheses corresponds to the best reconstruction for that plane. The statistic chosen is the $\chi^2$ statistic, defined for each hypothesis $i$ by

$$\chi_i^2 = \sum_{k=i}^{i+23} \frac{(RW_k - E_k)^2}{(W_k^2 + E_k^2)}, \tag{5.1}$$

where $W_k$ is the reconstructed signal on the west side of strip $k$ and $E_k$ is the reconstructed signal on the east side of that strip the hypothesis. The variable $R$ is the predictor of the signal on the west side of the plane, $S_W$, based on the signal on the east side, $S_E$. The predictor is

$$R = \frac{\sum_{plane} S_E}{\sum_{plane} S_W}, \tag{5.2}$$

where the sums are over all signals from the specified side of the plane. Smaller values of $\chi_i^2$ are considered to indicate better reconstructions.

Often the $\chi_i^2$ is the same for many hypotheses. In that case the algorithm uses

the rms of the reconstruction to rank those hypotheses. The rms, $\sigma_i$ is

$$\sigma_i^2 = \frac{\sum_{k=i}^{i+23} s_k (x_k - \overline{x_i})^2}{\sum_{k=i}^{i+23} s_k} \times \frac{N}{N-1}, \tag{5.3}$$

where $s_k$ is the signal on strip $x_k$ and $N$ is the total number of digits from the plane. The center of gravity, $\overline{x_i}$, is the signal weighted average of the strips hit in the reconstruction,

$$\overline{x_i} = \frac{\sum_{k=i}^{i+23} x_k s_k}{\sum_{k=i}^{i+23} s_k}. \tag{5.4}$$

Smaller values of $\sigma_i$ indicate that a reconstruction has a higher probability of being a better fit to the data.

The algorithm ranks the valid hypotheses in a shower plane by $\chi_i^2$ with $\sigma_i$ being the tie breaker for those hypotheses with the same $\chi_i^2$. The algorithm can use up to three distinct hypotheses from each plane when determining the solution based on the upstream and downstream planes.

Given the definitions of $\chi_i^2$ and $\sigma_i$, the reason for the mated signal requirement for valid hypotheses can be understood. If a plane has too little mated signal, then all of its hypotheses will have similar poor $\chi^2$ statistics and many will have the same $\sigma$. Thus, there is no way to distinguish between the possible reconstructions for that plane. The user may set the value for *f*. The default for the beam algorithm is 0.5 and the default for the cosmic ray algorithm is 0.33. Fig. 5.2 is a histogram of this fraction for the top 3 hypotheses for beam events. This histogram indicates

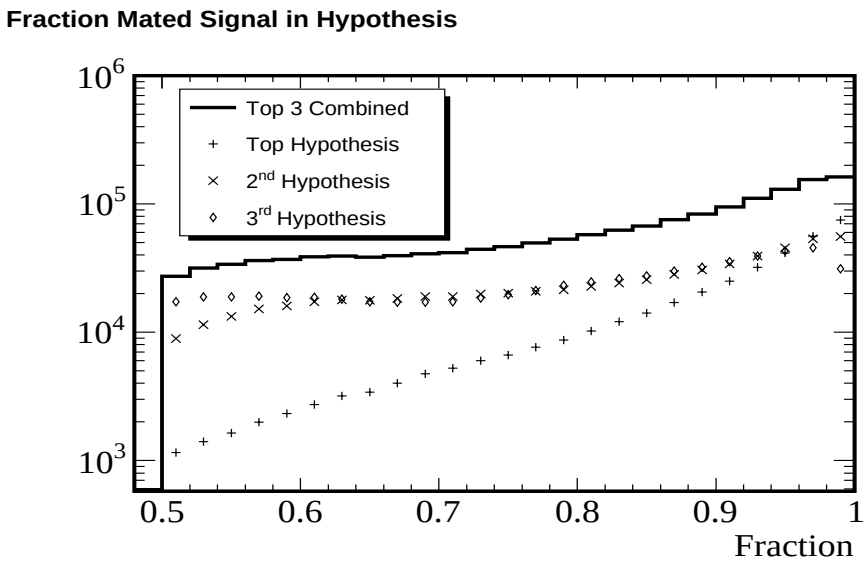


Figure 5.2: Fraction of signal mated in the top three hypotheses for a plane in beam events.

that 91% of the shower planes have at least 70% of the total signal mated in one or more hypotheses. Also notice that 95% of the best hypotheses have at least 90% of their signal mated. Although there are events with $f < 0.5$, they are not considered reliable for use in determining the DeMuxing solution for beam events. The default cut off value for the cosmic ray algorithm is somewhat lower, $f = 0.33$, as those muons tend to bremsstrahlung along the length of the track leaving single ended hits in several strips.

The DeMuxing algorithm only uses shower planes containing at least one valid hypothesis to determine the reconstruction over the entire event. Shower planes fulfilling this requirement are called "valid" shower planes.

#### 5.2.1.2 Muon Planes

Digits in muon planes are decoded in a straightforward manner from the multiplexing pattern. When two digits are from opposite sides of a plane, they are set to their common strip alternative. Muon planes with such digits are considered "valid" and are used in determining the event reconstruction. If two digits are both read out on the same side of a plane, the digits cannot come from the same strip. Muon planes may only have a single digit in the plane. Clearly, there is no way to resolve the ambiguity of the digits' origins in the last two cases and setting the digits is deferred for the upstream and downstream reconstruction. Testing the algorithm has also shown that there are muon planes whose digits have a common strip alternative, but they actually come from separate strips. Such a situation can arise due to the permuted east side multiplexing pattern. When this occurs the digits are initially decoded to a location at least one meter off from where the particle actually passed through the detector. The reconstruction can readjust the location of those digits using the upstream and downstream planes.

### 5.2.2 Determining the Event Length and Direction

After sorting the digits into planes and DeMuxing those planes, the algorithm determines the extent and direction of the event. The direction of beam events is always from the south end of the detector to the north as the beam is generated at Fermilab and aimed at Soudan, MN. Cosmic ray muons can come from either the north or

the south. For either type of event, the initial determination of the operational first plane, or vertex plane, and the end plane of the event is as follows. The vertex plane is found using a modified "3 out of 5" condition. That is, the first plane after plane 0 in a set of 5 planes containing 3 valid planes is called the preliminary vertex. The algorithm then looks to see if there is an upstream plane within two planes of the initial vertex that also has signal. If so, the upstream plane is labeled as an intermediate vertex. This process of examining upstream planes for signal continues until there is a gap of two planes without signal. The last plane labeled as the intermediate vertex is the new operational vertex. The end plane is the last plane to have signal before a gap of 5 planes without signal. The algorithm that reconstructs cosmic ray muon events may exchange the operational vertex and end planes if doing so is determined to yield a better solution.

## 5.3 Reconstructing the Event

As discussed in § 5.2 there are different algorithms for DeMuxing beam and cosmic ray events. The more difficult beam algorithm is discussed first, which is followed by the cosmic ray algorithm. There are similarities, however, between the two methods. In both methods the planes in the events are separated into two groups, each representing one view in (U,V). The algorithm further divides the groups into valid and non-valid planes as defined in § 5.2.1.1 and § 5.2.1.2. After these steps, the

algorithms diverge.

### 5.3.1 Beam Events

While cosmic ray events are typically muons going through the detector, beam events can be either neutral current-like shower events or charged current-like muon events. The beam event algorithm DeMuxes the shower and muon regions of an event separately. The algorithm determines the extent of these regions while it looks for the operational vertex and end planes. The beam algorithm is shown in Fig. 5.3

#### 5.3.1.1 The first $n$ valid Planes

Regardless of whether the event vertex is in a shower region or part of a muon track, the algorithm reconstructs the first $n$ valid planes of the event in the following manner. It first looks to see if there are enough valid planes in the event to allow the inclusion of upstream and downstream information. That number of valid planes, $n$, is specified by the user. If there are fewer than $n$ valid planes in a view, the algorithm will adjust and reset $n$ to the number of valid planes in that view as long as $n$ is still greater than 2. The algorithm does not reconstruct events that have fewer than 3 valid planes in a view because there is not enough information. The algorithm then finds the best reconstruction for the $n$ planes as follows. First it chooses a set of hypotheses, $l$, for the $n$ planes. The index $l$ can take up to $3^n$ possible values. For example, if $n = 4$ and the algorithm finds 3 valid hypotheses on each plane, there

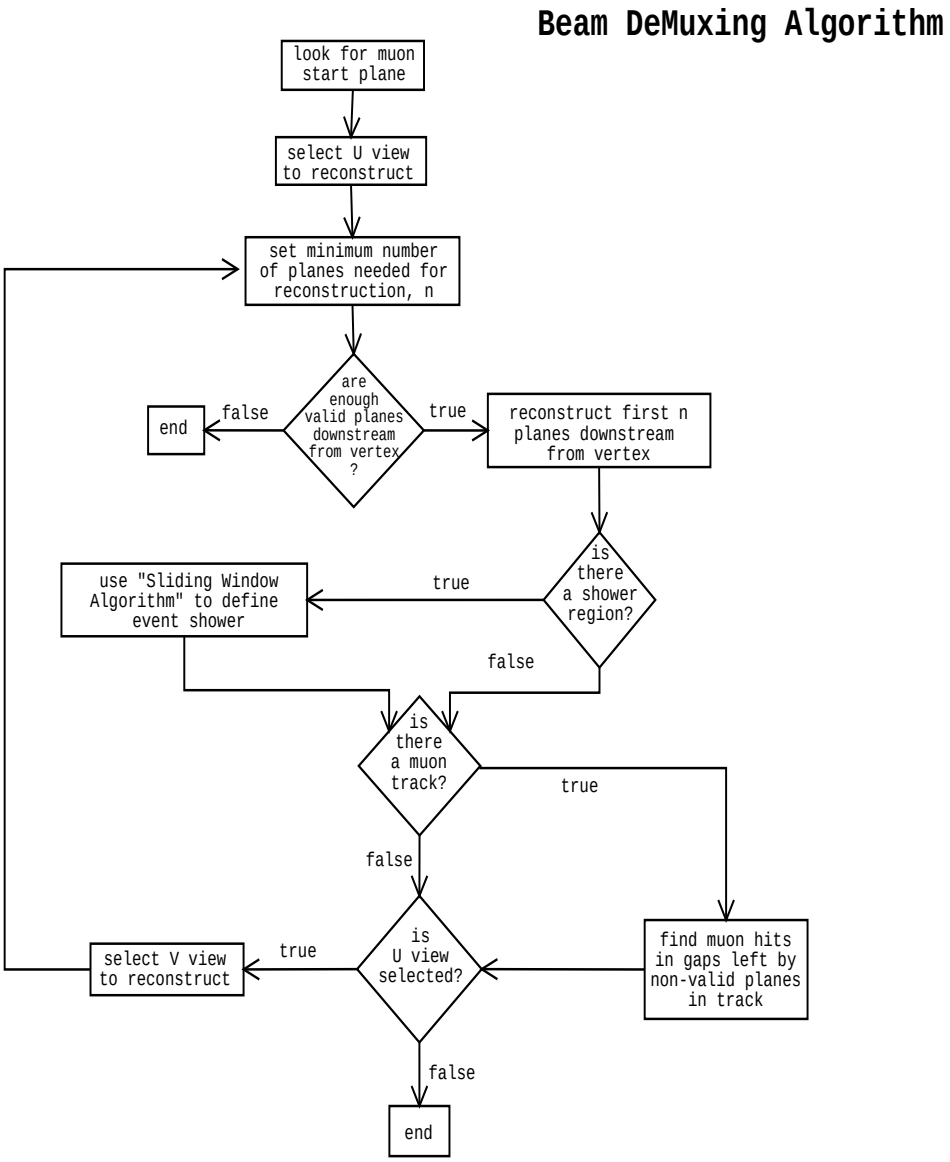


Figure 5.3: Flow chart for the beam DeMuxing Algorithm.

are 81 possible reconstructions. The first reconstruction, $l = 1$, chooses the best hypothesis on each plane and so on until $l = 81$ chooses the third best hypothesis on each plane. Then the algorithm defines the center of gravity, $\overline{X}_l$, for each set of hypotheses $l$,

$$\overline{X}_l = \frac{\sum_{j=1}^{n} \overline{x}_{jl} S_j}{\sum_{j=1}^{n} S_j}, \tag{5.5}$$

where $\overline{x}_{jl}$ is the center of gravity for plane $j$ with the hypothesis specified by the choice of $l$, and

$$S_j = (S_E + S_W)_j \tag{5.6}$$

is the total signal on plane $j$. Then the rms about $\overline{X}_l$,

$$\Delta_l^2 = \frac{\sum_{j=1}^{n} S_j (\overline{x}_{jl} - \overline{X}_l)^2}{\sum_{j=1}^{n} S_j} \times \frac{n}{n-1}, \tag{5.7}$$

is computed. The best reconstruction, $l^*$, is taken to have the lowest $\Delta_l$.

After determining $l^*$, it is possible to find that the three best hypotheses of one of the shower planes in the set are all more than a meter off from any of the choices given by the others. Such a plane will throw off the reconstruction. In this instance, the algorithm excludes that plane and then recomputes $l^*$ using $n - 1$ planes.

The reconstruction $l^*$ gives the initial guess for the event reconstruction. To improve $l^*$, the algorithm computes the center of gravity for the digits used in finding $l^*$. Each of the $n$ planes are reconstructed to the hypothesis centered at that value.

Finding the center of gravity for the event is an iterative process with each successive value of $l^*$ found by setting each valid plane to the last computed center of gravity. It was found that after 3 - 4 iterations all the digits are reconstructed to within one meter. Then each non-valid plane bounded by the vertex and the last valid plane in the set is reconstructed to the hypothesis centered at the final computed center of gravity.

#### 5.3.1.2 The Sliding Window Algorithm for the Shower Region

To finish the reconstruction of a shower region beyond the first $n$ valid planes in the event, the algorithm outlined in Fig. 5.4 is used. The first step is to see if there are any valid planes left in the shower region after reconstructing the initial set of $n$ planes. When there are no more valid planes left in the shower region, the algorithm reconstructs the remaining non-valid planes to the hypothesis centered at the center of gravity computed for the initial set of $n$ planes. If there are still valid planes left in the region, the algorithm uses a sliding window of $n$ valid planes, where the first $n-1$ valid planes in the window have already been reconstructed. The algorithm computes the center of gravity of the digits in the $n-1$ previously set valid planes. The $n^{th}$ valid plane in the window is set to whichever of its three best hypotheses is nearest to the computed center of gravity of the other planes in the window. If none of the three best hypotheses are within 1 meter of that center of gravity, then the $n^{th}$ plane is set to the last computed center of gravity. If the unset valid plane

in the window is a muon plane, a check is done to see if it is decoded to a location consistent with the other planes. If it is not, the algorithm resets it to the computed center of gravity. Again, the algorithm computes the center of gravity for the digits in the set of planes and reconstructs all non-valid, unset planes in the window and the $n^{th}$ valid plane to the computed center of gravity. If there is another valid plane in the shower region, the window slides downstream to include that plane and the algorithm outlined above is repeated. If any planes remain between the last valid plane and the end of the shower region, they are set to the hypothesis centered at the last computed center of gravity.

#### 5.3.1.3 The Muon Track

The start of a muon track in an event is the first of four consecutive planes with one or two hits each and three of the planes have a total signal of at least three photo-electrons. This requirement on the signal size was chosen by trial and error and can be reset. The choice was motivated by the fact that a particle with enough energy to leave a signal in the MINOS far detector deposits $\sim$ 8 photo-electrons. Even attenuated, the PMT signal should be above three photo-electrons. The minimum number of planes reflects the fact that muon tracks tend to be longer than four planes. Together these requirements distinguish between muon tracks and shower regions having a few digits and little signal. The valid muon planes are reconstructed when the digits are sorted into the types of planes and they guide the reconstruction

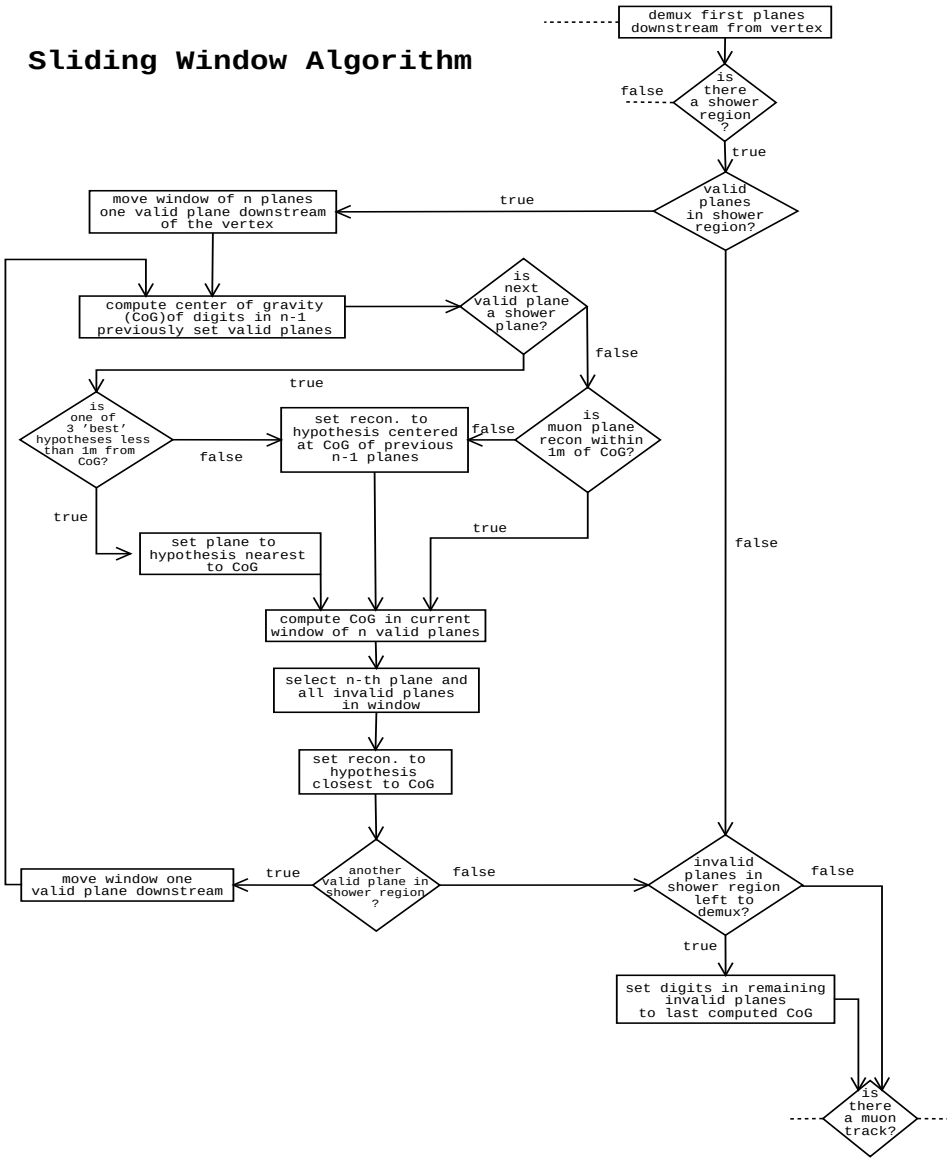


Figure 5.4: Flow chart for the beam DeMuxing sliding window algorithm.

of the shower planes and non-valid muon planes in the muon track. Specifically, the intervening planes between two valid muon planes are decoded to have the hypothesis centered on a straight line between the centers of gravity of the two consecutive valid muon planes. The user may define a limit for the absolute magnitude of the slope. Such a limit can prevent noise hits far from the muon track or planes incorrectly identified as valid muon planes from distorting the reconstruction. Several values for this limit were tested with Monte Carlo events, including no limit, and it was found that the cutoff $|slope| < 2.0$ reconstructs the largest number of tracks correctly. If the end plane of the event is not a valid plane, each plane between the last valid plane and the end plane is reconstructed to the last valid muon plane's center of gravity.

#### 5.3.1.4 Results from Testing the Algorithm

The algorithm was tested using Monte Carlo events from the far detector. The Monte Carlo files were generated by Robert Hatcher. The events were generated using the low energy beam which has a $\nu_\mu$ energy distribution that peaks at $E_{\nu_\mu} \approx 3$ GeV and has a long, high-energy tail out to 40 GeV. There were approximately 0.5% dead fibers or channels in these events. The transmission factor for the optical connectors was modeled at 0.93. There were no strip-to-strip variations in light output.

#### 5.3.1.5 Results for Shower DeMuxing

One way to test the efficiency of the algorithm for correctly decoding showers is to examine the amount of signal it places on the correct strips. This choice to use signal as the measured quantity was made because the showers tend to cover large numbers of strips with widely varying signal on the hit strips. It is acceptable for the algorithm to misreconstruct low energy hits, while the high energy ones must be correctly reconstructed as event topology is determined by the large signal hits. Fig. 5.5 shows the fraction of correctly reconstructed energy in the showers for those events which had showers. The area under the curve with values greater than 0.9 shows that 94% of the events containing showers have at least 90% of the total signal in the shower correctly reconstructed. Those events with 40-60% of the total shower signal correctly DeMuxed are of the class where one view is correctly DeMuxed while the other is not. The algorithm failed for both views in those events with less than 40% of the total shower signal correctly DeMuxed. Fig. 5.6 shows the total signal in a shower as a function of the correctly reconstructed signal and one can see that low energy events tend to be misreconstructed more often. Fig. 5.7 shows an example event with a reconstructed shower in strip versus plane orientation. The crosses are the DeMuxed hit locations, while the open circles are the truth hit locations. The top panel of the figure shows the UZ view, while the bottom panel shows the VZ view. Fig. 5.8 shows an example event where the algorithm misreconstructed the shower in the UZ view, as the crosses in planes 300 - 320 do not overlap with the

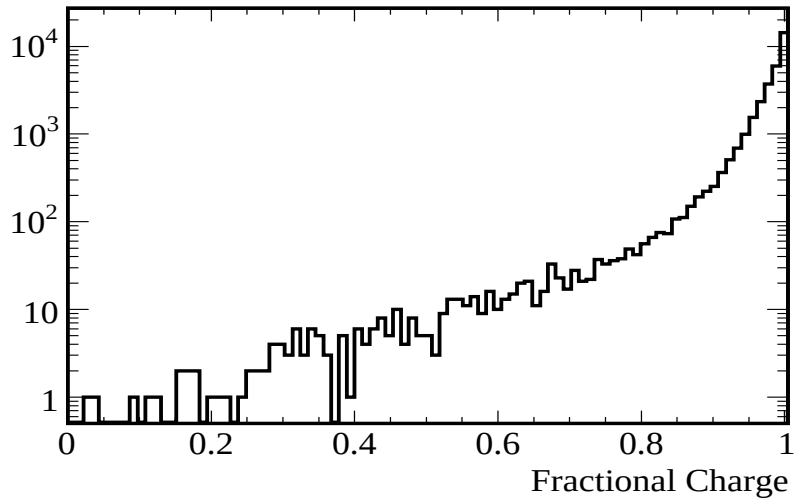


Figure 5.5: Fraction of total signal correctly DeMuxed in shower regions.

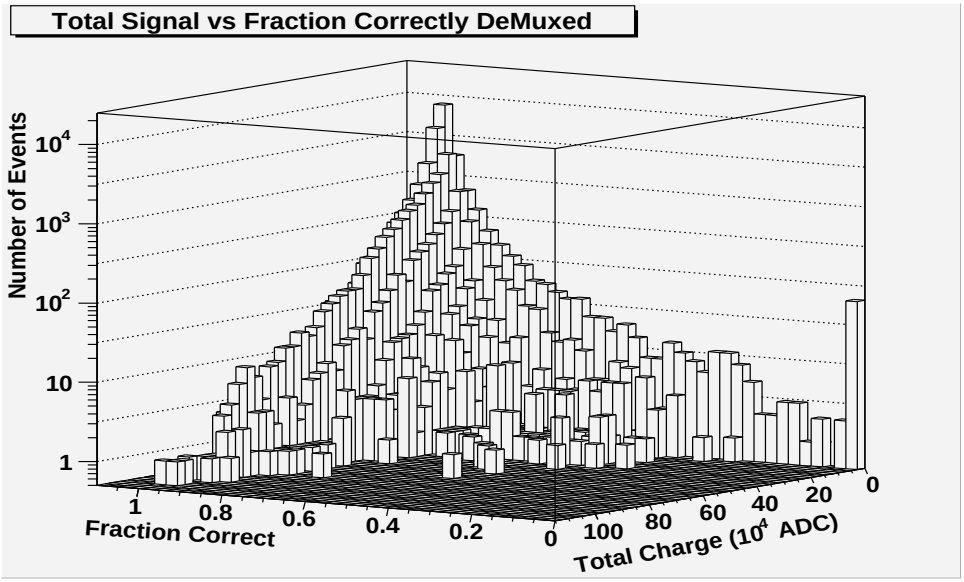


Figure 5.6: Fraction of total signal in a shower as a function of the correctly DeMuxed fraction of the total.

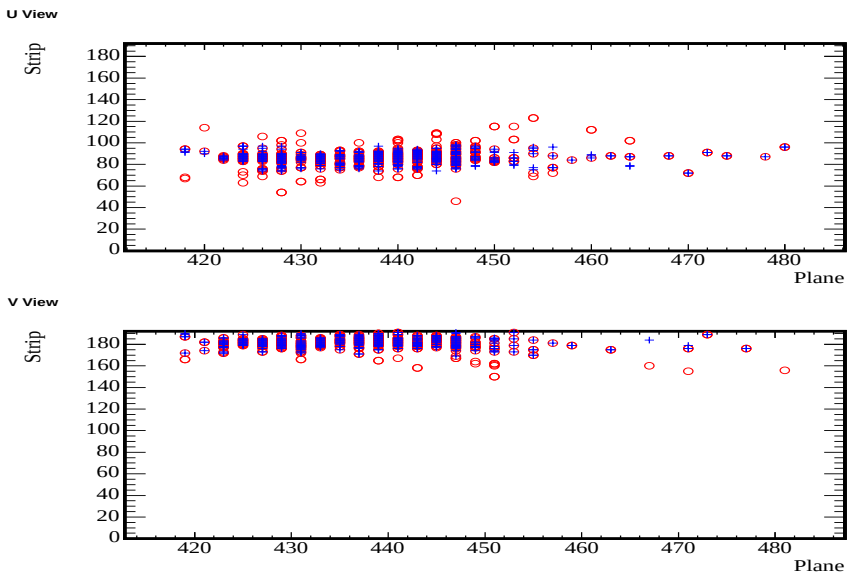


Figure 5.7: Example beam event containing a large shower. The event is shown in strip versus plane orientation with the top panel being the UZ view and the bottom the VZ view. The crosses are the DeMuxed hit locations while the open circles are the truth hit locations.

circles. In events such as this one with muons and showers, it should be possible to use the muon track to double check the location of the shower reconstruction.

#### 5.3.1.6 Results for Muon Track DeMuxing

The algorithm's ability to reconstruct muon tracks was determined by the number of digits in the track that were reconstructed to the correct strip alternative. The number of strips correctly reconstructed is the appropriate quantity to evaluate track DeMuxing as muons traversing the detector tend to only leave signals in one or two strips per plane. Fig. 5.9 shows the fraction of correctly reconstructed strips in the track for each muon event. The algorithm reconstructs at least 90% of the digits correctly in 97% of the events. Fig. 5.10 shows an event where the muon track

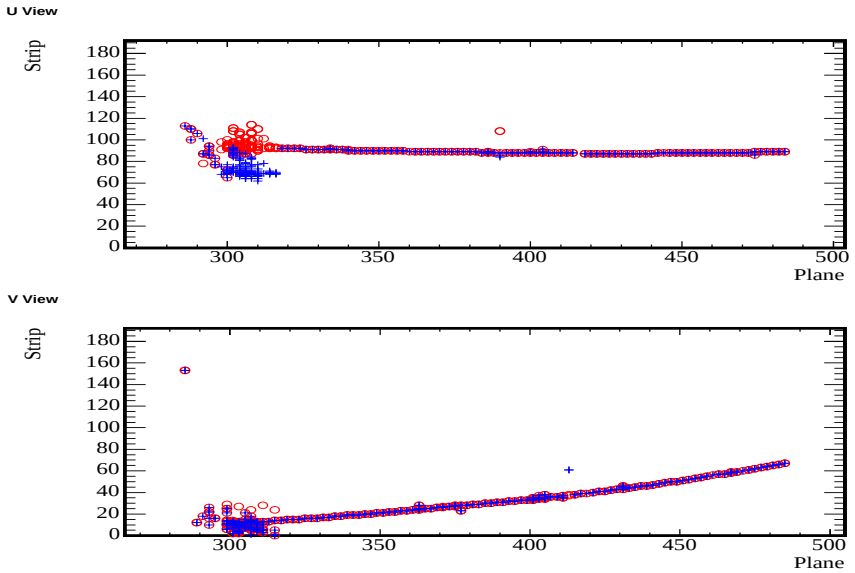


Figure 5.8: Example beam event where the shower was misreconstructed in the UZ view as the crosses in planes 300 - 320 do not overlap with the circles. The display is explained in figure 5.7

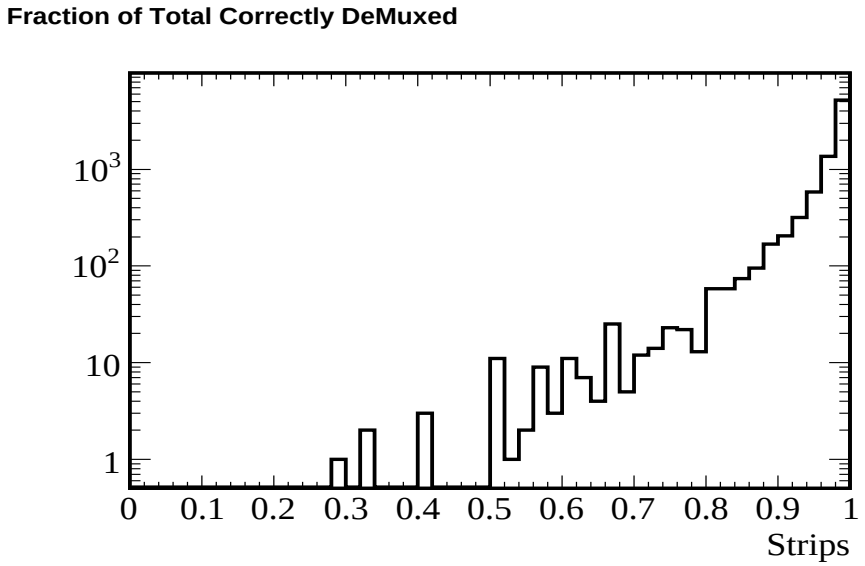


Figure 5.9: Fraction of total strips in a track correctly DeMuxed.

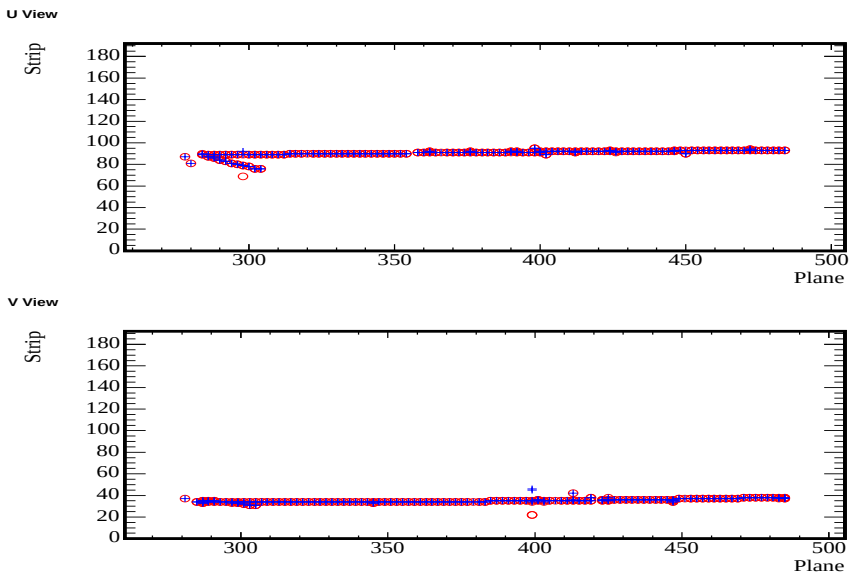


Figure 5.10: Example beam event showing a reconstructed track. The display symbols are explained in figure 5.7.

was DeMuxed very well. Also note the presence of a short track near the vertex of the event which the algorithm also correctly DeMuxed. The shorter track is a pion created in the CC interaction.

### 5.3.2 Cosmic Ray Events

Cosmic ray events appear to be much easier to DeMux than beam events because they are generally from high energy muons that deposit large amounts of energy in the scintillator, tend to follow straight line trajectories through the detector, and do not tend to have associated showers. Of course, in reality the situation is not so clean. The magnetic field causes particles to curve in the detector, and the associated cross-talk, noise and bremsstrahlung make finding the correct solution difficult.

Nevertheless, the cosmic ray algorithm is simpler than the beam algorithm.

#### 5.3.2.1 The first $n$ valid Planes

The event is reconstructed one view (U, V) at a time, using the algorithm shown in Fig. 5.11. First a check is made to see if there are enough valid planes in the event to allow upstream and downstream information to be used. That number of valid planes, $n$, is specified by the user, and can be in the range $2 \leq n \leq 6$. If there are fewer than $n$ valid planes in a view, the algorithm will adjust and reset $n$ to the number of valid planes in that view as long as $n$ is still at least 2. Events that have fewer than 2 valid planes in a view are not reconstructed because there is not enough information. The algorithm determines the reconstruction for the $n$ planes by finding the best least squares fit to a straight line through the centers of gravity, given by eq (5.4) of any combination of the three best hypotheses in those planes. Each plane is weighted by the signal from that plane so that the fit is most dependent on the planes with the largest signal. As with beam events, the algorithm defines the combinations of hypotheses by choosing a set, $l$, for the $n$ planes. Again the index $l$ can take up to $3^n$ possible values as each plane is allowed up to 3 hypotheses as probable reconstructions. It is possible that one of the planes in the set $l$ may have its chosen hypothesis significantly off from the others. To account for this possibility, the algorithm drops each plane from the set in turn, fitting a straight line to the remaining $n-1$ planes. If the refined fit has a lower $\chi^2$ per degree of freedom

value, that solution is the best fit for the $l^{th}$ combination. The algorithm never drops more than one plane at a time from the set when performing this check. The best reconstruction, $l^*$, has the lowest ${\chi_l}^2$. Once the best reconstruction is found, the algorithm sets all planes from the vertex to the $n^{th}$ valid plane to the hypothesis centered about the strip intersected by the fit line.

#### 5.3.2.2 The Sliding Window Algorithm for the Remaining Planes

The reconstruction $l^*$ gives the initial guess for the event reconstruction. If more than $n$ valid planes are in the event, the algorithm steps out into the rest of the event one valid plane at a time. A sliding window of $n$ valid planes guides the reconstruction, where the first $n-1$ planes are already DeMuxed. The algorithm for the sliding window is outlined in Fig. 5.12. The algorithm determines the best straight line fit to the $n$ planes using a process similar to that described in § 5.3.2.1. Recall that the first $n-1$ planes have been set by the previous step in the reconstruction, so the reconstruction for those planes cannot change. The sliding window algorithm determines which of the 3 highest ranked hypotheses of the $n^{th}$ plane in the set is most consistent with the previously set planes. It does this by finding $\chi_i^2$ for each combination, where $i$ is the rank of the current hypothesis in the $n^{th}$ plane. If the $\chi_i^2$ for any of the combinations is not as good as the ${\chi_{(n-1)}}^2$ for the fit to the previously set $n-1$ planes alone, the algorithm uses the fit represented by ${\chi_{(n-1)}}^2$. Again, all unset planes from the last previously set plane to the $n^{th}$ valid plane in the current

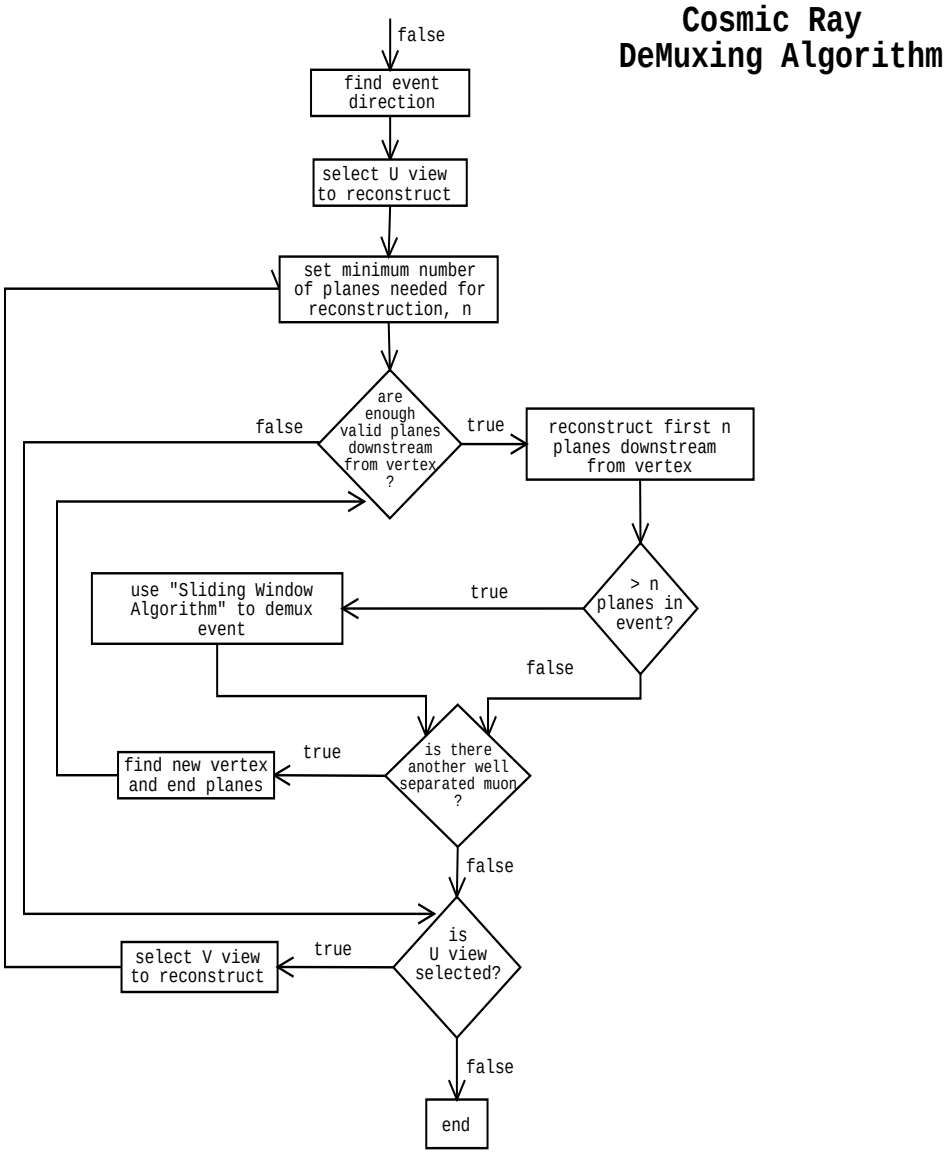


Figure 5.11: Flow chart for the cosmic ray DeMuxing Algorithm.

window are set to the determined reconstruction, as described above. The window then slides to include the next unset valid plane and the process repeats. For the last window, all planes from last valid plane in the previous window to the end plane of the event are set.

This algorithm has the advantage of being able to make small corrections in the straight line fit over the length of the event to account for multiple scattering and bending of the track in the magnetic field. An algorithm that fits a straight line to all of the planes or only a small section at the beginning of the event could be significantly wrong for long events.

#### 5.3.2.3 Multiple Muons

Energetic cosmic ray showers can produce many muons at the same time with the same trajectories and high energies. The muons from these showers can pass through the detector at the same time, with all the muons leaving observable signals. The algorithm can identify and DeMux multiple muon events if the muons are well separated in the detector. A separation of at least 5 planes with no signal between each of the muons is necessary to successfully DeMux all the muons. The algorithm identifies the vertex and end planes for the each muon in the event, and then follows the steps outlined in § 5.3.2.1 and § 5.3.2.2.

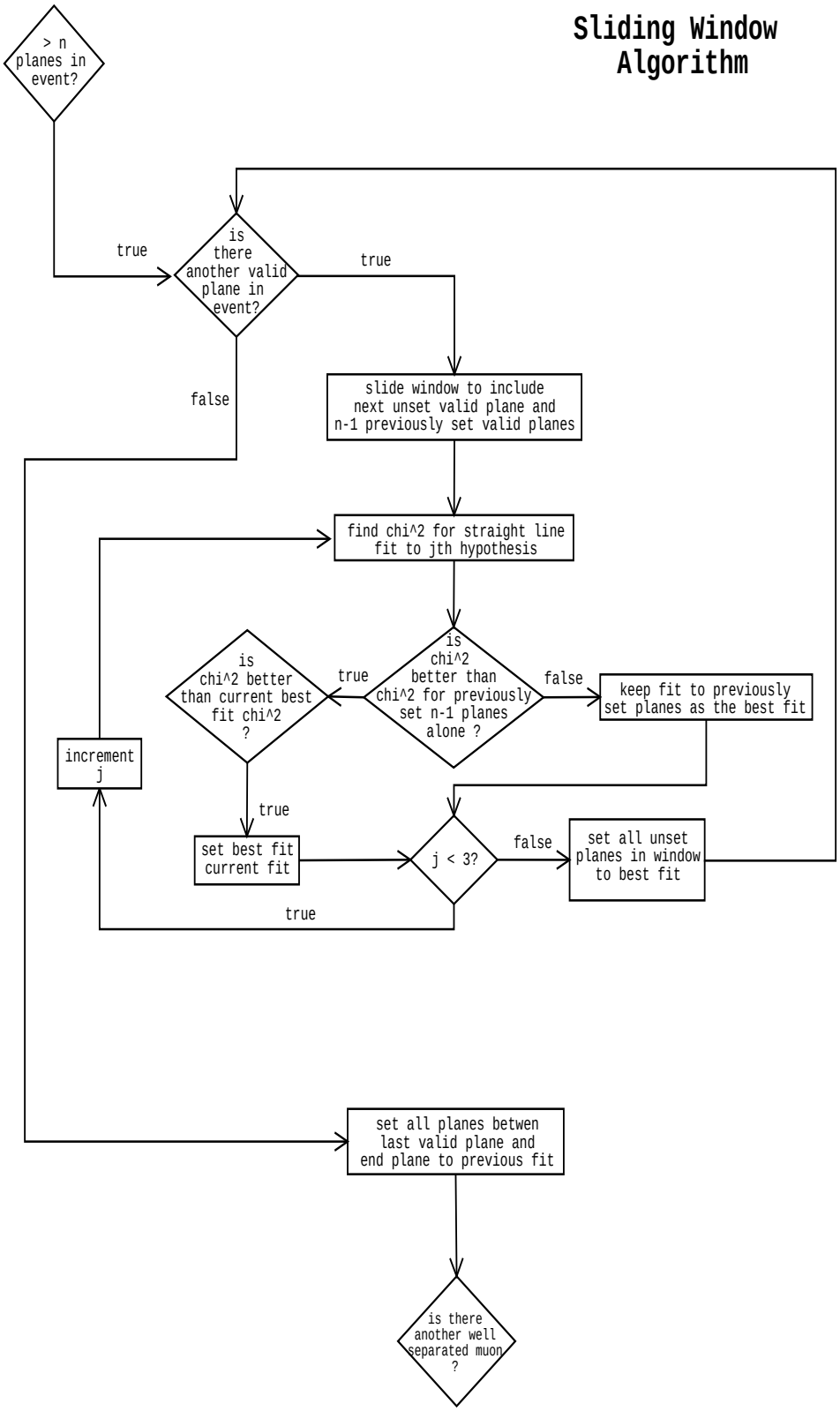


Figure 5.12: Flow chart for the Sliding Window Algorithm.

#### 5.3.2.4 Single Module Test

The algorithm was tested using 72910 cosmic ray events from the far detector. Several files were combined to obtain these events, including runs 2484, 2532, 2534, 2536, 2559, 2584, 2613, 2634, and 2986. The files are available from Fermilab and can be obtained by following the instructions at

`http://www-numi.fnal.gov/minwork/computing/enstore.html`

A variety of tests were done to determine the efficiency of the algorithm. The first test involved removing the multiplexing for one side of one plane by only connecting 2 clear fiber cables from the plane to its MUX box, with the others being sealed in a light-tight manner. The west side of plane 12 was used for this test, and the connected modules were 3 and 6. These modules were chosen because they are well separated in the plane, with over a meter between their closest strips. Fig. 5.13 shows 4 histograms demonstrating the algorithm's efficiency. The left side histograms show the signal in photo-electrons of digits that were not correctly DeMuxed to one of the connected modules, and the right side shows the signal for those that were. The top histograms show all digits. The bottom histograms show only those that were identified as not being probable cross talk digits and whose strips of origin had signal read out on both sides. Looking at the bottom histograms and comparing the number of entries in each, one sees that ∼94% of these digits are correctly DeMuxed. Also note that the average signal of these correctly DeMuxed digits is higher (∼ few

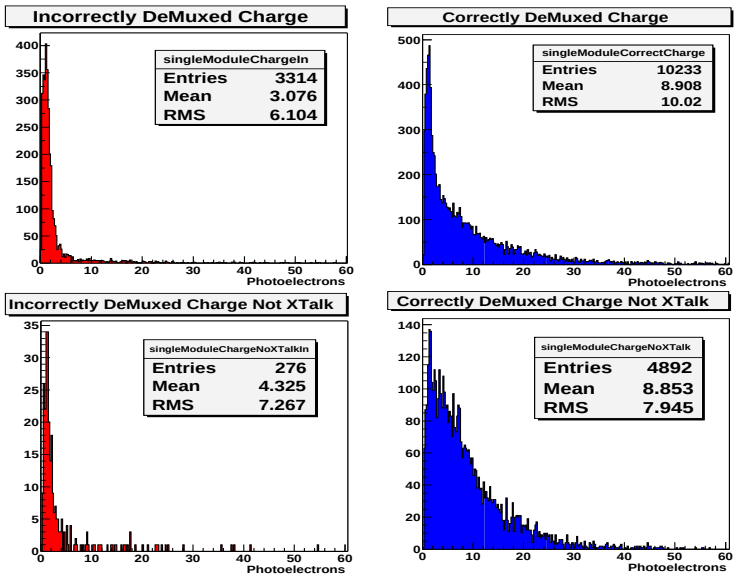


Figure 5.13: Results of the single module DeMuxing test. The left hand histograms represent all incorrectly DeMuxed digits, the right hand ones are for correctly DeMuxed digits. The top histograms show all digits, the bottom ones show only non-cross talk digits and digits whose strips of origin had signal from both sides.

photo-electrons) on average, with a larger tail out to the higher energies than the incorrectly DeMuxed digits.

#### 5.3.2.5 Figure Of Merit

Another way to judge the efficiency of the algorithm is through a figure of merit. The figure of merit for cosmic ray events is based on the centers of gravity for the top 3 hypotheses in a plane and the DeMux solution. If the centers of gravity of a plane's top 3 hypotheses are all more than $n$ strips off from the straight line fit for that plane, it is considered to be a "stray" plane. The value of $n$ may be set by the user, with the default value being $n = 6$. The figure of merit is the fraction of stray

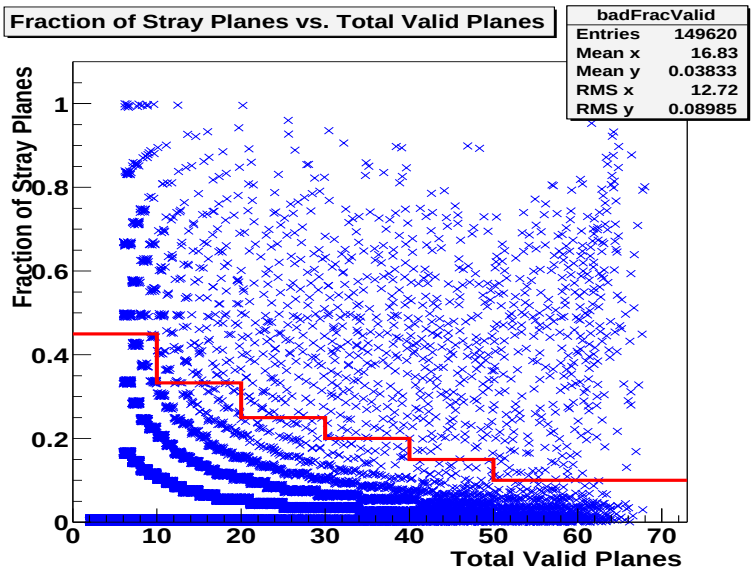


Figure 5.14: Fraction of stray planes in an event versus total valid planes. The cut for accepting a DeMux solution is shown by the solid line.

planes out of the total number of valid planes in a view. This is a reasonable way to evaluate the solution as the top 3 hypotheses in a plane are the guides for the upstream and downstream phase of the reconstruction. Fig. 5.14 plots the fraction of stray planes versus the total number of valid planes for both views. Each band in Fig. 5.14 represents a different total number of stray planes in an event. The $n_{strays} = 0$ band is the flat band across the bottom of the figure and the $n_{strays} = 1$ is the first band above it. As the total number of valid planes in an event decreases, the fraction represented by a constant number of stray planes increases. The cut based on the "strays" fraction is a function of the total number of valid planes in the event, and is shown by the solid line in Fig. 5.14. A total of 1000 events were scanned by eye and the list of unacceptable solutions found by that method was compared to the list

generated by the cut. The cut identified 29 events as unacceptable while scanning by eye found 25. The scanning method flagged 3 events that the cut did not flag and the cut identified 7 events that the scanning did not. The events flagged using the visual inspection method that the cut did not flag all had less than 8 total planes hit. Such short events are not currently used by the track fitter in the reconstruction. In total, only 3% of the events were identified by the cut, indicating a 97% efficiency for the algorithm.

Figs. 5.15 - 5.17 show examples of events DeMuxed using the algorithm. In the figures, the crosses represent the DeMuxed locations of the digits in the event, and the circles represent the centers of gravity for the top 3 hypotheses of each plane. Fig. 5.17 shows an event where the top 3 hypotheses line up in parallel straight lines while overlapping each other in plane number. Perhaps this is a multiple muon event where the muons are not well separated in the z direction.

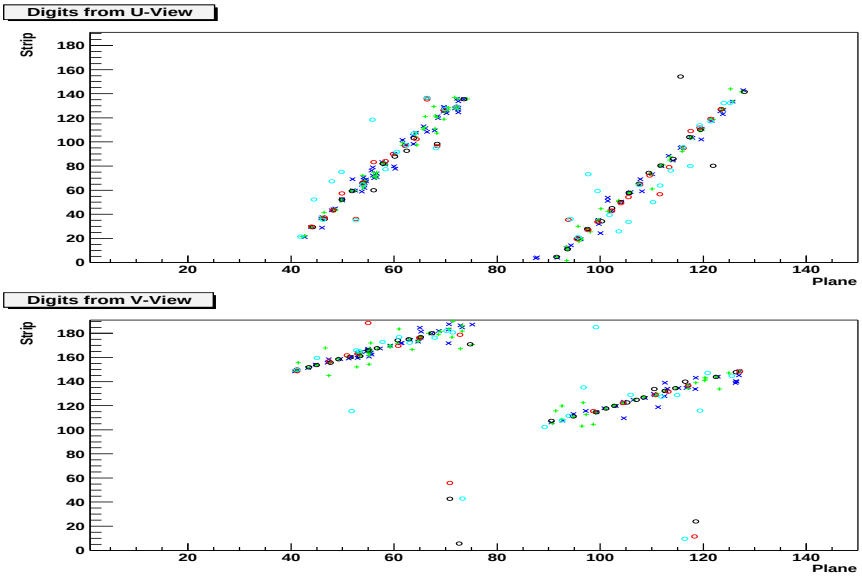


Figure 5.15: Event 96 from run 2532. This is a multiple event well separated in z.

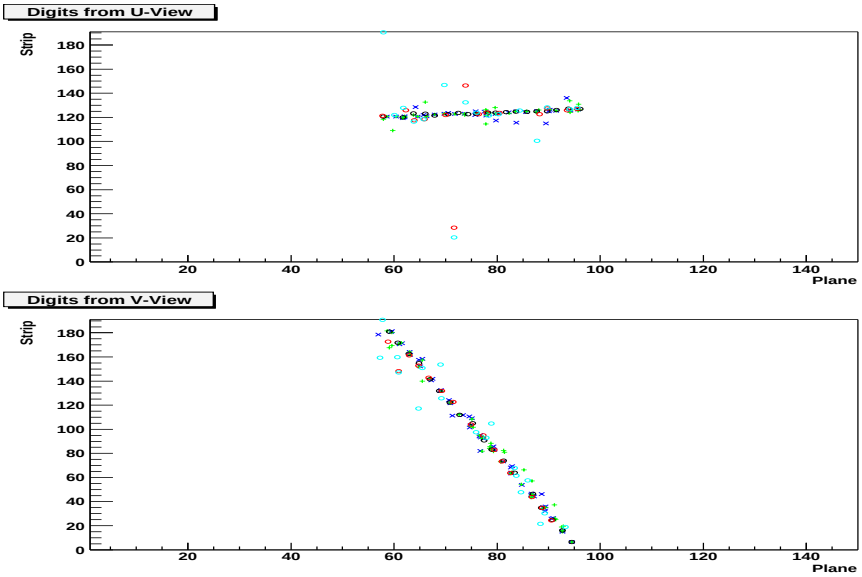


Figure 5.16: Event 102 from run 2532.

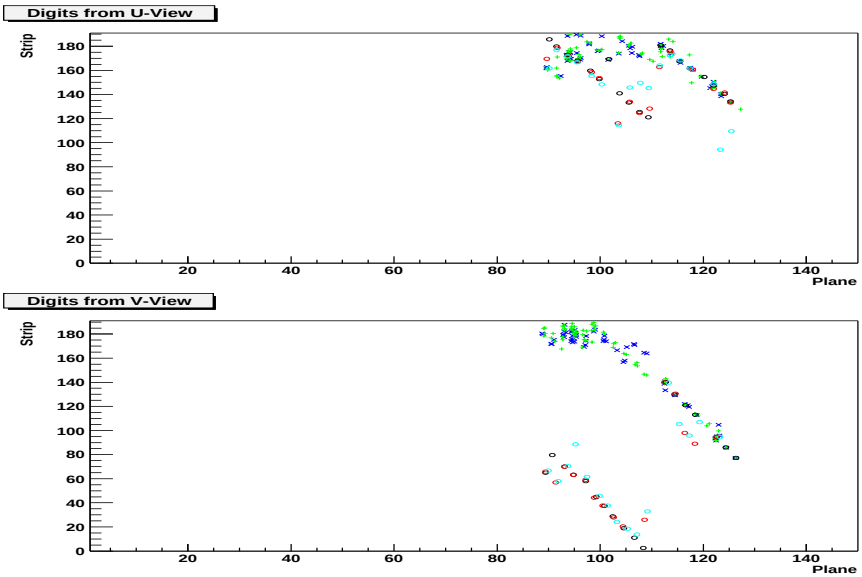


Figure 5.17: Event 138 from run 2532. This is an event that the figure of merit cut flagged as an unreliable solution. It appears to be a multiple event that is not well separated in z.

# Chapter 6

# Cosmic Ray Muons

## 6.1 Introduction

The cosmic ray muon analysis is important in the MINOS experiment for several reasons. MINOS is the first underground detector to have a magnetic field that can separate the $\mu^+$ and $\mu^-$ as a function of energy. Additionally, analysis of the cosmic ray muon data must be done to show that the detector is well-understood. The detector has collected cosmic ray muon data since September 2002. The detector has operated under two different configurations since data taking began. The first configuration had only the first supermodule (SM1) magnetized since construction on the second supermodule (SM2) was not complete. The data from this configuration is called the SM1 data set. The second configuration began in July 2003 and had both supermodules magnetized. These data are called the SM1+SM2 data set. For

the cosmic ray muon analysis, only the SM1+SM2 data are used as they represent the completed detector. The integrated time that the detector was operating and taking data is called its live-time. The SM1+SM2 data span 231 live-days.

## 6.2 Detector Acceptance and Efficiencies

To do any data analysis with the MINOS far detector, its acceptance must be understood. The acceptance is the product of the projected area of the detector seen by a muon arriving from a given direction, the probability of detecting and reconstructing the muon and the solid angle of the arrival direction.

The projected surface area for a given arrival direction can be calculated by taking the dot product of the vector normal to the surface of the detector with the arrival direction. For this calculation, the muon arrival directions are divided into bins of equal solid angle. The differential solid angle is $\sin\theta d\theta d\phi = d(\cos\theta)d\phi$. The analysis uses 200 bins in $\cos\theta$ in the range $-1 \leq \cos\theta \leq 1$ and 120 bins in azimuth in the range $0 \leq \phi \leq 360°$. The projected area of the detector is shown in Fig. 6.1 as a function of $\cos\theta$ and azimuthal angle $\phi$. This figure shows that the projected area falls near the horizon at the north and south faces, $\cos\theta \sim 0$ and $\phi = 0, 180$, where the detector cross section is low. The projected area increases moving away from the north and south faces along the horizon.

The parameter that describes the probability of detecting and reconstructing an

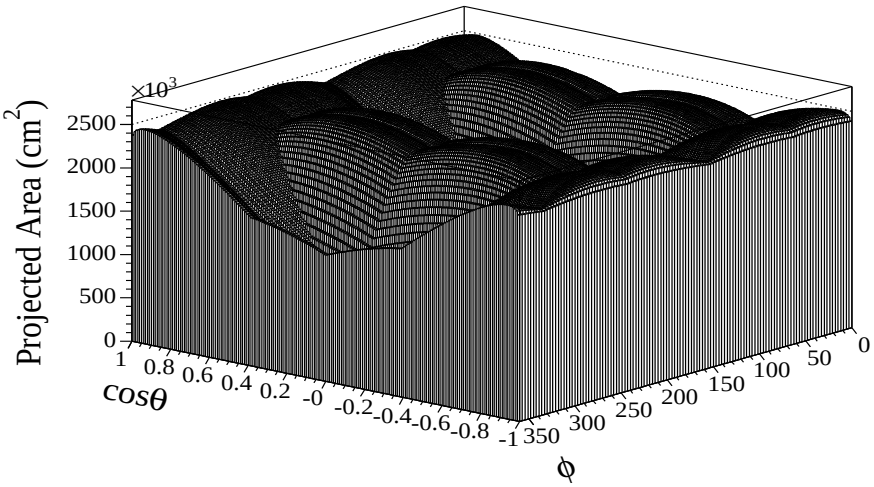


Figure 6.1: Projected area of the MINOS far detector in $\cos\theta$ and azimuth.

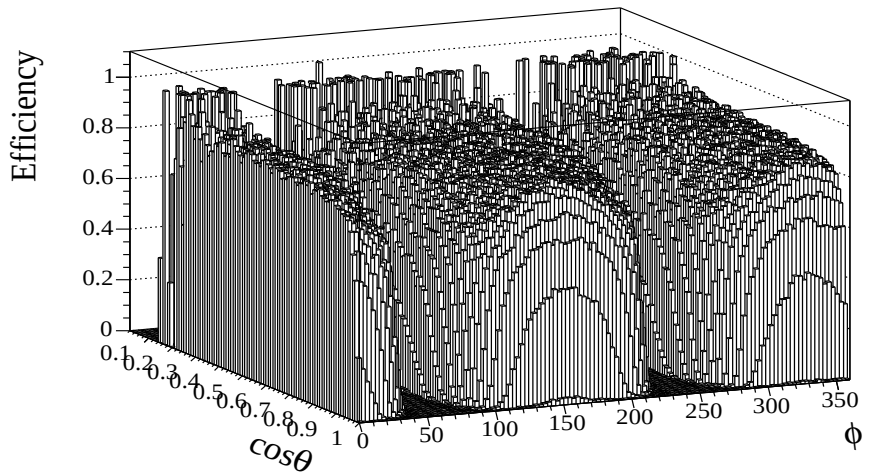


Figure 6.2: Efficiency of the MINOS far detector in $\cos\theta$ and azimuth.

Table 6.1: Cuts used to select data events for analysis.

| Cut | Name | Events Passing Cumulative Cuts |
|---|---|---|
| | Total Sample | 8053167 (100%) |
| 1 | Length | 5787738 (71.9%) |
| 2 | Fit Quality | 5642530 (70.1%) |
| 3 | End Points | 5626702 (69.9%) |
| 4 | Tracklike | 5622432 (69.8%) |
| 5 | Contained Vertex | 5493179 (68.2%) |

event is efficiency. Looking at the cosmic ray data, it is possible to identify several pathologies in the reconstruction software that contribute to detector efficiency. To find the detector efficiency, approximately $2 \times 10^6$ Monte Carlo cosmic ray muons were generated using the standard MINOS Monte Carlo generator, GMINOS. Monte Carlo events are used to determine the efficiency because the details of the event, such as the muon trajectory and energy, are known *a priori*. These details are called the "truth information", or "truth" for the event. The efficiency for each bin was determined by dividing the number of events in each $\cos\theta$ and $\phi$ bin that pass the selection criteria by the total number in each bin. The cuts used to define the cosmic ray sample for this analysis are as follows. As in § 4.3.1, multiple muon events and events that fail the DeMuxing figure of merit have been excluded from the data sample. The events remaining in the sample were examined for other pathologies. The cuts used to exclude other poorly reconstructed events are listed in Table 6.1. In this table the effect of each cut on the sample is also given. Cut (1), or the "Length" cut, requires that a track cross $\geq 20$ planes and that it have a total path length

of $\geq$ 2.0 m in the detector. This cut is used to get reliable tracks where there is enough information to determine the track parameters. Cuts (2), (3), and (4) are the same as the cuts with the same names in Table 4.2. The "Contained Vertex" cut (5) removes events where the vertex location appears to be more than 50 cm inside the detector's surface. Events that fail this cut are potential contained vertex neutrino events and are not cosmic ray muons.

Fig. 6.2 shows the efficiency for the detector as a function of $\cos\theta$ and $\phi$. Notice the gaps at azimuths corresponding to events coming from nearly perpendicular directions to the long sides of the detector. These gaps are the result of the detector geometry. Events coming from direction perpendicular to the long sides of the detector will not cross enough planes to pass cut (1).

One way to test of the quality of the track reconstruction after making these cuts is to look at the difference between the truth and reconstructed zenith and azimuthal angles. Fig. 6.3 shows the histogram of the differences in the zenith angles. The rms of the distribution shows the zenith angle determination to be good to within $\approx 0.3°$. Fig. 6.4 shows the difference between the truth and reconstructed values as a function of the truth zenith angle. The events with $\Delta\theta < -20$ and $\theta_{\text{truth}} \lesssim 25°$ are events that come from low acceptance regions of the detector and leave fewer observable hits making the direction determination difficult. The events forming the line from $\theta_{\text{truth}} = 70, \Delta\theta = -40$ to $\theta_{\text{truth}} = 20, \Delta\theta = -140$ are events where the direction of the event was reversed by the reconstruction. The remaining events with

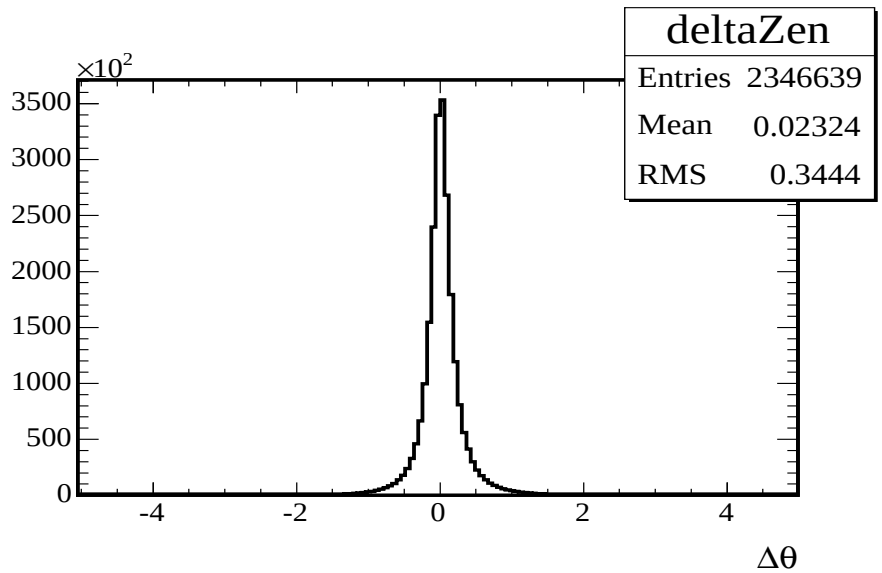


Figure 6.3: Difference in degrees between the truth and reconstructed zenith angle for cosmic ray Monte Carlo events.

$|\Delta\theta| > 10$ are events with short track lengths that just pass cut (1) making them more difficult to reconstruct correctly. Aside from these outliers, the distribution is flat indicating there is no bias in ability to reconstruct events based on zenith angle. The distribution of the differences between the truth and reconstructed azimuthal angles are shown in Fig. 6.5. The rms of the distribution shows that the azimuthal determination is good to within 0.6°. The difference between the truth and reconstructed values for the azimuth as a function of the truth value is shown in Fig. 6.6. The events with $|\Delta\phi| \approx 180°$ are instances where the track fitter reversed the vertex and end points of the track, making the azimuthal determination wrong by 180°. The points at $\phi_{\text{truth}} \approx 60, 250°$ are events with poor reconstruction because they come from directions where they just pass the track length cuts and have relatively

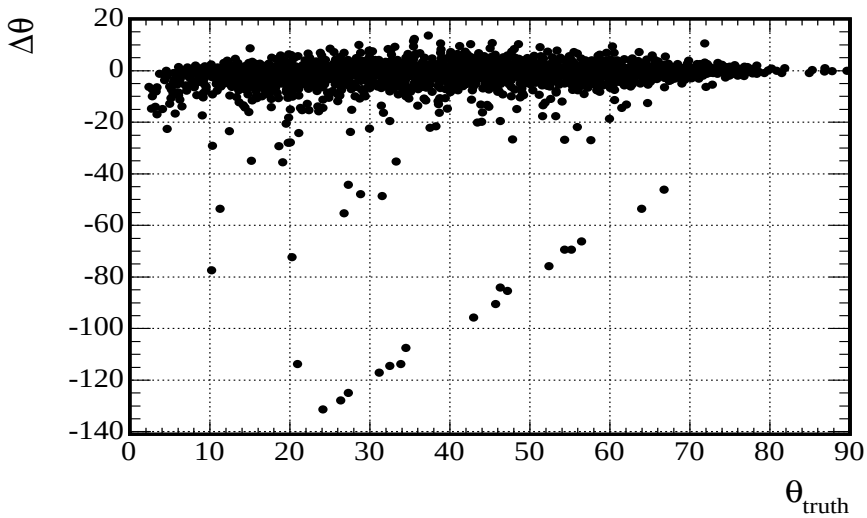


Figure 6.4: Difference in degrees between truth and reconstructed zenith angle as a function of truth zenith angle.

few hits to guide the reconstruction. The remaining outliers are events that just pass cut (1) and leave relatively few hits to guide the reconstruction, resulting in poor direction determination. There appears to be a slope to the distribution over each azimuthal range $0 - 60°$, $70 - 240°$ and $250 - 360°$. Close inspection of the events reveals that the appearance is due to the size of the points used in the figure relative to the bin size with the result that the outliers are more clearly seen. These outliers come mainly from directions with poor efficiency due to their large values of $\cos\theta$. Fig. 6.6 also shows that there is no bias in ability to reconstruct azimuthal angle based on incoming azimuth. Figs. 6.3 - 6.6 show that the cuts select tracks with good angular reconstruction.

The acceptance for the detector is the product of the efficiency, projected area,

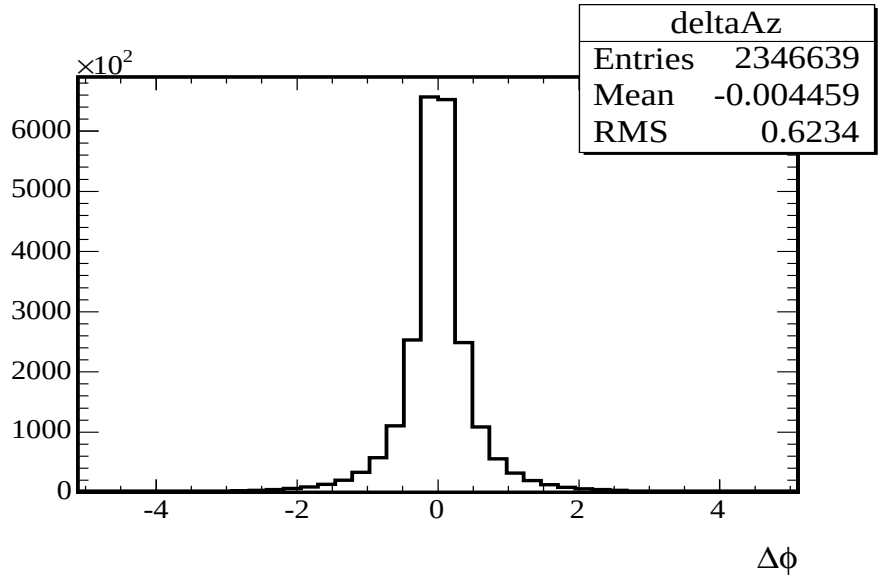


Figure 6.5: Difference in degrees between the truth and reconstructed azimuthal angle for cosmic ray Monte Carlo events.

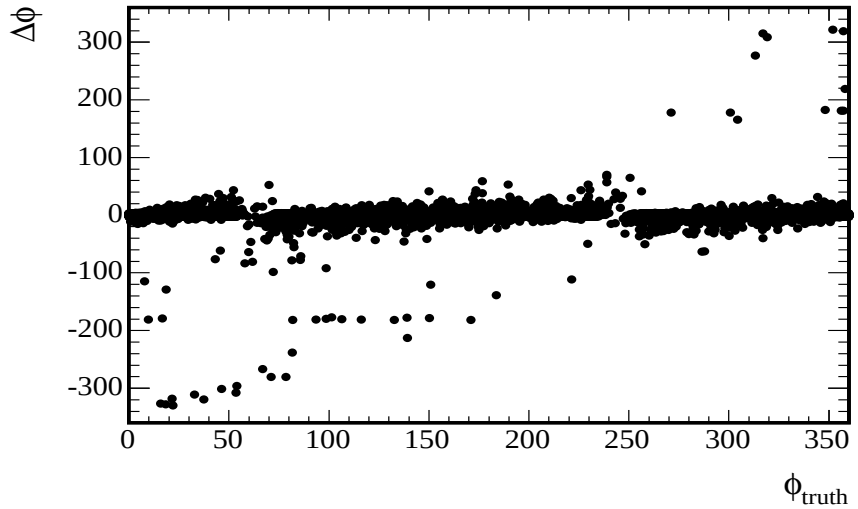


Figure 6.6: Difference in degrees between truth and reconstructed azimuthal angle as a function of truth azimuthal angle.

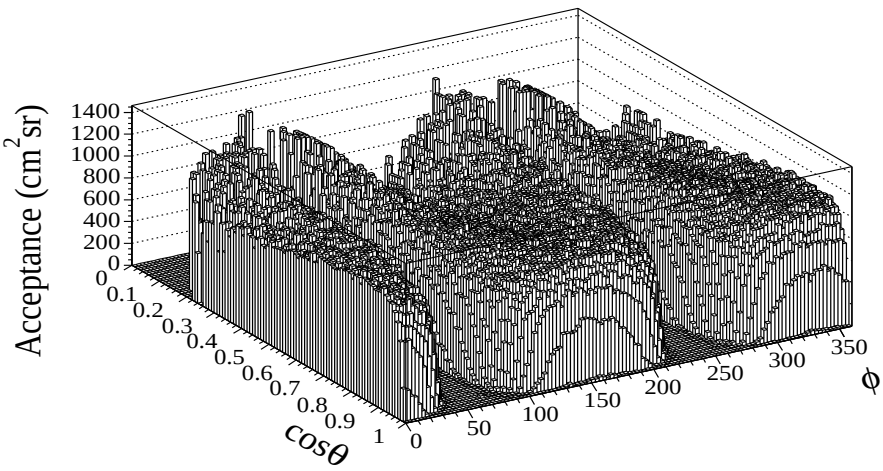


Figure 6.7: Acceptance of the MINOS far detector in $\cos\theta$ and azimuth.

and the solid angle for each bin. The acceptance as a function of $\cos\theta$ and $\phi$ is shown in Fig. 6.7. The integrated acceptance of the MINOS far detector for cosmic ray muons over all directions is $7.6 \times 10^6$ cm$^2$sr. The acceptance is lowest near the horizon at the north and south faces because of the projected area effects. The gaps in the acceptance reflect the gaps in the efficiency due to cut (1).

## 6.3 Cosmic Ray Muon Distributions

The cosmic ray muon analysis depends on knowing where the muons originate and how much rock they have traversed to reach the detector. The amount of rock between the detector and the atmosphere is called the overburden. The slant depth of the overburden is determined by a muon's point of origin and trajectory.

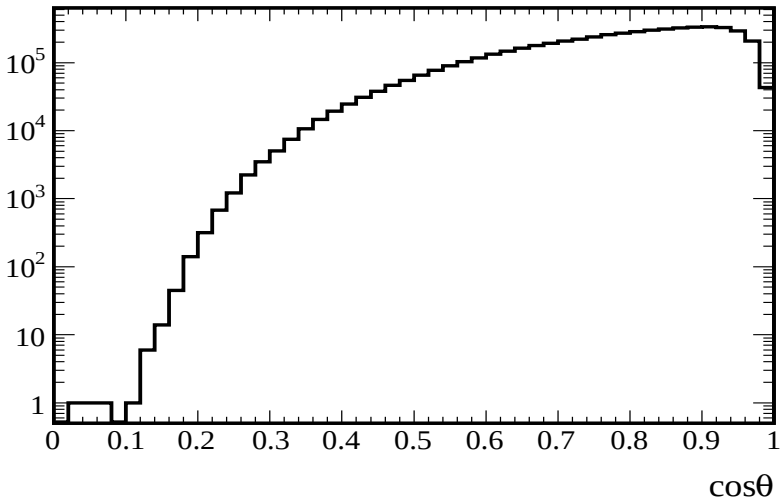


Figure 6.8: $\cos\theta$ distribution for downward-going muons.

When used to describe the overburden between the atmosphere and the detector, the slant depth may be quoted in terms of meters water equivalent (m.w.e) where 1 m.w.e = $10^2$ g/cm$^2$ or kilometers water equivalent, 1 km.w.e = $10^3$ m.w.e. The distribution of the cosmic ray muons as a function of $\cos\theta$ is shown in Fig. 6.8. The sharp drop off of the distribution near $\cos\theta = 1$ reflects the fact that muons coming from directly above the detector will not pass cut (1) of Table 6.1 due to low acceptance for those solid angles. The distribution also falls with increasing zenith angle. This behavior can be understood using an approximation for the number of muons expected to reach the detector. The number of muons at the surface with energy $E_\mu$ is approximated by [38]

$$\frac{dN_\mu}{dE_\mu} \approx \frac{0.14 E_\mu^{-2.7}}{\text{cm}^2\text{s sr GeV}} \left( \frac{1}{1 + \frac{1.1 E_\mu \cos\theta}{115\text{GeV}}} + \frac{0.054}{1 + \frac{1.1 E_\mu \cos\theta}{850\text{GeV}}} \right). \tag{6.1}$$

The minimum energy needed by a muon to traverse a slant depth $X$ is approximated by [38]

$$E_\mu^{\min} = \epsilon\Big[\exp(X/\xi) - 1\Big], \tag{6.2}$$

where $\epsilon \sim 500$ GeV and $\xi \approx 2.5 \times 10^5$ g/cm$^2$ in rock. Eq (6.1) shows that the number of muons at the surface falls as $E_\mu^{-2.7}$, and eq (6.2) shows that the energy required for a muon to reach the detector increases as $\exp(X)$. Thus the fall off of the $\cos\theta$ distribution toward the horizon reflects the fact that the overburden increases toward the horizon and filters all but the highest energy muons. The azimuthal distribution of the cosmic ray muons is shown in Fig. 6.9. In this figure and others showing azimuthal distributions, the muons with values of $\phi < 60°$ have had 360° added to their azimuths to make the muons from the north be in a contiguous region in azimuth, $240 < \phi \leq 420°$. The muons coming from the south have $60 \leq \phi \leq 240°$. More muons come from the south than the north because there is more rock to the north. The gaps in the distribution are due to the detector geometry as events coming from directions corresponding to the gaps will not cross enough planes to pass cut (1) of Table 6.1.

These distributions can be used to test the Monte Carlo. An overburden profile for the Soudan site [39] is included in the Monte Carlo event generation process. If the profile used accurately reflects the overburden, then the $\cos\theta$ and $\phi$ distributions for the Monte Carlo events will match the data distributions. The Monte Carlo

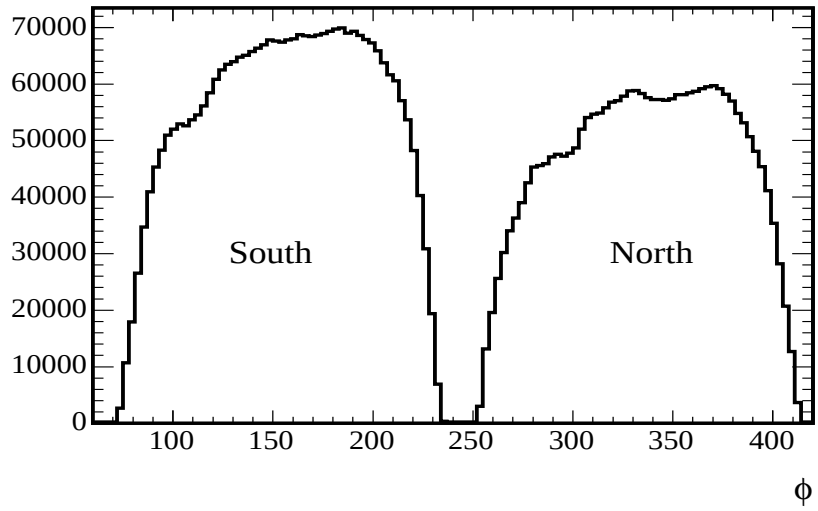


Figure 6.9: Azimuthal distributions for cosmic ray muons. Azimuth is defined to have $\phi = 0°$ due north and $\phi = 90°$ due east. Muons with $\phi < 60°$ have had 360° added to their azimuthal value to place those events from the north in a contiguous range in azimuth.

$\cos\theta$ distribution overlaid on the data is shown in Fig. 6.10. It has been scaled to have the same integral number of events as the data distribution. The top panel of the figure uses a linear scale to emphasize the comparison at large values of $\cos\theta$ and the bottom panel uses a log scale to emphasize the small values of $\cos\theta$. The shape of this distribution agrees with the data to within 5% for $0.6 \leq \cos\theta \leq 0.9$. However, for $\cos\theta = 0.5$ the Monte Carlo overestimates the number of muons by 10% and the overestimation increases to a factor of 2 or more near the horizon. For $0.95 < \cos\theta \leq 1$ the Monte Carlo underestimates the number of muons by 8%. At present these discrepancies are not well-understood but are likely due to the simplicity of the current Monte Carlo simulation, which is described below.

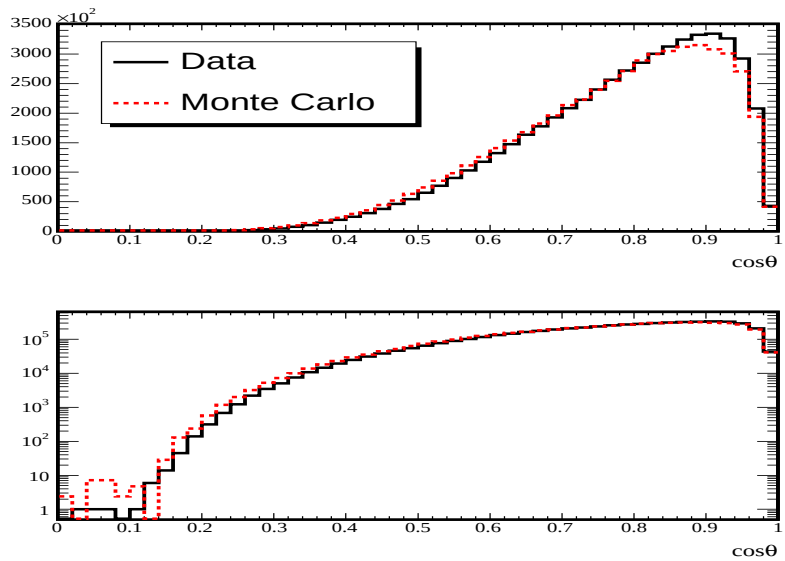


Figure 6.10: $\cos\theta$ distribution for Monte Carlo events (dashed line) with the data for reference (solid line).

The Monte Carlo generates cosmic ray muons events by selecting an arrival direction for each muon assuming that the events are uniformly distributed in solid angle. The energy of the muon is taken from the distribution given by eq (6.1). Once the muon arrival direction is selected for an event, the overburden is determined from the map. With an event energy and overburden, the muon is tested using eq (6.2) to determine if it has enough energy to reach the detector. The events are placed on the detector in the following way [40]. An imaginary box with dimensions 8.01 m $\times$ 8.01 m $\times$ 32.01 m is positioned around the detector. The differential flux of muons through the top face of the box is given by

$$d\Phi_{\text{top}} = A_{\text{top}} dN_\mu(\cos\theta, \ln E_\mu) E_\mu \cos\theta d(\ln E) d(\cos\theta) d\phi, \tag{6.3}$$

where $A_{\text{top}}$ is the area of the top face and $dN_\mu(\cos\theta, \ln E_\mu)$ is the flux of muons as a function of zenith angle and $\ln E_\mu$. The differential flux through the long sides of the box is

$$d\Phi_{\text{long}} = \pm A_{\text{long}} dN_\mu(\cos\theta, \ln E_\mu) E_\mu \sin\theta \sin\phi d(\ln E) d(\cos\theta) d\phi, \tag{6.4}$$

where $A_{\text{long}}$ is the area of a long side of the box and the $(+)$ is for the east side and $(-)$ is for the west side. The differential flux through a short side of the box is

$$d\Phi_{\text{short}} = \pm A_{\text{short}} dN_\mu(\cos\theta, \ln E_\mu) E_\mu \sin\theta \cos\phi d(\ln E) d(\cos\theta) d\phi, \tag{6.5}$$

where $A_{\text{short}}$ is the area of a short side of the box and the $(+)$ is for the north side and $(-)$ is for the south side.

This method of generating Monte Carlo events is approximate for two reasons. First, using eq (6.2) introduces a hard low energy cutoff for the allowed muon energy as a function of direction. In reality the energy required for muons on the surface to traverse a given slant depth is not a hard threshold. The propagation of the muons through the rock needs to simulate muon energy loss in rock correctly using a program such as GEANT. Second, the proper way to generate events is to simulate the interactions of the primary cosmic rays in the atmosphere and propagate the generated muons to the surface of the Earth. Work is in progress to produce such a cosmic ray simulation for MINOS.

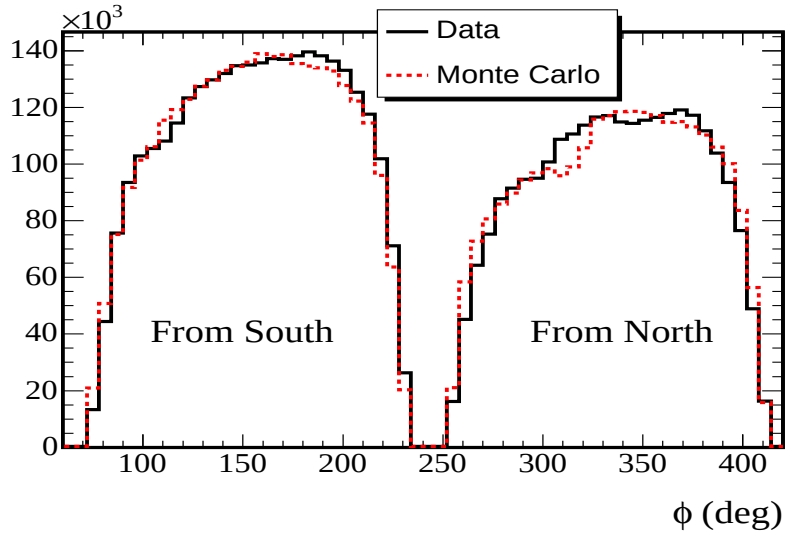


Figure 6.11: Azimuthal distribution for Monte Carlo events (dashed line) with the data for reference (solid line). See the caption of Fig. 6.9 for an explanation of the azimuthal values.

The azimuthal distribution of the muons with the Monte Carlo distribution scaled to have the same integral number of events as the data is shown in Fig. 6.11. The shape of the Monte Carlo distribution for events from the north was reflected about $\phi = 330°$, while the Monte Carlo events from the south were reflected about $\phi = 170°$ because the Monte Carlo has the overburden profile reversed for the east and west sides. Once the reflections are made, the azimuthal distribution in the Monte Carlo generally has the same features as the data. The data distribution shows a shoulder near $\phi = 300°$ that is not seen in the Monte Carlo, while the Monte Carlo has a shoulder at $\phi = 330°$ that is not in the data. These discrepancies could be the result of not taking into account the fact that the overburden profile is slightly different between the Soudan 2 and MINOS locations.

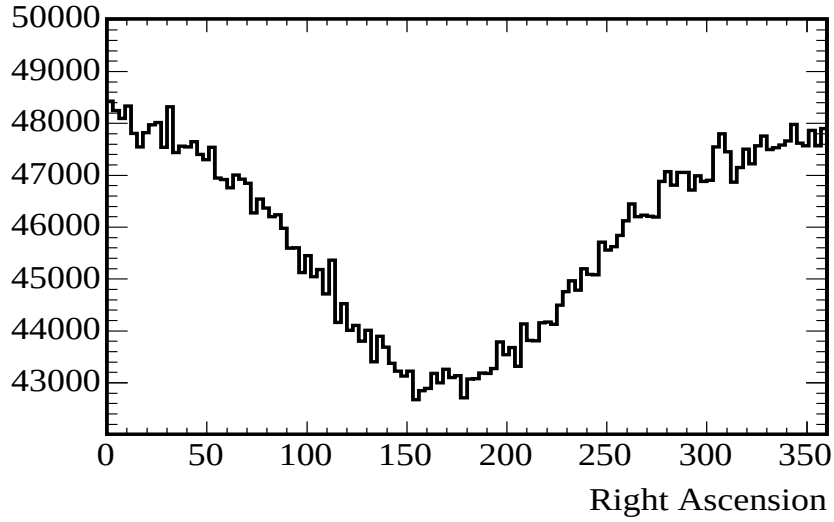


Figure 6.12: Right ascension distribution for cosmic ray muons.

Knowing a muon's zenith angle, azimuthal angle and arrival time, it can be projected back to the sky using standard astronomical coordinates. The right ascension distribution is shown in Fig. 6.12. The dip in the distribution is due to live-time effects as the detector is more likely to be offline for maintenance during certain times of the day. In the short exposure of the current data set, these times correspond to a narrow range of right ascension values. The declination distribution for the cosmic ray muons is shown in Fig. 6.13. The dip at declination of $\sim 45°$ is due to the detector acceptance near the zenith. There are no live-time effects seen in the declination distribution because the declinations viewed by the detector are independent of time.

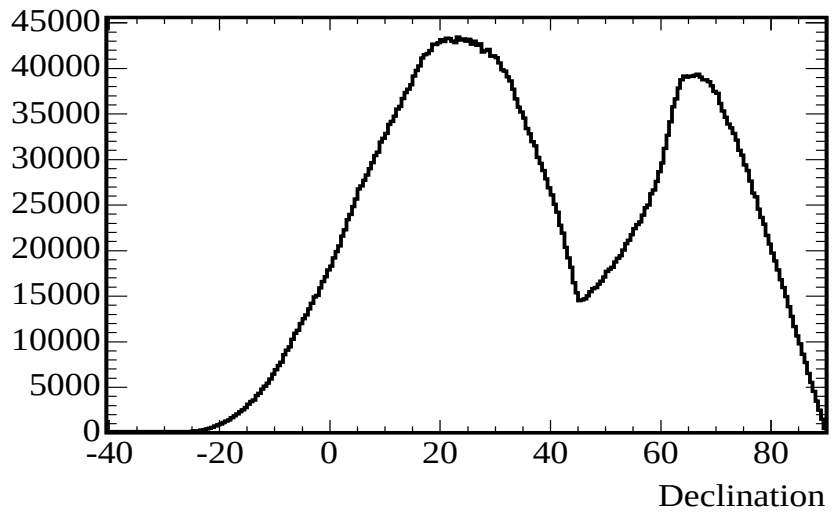


Figure 6.13: Declination distribution for cosmic ray muons.

## 6.4 Vertical Single Muon Intensity

The detector independent intensity of muons underground is called the vertical muon intensity, $I_\mu^v$, and it is measured as a function of slant depth. The vertical intensity for single muons in each solid angle bin is

$$I_\mu^v(X,\theta,\phi) = \frac{1}{\Delta T}\frac{\sum_i N_i}{\sum_j \Delta\Omega_j A_j \epsilon_j}, \tag{6.6}$$

where $\Delta T$ is the live-time of the exposure, $N_i$ is the number of observed muons in the solid angle bin $\Delta\Omega_j = \Delta\cos\theta\Delta\phi$ of slant depth $X$. The projected area for solid angle bin $j$ is $A_j$ and $\epsilon_j$ is the efficiency for that bin. The slant depth for each bin was found using the map of the Soudan Mine site overburden [39]. The vertical intensity as a function of slant depth is shown in Fig. 6.14. The data were fit to the three

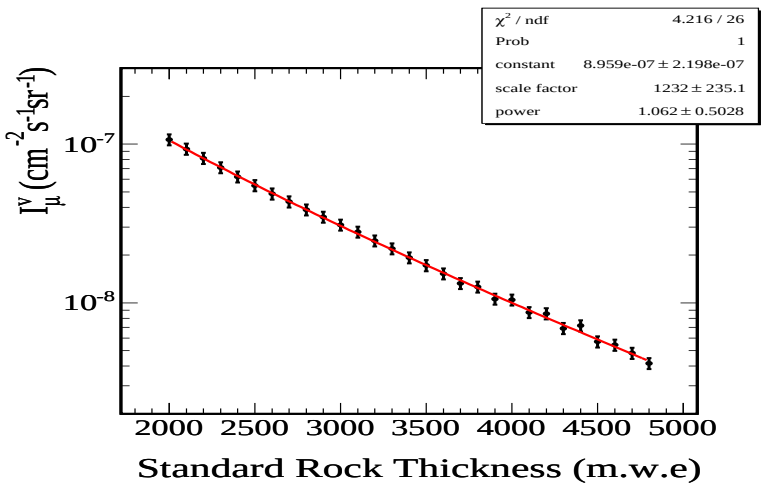


Figure 6.14: Measured vertical muon intensity for the MINOS data as a function of slant depth.

parameter empirical formula used by the MACRO collaboration [41],

$$I_\mu^v(h) = A\left(\frac{h_0}{h}\right)^{\mathcal{K}} \exp\left(-\frac{h}{h_0}\right). \tag{6.7}$$

The fit parameters for the MINOS data are $A = (0.87 \pm 0.24) \times 10^{-6}\text{cm}^{-2}\text{s}^{-1}\text{sr}^{-1}$, $\mathcal{K} = 1.11 \pm 0.5$ and $h_0 = 1257 \pm 252$ with $\chi^2/ndf = 4/26$. The very low value of $\chi^2/ndf$ is likely the result of overestimating the systematic error due to understanding of the efficiency in each solid angle bin. The MACRO parameters are [41] $A = (1.96 \pm 0.03) \times 10^{-6}\text{cm}^{-2}\text{s}^{-1}\text{sr}^{-1}$, $\mathcal{K} = 1.10 \pm 0.01$ and $h_0 = 972 \pm 3$, indicating that the MINOS vertical intensity does not fall as steeply as the MACRO vertical intensity.

Fig. 6.15 [3], shows the global vertical muon intensity as a function of slant depth in km.w.e. The slant depths at the Soudan site range between 2 - 5 km.w.e. For slant

depths above $\sim$ 10 km.w.e the intensity flattens out. The muons from these slant depths are the neutrino-induced muons [42]. The fit to these data is an empirical parameterization of slant depth, $X$, in m.w.e given by [42],

$$I_{\mu}^{v}(X) = \exp(\varpi + \varrho X) + \exp(\gamma + \delta X) + \Phi. \tag{6.8}$$

The constants are from the cosmic ray muon spectrum and are $\varpi = -11.22$, $\varrho = -0.002620$, $\gamma = -14.10$, and $\delta = -0.001213$. The neutrino-induced portion of the flux is given by $\Phi = 2.17 \times 10^{-13}\text{cm}^{-2}\text{sr}^{-1}\text{s}^{-1}$. The MINOS data were fit to the parameterization of eq (6.8) with $\Phi$ set to zero because the slant depths used were all $>$ 5000 m.w.e. The fit gives $\varpi = -13.22 \pm 1.8$, $\varrho = -0.001936 \pm 0.0018$, $\gamma = -14.51 \pm 1.6$, and $\delta = -0.000997 \pm 0.00029$ with $\chi^2/ndf = 4/25$.

## 6.5 Charge Sign Determination

MINOS is the first underground detector with a magnetic field, which means it can differentiate $\mu^+$ from $\mu^-$. The L3 collaboration published the value 1.25 for the ratio of the number of cosmic ray $\mu^+$ to $\mu^-$, $N_{\mu^+}/N_{\mu^-}$, at ground level [43]. The muons used had measured momenta up to 300 GeV. Other experiments have reported ratios of $\approx$ 1.25 for muon energies $E_\mu < 100$ GeV [38]. The ratio is not well known for high energy muons [38] such as those observed deep underground at MINOS. The muons seen in MINOS have energies much higher than 100 GeV at the point of

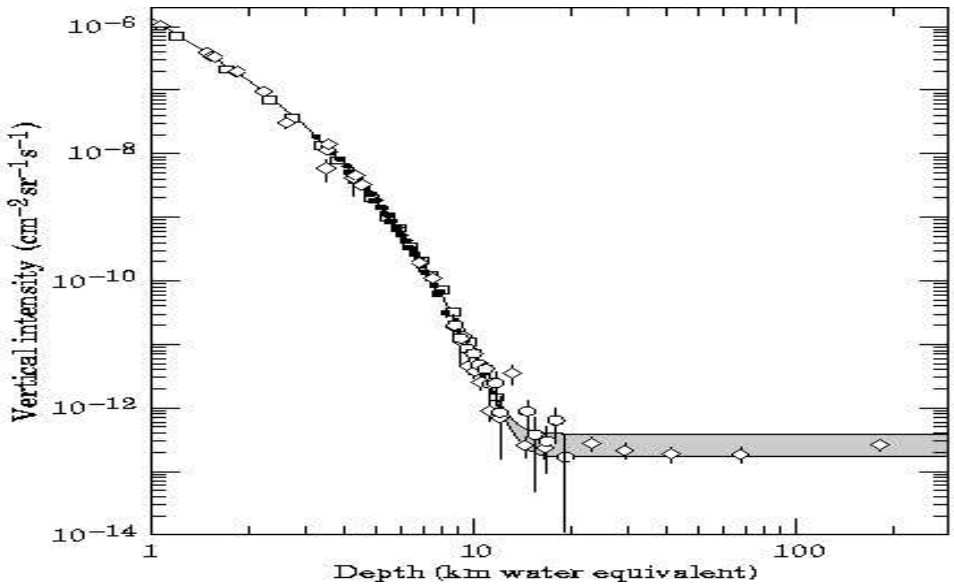


Figure 6.15: Global vertical muon intensity as a function of slant depth (1 km.w.e = $10^5$g/cm$^2$). The slant depths at the Soudan site range between 2 - 5 km.w.e. The figure is taken from [3] and the data points are referenced there. The horizontal shaded area represents neutrino-induced muons with $E > 2$GeV. The upper horizontal line is the prediction for horizontal neutrino-induced muons, the lower for upward-going neutrino induced muons.

production and the $N_{\mu^+}/N_{\mu^-}$ ratio is expected to be in the range 1.22 - 1.46 [38]. One key to understanding the efficiency of the charge sign determination in the MINOS detector is the cosmic ray $N_{\mu^+}/N_{\mu^-}$ ratio as that value has an established theoretical expectation.

The MINOS reconstruction software uses a Kalman filter [44, 45] technique to fit the charge and momentum of the tracks. The advantage of this technique is that it operates recursively and is able to combine determination of which hits belong on a track with fitting the momentum of the particle. The technique involves a series of matrix manipulations to determine the trajectory of the particle as well as the ratio of its charge to its momentum. The matrix manipulations are in the literature [44, 45] and are not described here. Rather, an overview of the technique as it relates to the MINOS reconstruction is given.

The trajectory of a track in the MINOS detector is specified at each hit point by 5 parameters, collectively known as the "state of the track" at the point. These parameters are the $u$ and $v$-positions of the hits, the way the trajectory changes in $z$ with respect to these positions, $du/dz$ and $dv/dz$, and the ratio of the charge of the particle to its momentum $q/p$. The hits seen on each active plane are grouped into clusters based on the location of the hit strips in the plane. A seed track is found that is the collection of clusters in an event that appear to lie along the same trajectory. The first hit plane selected in the seed track is the plane at the end of the track with the earliest time stamp. This plane is the vertex plane for the track. A

prediction for the location where the particle's trajectory crosses the second hit plane is made based on some reasonable assumptions about the track's state at the vertex plane. These assumptions include measurement errors for the $u$ and $v$ positions of the track being consistent with the strip width, the errors for $du/dz$ and $dv/dz$ having moderate values (0.01) and the $q/p$ having a large error indicating that the $q/p$ is not well known at that point. The prediction allows for noise due to multiple scattering of the particle and measurement error of the $u$ or $v$ position of the hit, depending on the view of the plane. The prediction for the second plane is compared to the recorded hit information for that plane and the parameters are adjusted to include the information from the second plane. The errors in the fit parameters on the second plane are calculated using the matrix manipulations and are used along with the fit values in the prediction of the hit location on the third plane. The process continues until the last plane with hits is reached and all hits are either used in the track or discarded as noise because they are too different from the predicted location for that plane. If multiple clusters are found on the same plane, each is examined to determine which is most consistent with the track based on the previously fit planes. The values for the state parameters and their errors are updated at each plane. Once the track is fit from the vertex to the last plane with hits that are consistent with the track, the same procedure is used to fit the track in the reverse direction. At each point along the track that is not the vertex or end, the track's state parameters are set to be the average of the forward and reverse fit. The state at the vertex

and its error are completely determined by the reverse fit as that fit has used all the information in the track to determine the state at the vertex. The forward fit completely determines the state at the end of the track for the same reason.

### 6.5.1 $N_{\mu^+}/N_{\mu^-}$ Ratio from Data

The reconstructed data were used to determine the underground $N_{\mu^+}/N_{\mu^-}$ ratio. A constraint based on the relative error in $q/p$, $(q/p)/\sigma_{q/p}$, is made to select tracks with good charge identification from those passing the cuts of Table 6.1. If $(q/p)/\sigma_{q/p} < 1$, then the value of $q/p$ is effectively unknown because the error is larger than the fit value. The empirical value for the cut is $(q/p)/\sigma_{q/p} \geq 2.5$, because the measured value is well away from the opposite charge sign according to the measured error. Using that value for the cut, the ratio for the total data set was found to be $1.44 \pm 0.002(stat)$, a value that is at the upper end of the theoretically allowed range. The data were then separated into the identified $\mu^+$ and $\mu^-$ and their $\cos\theta$ and $\phi$ distributions were compared. Fig. 6.16 shows the $\cos\theta$ distributions for the total sample and the two charge signs in the top plot, with the $\mu^+$ shown by the dot-dash line and the $\mu^-$ by the dotted line. The ratio as a function of $\cos\theta$ is shown in the bottom plot and the errors are statistical errors. The ratio is $\approx 1.4$ over the range $0.3 \leq \cos\theta \leq 0.85$. For values of $0.85 < \cos\theta \leq 1$ the ratio increases due to decreasing detector acceptance for that range of values as shown by the Monte Carlo studies below. The ratio is not well-determined for $\cos\theta \lesssim 0.2$ due to the

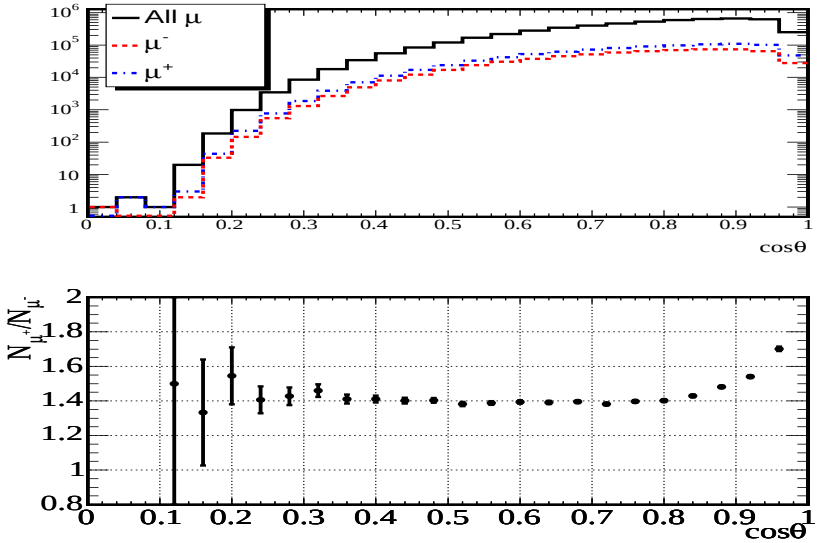


Figure 6.16: $\cos\theta$ distributions (top) for the total sample (solid line), $\mu^+$ (dot-dash line) and $\mu^-$ (dashed line). The bottom plot shows the $N_{\mu^+}/N_{\mu^-}$ ratio.

poor statistics in those bins. Fig. 6.17 shows the distributions for the $\mu^+$ and $\mu^-$ as well as their ratio as a function of azimuth. The $\mu^-$ appear to be enhanced coming from the south while the $\mu^+$ events appear to come more or less uniformly from all azimuths that are not suppressed due to acceptance effects. Moreover, the structure due to the varying overburden seen in the total distribution is not seen in the $\mu^+$ distribution and is exaggerated for the $\mu^-$ distribution. Also, the ratio shows significant structure over the entire azimuthal range. The ratio as a function of the fit momentum, $(q/p)^{-1}$, is shown in Fig. 6.18. The top panel shows the distributions of the total data sample, along with the identified $\mu^+$ and $\mu^-$, and the bottom panel shows the ratio. At low values of the fit momentum, $p_{\text{fit}} < 10$ GeV/c, the ratio is $\sim 1.3$. The value of $N_{\mu^+}/N_{\mu^-}$ increases from $\sim 1.3$ to $\sim 1.6$ from $0 - 35$ GeV/c. It

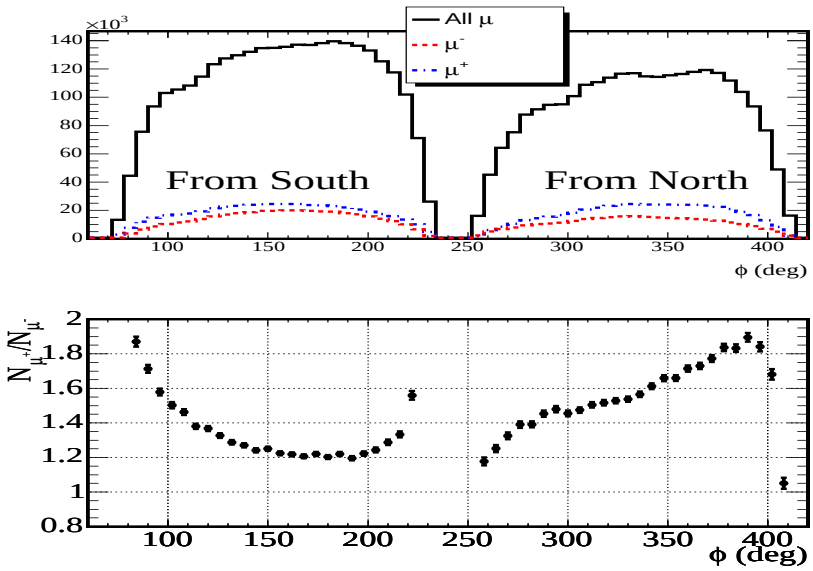


Figure 6.17: Azimuthal distributions (top) for the total sample (solid line), $\mu^+$ (dot-dash line) and $\mu^-$ (dashed line). The bottom plot shows the $N_{\mu^+}/N_{\mu^-}$ ratio. See the caption of Fig. 6.9 for an explanation of the azimuthal values.

then decreases back to $\sim 1.3$ for $35 \leq p_{\text{fit}} \leq 90$ GeV/c. For higher momenta the ratio is not well determined due to low statistics. The ratio of the $\mu^+$ to $\mu^-$ vertical intensities as a function of slant depth is shown in Fig. 6.19. The points have a weighted mean of $N_{\mu^+}/N_{\mu^-} = 1.43$. There does appear to be some statistically significant structure for the slant depths between 2000 and 3000 m.w.e. which is not presently understood. One possible explanation for the structure is that it is the result of the fact that no uncertainties are included in the overburden map making the uncertainties in the points appear much smaller than they should.

The $N_{\mu^+}/N_{\mu^-}$ ratio as a function of azimuth varies considerably from the expectation and much effort was invested in understanding it. The first attempt to understand the varying $N_{\mu^+}/N_{\mu^-}$ ratio as a function of $\phi$ was to restrict the data

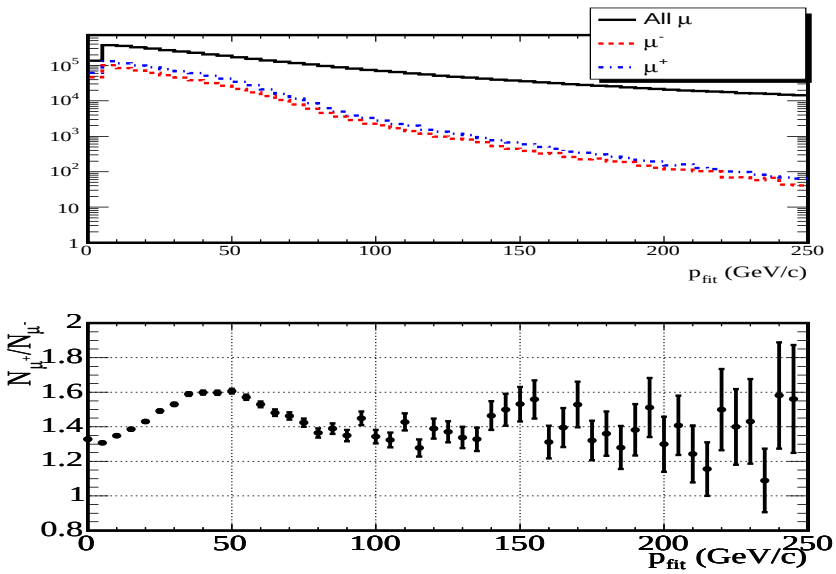


Figure 6.18: Fit momentum distributions (top) for the total sample (solid line), $\mu^+$ (dot-dash line) and $\mu^-$ (dashed line). The bottom plot shows the $N_{\mu^+}/N_{\mu^-}$ ratio.

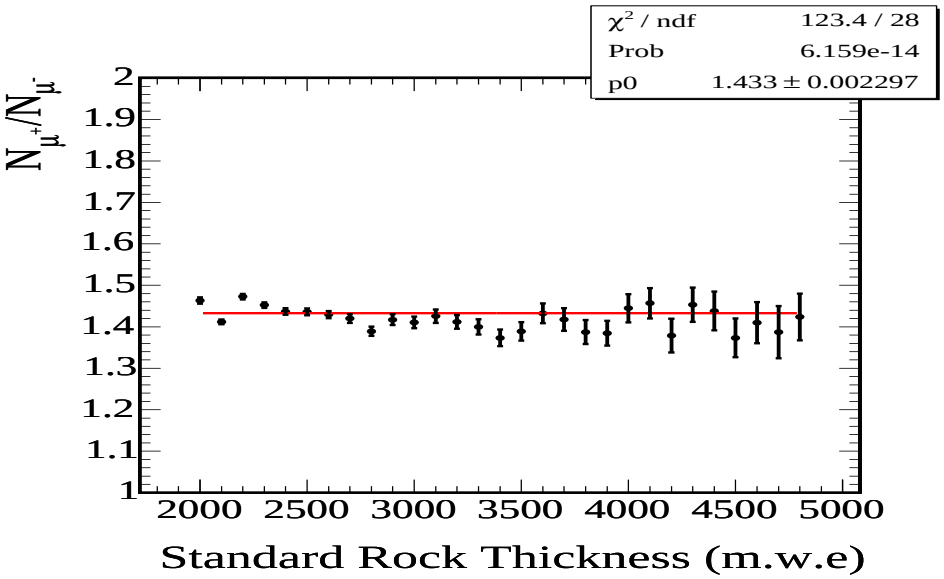


Figure 6.19: Ratio of $\mu^+$ to $\mu^-$ vertical intensity as a function of slant depth.

used to low momentum tracks, $p_{\text{fit}} < 50$ GeV/c, since these events almost certainly should show evidence of bending in the MINOS magnetic field. The resulting ratio as a function of azimuth showed the same structure as in Fig. 6.17. A second approach was to consider cuts based on the fit quality. The value of $(q/p)/\sigma_{q/p}$ should be a good indication of how well the charge sign is determined in the fit. The distributions for $(q/p)/\sigma_{q/p}$ for the total data sample and the $\mu^+$ and $\mu^-$ separately are shown in the top panel of Fig. 6.20. The bottom panel shows the ratio as a function of $(q/p)/\sigma_{q/p}$. For $(q/p)/\sigma_{q/p} \geq 2.5$, the ratio is flat with a value of $N_{\mu^+}/N_{\mu^-} \sim 1.4$. Below $(q/p)/\sigma_{q/p} = 2.5$ the ratio decreases toward 1 reflecting the fact that as $(q/p)/\sigma_{q/p}$ increases, the fitter becomes increasingly likely to assign charge at random. Based on this figure, a cut of $(q/p)/\sigma_{q/p} \geq 2.5$ should select events with well determined charge. However, the previous figures were made using this cut, indicating that the structure is not due poor to poor fitting alone.

Third the $N_{\mu^+}/N_{\mu^-}$ ratio was examined in several two dimensional views to see if correlations between azimuth, $\cos\theta$, and fit momentum were causing the observed structure. Fig. 6.21 shows several 2-dimensional plots used to look for such correlations. Each of the plots are made so that the gray scale for a given bin indicates the measured value of the acceptance (top left plot) or $N_{\mu^+}/N_{\mu^-}$ ratio (remaining plots) for that bin. The top left plot in the figure shows the acceptance of the detector as a function of $\cos\theta$ and $\phi$. The detector has low acceptance for events coming from directions that are nearly perpendicular to the $z$-axis. The remaining plots

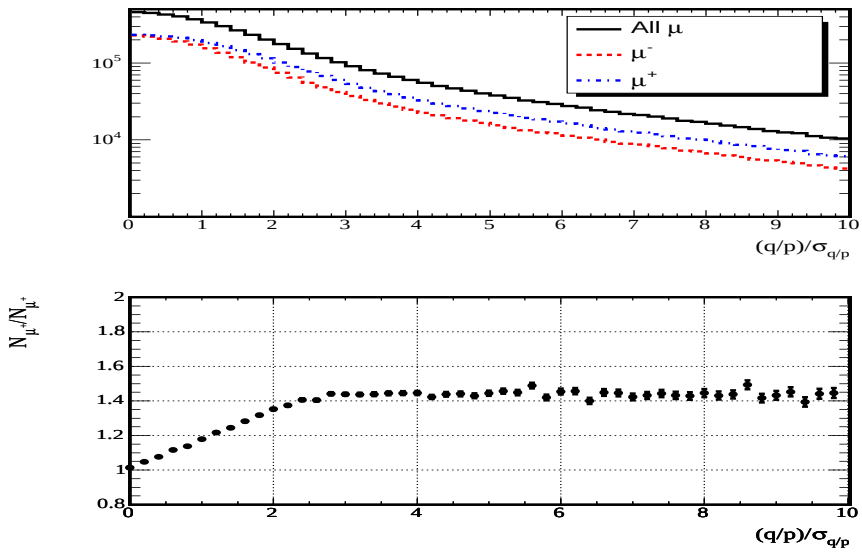


Figure 6.20: $(q/p)/\sigma_{q/p}$ distributions (top) for the total sample (solid line), $\mu^+$ (dot-dash line) and $\mu^-$ (dashed line). The bottom plot shows the $N_{\mu^+}/N_{\mu^-}$ ratio.

show the value of $N_{\mu^+}/N_{\mu^-}$ as a function of $\cos\theta$ and $\phi$ (top right), $\phi$ and fit momentum (bottom left) and $\cos\theta$ and fit momentum (bottom right). The top right plot shows that the ratio is very high or very low in regions corresponding to low detector acceptance, a result that is not surprising. However, it is surprising to see that the ratio is very large ($N_{\mu^+}/N_{\mu^-} > 2$) for muons coming from a region with good acceptance $\phi > 360°$ and $0.8 < \cos\theta < 0.9$. The ratio appears to be anomalously high for $\phi < 100$ and $0.85 \leq \cos\theta \leq 0.95$ as well. These are the regions in Figs. 6.16 and 6.17 that show the most structure. The bottom left and right plots show that these events all have $30 \leq p_{\text{fit}} \lesssim 50$ GeV/c, and should have good charge sign determination. The bottom two plots in the figure also show that there are no events with $p_{\text{fit}} \gtrsim 70$ GeV/c for $\cos\theta > 0.8$ and $\phi < 100°$ and $\phi > 350°$. The muons

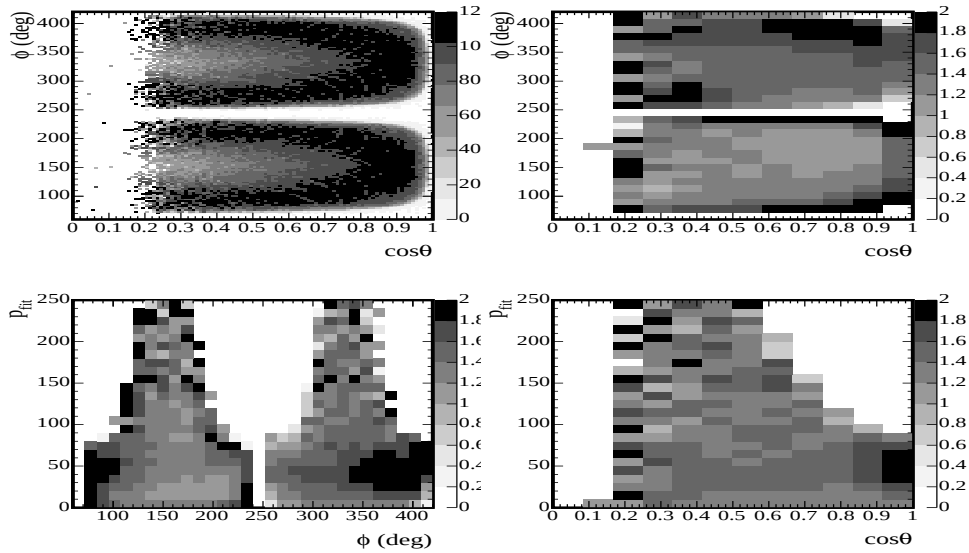


Figure 6.21: The detector acceptance and $N_{\mu^+}/N_{\mu^-}$ ratio for several 2-dimensional views. The top left plot shows the detector acceptance. The top right plot is the $N_{\mu^+}/N_{\mu^-}$ ratio as a function of $\cos\theta$ and $\phi$. The bottom left plot is the ratio as a function of fit momentum and $\phi$ and the bottom right plot shows the ratio as a function of $\cos\theta$ and fit momentum. (See the caption of Fig. 6.9 for an explanation of the azimuthal values.)

with higher momenta than 70 GeV/c are excluded from these directions as result of the cut on $(q/p)/\sigma_{q/p}$. Fig. 6.22 shows the same types of 2-dimensional views as in Fig. 6.21 for the Monte Carlo events. In these plots, the charge separation and momentum determination are based on the truth information. Also, no cut on $(q/p)/\sigma_{q/p}$ has been made in this figure as it shows truth information. This figure shows that there are no preferred trajectories for a given charge sign or momentum, aside from the regions of low detector acceptance. It also shows that there is no exclusion of high momentum events in the same regions of $\cos\theta$ and $\phi$ as seen in the data. Fig. 6.23 shows the same 2-dimensional views for Monte Carlo muons again,

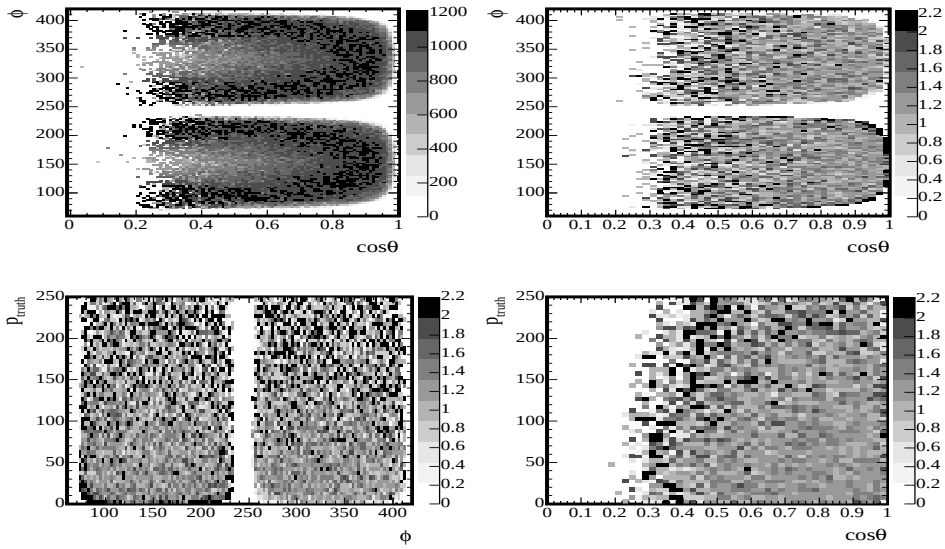


Figure 6.22: The detector acceptance and $N_{\mu^+}/N_{\mu^-}$ ratio based on Monte Carlo $p_{\text{truth}}$ for several 2-dimensional views. (See the caption of Fig. 6.21 for an explanation of different views.)

using the fit values to determine charge sign and momentum and using the cut on $(q/p)/\sigma_{q/p}$. This figure shows that the cut on $(q/p)/\sigma_{q/p}$ causes the same regions of $\phi$ and $\cos\theta$ to be excluded for high momentum events. High momentum events that do not traverse many planes in the detector do not leave enough information for a good fit to $q/p$ and will not pass the $fracError$ cut.

The structure in the data $N_{\mu^+}/N_{\mu^-}$ ratio could be the result of a poor understanding of the magnetic field in the detector. The most likely way for the field in the detector to vary is as a function of $z$-position because each plane of steel is at a specific $z$-position. Fig. 6.24 shows the data $N_{\mu^+}/N_{\mu^-}$ as a function of the vertex $z$-position of a track and its trajectory in $z$, $dz/ds$, in the upper left plot. Events coming directly from the north are centered at $dz/ds = -1$ and those coming di-

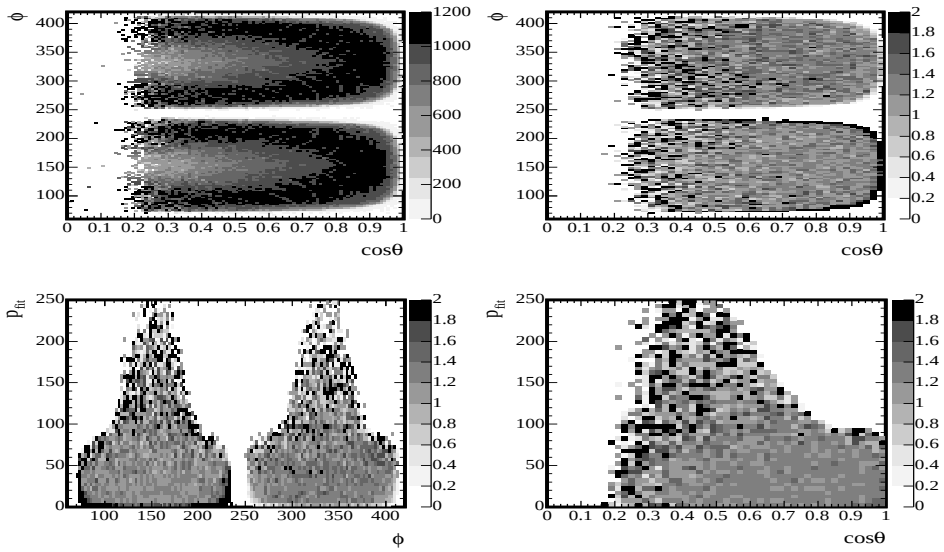


Figure 6.23: The $N_{\mu^+}/N_{\mu^-}$ ratio for several 2-dimensional views based on Monte Carlo $p_{\text{fit}}$. (See the caption of Fig. 6.21 for an explanation of different views.)

rectly from the south are centered at $dz/ds = 1$. Events from the north that entered the detector on the west side have $-2 < dz/ds < -1$ and those that entered from the east side have $-1 < dz/ds < 0$. Events from the south that entered the detector on the west side have $0 < dz/ds < 1$ and those that entered from the east side have $1 < dz/ds < 2$. The upper right plot in Fig. 6.24 shows the $N_{\mu^+}/N_{\mu^-}$ as a function of the vertex and end $z$-positions of the tracks; the bottom plots show the same for the Monte Carlo. Dark areas indicate regions where many more $\mu^+$ than $\mu^-$ are identified, and light areas indicate regions where the opposite is true. There is clear structure seen in the data plots that are not present in the Monte Carlo plots. The large bands in the $z_{\text{vertex}}$ vs $dz/ds$ plots that run from $15 < z_{\text{vertex}} < 21$ m in the events from the north and $10 < z_{\text{vertex}} < 15$ m for events from the south are events

that cross the gap between the supermodules. There are also bands for $z < 5$ m for events from the north and $z > 25$ m for events from the south. These bands represent events that cross the end planes of each supermodule. The magnetic coil returns runs vertically downward on the faces of each supermodule and the fields created by the coil returns are not modeled in the magnetic field map used for the event reconstruction. These fields will certainly influence how the muons move through the detector. Other bands of very high and very low data $N_{\mu^+}/N_{\mu^-}$ ratios are seen throughout the detector and they are not understood at this time, but they may be the result of differences between the steel making up the planes in those regions.

### 6.5.2 Monte Carlo Studies of Charge Identification

Several studies of Monte Carlo events were undertaken to understand the nature of the reconstructed charge and the effect of the magnetic field on charged particles moving through the detector. The Monte Carlo events were generated to have a constant $N_{\mu^+}/N_{\mu^-}$ ratio of 1.25 for all energies. The $N_{\mu^+}/N_{\mu^-}$ ratio for Monte Carlo events passing the track selection cuts of Table 6.1 and having $(q/p)/\sigma_{q/p} \geq 1$ is shown in Fig. 6.25. The figure shows the ratio is approximately 1.3 for events coming from the north, but drops to 1.1 for events coming from the south. While the Monte Carlo events show a different ratio for events from the north versus the south, this figure does not show the structure seen in the data ratio.

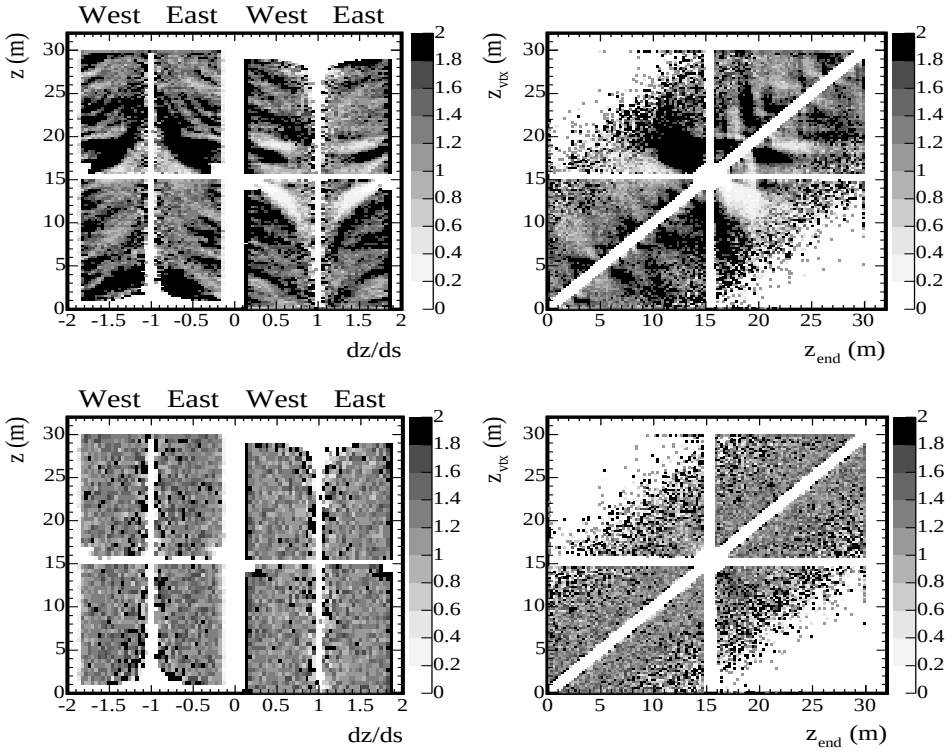


Figure 6.24: The $N_{\mu^+}/N_{\mu^-}$ ratio as a function of vertex $z$-position and $dz/ds$ (left) and vertex and end $z$-positions (right). The data ratios are the top plots and the Monte Carlo ratios are the bottom plots.

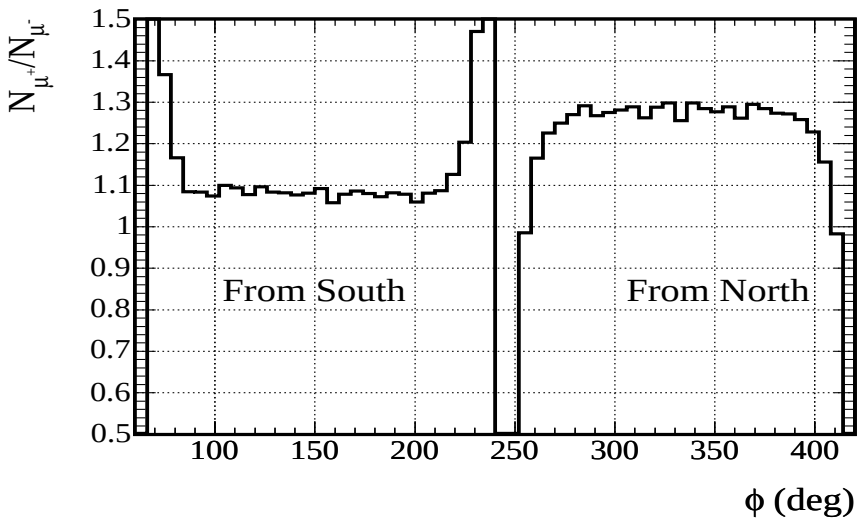


Figure 6.25: Ratio of cosmic ray Monte Carlo $\mu^+$ to $\mu^-$ events passing the track selection cuts as a function of azimuth. (See the caption of Fig. 6.9 for an explanation of the azimuthal values.)

#### 6.5.2.1 Magnetic Focusing

One hypothesis to account for the structure seen in the data and Monte Carlo events suggests that the structure is caused by focusing effects due to the magnetic field. The MINOS magnetic field was designed to focus negatively charged particles coming from the south toward the center of the detector. The reason for this choice is that the neutrino beam coming from Fermilab will consist of $\nu_\mu$ which produce $\mu^-$ in CC interactions. Given the toroidal magnetic field, the field will also focus positively charged particles coming from the north toward the center of the detector. Thus, the magnetic field focusing gives a possible explanation for structure as a function of azimuthal direction as the directions that focus $\mu^+$ events defocus $\mu^-$ events and vice

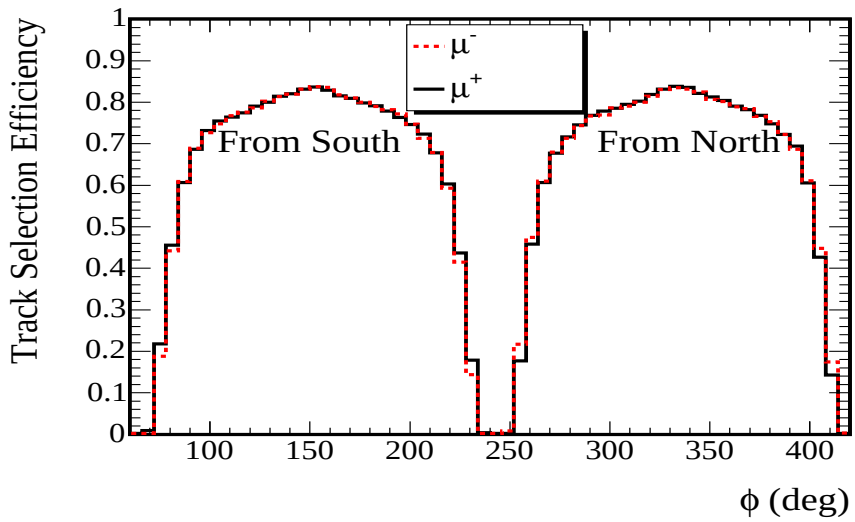


Figure 6.26: Efficiency for selecting $\mu^+$ (solid line) and $\mu^-$ (dashed line) in Monte Carlo events as a function of azimuth. (See the caption of Fig. 6.9 for an explanation of the azimuthal values.)

versa. To test this hypothesis the track selection cuts were first checked to ensure that they did not introduce a bias in the number of $\mu^+$ or $\mu^-$ reconstructed for any direction. Fig. 6.26 shows the efficiency for selecting tracks that pass the cuts of Table 6.1 as a function of azimuth and charge sign. The $\mu^+$ events are shown by the solid line and $\mu^-$ events by the dashed line. The charge of the events was determined using truth information and no cut was made on $(q/p)/\sigma_{q/p}$. The figure shows that the cuts are not biased as a function of azimuth.

Next, the ability of the reconstruction software to correctly identify $\mu^+$ and $\mu^-$ was tested. The purity of the charge identification is defined to be the ratio of the number of events with correctly identified charge to the number of events passing the track selection cuts. The truth information was used to separate $\mu^+$ from $\mu^-$.

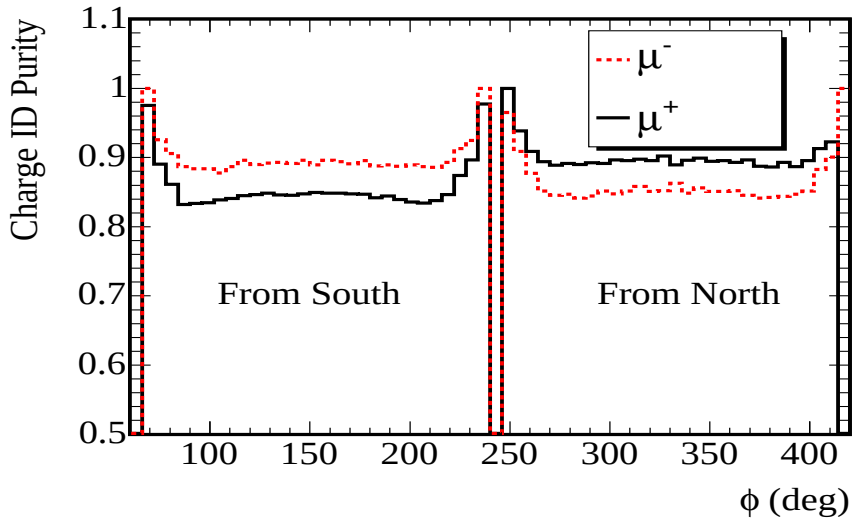


Figure 6.27: Purity of charge identification for $\mu^+$ (solid line) and $\mu^-$ (dashed line) in Monte Carlo events as a function of azimuth. (See the caption of Fig. 6.9 for an explanation of the azimuthal values.)

Fig. 6.27 shows the purity based on truth information for $\mu^+$ (solid line) and $\mu^-$ (dashed line) as a function of the azimuth. There is obviously a bias in the charge sign determination for the Monte Carlo events as a function of azimuth. This bias favors events that have the right combination of direction and charge sign to be focused. The purity curves for the tracks where the fit value of $q/p$ was used to separate $\mu^+$ from $\mu^-$ and the combination of the truth and reconstruction determined the correctness of the fit are shown in Fig. 6.28. From this figure it would appear that there is no bias in charge identification for events coming from the north and a substantial bias for events from the south. The discrepancy between Fig. 6.27 and Fig. 6.28 can be understood as follows. Positively charged events coming from the north are correctly identified 90% of the time, as seen in Fig. 6.27. The negatively

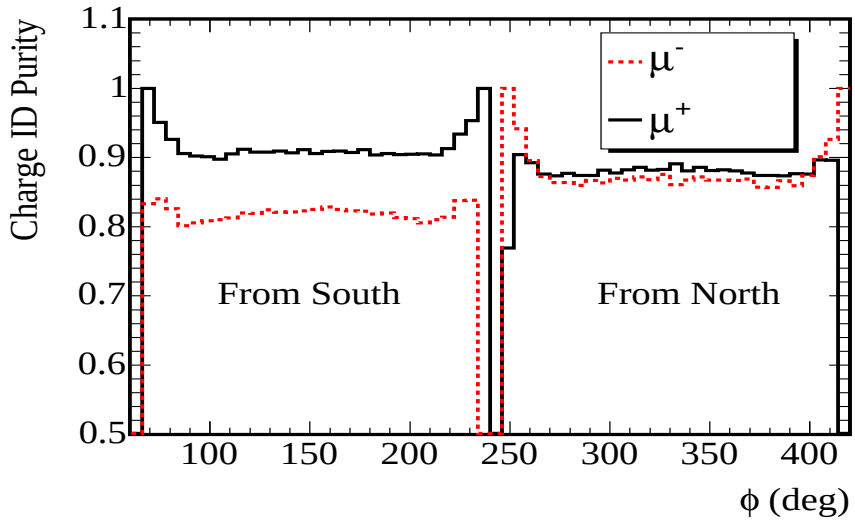


Figure 6.28: Purity of charge identification for $\mu^+$ (solid line) and $\mu^-$ (dashed line) using the fit $q/p$ to separate the charges as a function of azimuth. (See the caption of Fig. 6.9 for an explanation of the azimuthal values.)

charged particles from the north are correctly identified 85% of the time. That means that when the fit $q/p$ is used to separate $\mu^+$ from $\mu^-$, the purity for $\mu^-$ coming from the north will be

$$\mathcal{P}_{\mu^-,north} = \frac{0.85N_{\mu^-}}{0.85N_{\mu^-} + 0.1(1.25N_{\mu^-})} = 0.87, \tag{6.9}$$

where the first term in the denominator is the correctly identified $\mu^-$ and the second term is the incorrectly identified $\mu^+$, recalling that $\mu^+/\mu^- = 1.25$ for the Monte Carlo. A similar calculation shows the purity for $\mu^+$ from the north is $\mathcal{P}_{\mu^+,north} = 0.88$. For events coming from the south, $\mathcal{P}_{\mu^-,south} = 0.83$ and $\mathcal{P}_{\mu^+,south} = 0.91$. These results indicate that the bias seen in the charge identification is the cause of the varying

$\mu^+/\mu^-$ ratio as a function of azimuth for the Monte Carlo, because the observed ratio for a given direction is

$$\frac{N_{\mu^+}}{N_{\mu^-}} = \frac{N_{\mu^+0}\mathcal{P}_{\mu^+}}{N_{\mu^-0}\mathcal{P}_{\mu^-}}, \tag{6.10}$$

where the subscript 0 indicates the generated number of particles.

The origin of the bias in charge identification is related to magnetic focusing, so the bias may be dependent on the energy of a particle as higher energy particles do not bend as much as low energy particles having the same trajectory at the vertex. Several purity curves were generated using different cuts on the truth value of the muon momentum. For the remainder of this discussion, the purity curves shown were made by using the truth information to separate $\mu^+$ from $\mu^-$. Fig. 6.29 shows three sets of purity curves as a function of azimuth for different ranges of the momentum. As with the other purity curves, the solid lines indicate $\mu^+$ and the dashed lines indicate $\mu^-$. The top set of curves shows the purity for muons with $p < 25$ GeV/c, the middle shows $p < 50$ GeV/c, and the bottom shows $p > 100$ GeV/c. There is no bias for the low momentum events and the purity is 0.97. A small bias exists for events with $p < 50$ GeV/c, but the purity is still above 0.95 for these events. Events with $p > 100$ GeV/c show considerable bias and the purity for these events is much lower as well, 0.70-0.80 depending on the charge and direction combination. The conclusion to be drawn from these curves is that very high momentum events are preferentially reconstructed with the correct charge

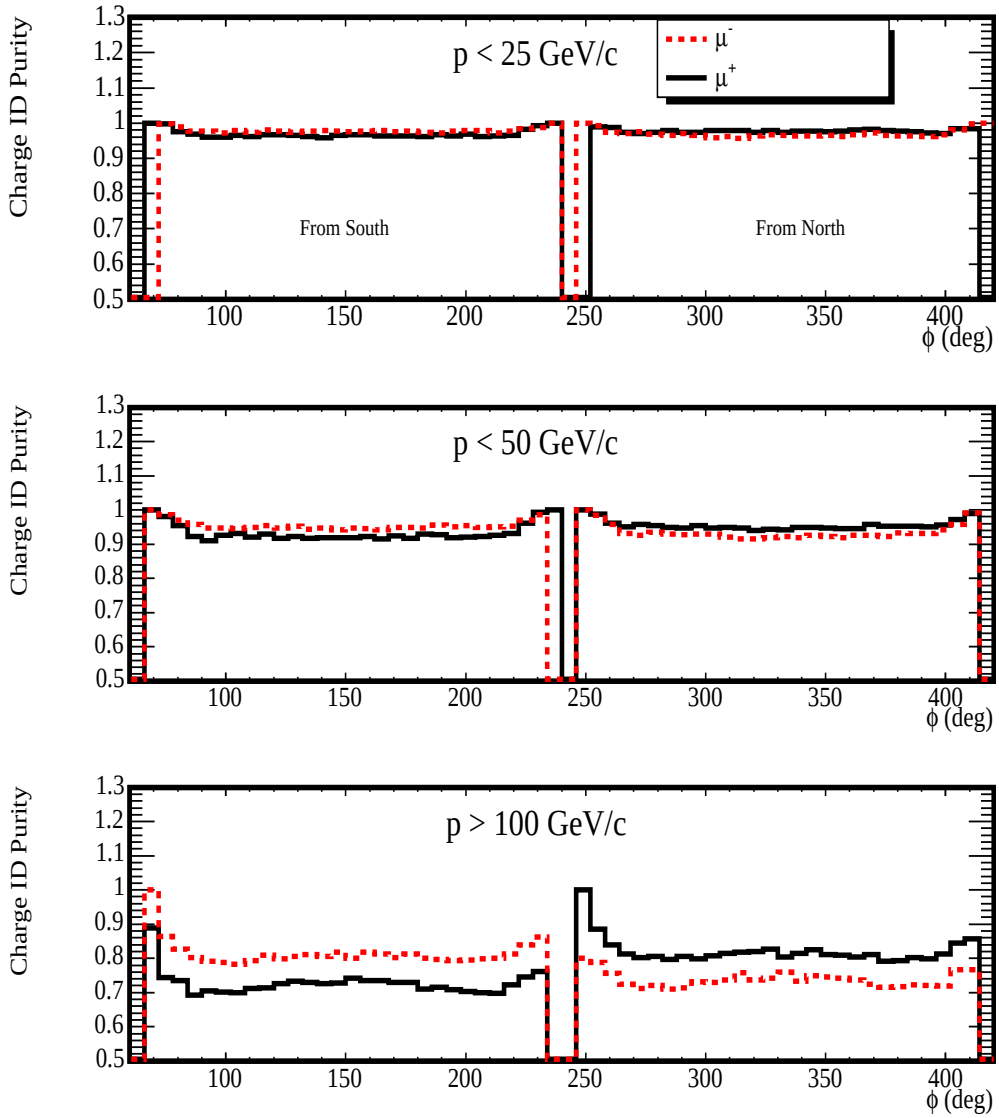


Figure 6.29: Purity of charge identification as a function of azimuth for Monte Carlo events with $p < 25$ GeV/c (top), $25 < p < 50$ GeV/c (middle) and $p > 100$ GeV/c (bottom). (See the caption of Fig. 6.9 for an explanation of the azimuthal values.)

if they have the charge and direction combination to be focused. The charge sign determination for high momentum events depends on the track fitting algorithm detecting a change from a straight line along the muon track. Such changes are seen when the muon crosses from one strip to another in a given view. High momentum muons that have the right combination of charge sign and direction to be focused could preferentially experience deflections that cause them to traverse more strips in a view than muons with the wrong charge sign and direction combination. This effect causes events that are focused to have more information to guide the fitter relative to defocused events, creating the bias.

The bias could also be related to a muon's distance of closest approach, or impact parameter, to the magnetic coil. Smaller values of the impact parameter, $b$, indicate that the muon has traveled through a larger magnitude field because the field strength falls off radially from the coil. Fig. 6.30 shows four sets of purity curves as a function of $b$ for $\mu^-$ (open circles) and $\mu^+$ (filled circles) with the statistical errors shown. Events coming from the south are on the left side and events from the north on the right side. The top set of curves is for events with $p < 25$ GeV/c while the bottom set is for events with $p > 100$ GeV/c. These curves show that there is no bias for events with low momentum and $b \lesssim 3.5$ m, but for low momentum events with larger values of $b$ there is a bias. Also the purity is 1 for the low momentum events events with $b \lesssim 2.5$ m and falls with increasing $b$. For the high momentum events, the bias in charge identification is present for all values of $b$, and the purity is

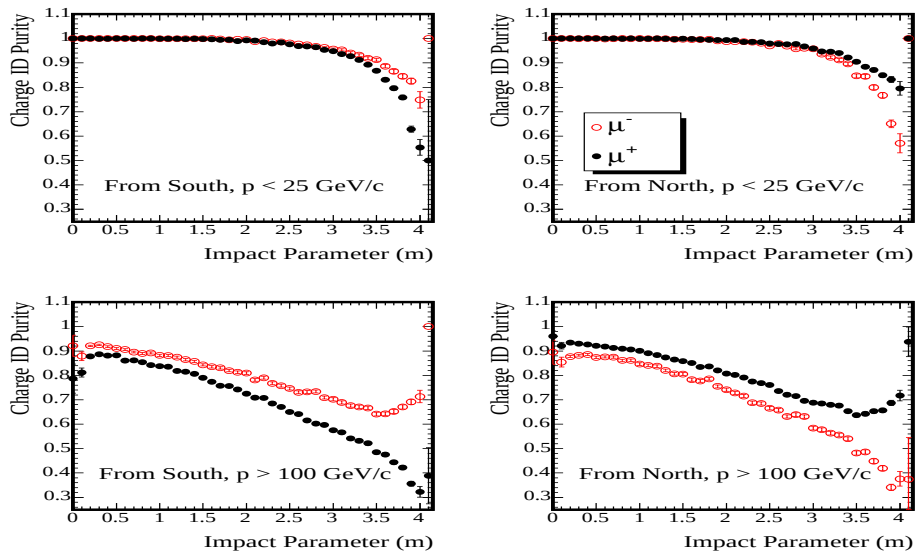


Figure 6.30: Purity of charge identification as a function of impact parameter for Monte Carlo $\mu^-$ (open circles) and $\mu^+$ (closed circles). The events from the south are on the left side and events from the north are on the right. The top plots are for events with $p < 25$ GeV/c and the bottom plots are for events with $p > 100$ GeV/c.

$\lesssim 0.9$ for those events. The bias becomes more pronounced in the high momentum sample with increasing values of $b$. These purity curves show the focusing effect in the detector as events with the correct charge sign and direction combination have larger purities at points near the edges of the detector than events with the incorrect combination. The focused events are deflected toward areas with stronger magnetic fields increasing the likelihood that they are identified with the correct charge sign.

Another factor that could influence the charge sign reconstruction is the distance a muon travels through the detector. Fig. 6.31 shows the purity as a function of the track length using the same conventions for charge sign, direction and momentum as in Fig. 6.30. These curves indicate that the purity does rise with increasing track

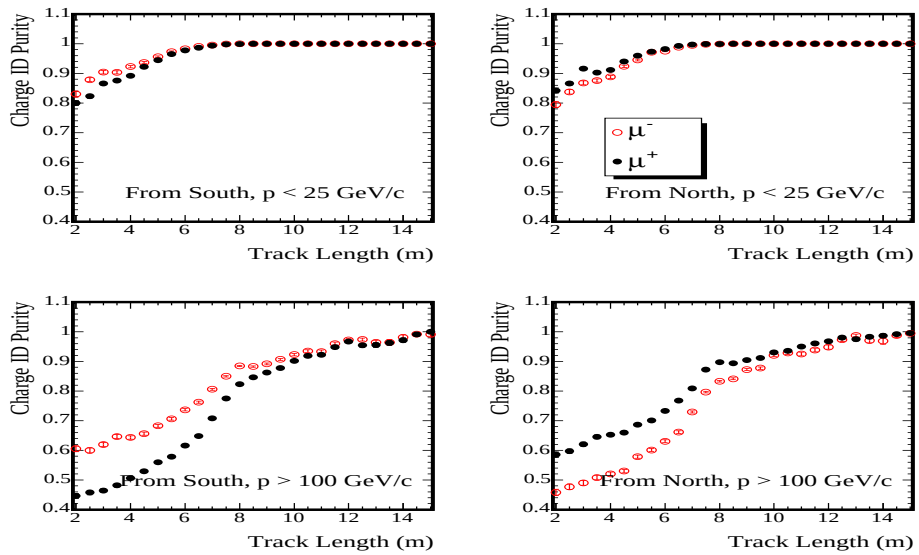


Figure 6.31: Purity of charge identification as a function of track length for Monte Carlo events. (See the caption to Fig. 6.30 for an explanation of the symbols and distributions.)

length as expected. A bias emerges for events with track length $< 5$ m in the low momentum sample. There is a clear bias in the high momentum sample. The bias, however, is small for events that travel at least 10 m in the detector in the high momentum sample and these events have a purity $\geq 0.9$. High momentum events with shorter track lengths show a considerable bias, though, and the purity falls rapidly with decreasing track length.

The purity curves used to this point have all been dependent on observable features of tracks that are independent of the fit. That is, the length of the track and its impact parameter can be determined from the hit locations alone. It is also important to determine how the purity changes as a function of the goodness of the fit $q/p$. The purity as a function of $(q/p)/\sigma_{q/p}$ for the Monte Carlo events is shown

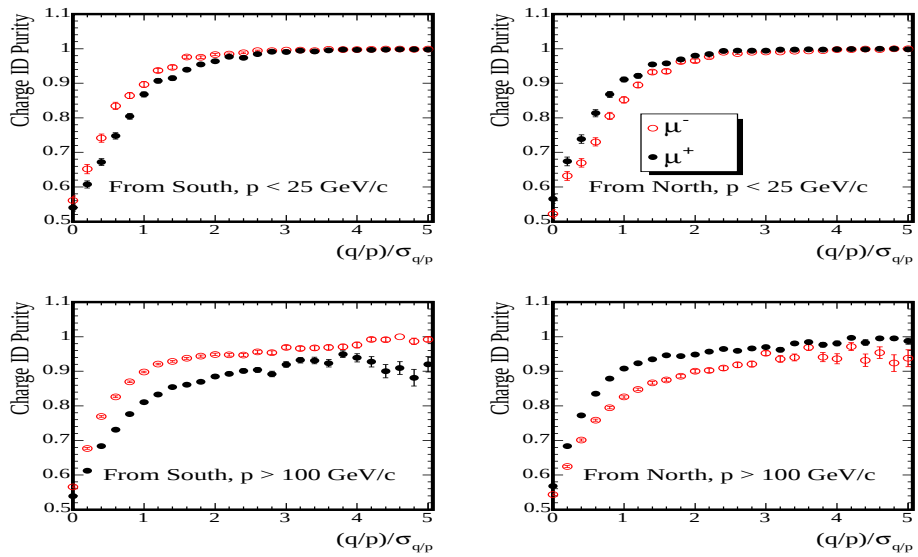


Figure 6.32: Purity of charge identification as a function of $(q/p)/\sigma_{q/p}$ for Monte Carlo events. (See the caption to Fig. 6.30 for an explanation of the symbols and distributions.)

in Fig. 6.32, which also uses the conventions of Fig. 6.30. There is no bias in the purity for low momentum events with $(q/p)/\sigma_{q/p} \gtrsim 2.$, and the purity is $\geq 0.95$ for those events. There is a bias in the purity as a function of $(q/p)/\sigma_{q/p}$ for the high momentum events. It is not possible to say if there is a bias in the purity for the high momentum events with $(q/p)/\sigma_{q/p} > 4.$ due to the large statistical errors of those bins.

This analysis of the purity curves shows that the reconstruction of charge sign is biased toward events that are focused toward the center of the detector. The bias is not large for low momentum events, and is only present in these events for shorter tracks or large values of $b$. The bias becomes larger with increasing muon momentum and is present in all events except for those with track lengths $\gtrsim 10$ m.

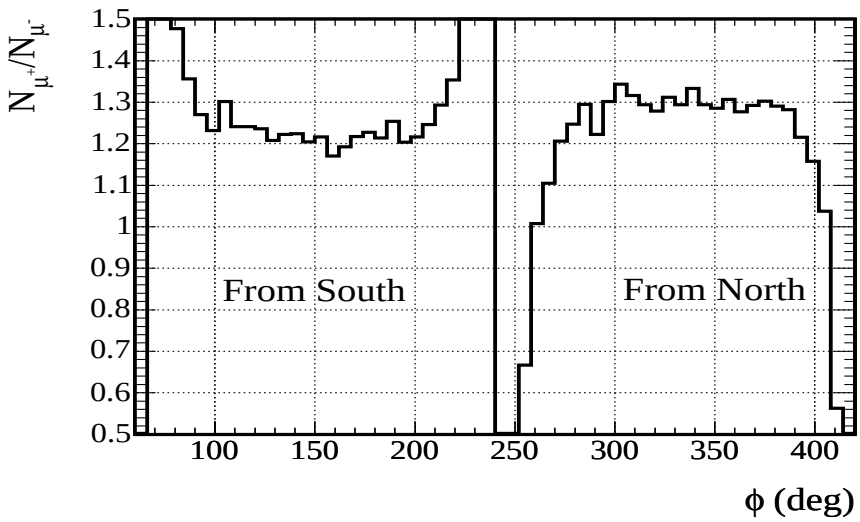


Figure 6.33: Ratio of cosmic ray Monte Carlo $\mu^+$ to $\mu^-$ for events passing the charge identification cuts as a function of azimuth. (See the caption of Fig. 6.9 for an explanation of the azimuthal values.)

Events with $(q/p)/\sigma_{q/p} > 2.5$ have purity $\gtrsim 0.9$, even for the high momentum events. There is no bias for the low momentum events satisfying this cut on $(q/p)/\sigma_{q/p}$, although there is a bias of a few percent in the high momentum events. Combining all of the information gained in this analysis, an empirical cut to select good charge identification in the Monte Carlo events is: $(q/p)/\sigma_{q/p} \geq 2.5$. Fig. 6.33 shows the $N_{\mu^+}/N_{\mu^-}$ ratio for Monte Carlo events that pass the charge identification cut. The ratio is much flatter across all azimuths with $N_{\mu^+}/N_{\mu^-} = 1.2$ for events from the south and $N_{\mu^+}/N_{\mu^-} = 1.3$ for events from the north. Recall that the value used to generate the events was $N_{\mu^+}/N_{\mu^-} = 1.25$. The charge identification cut appears to remove most focusing effects from the $N_{\mu^+}/N_{\mu^-}$ ratio in the Monte Carlo.

It should be possible to remove any structure due to focusing or acceptance effects

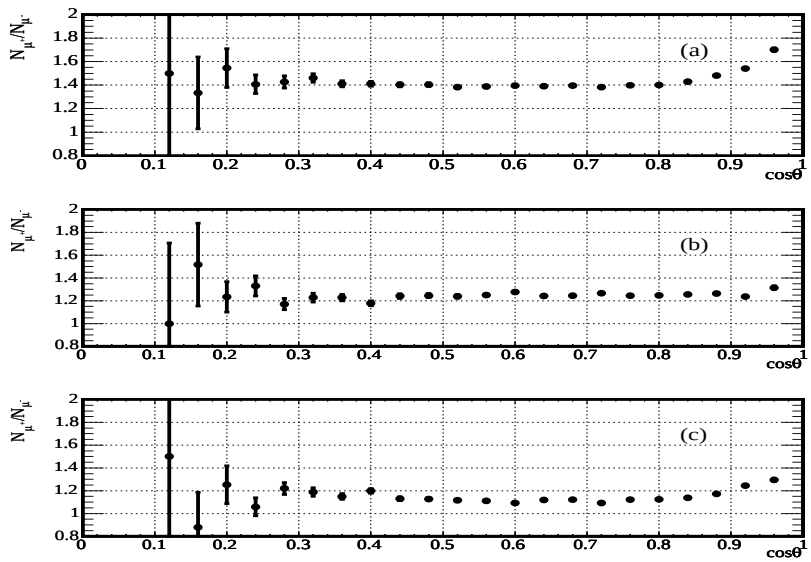


Figure 6.34: The data $N_{\mu^+}/N_{\mu^-}$ ratio for identified $\mu^-$ and $\mu^+$ as a function of $\cos\theta$ (a). The $N_{\mu^+}/N_{\mu^-}$ for the Monte Carlo as a function of $\cos\theta$ is shown in (b) and the ratio of data $N_{\mu^+}/N_{\mu^-}$ to Monte Carlo $N_{\mu^+}/N_{\mu^-}$ as a function of $\cos\theta$ is shown in (c).

remaining after the charge identification cut from the data $N_{\mu^+}/N_{\mu^-}$ ratio by dividing it by the Monte Carlo ratio. Figs. 6.34 - 6.36 show the results of taking the ratio of ratios for the $\cos\theta$, $\phi$ and fit momentum distributions respectively. In these figures, (a) is the $N_{\mu^+}/N_{\mu^-}$ ratio of data events passing the charge identification cuts, (b) is the $N_{\mu^+}/N_{\mu^-}$ ratio for the Monte Carlo events and (c) is the ratio of the data and Monte Carlo ratios. The errors shown for the points in (c) are the statistical errors for the data. The structure due to the low acceptance regions in the detector are removed in the $\cos\theta$ and $\phi$ distributions, as seen in the figures. However, a large amount of structure still remains and the structure seen in the various ratios must not be due entirely to focusing of muons in the magnetic field and another explanation

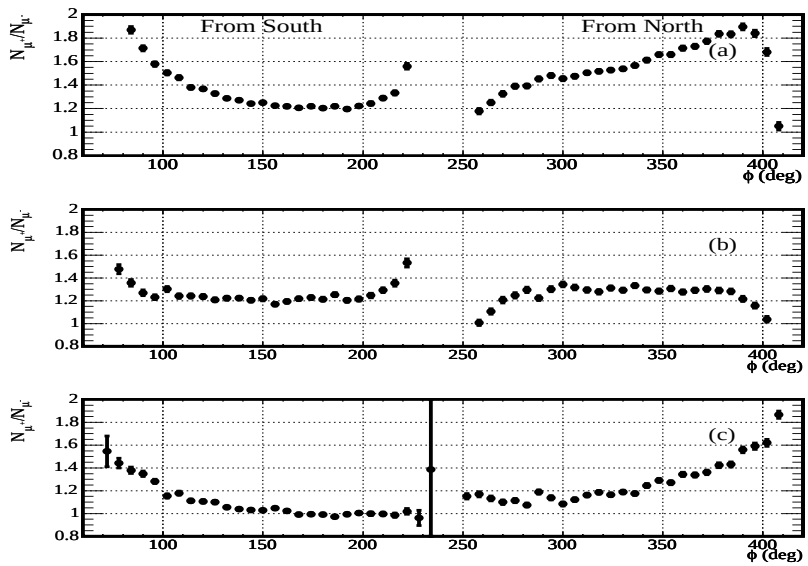


Figure 6.35: The data $N_{\mu^+}/N_{\mu^-}$ ratio for identified $\mu^-$ and $\mu^+$ as a function of $\phi$ (a). The $N_{\mu^+}/N_{\mu^-}$ for the Monte Carlo as a function of $\phi$ is shown in the (b) and the ratio of data $N_{\mu^+}/N_{\mu^-}$ to Monte Carlo $N_{\mu^+}/N_{\mu^-}$ as a function of $\phi$ is shown in (c). (See the caption of Fig. 6.9 for an explanation of the azimuthal values.)

for the structure must be found.

#### 6.5.2.2 Magnetic Field Variations

The map of the MINOS far detector magnetic used in event reconstruction field was generated by finite element analysis and was made before detector construction began. In addition, the standard field map assumes that the magnetic field is exactly the same for each plane in the detector. However, the magnetic field in the detector planes is likely different from the ideal field map as gaps between the steel plates making up each plane and the chemical composition of the steel influences the magnetic field at different points in each plane. These concerns could be a factor in the

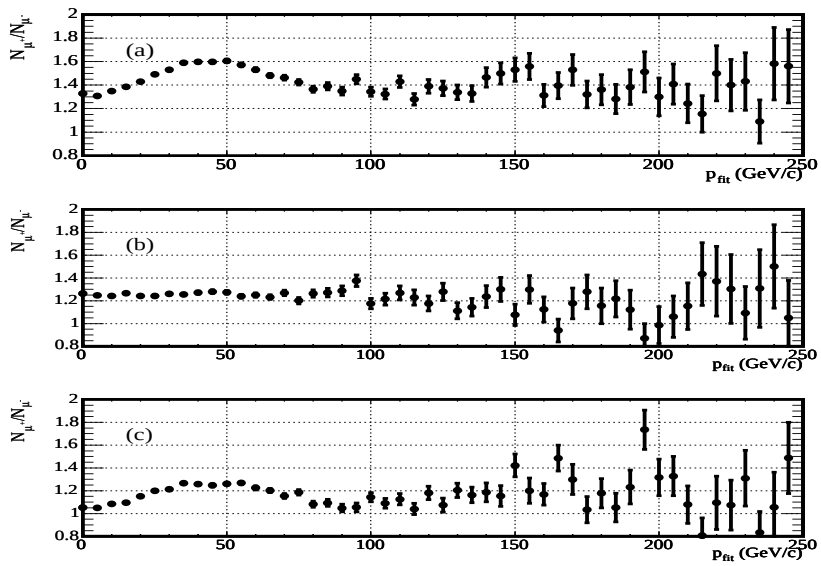


Figure 6.36: The data $N_{\mu^+}/N_{\mu^-}$ ratio for identified $\mu^-$ and $\mu^+$ as a function of $p_{\text{fit}}$ (a). The $N_{\mu^+}/N_{\mu^-}$ for the Monte Carlo as a function of $p_{\text{fit}}$ is shown in (b) and the ratio of data $N_{\mu^+}/N_{\mu^-}$ to Monte Carlo $N_{\mu^+}/N_{\mu^-}$ as a function of $p_{\text{fit}}$ is shown in (c).

peculiar $N_{\mu^+}/N_{\mu^-}$ behavior.

One indication that the magnetic field in the detector may be different from the field map used during reconstruction comes from the comparison of the $(q/p)/\sigma_{q/p}$ distributions for the data and Monte Carlo. The value of $(q/p)/\sigma_{q/p}$ for a track is dependent on all points along the track because of the way the Kalman filter operates. If there were a discrepancy between the magnetic field in the detector and the field map, then the data should have larger values of $(q/p)/\sigma_{q/p}$ than the Monte Carlo because the Monte Carlo tracks are generated with the same field used during reconstruction but the data tracks are not. Fig. 6.37 shows the $(q/p)/\sigma_{q/p}$ distribution for the data as the open circles and the Monte Carlo distribution scaled to have the same number of events as the data is the dotted line. Indeed, the Monte Carlo has

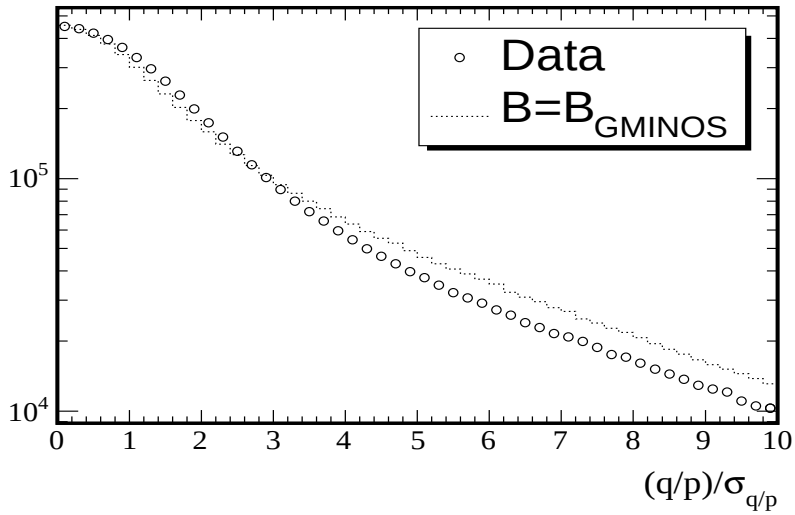


Figure 6.37: Relative error in fit $q/p$ for data and Monte Carlo.

relatively more events for $(q/p)/\sigma_{q/p} > 3$ and fewer events for $(q/p)/\sigma_{q/p} < 2.5$ than the data.

Several tests were done with the Monte Carlo to determine how altering the magnetic field map would affect the reconstruction. The Monte Carlo events were all generated using the standard magnetic field map. The field map used in the reconstruction was systematically altered from the one used to generate the events. The combination of generating and reconstructing Monte Carlo events with different field maps could show behavior similar to what is seen in the data if the magnetic field in the detector were different from the standard field map.

The first tests done changed the field by uniformly increasing and then decreasing the field by 10% for each point in each plane. No plane-to-plane variations were included in these tests. The $(q/p)/\sigma_{q/p}$ distributions for the different combinations

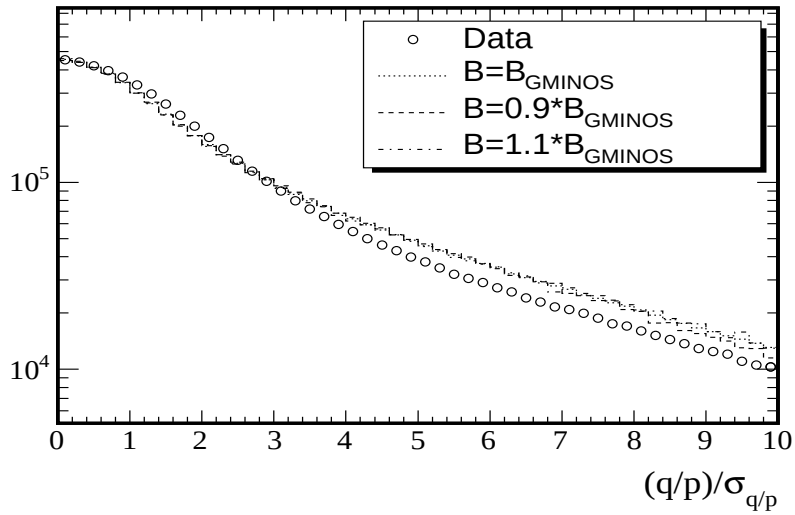


Figure 6.38: Relative error in fit $q/p$ for Monte Carlo events reconstructed with uniformly altered field maps.

of generator and reconstruction maps are shown in Fig. 6.38. The legend in the figure indicates the size of the reconstruction field relative to the size of the field used by GMINOS. The figure shows that changing the reconstruction map in a uniform way does not affect the reconstructed values of $(q/p)/\sigma_{q/p}$ as all the Monte Carlo curves lie on top of each other. A check was made to see if altering the reconstruction map had a predictable effect on the fit $q/p$. This check looked at the distribution of the fit $q/p$ values to see whether the peaks shifted by $\approx \pm 10\%$. Fig. 6.39 shows the $q/p$ distributions for the test fields and the standard field. The peak values for the test fields are different from the standard field by the expected $\approx \pm 10\%$.

Another set of tests altered the field map to account for variations due to gaps between the steel plates making up a plane and variations in the steel chemistry. An

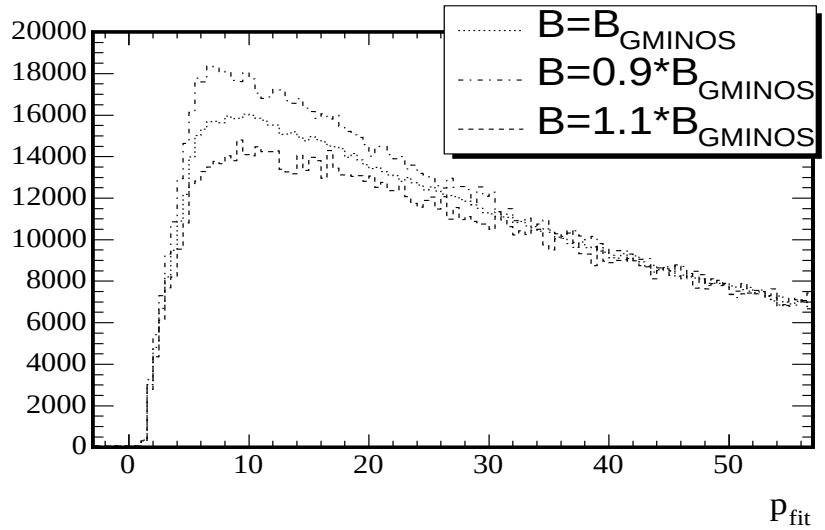


Figure 6.39: Fit $q/p$ for Monte Carlo events reconstructed with uniformly altered field maps.

empirical parameterization to account for the gaps was determined by Jeff Nelson of William and Mary College to be

$$B = \begin{cases} B_0, & (B > B_g) \\ B_0 \left[ 1 - D(1 - \frac{B_0}{B_g})^2 \right], & (B \leq B_g) \end{cases} \tag{6.11}$$

where $B_0$ is the value of the field in the standard map, $D$ is a constant taken to be 0.14 but may vary by as much as 50%, and $B_g$ is the cut off field magnitude given

as 1.6 T. The variations due to steel chemistry are given by

$$B = \begin{cases} B_0, & (B > B_c) \\ B_0\left[1 + G(1 - \frac{B_0}{B_c})\right], & (B_c/3 < B \leq B_c) \\ B_0\left[1 + \frac{2}{3}G\frac{B_0^2}{B_c}\right], & (B \leq B_c/3) \end{cases} \tag{6.12}$$

where $G$ is a constant that can be between $\pm 0.2$ and $B_c$ is the cut off field magnitude of 1.5 T. To include these variations, the magnitude of the field was found for a given $(x, y)$ point in a plane. The field was scaled by the gap correction first, then that value was further scaled by the chemistry correction. The $(x, y)$ components of the field were then set to have the same relative size to one another as in the standard field.

It was found that the field map increased by at least 10% for all points on a plane when $D = 0.14$ and $G = 0.8$, a value well outside the suggested range for $G$. The Monte Carlo events were reconstructed using the field obtained with those parameter values. Additionally, the field map was identical for each plane. Fig. 6.40 shows the resulting distribution for $(q/p)/\sigma_{q/p}$. The data are shown with the open circles. There is very little difference in $(q/p)/\sigma_{q/p}$ between the standard (dotted line) and altered (dash-dot line) field map results.

The results of these tests indicate that changing the magnetic field in the same way for each plane does not produce any major discrepancy between the $(q/p)/\sigma_{q/p}$

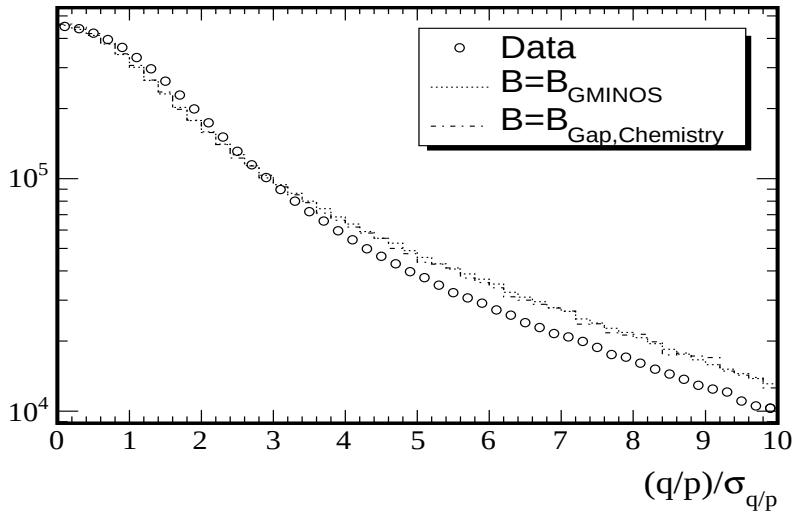


Figure 6.40: Relative error in fit $q/p$ for data (open circles), Monte Carlo with the standard field map (dotted line) and with the field map varied according to eq (6.11) and (6.12) (dash-dot line) with $D = 0.14, G = 0.8$.

distributions obtained for the standard field map.

Further tests were made by changing the magnetic field on selected planes. For these tests the standard field was altered by 5% on 10% of the planes in the detector, those planes being chosen randomly throughout the detector. The first test lowered the field by 5% in the chosen planes while the second test raised the field by the same amount. The results are shown in Fig. 6.41. The data are again shown with open circles and the standard field map Monte Carlo is shown with the dotted line. The results for the test with 10% of the planes having the field reduced by 5% is shown with the dot-dash line. This test reproduces the data distribution very well for $(q/p)/\sigma_{q/p} < 6$ but has many more events at higher values of $(q/p)/\sigma_{q/p}$ than the data. The test with the field increased by 5% is shown with the dashed line,

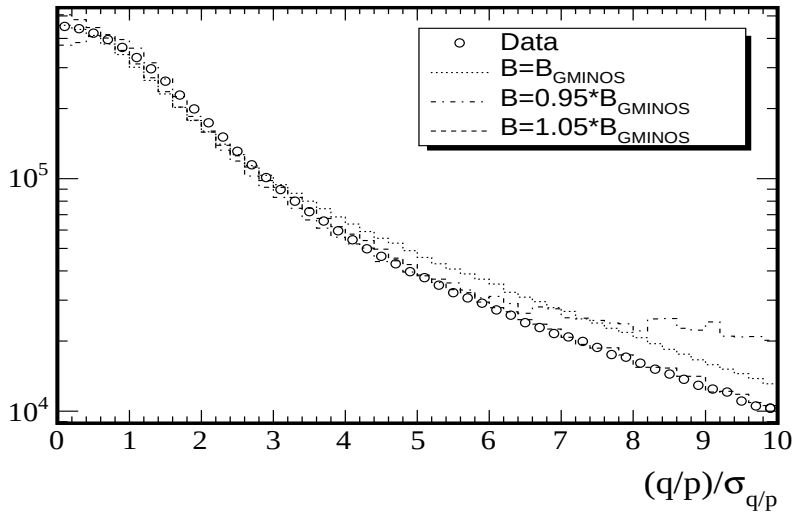


Figure 6.41: Relative error in fit $q/p$ for data (open circles), Monte Carlo with the standard field map (dotted line) and with the field map varied by $\pm 5\%$ for 10% of the planes (dot-dash and dashed lines).

which reproduces the data distribution very well over the entire range of $(q/p)/\sigma_{q/p}$ shown. These tests suggest that the magnetic field in the detector is different from the standard field map for some fraction of the planes.

## 6.6 Summary

The cosmic ray muon analysis presented in this chapter has distinguished those aspects of the detector and reconstruction that are well-understood from those that are not. The detector efficiency and acceptance are both well-understood given the excellent fit of the measured single muon vertical intensity to the parameterization of both the MACRO collaboration in eq (6.7) and the global parameterization of

Crouch in eq (6.8).

One area of the analysis that needs to be improved is the generation of cosmic ray muon events. The current Monte Carlo generator does not reproduce the data $\cos\theta$ and $\phi$ distributions well due to its approximation of the energy distribution of the muons on the surface and the fact that it does not propagate the muons through rock to the detector, as shown in § 6.3. Work is in progress to use models that generate the muons in the atmosphere and propagate them to the surface. From that point, the new Monte Carlo will propagate the muons through the rock using a package such as GEANT which provides a more accurate model of energy loss in the rock.

The area of the analysis that is least understood is the charge sign determination, as seen in § 6.5. The data show peculiar structure in the $N_{\mu^+}/N_{\mu^-}$ ratio as a function of $\cos\theta$, $\phi$ and $p_{\text{fit}}$. The Monte Carlo events were used to look for biases that could explain the structure seen in the data. A bias was found in the Monte Carlo events where muons with the charge sign and direction combination to be focused in the magnetic field have their charge correctly assigned more often than muons that are defocused. The bias is most pronounced in events with high momentum, short track lengths, or values of $(q/p)/\sigma_{q/p} < 2.5$. It should be possible to remove the bias due to focusing by dividing the data $N_{\mu^+}/N_{\mu^-}$ ratios by the Monte Carlo $N_{\mu^+}/N_{\mu^-}$ ratios. Doing so does not remove all the structure seen in the data $N_{\mu^+}/N_{\mu^-}$ ratios suggesting that some of this structure is due to something other than focusing effects.

Several tests were done to see how altering the magnetic field used in reconstruc-

tion from that used in the Monte Carlo event generation in various systematic ways affected the charge sign determination. Altering the field in the same for each plane of the detector has no effect on the charge sign determination. However, altering the field map used in reconstruction for only a fraction of the planes in the detector does affect the charge sign determination. In fact the Monte Carlo events can be made to reproduce the data $(q/p)/\sigma_{q/p}$ distribution if 10% of the planes in the detector have a magnetic field that is 5% higher than the nominal field. This result may indicate the origin of the structure seen in the data ratios of Fig. 6.24.

# Chapter 7

# Atmospheric $\nu$ Event Rates

## 7.1 Introduction

To detect an oscillation signal in the atmospheric neutrinos requires comparing the observed number to the expected number. Both physical effects and detector-related effects are important to understand in the calculation of the expected signal. The physical effects that influence the expected number of neutrinos are dominated by the expected rates of neutrinos from the cosmic ray interactions and the neutrino interaction cross-sections. The latter is also important when trying to understand differences between neutrinos and anti-neutrinos. The detector related effects were discussed in § 6.2.

## 7.2 Atmospheric $\nu$ Flux Calculations

Gaisser and Honda [4] calculate the neutrino flux for neutrino flavor $\alpha$ from cosmic ray interactions in the atmosphere as

$$\phi_{\nu_\alpha} = \phi_p \otimes R_p \otimes Y_{p\to\nu_\alpha} + \sum_A \phi_A \otimes R_A \otimes Y_{A\to\nu_\alpha}, \tag{7.1}$$

where $\phi_{p(A)}$ is the flux of primary protons (nuclei of mass A) from outside the geomagnetic field, $R_{p(A)}$ represents the filtering of low energy particles by the geomagnetic field, and $Y_{p(A)}$ is the yield of neutrinos per primary proton (nucleus of mass A). The geomagnetic field typically prevents cosmic ray primaries with energies below the threshold energy from entering the atmosphere and interacting. The threshold energy for this process varies with the detector's geomagnetic latitude, with the threshold decreasing with increasing geomagentic latitude.

As described in Chapter 3, the atmospheric neutrinos come primarily from two body decays of charged pions and kaons into muons, and the subsequent muon decays. Eq (3.16) and (3.18) show that if all particles were to decay

$$\begin{aligned} \frac{N_{\nu_\mu} + N_{\overline{\nu}_\mu}}{N_{\nu_e} + N_{\overline{\nu}_e}} &\sim 2, \\ \frac{N_{\nu_\mu}}{N_{\overline{\nu}_\mu}} &\sim 1 \text{ and} \\ \frac{N_{\nu_e}}{N_{\overline{\nu}_e}} &\sim \frac{N_{\mu^+}}{N_{\mu^-}}. \end{aligned} \tag{7.2}$$

Thus the charge ratio of cosmic ray muons constrains the ratio of $N_{\nu_e}$ to $N_{\overline{\nu}_e}$. The flux of $\nu_\mu$ and $\overline{\nu}_\mu$ are approximately the same because the meson decay produces a $\nu_\mu$ while the subsequent muon decay produces a $\overline{\nu}_\mu$. Further, the kinematics of the $\pi$ and $\mu$ decay results in same amount of energy being carried on average by each neutrino in the decay chain [4].

### 7.2.1 Analytic Approximations of the Atmospheric $\nu$ Flux

At neutrino energies much greater than 1 GeV, an analytic approximation for determining the neutrino flux can be used [4]. This approximation holds for a power-law primary energy spectrum and assumes inclusive cross sections that obey Feynman scaling in the fragmentation region. The differential flux for the primary nucleons, $\mathcal{N}$, of energy $E_0$ is

$$\frac{dN_{\mathcal{N}}}{dE_0} \equiv \phi_{\mathcal{N}}(E_0) = A \times E_0^{-(\gamma+1)}. \tag{7.3}$$

The spectral index is $\gamma = 1.70$ and $A = 1.8$ [38]. The differential flux for $\nu_\mu + \overline{\nu}_\mu$ is proportional to the primary nucleon spectrum evaluated at the neutrino energy, $E_\nu$ and is given by [4]

$$\frac{dN_\nu}{dE_\nu} \equiv \phi_\nu(E_\nu) = \frac{\phi_{\mathcal{N}}(E_\nu)}{(1 - Z_{\mathcal{N}\mathcal{N}})(\gamma+1)} \left[ \frac{Z_{\mathcal{N}\pi}(1-r_\pi)^\gamma}{1 + B_{\mathcal{N}\pi}(E_\nu/\epsilon_\pi)\cos\theta} \right] + 0.635 \left[ \frac{Z_{\mathcal{N}K}(1-r_K)^\gamma}{1 + B_{\mathcal{N}K}(E_\nu/\epsilon_K)\cos\theta} \right], \tag{7.4}$$

where $r_i$, for $i = \pi, K$, are the squares of the ratio of the muon mass to the $\pi$ or $K$ mass. The angle $\theta$ is the zenith angle of the meson. The $B_{\mathcal{N}i}$ are constants defined

by [38]

$$B_{\mathcal{N}i} \equiv \left(\frac{\gamma+2}{\gamma+1}\right)\left(\frac{1}{1-r_i}\right)\left(\frac{\Lambda_i - \Lambda_{\mathcal{N}}}{\Lambda_i \ln(\Lambda_i/\Lambda_{\mathcal{N}})}\right), \tag{7.5}$$

where $\Lambda_i$ is the attenuation length of meson $i$ in the atmosphere and $\Lambda_{\mathcal{N}}$ is the attenuation length of the primary nucleon. The $\epsilon_i$ are the "critical" energies (measured in GeV) below which decay of the meson and its energy loss in the atmosphere can be neglected [38]. The $Z_{\mathcal{N}i}$ are called spectrum-weighted moments and contain the physics of the parent $\pi$ and $K$ production. Define the normalized inclusive cross section for the reaction

$$\mathcal{N} + \text{air} \longrightarrow \pi^{\pm} + X, \tag{7.6}$$

as

$$F_{\mathcal{N}i}(E_i, E_{\mathcal{N}}) = \frac{E_i}{\sigma_{\mathcal{N}}}\frac{d\sigma_{\mathcal{N}}(E_i, E_{\mathcal{N}})}{dE_i} \approx c_i^{+}(1-x_i)^{p_i^{+}} + c_i^{-}(1-x_i)^{p_i^{-}} \equiv F_{\mathcal{N}i}(x_i), \tag{7.7}$$

where $x_i = E_i/E_{\mathcal{N}}$ and the $c_i^{+(-)}$ and $p_i^{+(-)}$ are constants that depend on which meson decays. In eq (7.7) $\sigma_{\mathcal{N}}$ is the cross section for the incoming nucleon to collide with an air nucleus. Then the $Z_{\mathcal{N}i}$ factors are

$$Z_{\mathcal{N}\to i} = \int_0^1 dx (x)^{\gamma-1} F_{\mathcal{N}i}(x). \tag{7.8}$$

The values of the parameters for eq (7.4) and eq (7.7) are given in Table 7.1. The approximation of eq (7.4) becomes increasingly accurate as the neutrino energy in-

Table 7.1: Example values for the parameters in eq (7.4) and eq (7.7) [4]

| | |
|---|---|
| $\gamma$ | 1.70 |
| $A$ | 1.8 $\mathrm{cm}^{-2}\mathrm{s}^{-1}\mathrm{sr}^{-1}(\mathrm{GeV})^{\gamma}$ |
| $r_i$ | 0.573 ($\pi$), 0.046 ($K$) |
| $B_{\mathcal{N}i}$ | 2.77 ($\pi$), 1.18 ($K$) |
| $\epsilon_i$ | 115 GeV ($\pi$), 850 GeV ($K$) |
| $Z_{\mathcal{N}\mathcal{N}}$ | 0.30 |
| $Z_{\mathcal{N}i}$ | 0.079 ($\pi$), 0.0118 ($K$) |
| $c^+$ | 0.92 ($\pi$), 0.037 ($K$) |
| $c^-$ | 0.81 ($\pi$), 0.045 ($K$) |
| $p^+$ | 4.1 ($\pi$), 0.87 ($K$) |
| $p^-$ | 4.8 ($\pi$), 3.5 ($K$) |

creases away from 1 GeV. Other points to note are that the angular and energy dependence of neutrinos from the decay of $\pi$'s and $K$'s are determined by the competition between decay and interaction in the atmosphere of the parent meson. Eq (7.4) shows that when $E_\nu \ll \epsilon_i/\cos\theta$, the neutrino spectrum follows approximately the same power as the production spectrum of the parent meson. However, when $E_\nu \gg \epsilon_i/\cos\theta$, the power law is one power of $E_\nu$ steeper and proportional to $\sec\theta$. Table 7.1 shows that $\epsilon_K > \epsilon_\pi$, which means that the spectrum of neutrinos from $\pi$ decay steepens before the spectrum from $K$ decay. Thus the $K$'s become increasingly important as the energy increases. Fig. 7.1 shows the relative contributions of $\pi$'s and $K$'s to the atmospheric neutrino and cosmic ray muon fluxes as a function of energy [4]. For $\pi$'s the solid curve represents events coming from the vertical and the dashed curve is for events with $\cos\theta = 0.5$. The opposite is true for $K$'s. Another effect that makes the contribution from $K$'s more important at high energies are the decay kinematics. In the $\pi \to \mu\nu$ decay most of the $\pi$ energy goes to

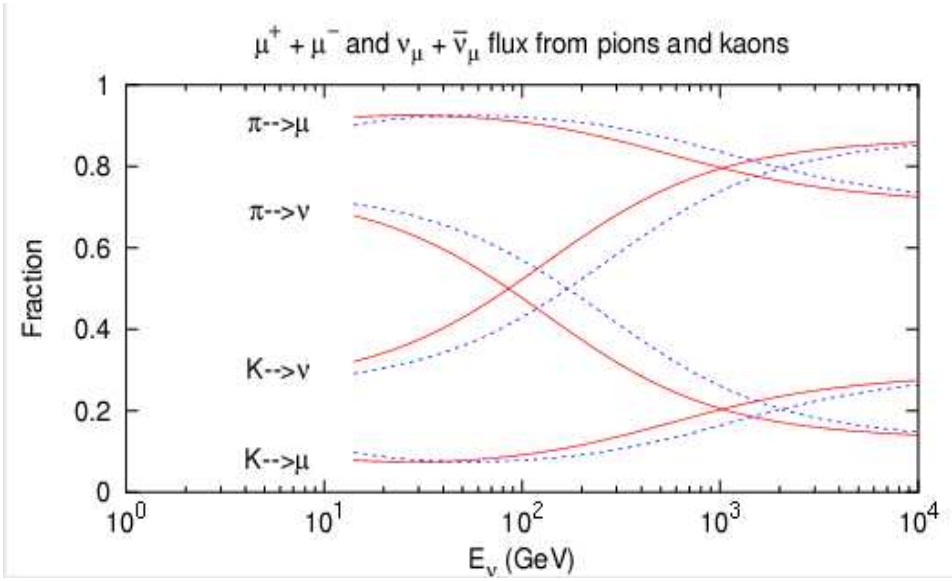


Figure 7.1: Relative contributions of $\pi$'s and $K$'s to atmospheric neutrinos and cosmic ray muons [4]. For $\pi$'s the solid curve represents events coming from the vertical and the dashed curve is for events with $\cos\theta = 0.5$. The opposite is true for $K$'s.

the muon instead of the neutrino, where in the $K \to \mu\nu$ decay the energy is equally divided between the two. In fact, the $K$'s are the major source of neutrinos with energies above 100 GeV as seen in the figure [4].

The fluxes for $\nu_e, \overline{\nu}_e, \nu_\mu$, and $\overline{\nu}_\mu$ as a function of the cosine of the zenith angle and energy are shown in Fig. 7.2. From top to bottom, the three sets of curves correspond to neutrino energies of 1, 10, and 100 GeV, respectively. The fluxes used to generate the figure are the Bartol 1996 (BARTOL96) flux values [46]. Comparing the $\nu_\mu(\overline{\nu}_\mu)$ curves to the $\nu_e(\overline{\nu}_e)$ curves in the figure shows that the $N_{\nu_\mu(\overline{\nu}_\mu)}/N_{\nu_e(\overline{\nu}_e)}$ ratio increases with increasing energy. Also notice how the $\nu_e$ and $\nu_\mu$ spectra decrease toward the zenith at low energies. At high energies the spectra decrease quite rapidly near the horizon and then begin to flatten out toward the zenith. These trends are the result

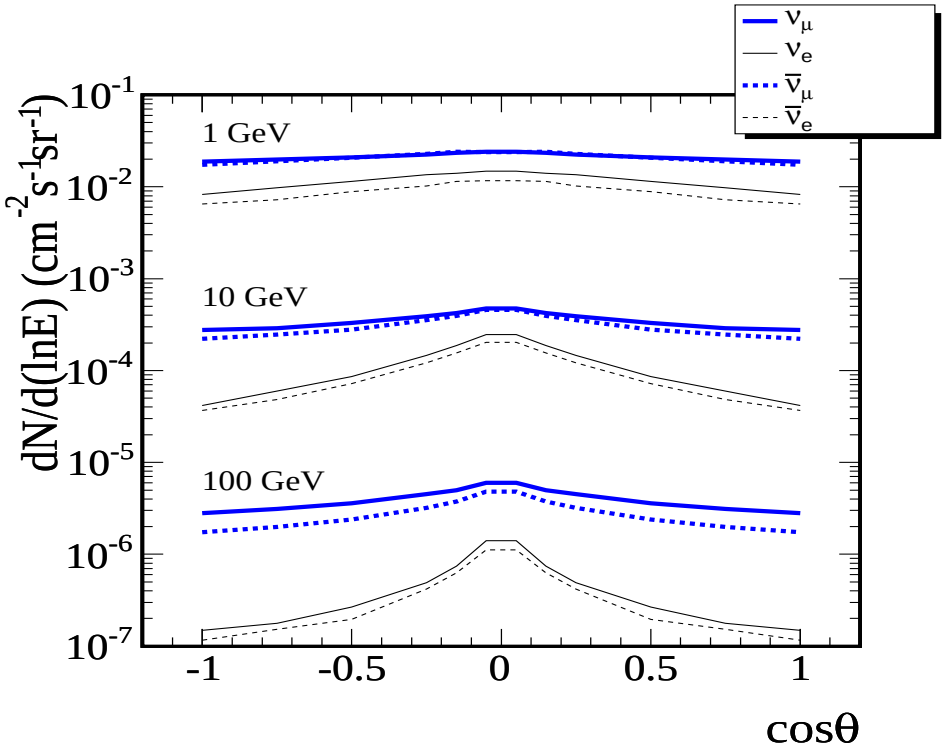


Figure 7.2: Zenith angle dependence of the atmospheric neutrino flux. The three sets of curves correspond from top to bottom to neutrino energies of 1 GeV, 10 GeV, and 100 GeV.

of the high energy muons ($E >$ several GeV) reaching the ground before decaying [4].

### 7.2.2 Uncertainties in the Calculations

The largest sources of uncertainty in the neutrino flux models come from the primary spectrum and hadronic interaction models, and are documented in [4]. The following is a summary of the discussion in that reference. Recent measurements allow for an estimate of the uncertainty in the primary spectrum of $\pm 5\%$ below 100 GeV/nucleon which increases to $\pm 10\%$ at 10 TeV/nucleon. However, a more conservative estimate using all the available data gives uncertainties of $\pm 20\%$ below 100 GeV/nucleon and $\pm 30\%$ above. The uncertainties due to the hadronic interactions result mainly from the lack of measurements for high momentum primary particles. The current data imply an uncertainty due to hadronic interactions of 20-25%. Combining the uncertainties from hadronic interactions and the primary spectrum, the overall theoretical uncertainty is $\pm$20-25% for lower energy ($E_\nu < 10$ GeV) neutrino interactions and somewhat larger for higher energy neutrinos.

Another source of uncertainty, although a small one, comes from the assumption made in the calculations that the Earth has a constant surface height at sea level. In reality detectors may be located under high mountains. Mesons that enter the ground above the detector before decaying lose energy very quickly through ionization and nuclear interactions, producing very low energy neutrinos. The detectors that are under mountains observe a reduced neutrino flux because the low energy neutrinos

do not produce interactions visible in the detector. The effect is typically only important near the vertical and only for decay products of muons [4]. A small source of uncertainty also comes from the assumption in the calculations that the atmosphere has a uniform scale height. The atmosphere varies according to seasonal effects which impacts the number of muons surviving to the surface because higher densities make muon interactions in the air more probable. However, as the neutrinos come mostly from the decay of the mesons, the varying atmosphere should only have a small effect on neutrinos. Both of these sources of uncertainty are at the few percent level [47].

## 7.3 Analytic Approximations of the Neutrino Production Heights

The point in the atmosphere where a neutrino is produced is called its "production height". The survival probability for a neutrino with flavor $\alpha$ to be detected before oscillating to flavor $\beta$ depends on the distance traveled by the neutrino from its point of origin to its interaction point, as seen in eq (2.23). For a neutrino coming from below the detector's horizon the total distance traveled by the neutrino is the sum of its production height in the atmosphere and the path length through the Earth. The production height is small compared to the distance it travels through the Earth for $\cos\theta \lesssim -0.4$ and the production height has little effect on its survival

Table 7.2: Values for the parameters in eq (7.9) and eq (7.10) [5]

| | |
|---|---|
| $\lambda_{\mathcal{N}}$ | 86 g/cm$^2$ |
| $\Lambda_{\mathcal{N}}$ | 120 g/cm$^2$ |
| $b_{\mathcal{N}K} \times Z_{\mathcal{N}K}$ | 0.0075 |
| $X_0$ | 1030 g/cm$^2$ |
| $h_0$ | 6.4 km |

probability. Neutrinos coming from above the detector's horizon travel a distance that is dominated by the production height. An analytic approximation to the production height for atmospheric neutrinos coming from above a detector's horizon is given in Ref. [5] and the results are summarized here.

The integral flux of neutrinos with $E_\nu \ll \epsilon_\pi$ produced by pion decay in the atmosphere can be expressed as a function of the the atmospheric depth, $X$, which has units of g/cm$^2$. The integral flux as a function of atmospheric depth is

$$\frac{dN(E_\nu)}{dX} = (1 - r_\pi)^{-\gamma} \frac{Z_{\mathcal{N}\pi}}{\lambda_{\mathcal{N}}} \exp(-X/\Lambda_{\mathcal{N}}) \frac{A}{\gamma(\gamma+1)} E_\nu^{-\gamma} \equiv C \times E_\nu^{-\gamma}, \tag{7.9}$$

where $\lambda_{\mathcal{N}}$ is the interaction length for nucleons and the remaining variables were defined in § 7.2.1. Table 7.2 gives the values of the parameters used in eq (7.9). The flux for neutrinos produced by kaon decay is similar to eq (7.9) with $r_\pi$ and $Z_{\mathcal{N}\pi}$ replaced by $r_K$ and $Z_{\mathcal{N}K}$. The expression for the $\nu$ flux from $K$ decay must be weighted by a factor of $b_K \times Z_{\mathcal{N}K}$, where $b_K$ is the branching ratio for $K \to \mu$ decay. The slant depth, $X$, where the pion (kaon) is produced and decays as a function of the cosine of the zenith angle $\theta$ and the production height $l$ is given by approximating

the atmosphere to have an exponential density structure,

$$X(\cos\theta, l) = \frac{X_0}{\cos\theta}\exp\left(-\frac{l\cos\theta}{h_0}\right), \tag{7.10}$$

where $X_0$ is the total vertical thickness and $h_0$ is the scale height for the exponential atmosphere in km. For values of $\theta > 70°$, the curvature of the earth must be taken into account and an effective value of $\cos\theta$ must be used. Finding $dX/dl$ and using the result in eq (7.9) gives the flux as a function of the production height,

$$\frac{dN_{\nu,i}(E_\nu)}{dl} = \frac{CX_0}{h_0}E_\nu^{-\gamma}\exp\left(-\frac{X}{\Lambda_{\mathcal{N}}}\right)\exp\left(-\frac{l\cos\theta}{h_0}\right). \tag{7.11}$$

In eq (7.11), $X$ is to be evaluated using eq (7.10).

The flux of neutrinos coming from muon decay is more complicated because the muons in the multi-GeV energy range have longer lifetimes than pions and kaons, and therefore will lose energy before decaying. The approximate expression for the flux of neutrinos from muon decay as a function of the production height $l$ is [5]

$$\frac{dN_{\mu\to\nu}(>E_\nu)}{dl} \approx \frac{C_\mu A\mathcal{B}}{(\gamma+1)(2E_\nu)^{(\gamma+1)}}\frac{\mu c^2}{c\tau_\mu}\frac{X}{\lambda_{\mathcal{N}}}\int_0^1 dz z^\rho \exp\left(-\frac{Xz}{\Lambda_{\mathcal{N}}}\right)\left(1+\frac{\Upsilon X}{2E_\nu}[1-z]\right)^{-(\rho+\gamma+1)}, \tag{7.12}$$

where $C_\mu$ is a normalization factor obtained by a fit to Monte Carlo results, $\tau_\mu$ is the muon lifetime, $z$ is the fractional height of the atmosphere and $\Upsilon$ accounts for muon

energy loss. The factor $\mathcal{B}$ is

$$\mathcal{B} = \frac{1}{\gamma+1}\left(\frac{1-r_\pi^{(\gamma+1)}}{1-r_\pi} Z_{\mathcal{N}\pi} + b_K \frac{1-r_K^{(\gamma+1)}}{1-r_K} Z_{\mathcal{N}K}\right), \tag{7.13}$$

and the value of $\rho$ is given by [5]

$$\rho = \frac{h_0}{c\tau_\mu \cos\theta} \frac{\mu c^2}{E_\mu + \Upsilon X}. \tag{7.14}$$

The relative contributions of $\pi/K$ and $\mu$ decay to the atmospheric $\nu_\mu$ and $\overline{\nu}_\mu$ flux as a function of $\cos\theta$ [5] are shown in Fig. 7.3. The figure shows the contributions for 3 ranges of neutrino energy, $E_\nu$, $0.3 < E_\nu < 2$ GeV (top left), $2 < E_\nu < 20$ GeV (top right), and $E_\nu > 20$ GeV (bottom left). The contributions from $\mu$ decay decreases with larger values of $\cos\theta$ as even the high energy muons decay in cascades in the horizontal direction. Also the $\pi/K$ contribution dominates except near the horizon for neutrinos with $E_\nu < 20$ GeV.

The production heights in km for $\nu_\mu$ and $\overline{\nu}_\mu$ as a function of $\cos\theta$ [5] are shown in Fig. 7.4. The production heights are symmetric in $\cos\theta$ about $\cos\theta = 0$ so that the production height for $\nu_\mu$ at $\cos\theta = 1$ is the same as the height for $\cos\theta = -1$. The figure shows production heights for three different ranges in $E_\nu$, $0.3 < E_\nu < 2$ GeV (open triangles), $2 < E_\nu < 20$ GeV (open squares), and $E_\nu > 20$ GeV (open circles). The uncertainties shown are the widths of the production distributions [5]. The production heights from pion and kaon decay are shown in the top plot, those from

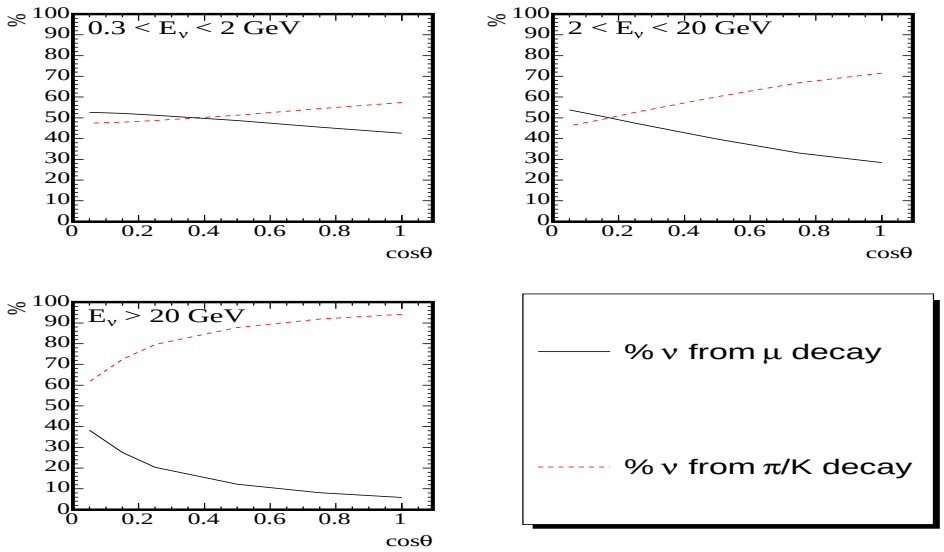


Figure 7.3: Fraction of atmospheric $\nu_\mu$ and $\overline{\nu}_\mu$ from $\pi/K$ (dashed line) and $\mu$ (solid line) decay. Three neutrino energy ranges are shown, $0.3 < E_\nu < 2$ GeV (top left), $2 < E_\nu < 20$ GeV (top right), and $E_\nu > 20$ GeV (bottom left).

muon decay are in the bottom plot. The production heights for the neutrinos from $\mu$ decay have a strong dependence on energy because the $\mu$ lifetime increases with energy in the lab reference frame. There is not a strong energy dependence on the neutrino production height for neutrinos from $\pi/K$ decays as those particles decay almost as soon as they are produced. The values shown in the figure are good to within $\sim 10\%$ [5].

The average distance traversed by $\nu_\mu$ producing the neutrino-induced muon events as a function of $\cos\theta$ is shown in Fig. 7.5. Fig. 7.5 was made using the NUANCE [48] neutrino generator and BARTOL96 fluxes. I chose this generator for the MINOS neutrino-induced analysis because it has been used by other experiments and is actively maintained. Also, it has the advantages of recording the energy and trajectory

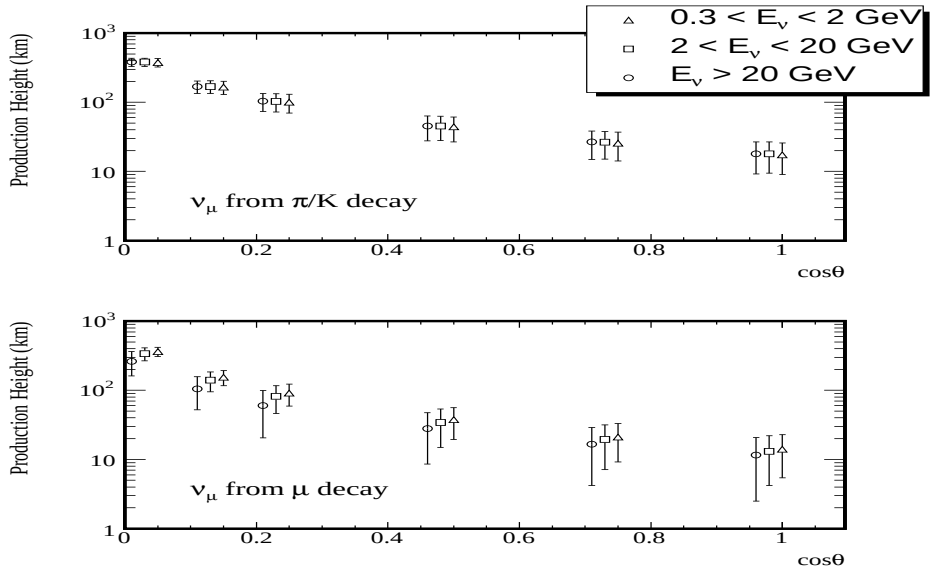


Figure 7.4: Production heights for neutrinos from $\pi/K$ decays (top) and $\mu$ decays (bottom). The heights for 3 different neutrino energy ranges are shown.

of each parent neutrino, being able to mimic simple detector geometries and producing neutrino events for specified exposure lengths.

## 7.4 Neutrino Cross Sections

The neutrinos that interact in the rock surrounding the MINOS detector and produce muons have energies ranging between $\sim$ 1 GeV and several TeV. Fig. 7.6 shows the neutrino energy distribution for these neutrinos and like Fig. 7.5 was made using the NUANCE neutrino generator and BARTOL96 fluxes. The distributions in the figure are divided into two classes, low momentum events with the neutrino-induced muon momentum <10 GeV/c and high momentum events with momentum $\geq$10 GeV/c. The low and high momentum events correspond to the stopping and through-

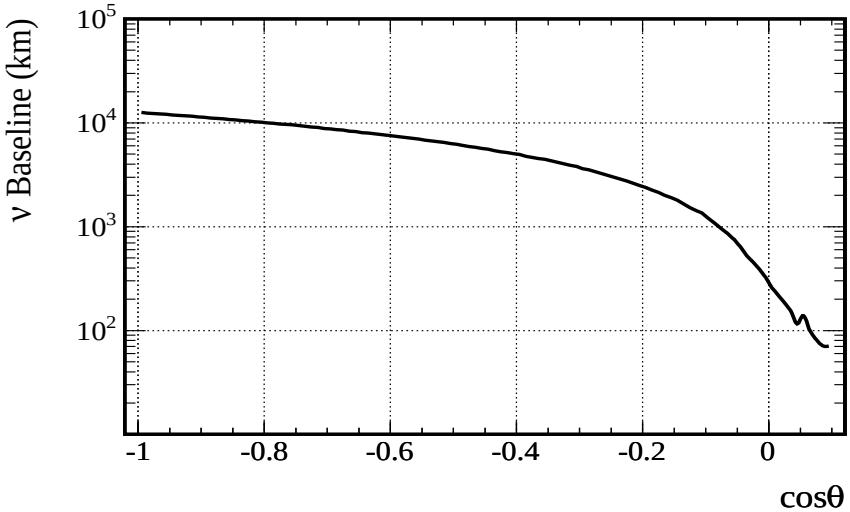


Figure 7.5: The average baseline traveled by $\nu_\mu$ producing neutrino-induced muons as a function of $\cos\theta$.

going neutrino-induced muons discussed in § 3.5.2. This analysis uses momentum separation rather than then "stopping" and "through-going" distinctions because the MINOS magnetic field provides good momentum resolution for all events in the low momentum sample, even for those events that exit the detector.

The total cross section for a neutrino interaction is the combination of three main classes of interactions: elastic scattering (ES), single pion production ($1\pi$) and deep inelastic scattering (DIS) which produces multiple pions. That is,

$$\sigma_{total} = \sigma_{elastic} + \sigma_{1\pi} + \sigma_{DIS}. \tag{7.15}$$

Fig. 7.7 shows the various neutrino interaction cross sections for charged and neutral current interactions for both neutrinos and anti-neutrinos. The total cross sections

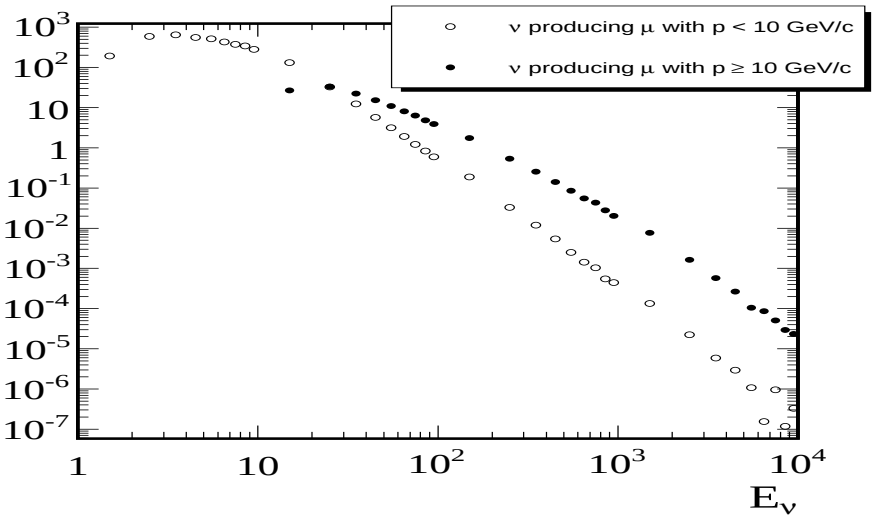


Figure 7.6: Distribution of energies for neutrinos producing upward-going and horizontal muons for low and high momentum muons.

are the solid lines, the elastic scattering cross sections are the dotted lines, and the single pion cross sections are the dashed lines. The contribution from DIS is the difference between the total cross section and the sum of the ES and $1\pi$ contributions. For energies above $\sim$5 GeV, the DIS cross section dominates. Fig. 7.6 shows that the neutrinos producing the neutrino-induced muons typically have $E_\nu > 3$ GeV, indicating that these muons are generally the result of DIS interactions. Fig. 7.8 shows the ratio of the total CC cross sections to the neutrino energy for $\nu$ and $\overline{\nu}$ as a function of neutrino energy [3]. The uncertainties shown in the figure include both statistical and systematic uncertainties. The dashed lines are the averaged values over all experiments. The average for $\nu$ is $0.677 \pm 0.014$ and for $\overline{\nu}$ the average is $0.334 \pm 0.008$ [3].

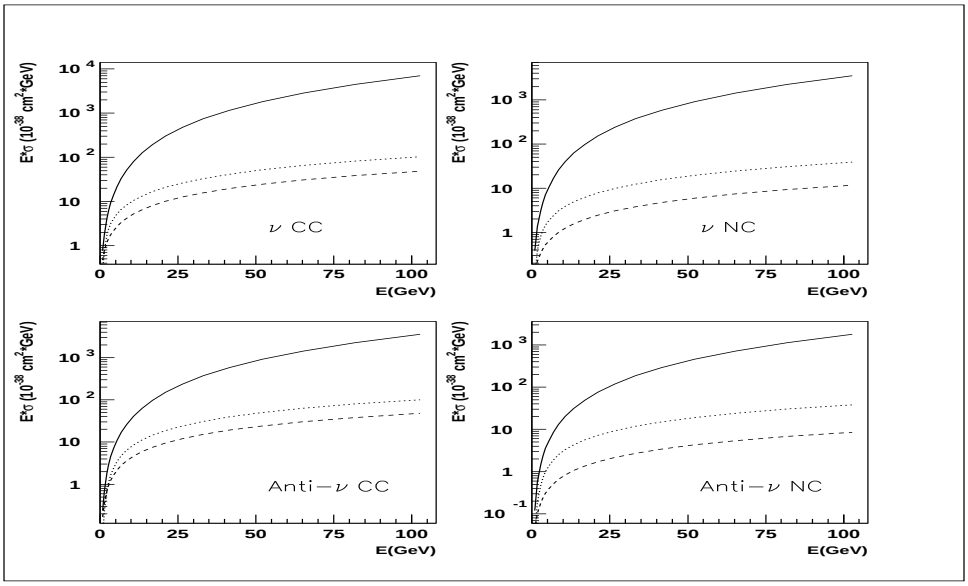


Figure 7.7: Neutrino and anti-neutrino cross sections. Total cross sections are the solid lines, the single pion cross sections are the dashed lines and quasi-elastic cross sections are the dotted lines. This figure was made by Hugh Gallagher using the NEUGEN neutrino interaction generator.

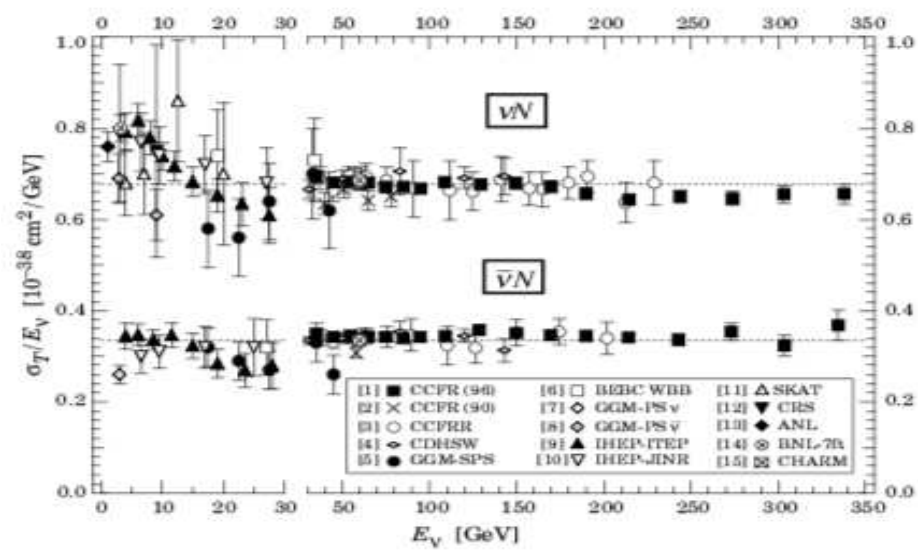


Figure 7.8: The ratio of the total CC cross sections to the neutrino energy for $\nu$ and $\overline{\nu}$ as a function of neutrino energy [3]. The average for cross sections are shown by the dashed lines with the average for $\nu$ being $0.677 \pm 0.014$ and for $\overline{\nu}$ the average is $0.334 \pm 0.008$ [3].

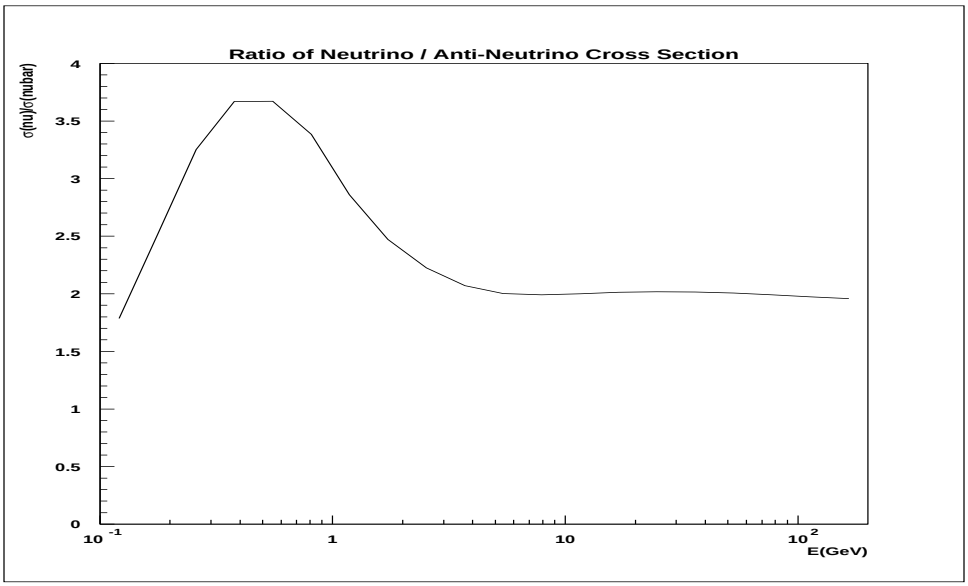


Figure 7.9: Ratio of neutrino to anti-neutrino cross sections. This figure was made by Hugh Gallagher using the NEUGEN neutrino interaction generator.

One important consideration for determination of the relative $\nu_\mu$ and $\overline{\nu}_\mu$ fluxes is the ratio of the neutrino and anti-neutrino cross sections since the uncertainty in this ratio directly affects the predicted number of neutrino-induced $\mu^-$ and $\mu^+$ in the detector. Fig. 7.8 shows that the neutrino cross sections are larger than the average for energies near 1 GeV, while the anti-neutrino cross sections remain at the average value. Fig. 7.9 shows the ratio of the neutrino to anti-neutrino cross sections made using the NEUGEN generator. For neutrino energies $E_\nu < 1$ GeV, the ratio of the cross sections varies considerably, peaking near 3.5 at $E_\nu \sim 0.8$ GeV. However, for $E_\nu \geq 3$ GeV, the ratio flattens to 2. The analysis of neutrino-induced muons should be relatively free from uncertainties due to this varying cross section ratio as $E_\nu > 3$ GeV.

# Chapter 8

# Neutrino Oscillation Analysis

## 8.1 Identifying Neutrino-Induced Upward-going and Horizontal Muons

Neutrino-induced muons observed in the MINOS far detector can come either from below the detector's horizon or slightly above it. Neutrino-induced muons coming from below the detector's horizon are called upward-going muons and those coming from along or slightly above the horizon are called horizontal muons. Identifying the direction of the muon's trajectory is important in identifying both types of events. The identification of upward-going muons also requires the determination of how the timing of hits along the track changes as a function of their $y$-position. For the horizontal muon selection, a knowledge of the rock surrounding the detector is also

necessary. The data used to find the neutrino-induced upward-going and horizontal muons come from both the SM1 and SM1+SM2 data sets. The muons comprising the SM1 data set come from September, 2002 through May, 2003. The muons in the SM1 set are those events that passed the cuts listed in Table 6.1 based only on the parts of the events observed in SM1. All events passing the cuts in Table 6.1 were used in the SM1+SM2 data set, which was taken from July, 2003 through April 2004. The SM1 data set represents 138 live days while the SM1+SM2 data set represents 231 live days.

### 8.1.1 Upward-Going Muons

Five additional cuts are applied to the events passing the cuts of Table 6.1 to select the upward-going muons and these cuts are listed in Table 8.1. The "Directional Consistency" cut (6) removes events in which the timing information indicates the track is upward-going (downward-going) but the fit trajectory at the vertex shows it is downward-going (upward-going). The events failing this cut do not have reliable tracking information and cannot be labeled as upward-going or downward-going with confidence. The next cut (7) checks the goodness of the fit of the time versus the $y$-position of the hits along the track to eliminate tracks with poor fits to $dt/dy$. The cut value of $\chi^2/ndf < 3$ was empirically determined. The $\chi^2/ndf$ distribution used to determine the cut on the fit to $dt/dy$ is shown in Fig. 8.1. As determined from the figure, this cut filters out only 1.1% of the total events. Events that are

Table 8.1: Cuts used to select upward-going events.

| Cut | Name | Events Passing Cumulative Cuts |
|---|---|---|
| 6 | Directional Consistency | 5492933 (68.2%) |
| 7 | $\chi^2_{dt/dy}/ndf$ | 5400541 (67.1%) |
| 8 | Double Ended Strips | 5399508 (67.1%) |
| 9 | $dt/dy$ | 45 |
| 10 | $1/\beta$ | 39 |

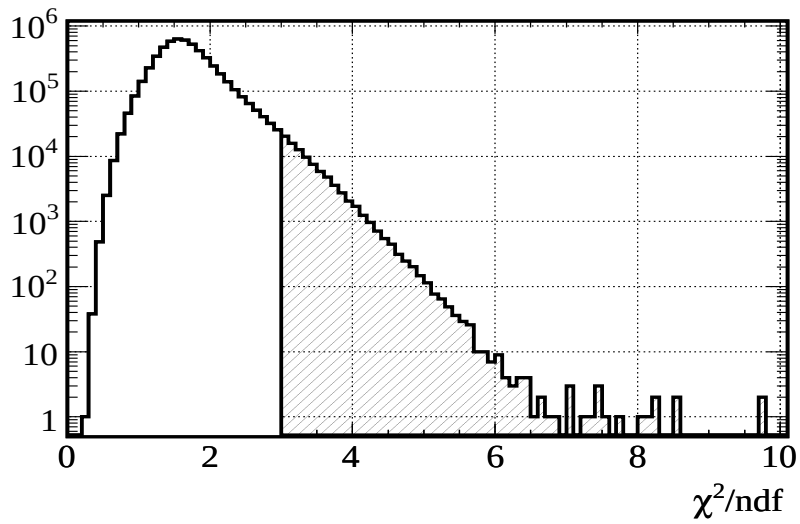


Figure 8.1: Distribution of $\chi^2/ndf$ for the time vs $y$-position fit for cosmic ray events.

incorrectly identified as upward-going muons usually have timing in the $y$-direction that appears random, giving very large values of $\chi^2/ndf$. The "Double Ended Strips" cut (8) checks the fraction of strips in the track that have signals read out on both ends. Strips that have signal read out from only one end are most likely due to noise and not reliable for tracking. This cut requires that at least half the strips in a track have signals read out from both ends. This cut excludes $\sim 0.01\%$ of the events. The next cut (9) looks at the value of $dt/dy$. Events with positive slopes are selected

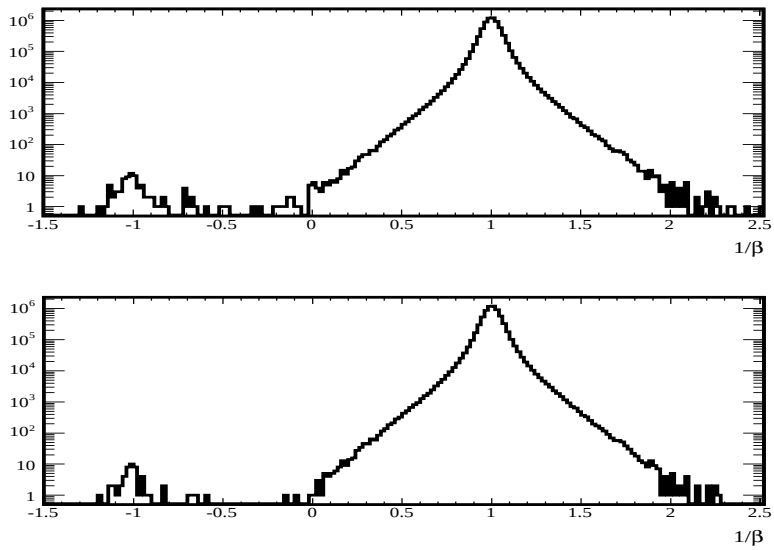


Figure 8.2: $1/\beta$ distribution for events passing the track selection cuts(top) and those passing the upward-going selection cuts (bottom).

as those events indicate that the times of the hits along the track increase with increasing $y$-position. The top histogram in Fig. 8.2 shows $1/\beta = 1/(v/c)$ multiplied by $-dt/dy$ for all events passing the selection cuts of Table 6.1. The $1/\beta$ value for each event passing cuts (1) - (5) is multiplied by $-dt/dy$ to distinguish potential upward-going events from the down-going events. The bottom histogram shows the distribution after applying the cuts (6) - (8) in Table 8.1. Several events are seen near $1/\beta \sim -1$. A Gaussian fit to the $1/\beta$ distribution of these upward-going events shows a peak at $1/\beta = -1.01$ with $\sigma_{up} = 0.05$. The downward-going events are peaked at $1/\beta = 1.01$ with $\sigma_{down} = 0.05$. Tables 8.2 and 8.3 lists the events with $1/\beta < -0.5$ from the SM1 and SM1+SM2 data sets respectively as those events are potential upward-going muons. The events are ordered by their $1/\beta$ values. The

Table 8.2: Potential Upward-going Muon Events from SM1 Data Set.

| Event | $1/\beta$ | Run | Snarl | Vertex $(x, y, z)$ | $\Delta s$ | Planes | $\chi^2_{dt/dy}/ndf$ |
|---|---|---|---|---|---|---|---|
| 1 | 0.82 | 12025 | 35143 | $(2.80, 2.20, 0.11)$ | 2.94 | 41 | 2.34 |
| 2 | 0.94 | 8237 | 38607 | $(-2.55, -1.26, 0.11)$ | 5.74 | 89 | 1.51 |
| 3 | 0.94 | 8291 | 47823 | $(-2.25, -3.36, 4.51)$ | 5.31 | 74 | 2.17 |
| 4 | 0.99 | 9104 | 43169 | $(0.04, -3.93, 5.28)$ | 7.19 | 64 | 1.64 |
| 5 | 1.00 | 8985 | 8054 | $(-3.37, -2.25, 11.17)$ | 6.27 | 62 | 1.64 |
| 6 | 1.01 | 9992 | 16177 | $(-2.36, -3.27, 8.43)$ | 10.18 | 138 | 1.67 |
| 7 | 1.04 | 7962 | 33013 | $(-3.14, 2.34, 7.54)$ | 6.56 | 43 | 2.39 |
| 8 | 1.04 | 8918 | 42108 | $(3.89, 0.53, 4.51)$ | 6.02 | 47 | 1.60 |
| 9 | 1.07 | 10933 | 22087 | $(-1.37, -0.29, 0.11)$ | 5.18 | 51 | 1.34 |

table also shows the event run and snarl numbers, $(x, y, z)$ coordinates of the track vertex, track length ($\Delta s$), number of planes crossed, $\chi^2_{dt/dy}/ndf$. The events with $1/\beta \sim -0.6$ are potential upward going events, but their $1/\beta$ values make them suspect and closer examination is needed to determine the nature of these events. Table 8.3 shows that these events all just pass the requirement of crossing at least 20 planes and their track lengths are $\Delta s < 3$ m. The $\chi^2_{dy/dt}/ndf$ values for these events are not unreasonable compared to the other potential upward-going events. The events with $1/\beta \sim -0.6$ are shown in Figs. 8.3 - 8.5. The top panel in the event display is for the UZ view of the detector, and the middle one is the VZ view. The histogram along the top of the UZ view shows the number of hits in each plane. The hits used in the track are represented by the filled histogram. The relative size of the signal strength from each hit in the event is shown by the histogram along the sides of the UZ and VZ views. Again the filled histograms show the signal of the hits used in the track. The lower left panel shows the XY projection of the track hits. The lower right graph shows the time for each hit along the track versus

the $y$-position of the hit. The stars indicate the location of the track and shower verticies. The verticies can be distinguished in the event display only by using the information in the legend on the lower right. The line shows the track and the hits are the square points in the UZ and VZ views. These events all have reasonable tracking as the track intersects the hits in each plane. There are no in-time hits in the veto shield for these events indicating that they are not cosmic ray muons that traveled through the steel and then scattered outward to leave a detectable signal. The shower and track verticies are at opposite ends of each of the events, which makes them somewhat suspect. However, a muon may bremsstrahlung at any point along its trajectory in the detector producing an electromagnetic shower. The event shown in Fig. 8.3 has poor timing. It comes from a region of the detector where a piece of the readout electronics hardware was changed and the timing calibration was not regenerated for the new hardware. This is an interesting event as its end points are at the bottom of the detector and in the middle of the detector. The fact that there are no veto shield hits associated in time with this event indicates that it is not a cosmic ray muon that traveled down a steel plate for some distance before being scattered into a trajectory that would cause it to leave an observable signal. One possibility is that this is a neutrino event where the neutrino interacted within the detector. Given the ambiguity in the timing due to the hardware change, this event is excluded from the upward-going sample. However, new timing constants are being generated and the data will be reprocessed to see if the timing of this

Table 8.3: Potential Upward-going Muon Events from SM1+SM2 Data Set.

| Event | $1/\beta$ | Run | Snarl | Vertex $(x, y, z)$ | $\Delta s$ | Planes | $\chi^2_{dt/dy}/ndf$ |
|---|---|---|---|---|---|---|---|
| 10 | 0.59 | 23692 | 85806 | $(0.41, -3.90, 9.00)$ | 2.81 | 22 | 1.61 |
| 11 | 0.66 | 23087 | 130718 | $(-3.2, -2.4, 1.40)$ | 2.3 | 23 | 2.5 |
| 12 | 0.69 | 18761 | 65898 | $(-3.7, -1.9, 1.40)$ | 2.81 | 23 | 1.51 |
| 13 | 0.82 | 22165 | 69462 | $(1.59, -3.99, 3.32)$ | 3.28 | 50 | 1.86 |
| 14 | 0.91 | 20814 | 1300 | $(-0.03, -1.29, 0.11)$ | 5.41 | 25 | 2.70 |
| 15 | 0.94 | 20617 | 11732 | $(-1.79, -3.85, 17.65)$ | 3.62 | 20 | 1.74 |
| 16 | 0.95 | 21485 | 35404 | $(-2.25, -3.32, 2.96)$ | 6.80 | 39 | 1.61 |
| 17 | 0.95 | 22650 | 124339 | $(-3.61, 1.94, 24.01)$ | 8.04 | 78 | 1.96 |
| 18 | 0.99 | 19025 | 18948 | $(-3.89, 0.90, 23.71)$ | 8.49 | 57 | 1.57 |
| 19 | 0.99 | 19302 | 14996 | $(-0.98, -3.95, 25.38)$ | 7.73 | 74 | 1.83 |
| 20 | 0.99 | 21845 | 463 | $(-1.19, -3.96, 7.01)$ | 10.16 | 99 | 1.37 |
| 21 | 0.99 | 21865 | 84239 | $(-3.94, -1.25, 13.07)$ | 7.29 | 30 | 1.56 |
| 22 | 0.99 | 22213 | 178971 | $(1.85, -3.70, 5.28)$ | 7.22 | 85 | 2.00 |
| 23 | 0.99 | 22351 | 22703 | $(-1.91, -3.69, 9.74)$ | 12.10 | 162 | 1.86 |
| 24 | 0.99 | 23285 | 23840 | $(-0.49, -0.31, 0.11)$ | 7.82 | 103 | 1.33 |
| 25 | 0.96 | 24884 | 15375 | $(-0.29, -3.98, 19.37)$ | 8.44 | 45 | 2.45 |
| 26 | 1.00 | 21361 | 12693 | $(3.40, -2.21, 9.80)$ | 13.38 | 153 | 1.63 |
| 27 | 1.00 | 20566 | 63713 | $(-2.45, -3.05, 4.03)$ | 7.86 | 62 | 1.44 |
| 28 | 1.00 | 22968 | 39057 | $(-1.39, -1.91, 29.96)$ | 26.07 | 397 | 1.56 |
| 29 | 1.01 | 18019 | 97349 | $(3.95, 0.13, 6.29)$ | 9.81 | 108 | 2.05 |
| 30 | 1.01 | 19334 | 84654 | $(0.79, -3.92, 18.07)$ | 7.89 | 41 | 1.83 |
| 31 | 1.01 | 22734 | 94200 | $(2.01, -3.46, 26.92)$ | 6.39 | 24 | 1.71 |
| 32 | 1.01 | 24767 | 22875 | $(4.01, -1.57, 24.31)$ | 23.68 | 335 | 1.58 |
| 33 | 1.02 | 20941 | 40478 | $(-2.36, -3.14, 0.65)$ | 7.41 | 50 | 2.23 |
| 34 | 1.02 | 21361 | 8220 | $(-3.91, -0.17, 10.69)$ | 5.71 | 35 | 1.70 |
| 35 | 1.02 | 24189 | 55106 | $(-2.34, -0.77, 0.11)$ | 4.59 | 65 | 2.03 |
| 36 | 1.03 | 19302 | 40691 | $(3.36, -2.43, 7.42)$ | 8.94 | 84 | 1.37 |
| 37 | 1.03 | 20966 | 27391 | $(3.98, -0.92, 19.49)$ | 10.98 | 105 | 1.76 |
| 38 | 1.03 | 22479 | 70626 | $(-0.51, -3.96, 3.68)$ | 8.28 | 22 | 1.73 |
| 39 | 1.04 | 20012 | 63105 | $(1.85, -3.70, 25.79)$ | 5.36 | 69 | 1.88 |
| 40 | 1.04 | 22342 | 9399 | $(2.79, -2.76, 6.17)$ | 8.84 | 83 | 1.87 |
| 41 | 1.04 | 24871 | 49226 | $(4.01, 0.087, 27.99)$ | 2.14 | 20 | 2.52 |
| 42 | 1.05 | 18324 | 72689 | $(-2.80, -2.73, 16.46)$ | 9.03 | 74 | 1.57 |
| 43 | 1.06 | 22672 | 46426 | $(-1.04, 1.22, 0.11)$ | 4.90 | 66 | 1.72 |
| 44 | 1.07 | 24168 | 85867 | $(3.99, 1.03, 25.50)$ | 2.80 | 37 | 1.94 |
| 45 | 1.09 | 19292 | 49901 | $(-1.34, -3.87, 3.38)$ | 7.94 | 54 | 1.65 |
| 46 | 1.11 | 18890 | 67171 | $(-2.51, -3.05, 28.23)$ | 5.67 | 50 | 2.36 |
| 47 | 1.12 | 25037 | 112493 | $(1.93, 3.63, 6.11)$ | 3.74 | 21 | 1.65 |
| 48 | 1.13 | 21398 | 51585 | $(-0.71, -3.99, 22.47)$ | 3.57 | 22 | 1.83 |
| 49 | 1.13 | 21853 | 22982 | $(-2.72, -2.80, 17.41)$ | 7.75 | 36 | 1.95 |
| 50 | 1.20 | 22566 | 95838 | $(-2.68, 2.89, 26.68)$ | 5.26 | 47 | 2.42 |

event can be improved. The events from runs 18761 and 23087 have similar vertex $z$-positions, indicating that those events started from planes near each other in the detector. These events have one end point at the first plane in the detector. Given the random nature of the timing for the hits in the events, they may be downward going muons that entered the detector through the south face. There is no coverage of the end planes of the detector from the veto shield so there would be no shield hits even if these events are downward-going muons. A major component of the readout electronics connected to these planes was changed after run 18761 was taken but before run 23087 was taken. The timing constants were not recalculated after the hardware change, which accounts for the considerable scatter in the timing of the hits for the event from run 23087. Although the event shown in Fig. 8.4 has timing in the $y$-direction that appears to be increasing with larger $y$-positions, there is noticeable scatter in the points. Additionally, the fact that this event comes from a region of the detector that was connected to faulty electronics hardware makes the timing of the event suspect. These events are also excluded from the upward-going event sample because of poor timing. New calibration constants may allow the event from run 23087 to be reclassified as upward-going.

The final upward-going muon identification cut requires that the $1/\beta$ value for an event have $|1 - 1/\beta| < 0.3$ as the downward-going $1/\beta$ distribution falls 2 orders of magnitude from its peak value at the boundaries indicated by this cut. The cut includes 99.4% of all downward-going events and is $6\sigma$ from the peak value of $1/\beta =$

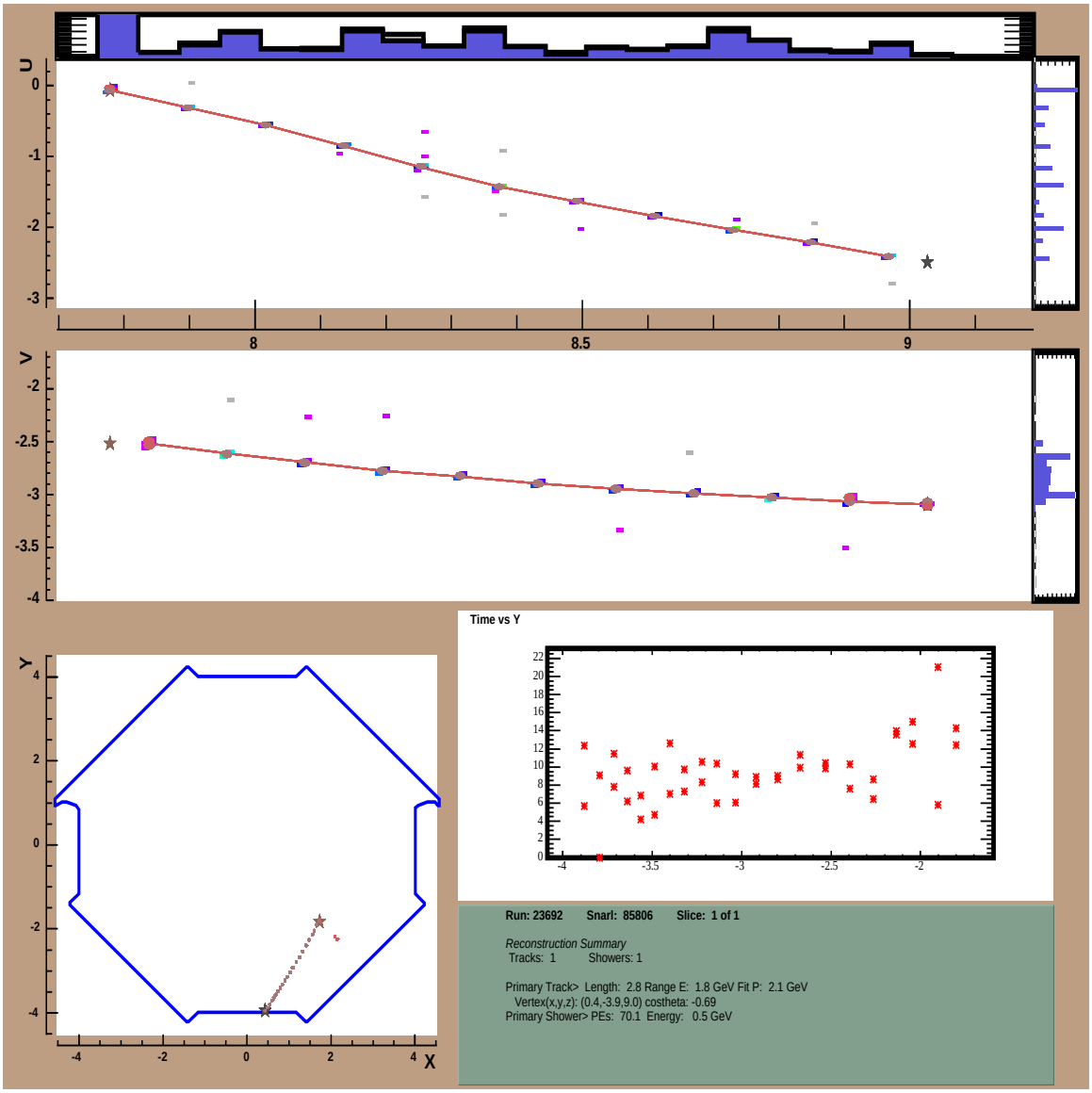


Figure 8.3: Potential upward-going muon event, run 23692, snarl 85806. The top panel shows the transverse position of a hit strip in U versus the Z position of the plane. The middle panel shows the same for V versus Z. The histogram along the top of the UZ view shows the number of hits in each plane. The hits used in the track are represented by the filled histogram. This event uses each hit in the event for the track. The relative size of the signal from each hit in the event is shown by the histogram along the sides of the UZ and VZ views. Again the filled histograms show the relative signal strength of the hits used in the track. The lower left panel is the XY projection of the track. The lower right graph shows the time for each digit along the track versus its $y$-position. The lower right hand legend gives a summary of the event information.

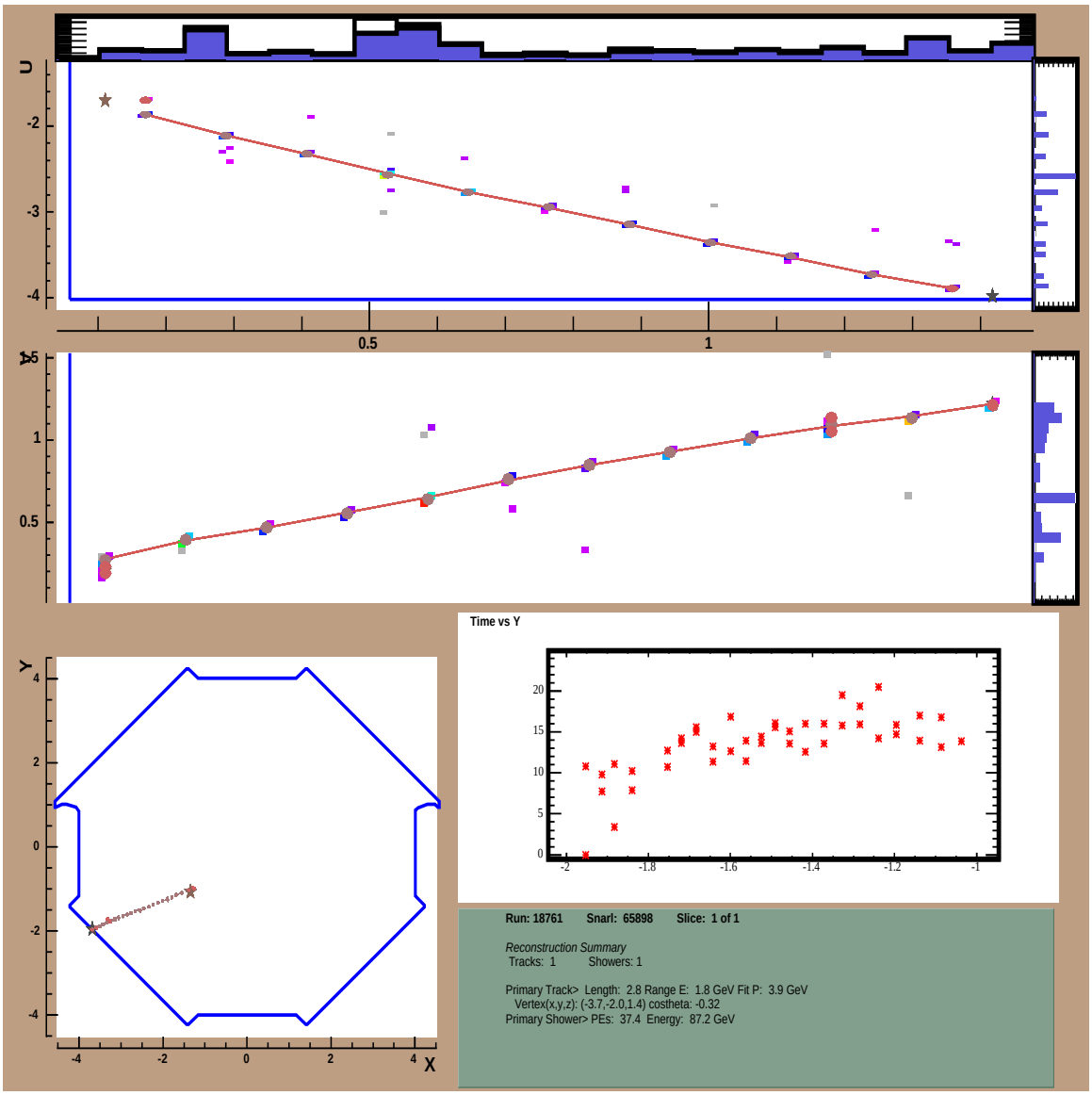


Figure 8.4: Potential upward-going muon event, run 18761, snarl 65898. (See the caption to Fig. 8.3 for an explanation of the event display.)

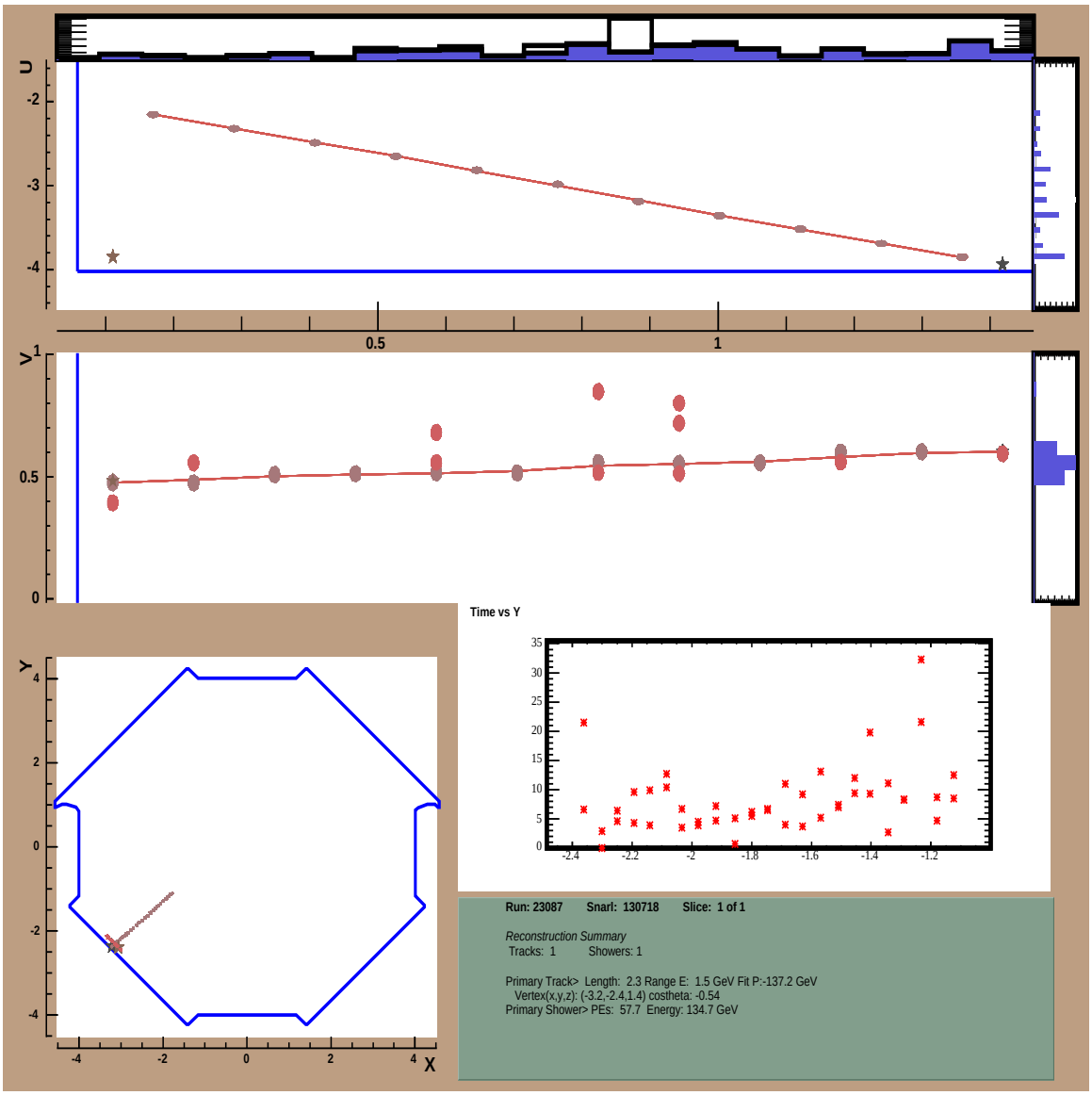


Figure 8.5: Potential upward-going muon event, run 23087, snarl 130718. (See the caption to Fig. 8.3 for an explanation of the event display.)

$-1$ for the upward-going events. Previous experiments [49] used the distribution of events with $-1 \leq 1/\beta < 0$ to estimate the background in the upward-going sample. The MINOS background in this region is negligible. The reason for the low background is a combination of the requirement that selected events be a reasonable length and the good timing system of the detector. Additionally, the data sample is still quite small and the background may become more apparent after more data taking. The tail in the bottom $1/\beta$ distribution of Fig. 8.2 where $1/\beta > 1.5$ comes from events that have long enough track lengths for the track fitting algorithm to determine the vertex and end points well. The timing for the $dt/dy$ value clearly indicates that the track is downward going. However, these events have poor timing calibrations for some large fraction of the hits causing a large spread of the times resulting in large $1/\beta$ values. The events with $|1/\beta| < 0.5$ are those events where the timing appears random and the line fit to $dt/ds$ has a small slope.

After imposing all upward-going muon cuts, 9 events were found in the SM1 data set and 38 were found in the SM1+SM2 data set, as recorded in Tables 8.2 and 8.3. An example upward-going event is shown in Fig. 8.6. This event is a low momentum $\mu^+$ and bends significantly in the presence of the magnetic field.

### 8.1.2 Horizontal Muons

The flat overburden of the Soudan mine makes the search for neutrino-induced muons coming along and slightly above the horizon possible. The $\cos\theta$ distribution for the

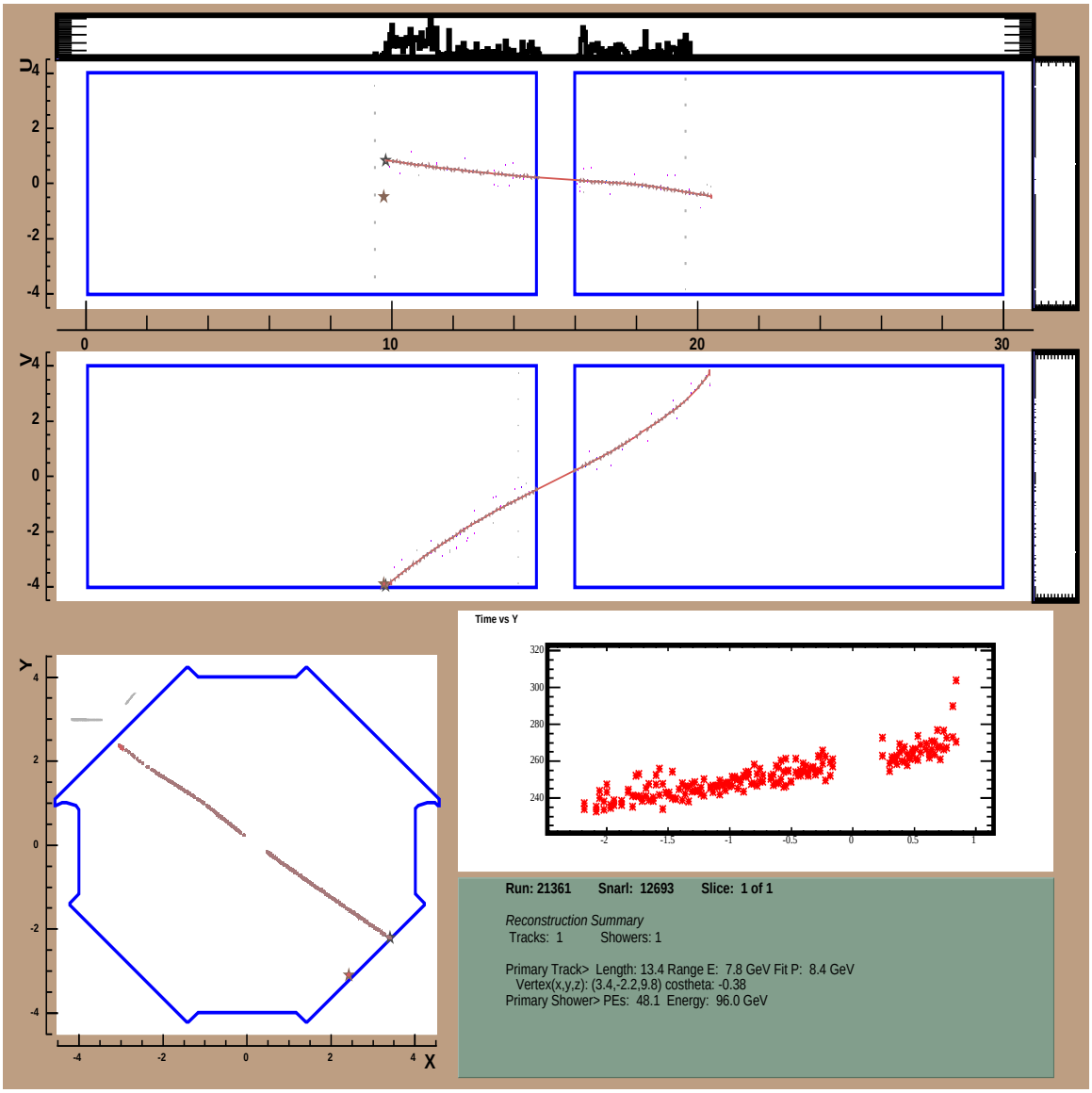


Figure 8.6: Example upward-going muon event, run 21361, snarl 12693. This is a low momentum $\mu^+$ event. (See the caption to Fig. 8.4 for an explanation of the event display.)

data events in Fig. 6.8 shows that the number of observed events falls rapidly for $\cos\theta < 0.2$. This fall off is the result of the increasing overburden for directions near the horizon. These events are important because they represent a region of parameter space for the values of $L/E$ in eq (2.22) that has not been extensively explored using neutrino-induced muons. Specifically, the neutrinos that produce the neutrino-induced muons coming from along the horizon travel distances of order $10^2$ km versus the $10^3$ - $10^4$ km traveled by the upward-going neutrino-induced muons. Because the horizontal muons have similar energies to the upward-going muons, the value of $L/E$ is lower for the horizontal muons on average. These lower values mean that the average oscillation probability will also be lower and that the horizontal muons will aid in determining the neutrino flux normalization.

The expected intensity of muons near the horizon is found by integrating eq (6.8) from the slant depth of the direction near the horizon to infinity. That intensity is multiplied by the detector exposure and the detector acceptance for directions near the horizon to get the expected number of events. The Soudan 2 experiment, which was located in the hall adjacent to the MINOS far detector hall, used a slant depth cut of $X = 14$ km.w.e [50] to reduce the cosmic ray muon background to 1%. The slant depth cut of the Soudan 2 analysis corresponds to $\cos\theta \lesssim 0.14$ over most values of $\phi$. There are some azimuthal regions to the south of the detector where the cut must be $\cos\theta < 0.12$ to satisfy the slant depth requirement. The expected intensity of cosmic ray muons for all $X > 14$ km.w.e is $2.62 \times 10^{-11}$ cm$^{-2}$s$^{-1}$sr$^{-1}$. The

acceptance of the detector for cosmic ray muons for $\cos\theta < 0.14$ is $\sim 1 \times 10^4$ cm$^2$sr. Taking the product of the expected intensity with the detector acceptance gives the expected frequency of cosmic ray events from near the horizon to be $\sim 3 \times 10^{-7}$ Hz. This rate corresponds to 6 events for the 230 live day exposure of the SM1+SM2 data set. Examination of Fig. 6.8 shows that there are 10 events with $\cos\theta < 0.14$, 7 of those being in the range $0.1 \leq \cos\theta \leq 0.14$. The slant depth for $\cos\theta = 0.1$ is estimated to be 19 km.w.e using the definition of the cosine and the known slant depth for $\cos\theta = 0.14$, $X = 14$ km.w.e. The expected intensity of cosmic ray muons for all $X \geq 19$ km.w.e is $6.07 \times 10^{-14}$ cm$^{-2}$s$^{-1}$sr$^{-1}$. The acceptance of the detector for $\cos\theta < 0.1$ is $\sim 1 \times 10^4$ cm$^2$sr. Then the expected number of cosmic ray muons coming from directions with $\cos\theta < 0.1$ is 0.01. Thus the events seen from directions having $0.1 \leq \cos\theta < 0.14$ are well described by the approximation of eq (6.8) and the events having directions $\cos\theta < 0.1$ appear to be neutrino induced.

The steeply falling distribution below $\cos\theta = 0.2$, suggests that the data may follow an exponential distribution for that range of $\cos\theta$ values. The Super-K collaboration estimated the cosmic ray muon background for its upward-going muon analysis in bins near the horizon using an exponential fit to the data from $\cos\theta$ values above the cut off value [1]. An exponential was fit to the distribution of Fig. 6.8 for $0.1 \leq \cos\theta \leq 0.2$ to provide an estimate of the background due to cosmic rays in the signal region. The exponential fit is shown in Fig. 8.7 and it has the form $y = \exp(a + bx)$, where $a = -5.9$ and $b = 57.0$. The background estimated by the

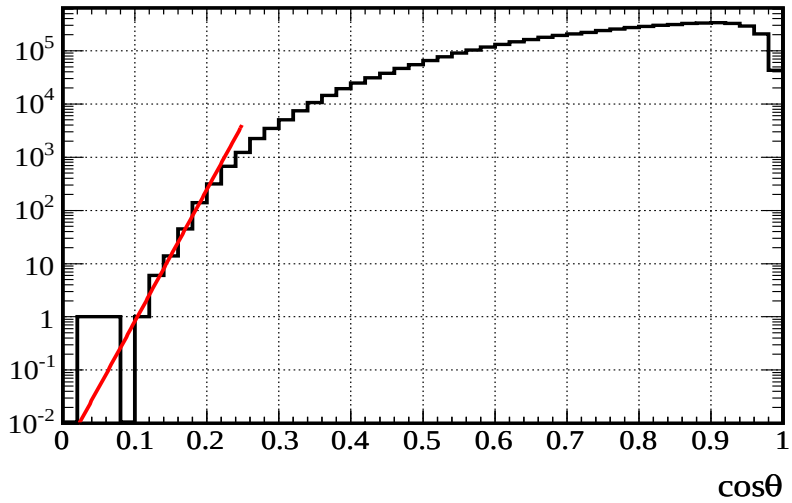


Figure 8.7: The $\cos\theta$ distribution for downward-going muons showing an exponential fit to the region $0.1 \leq \cos\theta \leq 0.2$.

exponential fit to the $\cos\theta$ distribution is 0.52 events at $\cos\theta = 0.1$ and is taken to be negligible for the rest of the signal region.

Both methods of estimating the cosmic ray muon event rate near the horizon show that the background to the neutrino-induced muons coming from these directions is small. The present analysis makes a more conservative cut than the Soudan 2 analysis, $\cos\theta < 0.1$, to select horizontal muons in a region that is free from background cosmic ray muons. The data show the cut to be reasonable as seen in Fig. 8.7. Using this $\cos\theta$ cut, 0 events are seen in the signal region for the SM1 data set, and 3 events are seen for the SM1+SM2 data set.

## 8.2 Event Distributions

As shown in Figs. 8.2 and 8.7, there are 47 upward-going events and 3 horizontal muon events in the combined SM1 and SM1+SM2 data sets. These events cover the range in $\cos\theta$ from $-1 \leq \cos\theta \leq 0.1$ and represent a wide range of momenta, as well as both $\mu^-$ and $\mu^+$. The neutrino oscillation parameter analysis is done in two ways. The first uses only the $\cos\theta$ information and attempts to determine the oscillation parameters based on the shape of that distribution over 6 bins in $\cos\theta$. The $\cos\theta$ bins below the horizon are each of width 0.2 and the bin above the horizon has a width of 0.1. The second way uses the charge sign and momentum information as well. The charge sign selection puts events into 3 bins: $\mu^-, \mu^+$, and events with ambiguous charge identification, labeled by $\mu^?$. The events were further separated into two momentum bins: those events with $p_{\text{fit}} < 10$ GeV/c and those with $p_{\text{fit}} \geq 10$ GeV/c. This separation in momentum corresponds roughly to the stopping and through-going event sample cuts used by previous experiments [49] [34]. Fig. 8.8 shows the $\cos\theta$ distribution for the analysis of the $\cos\theta$ shape and Fig. 8.9 shows the $\cos\theta$ distributions separated according to various charge sign and momenta. The errors shown in both figures are statistical errors only. In the latter figure, the top left and middle plots are for the low momentum $\mu^-$ and $\mu^+$ respectively. The bottom left and middle plots are for the high momentum events with the same charge assignments. The bottom right distribution is for those events that failed the

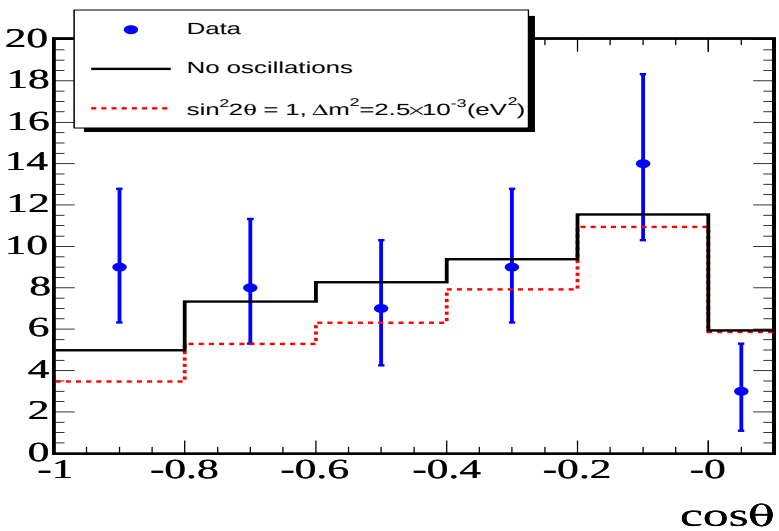


Figure 8.8: The $\cos\theta$ distribution for the data set. The data are the points with statistical errors shown; the solid line is for the no oscillation case and the dashed line is for oscillations of $\nu_\mu \rightarrow \nu_\tau$ with the oscillation parameters $\sin^2 2\theta = 1$ and $\Delta m^2 = 2.5 \times 10^{-3}$ eV$^2$ [34] [49].

charge sign identification cuts. For reference, the Monte Carlo predictions for the number of events to be seen for both the no oscillation case (solid line) and the case with $\nu_\mu \rightarrow \nu_\tau$ oscillations following the Super-K [34] and MACRO [49] parameters $\sin^2 2\theta = 1$ and $\Delta m^2 = 2.5 \times 10^{-3}$ eV$^2$ (dashed line) are shown in both figures.

The momentum distribution for the events passing the charge sign identification cut, $(q/p)/\sigma_{q/p} > 2.5$ is shown in Fig. 8.10. The negative values of $p_{\text{fit}}$ indicate $\mu^-$ events, while positive values are used for $\mu^+$ events. There are 23 events that passed the charge sign identification cut, 13 are $\mu^-$ and 10 are $\mu^+$.

The right ascension and declination for the neutrino-induced muons is shown in Fig. 8.11. Each bin in right ascension is 3° wide and each declination bin is 1° wide.

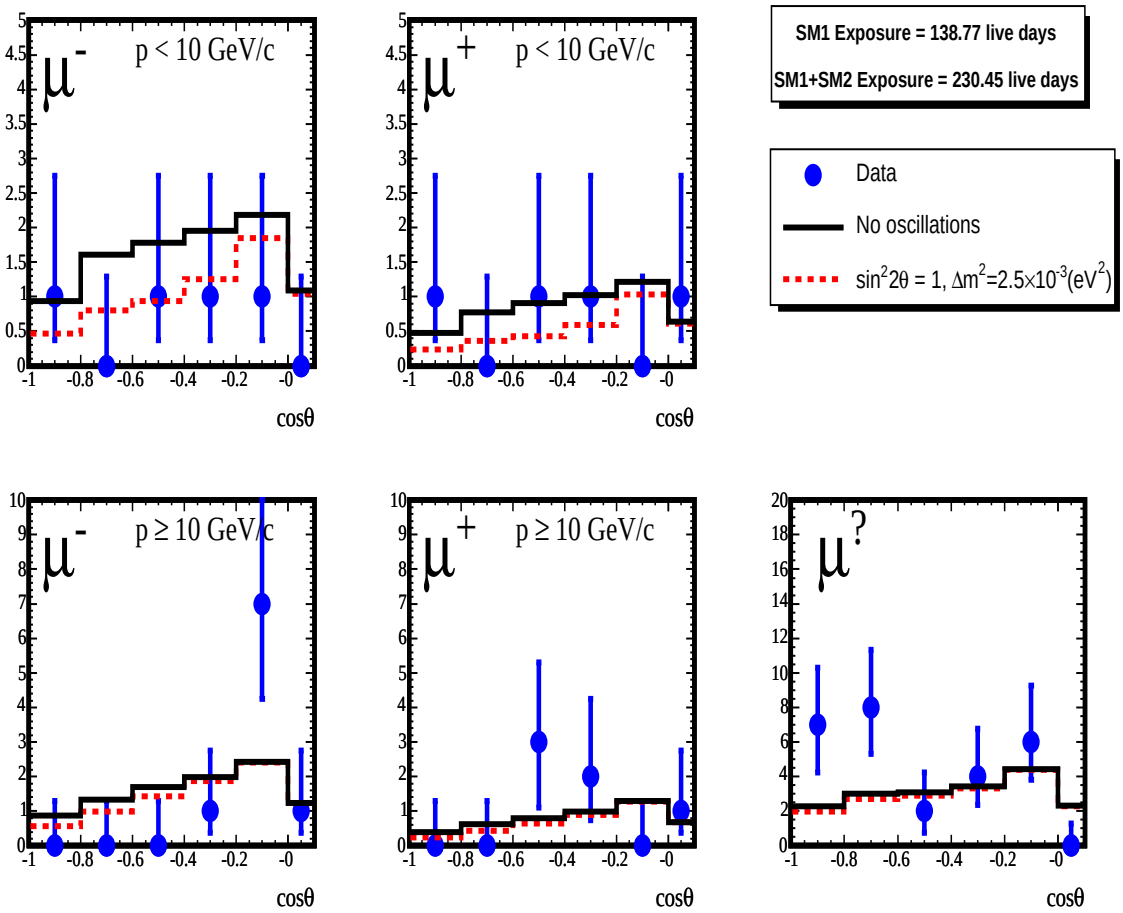


Figure 8.9: The $\cos\theta$ distributions for the data set with charge sign and momentum information included. The left column of plots is for $\mu^-$; the middle for $\mu^+$; and the bottom right is for events with poor charge and/or momentum determination. The top plots are for events with $p_{\rm fit} < 10$ GeV/c and the bottom left and middle plots are for events with $p_{\rm fit} \geq 10$ GeV/c. The data are the points with statistical errors shown; the solid line is for the no oscillation case; and the dashed line is for oscillations of $\nu_\mu \rightarrow \nu_\tau$ with the oscillation parameters $\sin^2 2\theta = 1$ and $\Delta m^2 = 2.5 \times 10^{-3}$ eV$^2$ [34] [49].

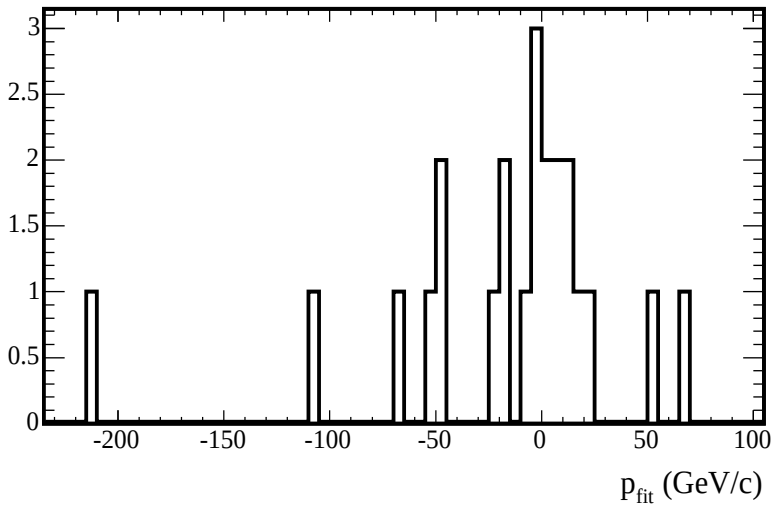


Figure 8.10: The fit momentum distributions for the data set. Negative values of $p_{\text{fit}}$ are for $\mu^-$, positive values are for $\mu^+$.

No more than one event is seen in each bin indicating that no neutrino point sources have been found. The neutrino-induced muons observed in the MINOS detector are free from background contamination as shown in § 8.1.1 and § 8.1.2. If two neutrino-induced muons come from the same location on the sky it would evidence for a neutrino point source. MINOS does not see evidence for neutrino point sources using the neutrino-induced muons as there are 50 events spread over 120 bins in right ascension and 180 bins in declination with no two events in the same bin.

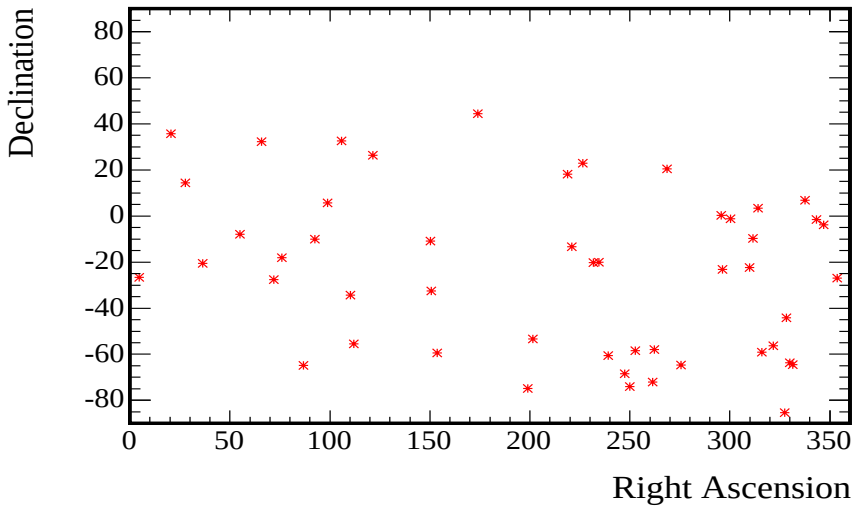


Figure 8.11: All-sky map of neutrino-induced muons. No more than one event is seen in each bin of size 3° in right ascension and 1° in declination.

## 8.3 Oscillation Analysis

### 8.3.1 Fitting the Data

The MINOS neutrino-induced muon analysis described here adopts the NUANCE Monte Carlo event generator. The Monte Carlo events are generated on the surfaces of a cube just larger than the detector in each dimension. A total of exposure of 2500 years of Monte Carlo events each were generated for the SM1 only and full detector configurations. The events are processed using the detector Monte Carlo, GMINOS, and reconstructed using the standard software. The energy of each neutrino producing a muon in the Monte Carlo and the distance each neutrino traveled are saved to be used when determining the neutrino's survival probability.

To extract the oscillation parameters $(\sin^2 2\theta, \Delta m^2)$ from the data, the data and Monte Carlo are compared using the following $\chi^2$ statistic,

$$\chi^2 = \sum_i \left( N_{\mathrm{MC},i} + b_i - N_{\mathrm{DATA},i} + N_{\mathrm{DATA},i} \ln \frac{N_{\mathrm{DATA},i}}{N_{\mathrm{MC},i} + b_i} \right) + \sum_k \left( \frac{(\epsilon_k - \langle \epsilon_k \rangle)^2}{\sigma^2_{\epsilon_k}} \right). \quad (8.1)$$

The first sum is the $\chi^2$ for Poisson distributed data [3] over all bins. The number of data events seen in bin $i$ is $N_{\mathrm{DATA},i}$ and the expected background in that bin is $b_i$. The background in each bin is set to 0 as § 8.1.1 and § 8.1.2 showed that the backgrounds are negligible.

The number of events predicted in bin $i$ by the Monte Carlo is $N_{\mathrm{MC},i}$. The $N_{\mathrm{MC},i}$ are calculated accounting for the effects of neutrino oscillations and systematic errors, such that $N_{\mathrm{MC},i} = N_{\mathrm{MC},i}(\sin^2 2\theta, \Delta m^2, \epsilon_1, \epsilon_2, \epsilon_3, \epsilon_4)$. The parameters $\epsilon_k$ account for the systematic uncertainties in the predicted number of events and are introduced such that their expectation values, $\langle \epsilon_k \rangle$, are 0. The parameters $\epsilon_k$ are assumed to be Gaussian distributed so that excursions of the fit values from the expected values contribute an amount $(\epsilon_k - \langle \epsilon_k \rangle)^2/\sigma^2_{\epsilon_k}$ to $\chi^2$. This form of the $\chi^2$ has been used by several experiments, including the Super-K [51] upward-going muon analysis.

Four sources of systematic uncertainties are considered in this analysis. The first uncertainty considered is in the overall normalization of the calculated neutrino event rates and is parameterized by $\epsilon_1$. Different calculations of the atmospheric neutrino event rate differ by $\sim 25\%$, as shown in § 7.2.2, implying that $\sigma_{\epsilon_1} = 25\%$. For

example the choice of the BARTOL96 flux model for this analysis yields estimates of event rates which are 25% smaller than those predicted by the model of Honda [52]. Note that these variations are comparable to the statistical variations accounted for in the first sum in eq (8.1).

The systematic uncertainty due to the relative normalization of the events that pass the charge identification cut, $(q/p)/\sigma_{q/p} \geq 2.5$, to those that do not is characterized by $\epsilon_2$. The uncertainty in this parameter is dominated by the differences between the data and Monte Carlo distributions of $(q/p)/\sigma_{q/p}$, as seen in Fig. 6.37. These differences are likely the result of incomplete modeling of the magnetic field in the far detector, as shown in § 6.5. As a result, the efficiency for selecting events that pass the $(q/p)/\sigma_{q/p}$ cut is systematically higher for Monte Carlo events than data events. The uncertainty in $\epsilon_2$ is estimated to be $\sim 20\%$ from a comparison of the $(q/p)/\sigma_{q/p}$ distributions for data and Monte Carlo events. It can be argued that there is likely to be a dependence on the fit momentum to the uncertainty in this parameter. Low momentum events may be expected to pass the cut more often than the high momentum events. Given the limited statistics of the data, this effect has been ignored to simplify the systematic uncertainty model.

The systematic uncertainty in the $N_{\mu^+}/N_{\mu^-}$ ratio is parameterized by by $\epsilon_3$. Differences between the charge identification efficiency between the data and Monte Carlo contributes 10% to the uncertainty in $\epsilon_3$, a value that was estimated by scanning the neutrino-induced muons in the data for evidence of curvature. Another

source of uncertainty in this parameter is due to uncertainties in the relative fluxes of the $\nu_\mu$ and $\overline{\nu}_\mu$. This uncertainty is estimated to be 8% by comparing the BARTOL96 and Honda [52] flux models. The size of the neutrino and anti-neutrino cross sections each have an uncertainty of order 2% [3]. The uncertainty in the ratio of the neutrino cross section to the anti-neutrino cross section is estimated to be $\sim 3\%$ over the energy range relevant for neutrinos producing the neutrino-induced muons. The total uncertainty from these sources is 14%.

The systematic uncertainty in the shape of the momentum spectrum of the neutrino-induced muons is parameterized by $\epsilon_4$. This parameter accounts for the fact that the ratio of the number of low momentum events to high momentum events may differ between the data and Monte Carlo. Differences in the momentum resolution between the data and Monte Carlo contribute 8% to the uncertainty in the ratio of the number of events in the $p_{\text{fit}} < 10$ GeV/c and $p_{\text{fit}} \geq 10$ GeV/c samples. A second contribution comes from the atmospheric neutrino energy spectrum. The neutrino flux is proportional to $E_\nu^{-(\gamma+1)}$, as shown in eq (7.4). The value of the spectral index, $\gamma$, is $1.7 \pm 0.05$ [38]. Potential variations in the spectral index of the atmospheric neutrino flux contributes 8% to the uncertainty in $\epsilon_4$. The uncertainties in the neutrino and anti-neutrino cross sections contribute another 2% [3] to the uncertainty in $\epsilon_4$. The total uncertainty in $\epsilon_4$ is estimated to be 11%.

Using the above model for the systematic uncertainties, the expression for $N_{\text{MC},i}$

is

$$N_{\mathrm{MC},i}(\sin^2 2\theta, \Delta m^2, \quad \epsilon_1, \quad \epsilon_2, \epsilon_3, \epsilon_4) = (1+\epsilon_1)\sum_{j=1}^{2}\sum_{m=1}^{N_{\mathrm{total},j}} \frac{L_{\mathrm{DATA},j}}{L_{\mathrm{MC},j}} P(\sin^2 2\theta, \Delta m^2)_{j,m}$$
$$\times \begin{cases} (1-\frac{\epsilon_2}{2})(1-\frac{\epsilon_3}{2})(1-\frac{\epsilon_4}{2}), & \mu^-, p_{\mathrm{fit}} < 10 \text{ GeV/c} \\ (1-\frac{\epsilon_2}{2})(1-\frac{\epsilon_3}{2})(1+\frac{\epsilon_4}{2}), & \mu^-, p_{\mathrm{fit}} \geq 10 \text{ GeV/c} \\ (1-\frac{\epsilon_2}{2})(1+\frac{\epsilon_3}{2})(1-\frac{\epsilon_4}{2}), & \mu^+, p_{\mathrm{fit}} < 10 \text{ GeV/c} \\ (1-\frac{\epsilon_2}{2})(1+\frac{\epsilon_3}{2})(1+\frac{\epsilon_4}{2}), & \mu^+, p_{\mathrm{fit}} \geq 10 \text{ GeV/c} \\ (1+\frac{\epsilon_2}{2}), & \mu^?, p_{\mathrm{fit}} \ ?. \end{cases} \tag{8.2}$$

The first sum over $j$ accounts for the fact that this data analysis includes events taken with only SM1 ($j = 1$) and events taken with the full detector ($j = 2$). The detector exposure for each data sample is represented by $L_{\mathrm{DATA},j}$ and for each Monte Carlo sample by $L_{\mathrm{MC},j}$. For the SM1 event samples, $L_{\mathrm{DATA},1} = 0.38$ yr and $L_{\mathrm{MC},1} = 2500$ yr. For the SM1+SM2 event samples $L_{\mathrm{DATA},2} = 0.63$ yr and $L_{\mathrm{MC},2} = 2500$ yr.

In the second sum $m$ labels each event in the Monte Carlo sample $j$, running from $m = 1$ to $N_{total,j}$, where $N_{\mathrm{total},j}$ represents the total number of events in the Monte Carlo subset. Each event $m$ is weighted to account for the effects of neutrino oscillations and systematic uncertainties. The $P(\sin^2 2\theta, \Delta m^2)_{m,j}$ factor is the survival probability for event $m$ given by eq (2.23). The factor $(1 + \epsilon_1)$ adjusts the overall predicted rate of atmospheric events by the fraction $\epsilon_1$. For example, taking

$\epsilon_1 = 0.1$ increases the overall predicted rate of atmospheric neutrino events by 10%. The ratio of the number of events selected for charge identification ($\mu^-$ or $\mu^+$) to the number of events not selected for charge identification ("$\mu^?, p_{\text{fit}}$?") is adjusted by $\epsilon_2$. For example, $\epsilon_2 = 0.1$ would increase the predicted number of events failing the selection cut by 5% and reduce the number of events passing the cut by 5%, changing their ratio by 10%. The parameter $\epsilon_3$ adjusts the ratio of the number of identified $\mu^+$ to the number of identified $\mu^-$, by scaling the number of $\mu^-$ by a factor of $(1 - \epsilon_3/2)$ and scaling the number $\mu^+$ by a factor of $(1 + \epsilon_3/2)$. The last factors containing $\epsilon_4$ adjust the ratio of the number of predicted events with $p_{\text{fit}} < 10$ GeV/c to the number of events with $p_{\text{fit}} \geq 10$ GeV/c. This is done by weighting the expected number of events with $p_{\text{fit}} < 10$ GeV/c by the factor $(1 - \epsilon_4/2)$ and the number with $p_{\text{fit}} \geq 10$ GeV/c by the factor $(1 + \epsilon_4/2)$.

The value of $\chi^2$ is calculated at each point on a grid in the $(\sin^2 2\theta, \Delta m^2)$ space with the $\epsilon_k$'s varied at each point to minimize the $\chi^2$. The minimization of eq (8.1) is done using Powell's method which is described in [53]. The code for the minimization was taken from that source as well.

### 8.3.2 Confidence Intervals

Once the oscillation parameters are determined by the fit, the range of parameters that could describe the oscillation hypothesis with the same statistical significance must be determined. This estimate is given by the confidence interval for a given

fit. The standard method of finding the confidence interval for the fit parameters is to evaluate the difference between the $\chi^2$ values of the best fit point and every other point in the space, $\delta\chi^2$ [3]. This method works well when none of the fit parameters are bounded by physical constraints. In such cases 68% of the points in the space have $\delta\chi^2 < 2.28$, 90% have $\delta\chi^2 < 4.61$ and 99% have $\delta\chi^2 < 9.21$. The neutrino oscillation hypothesis does not meet this criteria as $\sin^2 2\theta$ is bounded between 0 and 1 and the use of the standard technique may underestimate the size of the confidence intervals if a significant fraction of an interval lies outside the physical region. Two methods for treating the physical boundary are discussed below. The first is a Gaussian approximation [3] [54] and the second is a method developed by Feldman and Cousins [22].

#### 8.3.2.1 Gaussian Approximation

The Gaussian approximation to the confidence interval for a bounded parameter in a two dimensional parameter space is an extension of the one dimensional case [3]. Assuming the likelihood function $\mathcal{L}(\sin^2 2\theta, \Delta m^2)$ may be approximated as a two dimensional Gaussian. Further, scale the units of $\sin^2 2\theta$ and $\Delta m^2$ by the rms of each parameter such that $x = (\sin^2 2\theta - \sin^2 2\theta_{\text{Best}})/\sigma_{\sin^2 2\theta}$ and $y = (\Delta m^2 - \Delta m^2_{\text{Best}})/\sigma_{\Delta m^2}$, where the subscript "Best" indicates the value of the parameter at the best fit point. Then the likelihood is

$$\mathcal{L} = Ae^{-(x^2+y^2)/2}, \tag{8.3}$$

and the $\chi^2$ for a given set of $x$ and $y$ is

$$\chi^2 = -2\ln\mathcal{L} = (x^2 + y^2) + \chi^2_{min}, \tag{8.4}$$

where $\chi^2_{min}$ is the minimum value of $\chi^2$. In the case where there is no physical boundary, the likelihood is normalized by

$$\int_{-\infty}^{\infty}\int_{-\infty}^{\infty}\mathcal{L}(x,y)dxdy = 1. \tag{8.5}$$

However, for cases where values of one parameter larger than a value $b$ are unphysical the normalization becomes

$$\kappa = \int_{-\infty}^{\infty}\int_{-\infty}^{b}\mathcal{L}(x,y)dxdy < 1. \tag{8.6}$$

At point $(b, 0)$ the $\chi^2$ value on the boundary is at its minimum value and is given by eq (8.4)

$$\chi^2_b = b^2 + \chi^2_{min}, \tag{8.7}$$

and the difference between the minimum $\chi^2$ on the physical boundary and the minimum value in the entire space is

$$\Delta\chi^2 = \chi^2_b - \chi^2_{min}. \tag{8.8}$$

The effect of the physical boundary on the confidence intervals is completely determined by the value of $\Delta\chi^2$. Once a fit is done for the desired parameters, the value of $\Delta\chi^2$ can be found. Using that value, the confidence level, $\lambda$, for a point $(x\prime, y\prime)$ based on the value of $\chi^2_{(x\prime,y\prime)} - \chi^2_{min}$ can be found using $\Delta\chi^2$ and eq (8.6),

$$\lambda = 1 - \frac{\int_{\infty}^{\infty}\int_{-\infty}^{\sqrt{\Delta\chi^2}} e^{-(x^2+y^2)/2}\Theta(\chi^2(x,y) - \chi^2(x\prime, y\prime))dxdy}{\kappa}, \tag{8.9}$$

where $\Theta(u) = 0$ for $u < 0$ and $\Theta(u) = 1$ for $u \geq 0$. Fig. 8.12 shows the 68%, 90%, and 99% confidence limits on the values of $\chi^2_{(x,y)} - \chi^2_{min}$ as a function of the measured value of $\Delta\chi^2$. The left side is for $\chi^2_{min}$ outside the physical region and the right side is for $\chi^2_{min}$ inside the physical region. If $\Delta\chi^2 = 6$ were found with the best fit outside the physical region, then the 68% confidence limit includes all points with $\chi^2_{(x,y)} - \chi^2_{min} < 9.21$. If the best fit point is inside the physical region and well away from the boundary, the confidence limits for 68%, 90%, and 99% approach their standard values of 2.28, 4.61, and 9.21 respectively.

#### 8.3.2.2 The Unified Approach of Feldman and Cousins

Another method for handling the physical boundary is called the "unified approach", which was developed by Feldman and Cousins [22]. In this method a large number of Monte Carlo experiments are performed at each point in the physical space. For each experiment, the "data" value for a bin is taken from a Poisson distribution

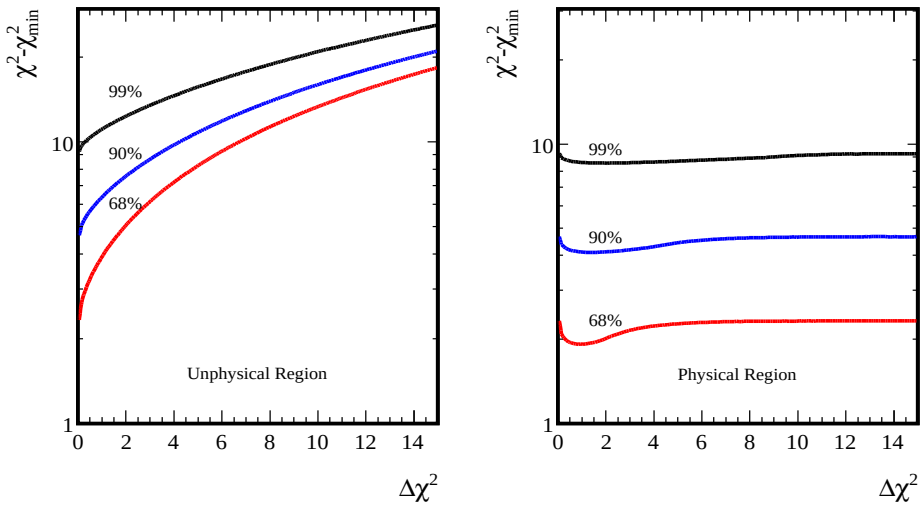


Figure 8.12: The 68%, 90%, and 99% confidence limits for a bounded physical region. The limits for the case when $\chi^2_{min}$ is in the unphysical(physical) region is on the left(right). The value of $\Delta\chi^2$ is the difference between the minimum value of $\chi^2$ in the space and the minimum value on the physical boundary.

whose mean is given by the number of events in the average experiment where the oscillation parameters are the point of interest. A fit is done to those "data" and the $\delta\chi^2$ given by

$$\delta\chi^2 = \sum_i N_{\mathrm{MC},i} - N_{\mathrm{MC}_{best},i} + N_{\mathrm{DATA},i} \ln \frac{N_{\mathrm{MC}_{best},i} + b_i}{N_{\mathrm{MC},i} + b_i}, \tag{8.10}$$

where $N_{\mathrm{MC}_{best},i}$ is the number of events in bin $i$ for the best fit parameters, $N_{\mathrm{MC},i}$ is the number of events in bin $i$ according to the Monte Carlo for the parameters at the chosen point and $N_{\mathrm{DATA},i}$ are the number of "data" events. The value of $b_i$ is the expected background contribution to bin $i$. The value of $\delta\chi^2_\xi$ for the point corresponding to the $\xi$% confidence level is the value of $\delta\chi^2$ such that $\xi$% of the

Monte Carlo experiments had $\delta\chi^2 < \delta\chi^2_\xi$.

An example will help clarify the technique. Assume the 68% confidence level boundary of $\delta\chi^2$, for the point $\Delta m^2 = 2.5 \times 10^{-3}$ eV$^2$, $\sin^2 2\theta = 1.0$, $\delta\chi^2_{68}$ is desired. For one experiment, the "data" value for the $i^{th}$ bin at this point is taken from Poisson distribution whose mean is given by eq (8.2) for the bin. The value of $N_{\mathrm{MC},i}$ is given directly by that equation. The value of $N_{\mathrm{MC}_{best},i}$ is given by the same equation, but uses the best fit parameters to the "data" determined by the minimization routine. These numbers are input along with the estimated background levels into eq (8.10) to get one measure of $\delta\chi^2$ for this point. This value of $\delta\chi^2$ is put into a histogram. The process is repeated for each Monte Carlo experiment at this point. The value of $\delta\chi^2$ that bounds the lower 68% of the area under the curve is $\delta\chi^2_{68}$. The process is repeated for all points in the space.

Obviously, this method is very computationally intensive. For each point in the space, a minimization must be done for each experiment. If it was determined to perform 1000 experiments for each point on a grid of 50 points in $\sin^2 2\theta$ and 50 points in $\Delta m^2$, then $2.5 \times 10^6$ minimizations must be done. Thankfully, the Research and Technical Computing division of Indiana University has made the AVIDD clusters available to the university community. There are two clusters, one in Bloomington and one in Indianapolis, each having between 40 and 180 processors available to users. The machines are all Pentium 4 dual processor computers.

The contours presented for the data are generated using the Gaussian approxi-

mation rather than the method of Feldman and Cousins. The reason for this choice is that the experiment is limited by statistics at the present time and there is little justification for using the computational resources needed for the unified approach. A comparison of the predicted contours for 4 years of data taking obtained using both methods is made in § 8.6.

## 8.4 Results for $\nu_\mu \rightarrow \nu_\tau$ Oscillations

The data were tested for evidence of $\nu_\mu \rightarrow \nu_\tau$ oscillations using the overall shape of the $\cos\theta$ distribution. The values of $\epsilon_2, \epsilon_3$ and $\epsilon_4$ in eq (8.2) were set to 0 as this test does not distinguish charge sign or momentum. The best fit parameters for this test are shown in Table 8.4. The table also shows the $\chi^2/ndf$ for the fit. The confidence intervals for this test are shown in Fig. 8.13. This figure is an exclusion plot and shows that the current MINOS oscillation parameter measurement based on the shape of the $\cos\theta$ distribution of neutrino-induced muons excludes oscillations in the physical region for $\sin^2 2\theta > 0.7$ and $\Delta m^2 > 5 \times 10^{-3}\mathrm{eV}^2$ at the 90% confidence level. The confidence intervals also suggest that the measurement is consistent with any set of parameters to the left of the 90% confidence level curve. Oscillations are excluded at the 99% confidence level in the physical region for $\sin^2 2\theta > 0.99$ and $\Delta m^2 > 8 \times 10^{-2}$

The data were also analyzed using charge sign and momentum information. For

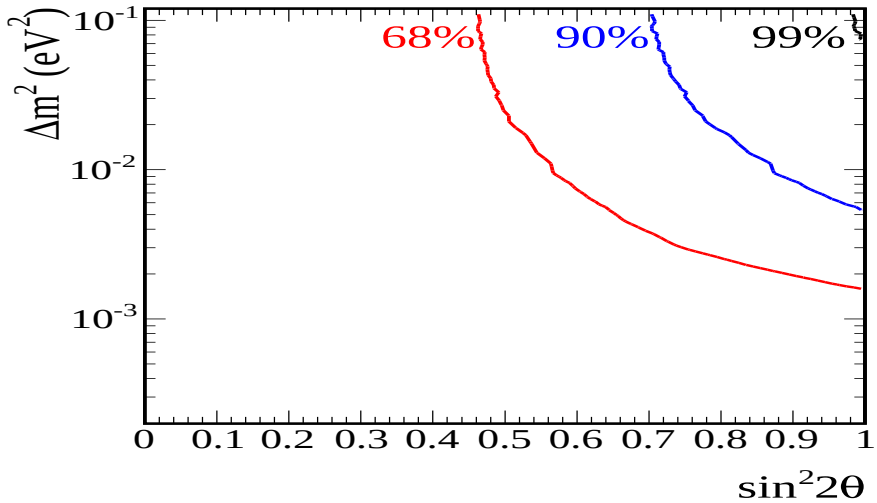


Figure 8.13: Confidence intervals for the oscillation parameter measurement based on the shape of the $\cos\theta$ distribution. Values to the left of the curves are allowed with the indicated confidence.

this test, the data were divided into 2 $\cos\theta$ bins, with the division between the bins at $\cos\theta = -0.4$; the data were also separated into 3 bins in charge sign and 2 in momentum. The number of bins in $\cos\theta$ was reduced from 6 shown in Fig. 8.9 to 2 because there are not enough events to justify so many $\cos\theta$ bins along with the charge sign and momentum bins. The best fit to the data is given in Table 8.4. The best fit on the physical boundary has $\sin^2 2\theta = 1$ with the remaining parameters at this point the same as in the table. The best fit is shown with the data in Fig. 8.14. The confidence intervals found using the Gaussian approximation of § 8.3.2.1 are shown in Fig. 8.15. The contours for the measurements based on the shape of the $\cos\theta$ distribution and the charge sign and momentum information exclude less parameter space than the intervals for the analysis based on the shape of the $\cos\theta$ distribution

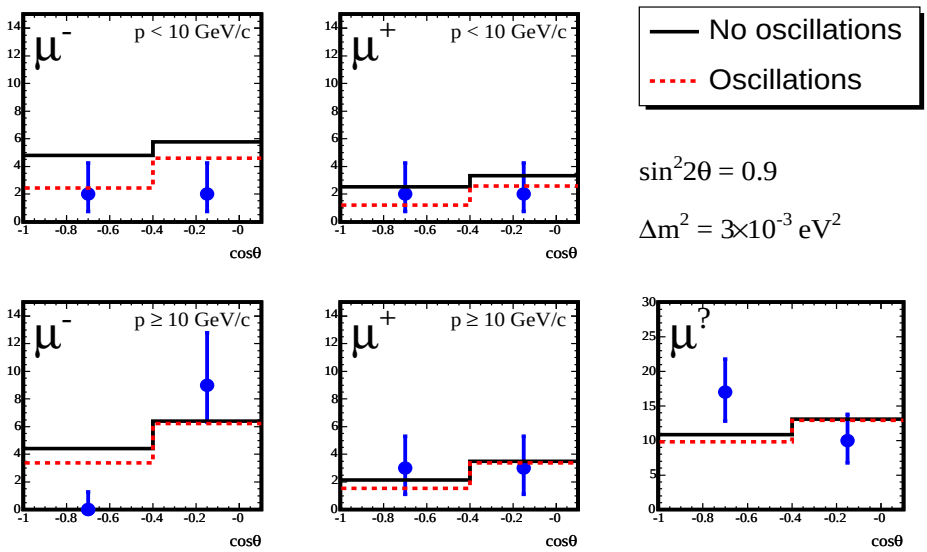


Figure 8.14: The $\cos\theta$ distributions of the data with the best fit shown by the dotted line.

Table 8.4: Neutrino oscillation fit parameters.

| Test | $\sin^2 2\theta$ | $\Delta m^2$ (eV$^2$) | $\epsilon_1$ | $\epsilon_2$ | $\epsilon_3$ | $\epsilon_4$ | $\chi^2/ndf$ |
|---|---|---|---|---|---|---|---|
| Shape | 0 | $1 \times 10^{-4}$ | 0.04 | - | - | - | 5/4 |
| Charge/Momentum | 0.9 | $3 \times 10^{-3}$ | 0.2 | 0.1 | 0.05 | 0.02 | 18/8 |

alone. The low statistics of the data account for the discrepancy between the two tests. The measurements based on both tests are consistent with the null oscillation hypothesis and the Super-K oscillation parameters, as the points representing those hypotheses are allowed at 90% confidence.

## 8.5 *CPT*-Violation Search

The magnetic field of the MINOS far detector allows the discrimination of $\mu^-$ from $\mu^+$. The neutrino-induced muons can be separated into these charge sign categories

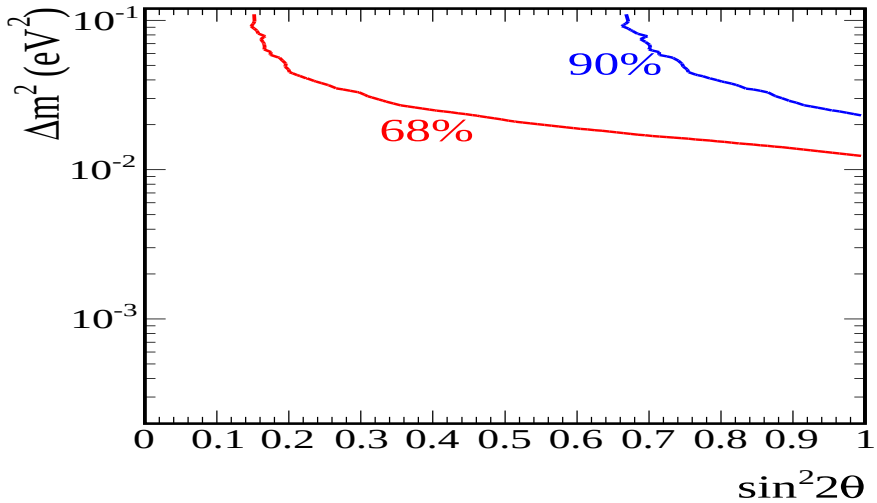


Figure 8.15: Confidence intervals for oscillation parameter measurement using charge sign and momentum information. Allowed values are to the left of the curves.

to look for *CPT*-violation in the oscillations of $\nu_\mu \rightarrow \nu_\tau$ and $\overline{\nu}_\mu \rightarrow \overline{\nu}_\tau$. The signature of *CPT*-violation is different oscillation probabilities for $\nu_\mu$ and $\overline{\nu}_\mu$, which is also the signature of *CP*-violations. MINOS can look for *CPT*-violation in the atmospheric neutrinos but not for *CP*-violation because MINOS is a disappearance experiment. A disappearance experiment only observes a deficit of the expected neutrino flavor, it cannot observe the neutrinos of the new flavor. To detect *CP*-violation it is necessary to observe the different deficits of $\nu_\mu$ and $\overline{\nu}_\mu$ as well as different appearance rates for $\nu_\tau$ and $\overline{\nu}_\tau$. MINOS cannot detect $\nu_\tau$ and $\overline{\nu}_\tau$ which means that different observed deficits of $\nu_\mu$ and $\overline{\nu}_\mu$ indicate that those neutrinos are oscillating into different neutrino flavors, but not necessarily $\nu_\mu \rightarrow \nu_\tau$ and $\overline{\nu}_\mu \rightarrow \overline{\nu}_\tau$. If *CPT*-violation is observed, it would indicate new physics beyond the SM. The Super-K collaboration has already

shown that its data are consistent with no *CPT*-violation [55]. However, this result is not based on a direct measurement of the two charge sign categories. Rather, the Super-K collaboration looked to see how different the $\Delta m^2_{\nu_\mu}$ and $\Delta m^2_{\overline{\nu}_\mu}$ could be while still being consistent with its global oscillation parameter fit.

The search for *CPT*-violation is similar to the oscillation parameter fit. The $\nu_\mu$ and $\overline{\nu}_\mu$ are assumed to oscillate with $\sin^2 2\theta = 1$ but with different values of $\Delta m^2$. The choice of $\sin^2 2\theta = 1$ is made because the Super-K data indicate maximal mixing [34, 56, 51]. The data are fit for $\Delta m^2_{\nu_\mu}$ and $\Delta m^2_{\overline{\nu}_\mu}$ using the $\chi^2$ statistic defined in eq (8.1). The predicted number of events based on the Monte Carlo is given by eq (8.2). The confidence intervals for the fit values of $\Delta m^2_{\nu_\mu}$ and $\Delta m^2_{\overline{\nu}_\mu}$ are given by the standard method of finding $\delta\chi^2$ because these values are not constrained by a physical boundary.

The fit to the data for $\nu_\mu \rightarrow \nu_\alpha$ and $\overline{\nu}_\mu \rightarrow \overline{\nu}_\beta$ oscillations is shown in Table 8.5. The normalization for the *CPT*-violation analysis agrees with the value given by the oscillation parameter fit over all $\cos\theta$, charge and momentum bins. The confidence intervals are shown in Fig. 8.16. The intervals are labeled in the figure. The best fit indicates that the $\nu_\mu$ and $\overline{\nu}_\mu$ oscillate with different values of $\Delta m^2$. The confidence regions are quite broad, however, and more data are needed to make a definite statement.

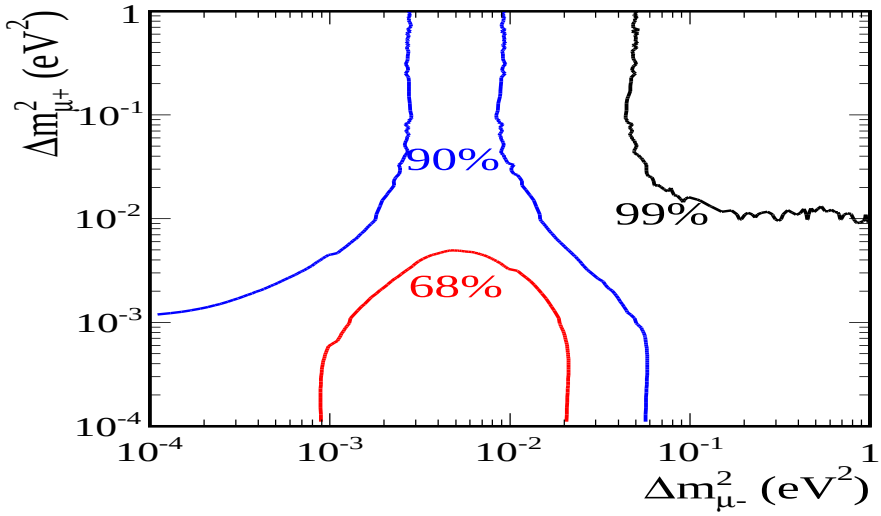


Figure 8.16: Confidence intervals for the *CPT*-violation measurement. The best fit point is $\Delta m^2_{\nu_\mu} = 5 \times 10^{-3}$ eV$^2$ and $\Delta m^2_{\overline{\nu}_\mu} = 3 \times 10^{-4}$ eV$^2$. The 68% allowed region contains all points inside the contour. The 90% allowed region contains all points between the 68% and 90% contours. Points with $\Delta m^2_{\nu_\mu} > 6 \times 10^{-2}$eV$^2$ and $\Delta m^2_{\overline{\nu}_\mu} > 10^{-2}$ eV$^2$ are excluded at 99% confidence.

Table 8.5: *CPT*-violation fit parameters.

| $\Delta m^2_{\nu_\mu}$ (eV$^2$) | $\Delta m^2_{\overline{\nu}_\mu}$ (eV$^2$) | $\epsilon_1$ | $\epsilon_2$ | $\epsilon_3$ | $\epsilon_4$ | $\chi^2/ndf$ |
|---|---|---|---|---|---|---|
| $5 \times 10^{-3}$ | $3 \times 10^{-4}$ | 0.18 | 0.14 | 0.02 | 0.03 | 16/8 |

## 8.6 4 Year Predictions

While the current data set is limited by statistics, the expected data set after 4 years should be large enough to make much stronger claims about the oscillation parameters and potential *CPT*-violation. To get the expected sample for the average 4 year exposure, the total Monte Carlo data set was scaled accordingly.

The event rate for neutrino-induced muons observed in the far detector is approximately 1 event/6 live days. The Monte Carlo shows a similar rate, giving an expected data set of $\sim 250$ events for 4 years. The expected distributions for the various $\cos\theta$, charge sign, and momentum bins are shown in Fig. 8.17. The high momentum bins should give a good handle on the overall flux normalization, as the neutrinos producing the muons in these bins do not have large oscillation probabilities. Also the highest $\cos\theta$ bin will help determine the normalization for all neutrino energies for the same reason. The figure shows both the unoscillated prediction (solid line) and the oscillated prediction using $\sin^2 2\theta = 1$ and $\Delta m^2 = 2.5 \times 10^{-3}\mathrm{eV}^2$ (dashed line).

The predicted confidence intervals for the oscillation measurement based on the oscillated distributions are shown in Fig. 8.18. This figure provides a comparison of the intervals obtained using the Gaussian approximation (a) and the method of Feldman and Cousins (b). The indicated 68% and 90% allowed regions are approximately the same for both methods, while the 99% region is much smaller using the method of Feldman and Cousins. These intervals were made by fitting for the oscil-

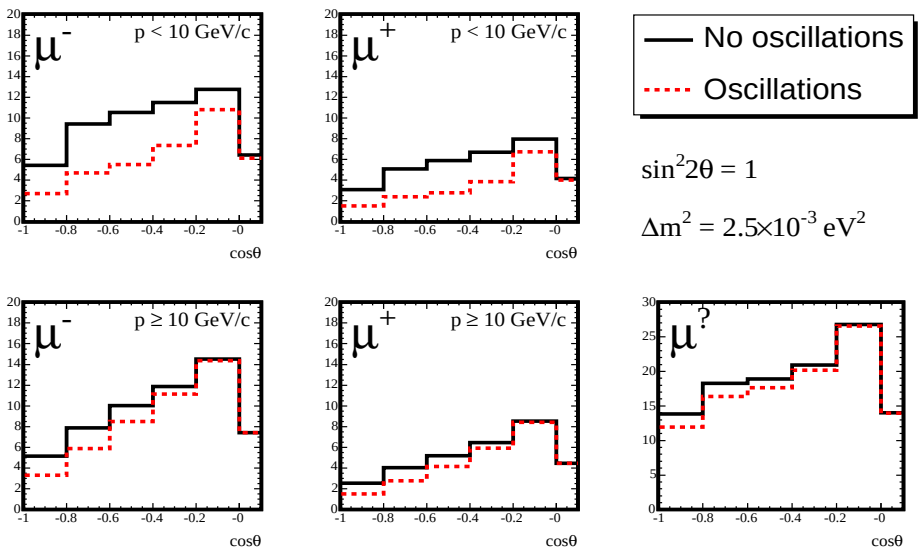


Figure 8.17: Predicted event rates for the various $\cos\theta$, charge sign, and momentum bins for a 4 year exposure. The unoscillated prediction is the solid line, and the oscillated prediction using $\sin^2 2\theta = 1$ and $\Delta m^2 = 2.5 \times 10^{-3}\text{eV}^2$ is represented by the dashed line.

lation parameters and the $\epsilon_k$ using the errors given in § 8.3.1. The systematic errors will likely be smaller after 4 years of running because the detector will be better understood by that time so the intervals in Fig. 8.18 should be taken as a conservative prediction. Even so, they indicate that MINOS can determine $\sin^2 2\theta \geq 0.35$ and $5 \times 10^{-4}$ eV$^2 \leq \Delta m^2 \leq 2 \times 10^{-2}$ eV$^2$ at 90% confidence using only the neutrino-induced muons. The predicted confidence intervals for the *CPT*-violation measurement based on the distributions of Fig. 8.17 are shown in Fig. 8.19. The 68%, 90%, and 99% intervals are marked in the figure. Again, these intervals should be considered a conservative estimate. The point marked by the star in the figure is where $\Delta m^2_{\nu_\mu} = \Delta m^2_{\overline{\nu}_\mu} = 2.5 \times 10^{-3}$ eV$^2$. Fig. 8.20 shows the predicted confidence intervals

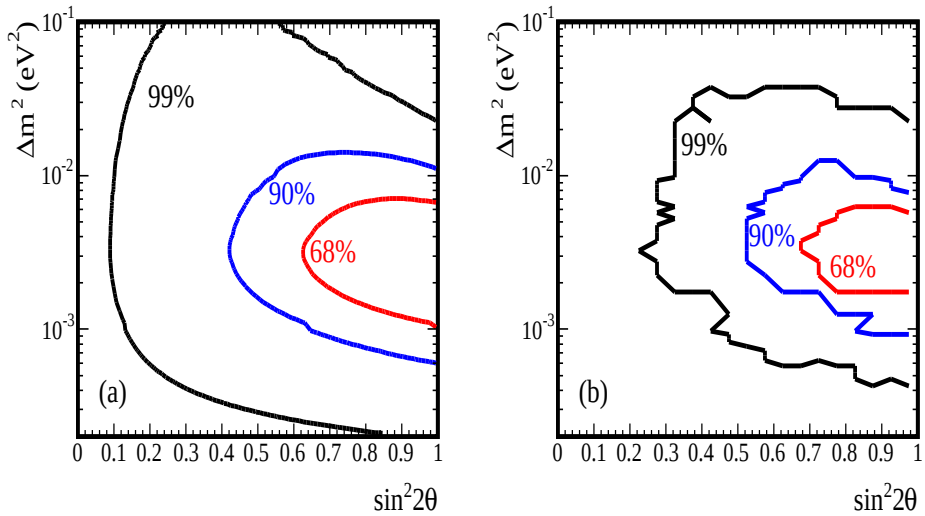


Figure 8.18: Predicted confidence intervals for a measurement of the oscillation parameters after 4 live years for the Gaussian approximation (a) and the method of Feldman and Cousins (b). The oscillation parameters used to make these figures are $\sin^2 2\theta = 1$ and $\Delta m^2 = 2.5 \times 10^{-3}$ eV$^2$.

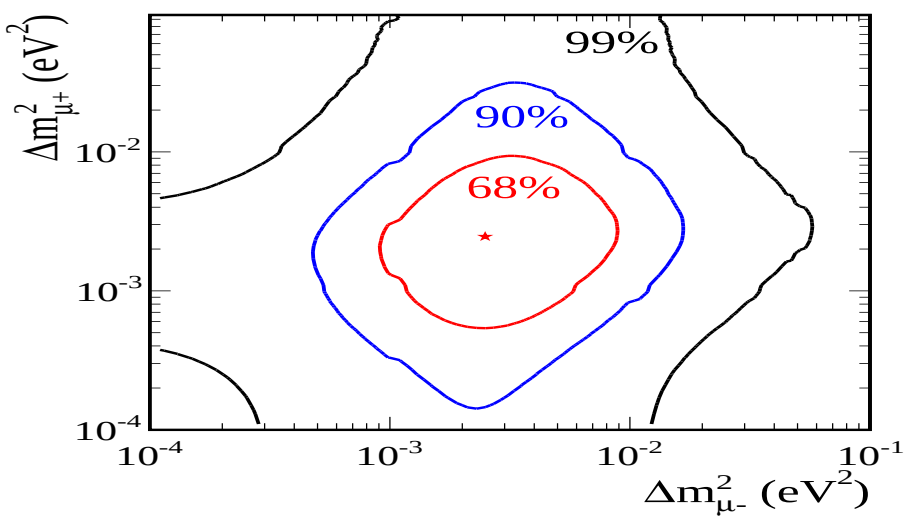


Figure 8.19: Predicted confidence intervals for a measurement of *CPT*-violation after 4 live years. The star marks $\Delta m^2_{\nu_\mu} = \Delta m^2_{\bar{\nu}_\mu} = 2.5 \times 10^{-3}$ eV$^2$. The 68%, 90% and 99% intervals are labeled.

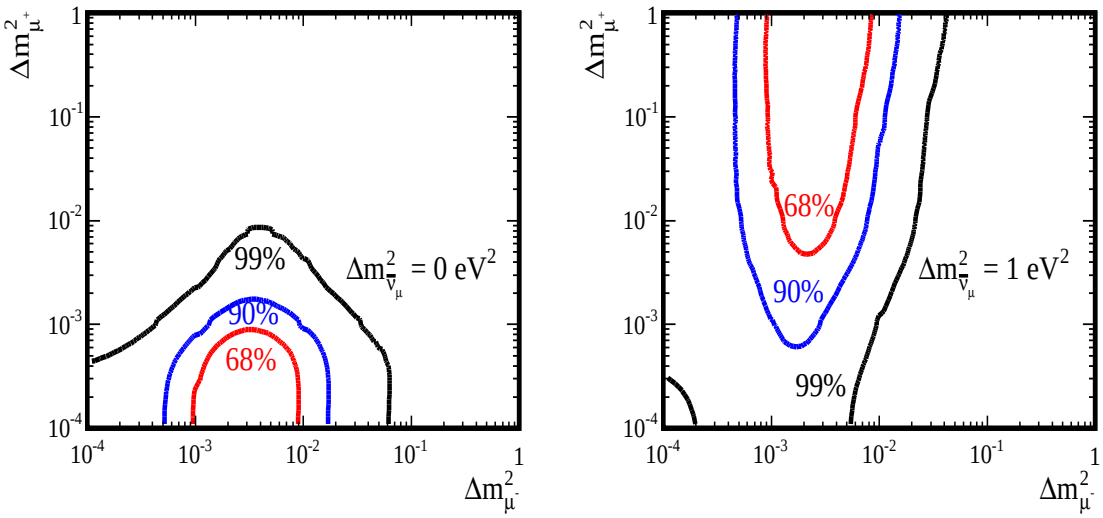


Figure 8.20: Predicted confidence intervals for a measurement of *CPT*-violation after 4 live years with $\Delta m^2_{\nu_\mu} = 2.5 \times 10^{-3}$ eV$^2$ and the cases $\Delta m^2_{\overline{\nu}_\mu} = 0$ eV$^2$ (left) and $\Delta m^2_{\overline{\nu}_\mu} = 1$ eV$^2$ (right).

for two cases where $\Delta m^2_{\overline{\nu}_\mu}$ is very different from $\Delta m^2_{\nu_\mu} = 2.5 \times 10^{-3}$ eV$^2$. The left side of the figure shows $\Delta m^2_{\overline{\nu}_\mu} = 0$ eV$^2$, which corresponds to no oscillations in the $\overline{\nu}_\mu$. The right side of the figure shows the case for $\Delta m^2_{\overline{\nu}_\mu} = 1$ eV$^2$. This case corresponds to the same region in parameter space as the LSND result. Figs. 8.19 and 8.20 show that MINOS should be able to distinguish *CPT*-violation from no *CPT*-violation using only the neutrino-induced muons at 68% confidence in either of these two cases.

# Chapter 9

# Conclusions

This dissertation represents a wide variety of contributions to the MINOS experiment. It details work done during detector design and construction, software written for the event reconstruction, and analyses of the cosmic ray and atmospheric neutrino data taken with the far detector.

The optical connectors described in § 4.2.3 and the MUX boxes described in § 4.2.4 are an integral part of the scintillator system. These connectors enable the routing of signal from the active detector elements to the readout PMTs with minimal loss of light. The MUX boxes provide a sturdy environment to house the PMTs and the multiplexing done inside the boxes allowed the electronics cost of the experiment to be minimized. I was involved in making both of these pieces of the scintillator system operational by helping to design the procedures used to construct and test them.

The DeMux software that I wrote and that is described in Chapter 5 removes the ambiguity of the origin of signals in the far detector that is introduced due to the multiplexing pattern. The algorithm takes the signals from each plane in the detector and decides the most likely strips of origin for the signal on each plane by using the amount of signal seen on one side of the plane to predict the location of the signals on the other side. It then takes the most likely origins from the individual planes in each event and combines the information from all planes in the event to determine the DeMuxed solution. This software is the default algorithm used by the collaboration and is the first step in the reconstruction chain for events in the far detector. It has been shown to be have an efficiency of greater than 90% for both beam and cosmic ray events.

The MINOS far detector has taken data under two detector configurations since July, 2002. In the first configuration, lasting from July, 2002 through May, 2003, the first supermodule was complete and magnetized while the second supermodule was still under construction. The second configuration had both supermodules complete and magnetized. Two analyses were presented using these data. The first analysis looked at cosmic ray muons and used only the SM1+SM2 data set. The second looked at neutrino-induced muons and used both data sets.

The analysis of the cosmic ray muon data had two purposes. The first was to determine how well the far detector performance was understood. The cosmic ray muon data were used to measure the vertical muon intensity at the MINOS

detector. The intensity for all single muons agrees well with previous measurements done by the MACRO collaboration. This result indicates that the efficiency and acceptance of the detector are understood. The second purpose of the cosmic ray muon analysis was to separate the muons into $\mu^+$ and $\mu^-$ as no previous underground experiment had done so. The muons were separated into $\mu^+$ and $\mu^-$ and the ratio of the $\mu^+$ to $\mu^-$ intensity was found. The ratio found was $N_{\mu^+}/N_{\mu^-} = 1.43$, although it shows statistically significant structure over the range of slant depths used. The $N_{\mu^+}/N_{\mu^-}$ ratio was also examined as a function of several other parameters such as $\cos\theta$, $\phi$ and $p_{\text{fit}}$. All methods of examining the charge ratio show peculiar structure that is not understood as yet. The magnetic field of the detector was designed to focus $\mu^-$ coming from the south, which means it also focuses $\mu^+$ coming from the north. The effect of focusing on the charge identification was examined, and it was determined that the structure seen in the $N_{\mu^+}/N_{\mu^-}$ ratios is not entirely due to focusing. One possible origin of the structure is the magnetic field map used during event reconstruction. The magnetic field in the detector may be different from the field map used for reconstruction,resulting in poor charge and momentum determination. Several studies to determine the effect of reconstructing Monte Carlo events with a different field map than the one used to generate the events were done. One study showed that the Monte Carlo can be made to reproduce certain data distributions when the magnetic field map is altered to have a field that is 5% larger than the field used to generate the Monte Carlo events on 10% of the

planes in the detector. The results of that study agree well with the data, which show that the charge sign determination depends on the section of the detector traversed by the muon. While the charge separation for the cosmic rays is not yet fully understood, substantial progress has been made. The charge separation is expected to be understood in the near future.

The neutrino-induced muon analysis represents several new aspects of an analysis of atmospheric neutrino oscillations using this class of events. First, this is the first analysis to be able to determine the momenta of the neutrino-induced muons over a wide range of momenta. The second aspect, related to the first, is that this is the first analysis to separate these muons into $\mu^-$ and $\mu^+$, enabling a search for *CPT*-violation to be done. Third, the flat overburden of the Soudan site allows MINOS to look for neutrino-induced muons coming from slightly above the horizon without having the data sample contaminated by cosmic ray muons. This aspect allows a new range of values of $L/E$, the ratio of the distances traveled by the neutrinos to their energies, to be explored in the neutrino oscillation analysis.

A total of 50 neutrino-induced muons were identified in the SM1 and SM1+SM2 data sets. These data were used to do two tests for neutrino oscillations in the atmospheric neutrinos. The first test looked at the shape of the $\cos\theta$ distribution of the muons to probe for neutrino oscillations. The second test looked at the shape as a function of fit momentum and charge sign. Both tests are consistent with either oscillations or no oscillations. These data were also used to look for *CPT*-

violation in the atmospheric neutrino oscillations. The measurement has a best fit at $\Delta m^2_{\nu_\mu} = 5 \times 10^{-3}\text{eV}^2$ and $\Delta m^2_{\overline{\nu}_\mu} = 3 \times 10^{-4}\text{eV}^2$. While the best fit point indicates that there is *CPT*-violation, the 68% confidence level contour contains points that are consistent with no *CPT*-violation as well.

Although the number of events used to make the oscillation and *CPT*-violation measurements is still small, the experiment can expect to collect $\sim$ 250 events over the next 4 years assuming that the Super-K oscillation parameters are correct. This number of events should be enough to provide a measurement on the oscillation parameters with 90% confidence intervals bounded by $\sin^2 2\theta \geq 0.35$ and $5 \times 10^{-4}$ eV$^2 \leq \Delta m^2 \leq 10^{-2}$ eV$^2$ using only the neutrino-induced muons. This bound is a conservative estimate of the MINOS measurement of the oscillation parameters using neutrino-induced muons because the systematic errors are expected to decrease as the detector becomes better understood over time. The predicted 90% confidence interval bounds for the *CPT*-violation measurement assuming that *CPT* is not violated are $4 \times 10^{-4} < \Delta m^2_{\nu_\mu} < 2 \times 10^{-2}$ eV$^2$ and $1 \times 10^{-4} < \Delta m^2_{\overline{\nu}_\mu} < 2 \times 10^{-2}$ eV$^2$. Furthermore, MINOS should be able to distinguish no *CPT*-violation from *CPT*-violation for the cases $\Delta m^2_{\overline{\nu}_\mu} = 0$ and $\Delta m^2_{\overline{\nu}_\mu} = 1$ eV$^2$ at the 68% confidence level in 4 years.

While both the cosmic ray muon and neutrino-induced muon analyses will continue for the duration of the experiment, a new phase of the experiment is about to begin. MINOS will see the first events from the neutrino beam starting in 2005. My

analysis responsibilities will expand to include the beam data, and I expect to play a major role in the analysis of the observed neutral current events.

# Bibliography


[1] Y. Fukuda et al. *Phys. Lett.*, B467:185–193, 1999.

[2] M. Ambrosio et al. *Phys. Lett.*, B434:451–457, 1998.

[3] K. Hagiwara et al. Review of particle physics. *Physical Review D*, 66, 2002.

[4] T. K. Gaisser and M. Honda. *Ann. Rev. Nucl. Part. Sci.*, 52:153–199, 2002.

[5] T. K. Gaisser and Todor Stanev. *Phys. Rev.*, D57:1977–1982, 1998.

[6] M. C. Gonzalez-Garcia and Yosef Nir. *Rev. Mod. Phys.*, 75:345–402, 2003.

[7] F. Reines and C. L. Cowan. *Phys. Rev.*, 92:830–831, 1953.

[8] L. Goldhaber, M. Grodzins and A.W. Sunyar. *Phys. Rev.*, 109:1015, 1958.

[9] B. Pontecorvo. *JETP*, 10:1236, 1960.

[10] G. Danby et al. *Phys. Rev. Lett.*, 9:36–44, 1962.

[11] Martin L. Perl et al. *Phys. Rev. Lett.*, 35:1489–1492, 1975.

[12] K. Kodama et al. *Phys. Lett.*, B504:218–224, 2001.

[13] LEP Collaborations. *Phys. Lett.*, B276:247–253, 1992.

[14] D. H. Perkins. *Introduction to High Energy Physics*. Cambridge University Press, Cambridge, U.K., 2000.

[15] Boris Kayser. *Nucl. Phys. Proc. Suppl.*, 118:425–437, 2003.

[16] Gautam Bhattacharyya, Heinrich Paes, Li-guo Song, and Thomas J. Weiler. *Phys. Lett.*, B564:175–182, 2003.

[17] A. Osipowicz et al. *hep-ex/0109033*, 2001.

[18] Boris Kayser. *hep-ph/0211134*, 2002.

[19] H. V. Klapdor-Kleingrothaus et al. *Eur. Phys. J.*, A12:147–154, 2001.

[20] C. Arnaboldi et al. *Phys. Lett.*, B584:260–268, 2004.

[21] B. Pontecorvo. *Zh. Eksp. Teor. Fiz.*, 53:1717, 1967.

[22] Gary J. Feldman and Robert D. Cousins. *Phys. Rev.*, D57:3873–3889, 1998.

[23] D. D. Clayton. *Principles of Stellar Evolution and Nucleosymthesis*. University of Chicago Press, Chicago, 1983.

[24] J.N. Bahcall, M.H. Pinsonneault, and S. Basu. *Astrophys. J.*, 555:990, 2001.

[25] John N. Bahcall, M. H. Pinsonneault, and Sarbani Basu. *Astrophys. J.*, 555:990–1012, 2001.

[26] John N. Bahcall, M. H. Pinsonneault, Sarbani Basu, and J. Christensen-Dalsgaard. *Phys. Rev. Lett.*, 78:171–174, 1997.

[27] L. Wolfenstein. *Phys. Rev.*, D17:2369, 1978.

[28] S. P. Mikheyev and A. Yu. Smirnov. *Prog. Part. Nucl. Phys.*, 23:41–136, 1989.

[29] Q. R. The SNO Collaboration, Ahmad et al. *Phys. Rev. Lett.*, 89:011301, 2002.

[30] F. Reines and C.L. Cowan. *Phys. Rev.*, 92:830, 1953.

[31] K. Eguchi et al. *Phys. Rev. Lett.*, 90:021802, 2003.

[32] B. Kayser. Neutrino physics as explored by flavor change (new). *Phys. Rev.*, D66, 2002.

[33] G. Gratta. Neutrino04. 2004.

[34] Y. Hayato. Noon03. 2003.

[35] M. H. Ahn et al. *Phys. Rev. Lett.*, 90:041801, 2003.

[36] The MINOS Collaboration. Technical design report for minos detectors. 1996.

[37] R. Lee and S Seun. Crosstalk measurements at the far detector. *NuMI-NOTE-SCINT,ELEC-0795*, 2001.

[38] T. K. Gaisser. Cosmic rays and particle physics. Cambridge, UK: Univ. Pr. (1990) 279 p.

[39] S. M. S. Kasahara. A study of cosmic ray composition in the knee region using multiple muon events in the soudan 2 detector.

[40] Alice Michel Hawthorne. A detailed study of upward through going muons in the macro detector. UMI-98-25449.

[41] M. Ambrosio et al. *Phys. Rev.*, D52:3793–3802, 1995.

[42] M. Crouch. *Proceedings of the 20th International Cosmic Ray Conference*, HE 4.1-2:165, 1987.

[43] C. Timmermans. Cosmic rays with the lep detectors. Prepared for 31st International Conference on High Energy Physics (ICHEP 2002), Amsterdam, The Netherlands, 24-31 Jul 2002.

[44] R. Fruhwirth. *Wien Inst. Hochenergiephys. - HEPHY-PUB-87-503 (87,REC.JUN.) 19p.*

[45] E. J. Wolin and L. L. Ho. *Nucl. Instrum. Meth.*, A329:493–500, 1993.

[46] Gaisser T. K. Lipari P Agrawal, V. and T. Stanev. *Phys. Rev.*, D53:1314–1323, 1996.

[47] M. Ambrosio et al. *Phys. Rev.*, D67:042002, 2003.

[48] D. Casper. *Nucl. Phys. Proc. Suppl.*, 112:161–170, 2002.

[49] M. Ambrosio et al. *Phys. Lett.*, B566:35–44, 2003.

[50] Jr. Demuth, David M. A search for neutrinos from active galactic nuclei. UMI-99-41724.

[51] S. Fukuda et al. *Phys. Rev. Lett.*, 85:3999–4003, 2000.

[52] M. Honda, T. Kajita, K. Kasahara, and S. Midorikawa. *Phys. Rev.*, D52:4985–5005, 1995.

[53] W. H. Press et al. Numerical recipes in c. Cambridge, UK: Univ. Pr. (1992) 994 p.

[54] Mark D. Messier. Evidence for neutrino mass from observations of atmospheric neutrinos with super-kamiokande. UMI-99-23965.

[55] A. Habig. Atmospheric neutrino oscillations in sk-i. Prepared for 28th International Cosmic Ray Conferences (ICRC 2003), Tsukuba, Japan, 31 Jul - 7 Aug 2003.

[56] Y. Ashie et al. Evidence for an oscillatory signature in atmospheric neutrino oscillation. 2004.